THE SEARCH FOR THE DECAY $K^+ \to \pi^+ \nu\overline{\nu}$

by

André Spence Turcot
B.Sc., Concordia University, 1985
M.Sc., University of Victoria, 1987

A Dissertation Submitted in Partial Fulfillment of the
Requirements for the Degree of

DOCTOR OF PHILOSOPHY

in the Department of Physics and Astronomy

We accept this thesis as conforming
to the required standard

Dr. D.A. Bryman, Co-Supervisor, (Department of Physics & Astronomy)

Dr. A. Astbury, Co-Supervisor, (Department of Physics & Astronomy)

Dr. L.P. Robertson, Departmental Member (Department of Physics & Astronomy)

Dr. R.K. Keeler, Departmental Member (Department of Physics & Astronomy)

Dr. D.J. Leeming, Outside Member, (Department of Mathematics)

Dr. A. McAuley, Outside Member, (Department of Chemistry)

Dr. M.S. Dixit, External Examiner, (CRPP, Carleton University)

Supervisor: Dr. Douglas Bryman

ABSTRACT

The search for the rare kaon decay $K^+ \to \pi^+\nu\overline{\nu}$ performed at Brookhaven National Laboratory using the E-787 Spectrometer is described. The data presented was acquired over the three year period 1989 to 1991. The decay $K^+ \to \pi^+\nu\overline{\nu}$ is an example of a Flavour-Changing-Neutral-Current process and is allowed to proceed only at second-order in the weak interaction. The Standard Model prediction for the $K^+ \to \pi^+\nu\overline{\nu}$ branching ratio is in the range of 0.6 to 6 $\times 10^{-10}$, where the uncertainty is from experimental knowledge of the fundamental parameters of the theory. The measurement of the branching ratio provides a unique test of the Glashow-Iliopoulos-Maiani Mechanism of Flavour-Changing-Neutral-Current suppression.

Based on observation of no candidate events in the kinematic region $P > 211$ MeV/c and an integrated flux of $(3.47 \pm 0.03) \times 10^{11}$ stopped kaons, an upper limit for the $K^+ \to \pi^+\nu\overline{\nu}$ branching ratio of 3.6×10^{-9} at the 90% confidence level has been set. For the two-body decay $K^+ \to \pi^+ X^0$, where X^0 is a hypothetical massless weakly interacting particle, a 90% C.L. upper limit of 6.1×10^{-10} has been obtained.

Examiners:

Dr. D.A. Bryman, Co-Supervisor, (Department of Physics & Astronomy)

Dr. A. Astbury, Co-Supervisor, (Department of Physics & Astronomy)

Dr. L.P. Robertson, Departmental Member (Department of Physics & Astronomy)

Dr. R.K. Keeler, Departmental Memeber (Department of Physics & Astronomy)

Dr. D.J. Leeming, Outside Member, (Department of Mathematics)

Dr. A. McAuley, Outside Member, (Department of Chemistry)

Dr. M.S. Dixit, External Examiner, (CRPP, Carleton University)

Table of Contents

List of Tables

List of Figures

Acknowledgments

It seems like it was just yesterday that I was a child reading stories of strange far away places like BNL and SLAC, and of even stranger particles like the Ω^- in the Time-Life book on physics. Many years have passed since then and a lifelong dream has been fulfilled.

Among the many people that have made this possible, there are two people that stand out and to whom I am deeply indebted. First and foremost is my dear Natasha and second is Doug Bryman. They share the rare distinction of keeping me around after knowing me for more than 2 years.

I would like to thank all the great people from BNL and Princeton that I have had the pleasure of working with on E-787. I cannot help but feel that I have worked with some of the finest and most dedicated people in the business. Special thanks to those 787'ers who performed various calibrations, kept the detector running smoothly, and, of course, to my collegues on the PASS0 and PASS1 teams.

I would like to thank Akira Konaka and Paul Padley for many entertaining discussions which have helped shaped this work. Finally, to all my friends here at TRIUMF, much thanks for all the fun. Just remember that when in doubt:

- Throw it to the shortstop.
- Call two banks instead of one.
- No, they aren't real.
- The best time to buy/sell is when nobody else is.

Chapter 1

Introduction

The precious rare decay par-excellence.

- I. Bigi

1.1 Overview

The Standard Model of electroweak and strong interactions could be described as the most successful theory ever devised. There are no experimental data at present which require modifications or extensions to the theory. The Standard Model, despite its successes, does leave an enormous number of questions unanswered. In its present form, there are 18 arbitrary parameters (assuming massless neutrinos, 25 otherwise!) corresponding to 3 coupling constants, 6 quark masses, 3 lepton masses, 3 mixing angles, 1 CP violating phase as well as 2 parameters needed to describe the Higgs potential. There is also the curious three-fold replication of the generations that differ only in mass and their weak interaction decays. Questions that come to mind are: Why are the weak interaction eigenstates not the eigenstates of the strong interaction? Why are there three generations and not more (or less)?

There are two ways to probe the Standard Model. The first is to search at the highest possible energy frontier and find direct evidence for new particles or interactions. The second method is to test the predictions of the Standard Model at relatively low energy by studying or searching for processes whose rates are definitively predicted within the framework of the theory. This thesis, describing the search for $K^+ \to \pi^+\nu\overline{\nu}$ is an example of the second approach.

The decay $K^+ \to \pi^+\nu\overline{\nu}$ has historically been a "litmus test" for theory. The non-observation of this decay (among others) prompted Glashow, Iliopoulos and Maiani to postulate a new quark, *charm*, to suppress flavour changing neutral currents (FCNC) [1]. The so called GIM mechanism was an elegant means of removing the undesirable FCNC

by enabling their exact cancellation in a first order weak interaction. The present interest in $K^+ \to \pi^+\nu\overline{\nu}$ is motivated by the observation that, for a second order weak process, the GIM cancellation is not exact, as it is spoiled by the quark mass differences. Gaillard and Lee used this effect to correctly estimate the charm quark mass before its discovery by using constraints from the measured $K_L^0 - K_S^0$ mass difference [2].

The first calculation of the $K^+ \to \pi^+\nu\overline{\nu}$ decay rate in the framework of the present 3 generation, 6 quark Standard Model was performed by Inami and Lim [3] who noted that a heavy top quark could significantly enhance the $K^+ \to \pi^+\nu\overline{\nu}$ branching ratio to $O(10^{-9})$, a factor of 10 higher than the earlier 4 quark model based estimate of Gaillard and Lee [2]. More recent calculations of the $K^+ \to \pi^+\nu\overline{\nu}$ branching ratio, using updated Standard Model parameters, estimate the branching ratio to be in the range of $0.6 - 6 \times 10^{-10}$ [4, 5, 6]. The wide range reflects the experimental uncertainty in the Standard Model parameters.

At present, one of the missing Standard Model components is the top quark.[1] The top quark has yet to be observed due to its surprisingly high mass. Given that the $K^+ \to \pi^+\nu\overline{\nu}$ decay rate is sensitive to quark mass differences, this decay is an excellent probe of the top quark mass and its weak interaction couplings. Measurement of the $K^+ \to \pi^+\nu\overline{\nu}$ branching ratio offers the potential of providing the best estimate of the Standard Model parameter $|V_{td}|$ which measures the "mixing" of the down and top quarks in the weak interaction.

Experimentally, what is observed in $K^+ \to \pi^+\nu\overline{\nu}$, or more precisely, what is *not* observed, is the system of particles recoiling off of the π^+. Observation of a signal for $K^+ \to \pi^+$ with nothing else in the detector at a rate in excess of the Standard Model prediction would signify new physics. The GIM mechanism that suppresses FCNC processes also makes FCNC processes an excellent hunting ground for new heavy particle effects from non Standard Model physics. There are a number of theories which could produce an unexpectedly large $K^+ \to \pi^+ +$ *nothing* signal. Among these include an extension of the Standard Model to include a fourth family (necessarily associated with a massive neutrino $m_{\nu'} > M_{Z^0}/2$) that could raise the branching ratio to $O(10^{-9})$ [7]. Non Standard Model enhancements could arise from supersymmetry [8], Majorons [9], or light Goldstone bosons associated with the symmetry breaking of new gauge groups. An example of the latter includes the Wilczek familon arising from the breaking of global family symmetry [10]. Any two body kaon decay of the type $K^+ \to \pi^+ X^0$, where X^0 is not a π^0, would herald new physics.

Although there are other processes that probe the weak interaction at second order, $K^+ \to \pi^+\nu\overline{\nu}$ is one of the cleanest processes to theoretically evaluate. The lack of long-

[1] The other fundamental particles predicted by the Standard Model that have eluded direct detection to now are the tau type neutrino, ν_τ, and the Higgs boson, H^0, which is responsible for generating particle masses. There is strong indirect evidence for the τ type neutrino from the observed width of the Z^0.

distance hadronic and electromagnetic contributions, combined with a well known matrix element describing the hadronic aspects of decay, implies that the theoretical uncertainty in the decay rate is dominated by the knowledge of the input Standard Model parameters. Therefore, the $K^+ \rightarrow \pi^+\nu\bar{\nu}$ branching ratio provides a powerful constraint when evaluating Standard Model parameters. By simultaneously examining other GIM suppressed FCNC processes, it is possible to over-constrain these parameters which, if new physics is present, could lead to insights on the source of the discrepancy.

This thesis describes the search for $K^+ \rightarrow \pi^+\nu\bar{\nu}$. The experiment, BNL E-787, was performed at the Alternating Gradient Synchrotron located in Brookhaven National Laboratory situated in Upton New York by a collaboration of BNL, Princeton and TRIUMF physicists. A list of the E-787 members is given in Appendix A. The ultimate goal of E-787 is to achieve a sensitivity for the $K^+ \rightarrow \pi^+\nu\bar{\nu}$ branching ratio at the 1×10^{-10} level. Based on the 1989 data set, E-787 has set the upper limit for the $K^+ \rightarrow \pi^+\nu\bar{\nu}$ branching ratio at,

$$\mathrm{BR}(K^+ \rightarrow \pi^+\nu\bar{\nu}) \leq 7.5 \times 10^{-9} \ \ 90\% \ \ \mathrm{C.L.}$$

for the kinematic region $P_\pi > 211$ MeV/c [11]. The experiment simultaneously studies the two body process $K^+ \rightarrow \pi^+ X^0$. For the case where X^0 is any weakly interacting massless particle, the present experimental upper limit is [11],

$$\mathrm{BR}(K^+ \rightarrow \pi^+ X^0) \leq 1.7 \times 10^{-9} \ \ 90\% \ \ \mathrm{C.L.}$$

The experiment is continuing; the data analysed in this thesis was amassed during 3 running periods spanning 1989 to 1991. Chapter ? describes the experiment and outlines the strategy used to identify $K^+ \rightarrow \pi^+\nu\bar{\nu}$ candidates and the techniques used to suppress potential backgrounds to the 10^{-10} level. The E-787 detector is presented with a focus on how the various detector subsystems are used to suppress the backgrounds. Chapter 3 summarizes the off-line analysis. The analysis was performed "blind"; all the $K^+ \rightarrow \pi^+\nu\bar{\nu}$ selection criteria were devised without inspection of the events in the signal region. The success of such an approach depends on the detailed understanding of the potential backgrounds. Chapter 3 also describes and summarizes the *a priori* background studies. The off-line selection criteria used to select $K^+ \rightarrow \pi^+\nu\bar{\nu}$ candidates are described in detail in chapter 4. The method of estimating the background levels from the various sources are described in chapter 5. In chapter 6, the final spectrum of events passing the off-line analysis is discussed. Chapter 7 describes the measurement of the acceptance and overall sensitivity, and finally, chapter 8 summarizes the results and discusses the future for E-787.

1.2 Theoretical Considerations

Before the phenomenology of flavour changing neutral current processes can be introduced and the case for $K^+ \to \pi^+\nu\overline{\nu}$ presented, a brief overview of the Standard Model is mandatory. It is also instructive to review the history of kaon physics.

1.2.1 A Little History

In the relatively new discipline of particle physics, the most surprising of all the additions to the pantheon of sub-atomic particles has been the kaon. Study of the charged kaon and its neutral counterparts, the K_L^0 and K_S^0, have fundamentally altered the way the Universe was originally thought to be.

In the early 1950's, Gell-Mann and Nishijima [12] proposed a new quantum number "strangeness", S, to reconcile the surprisingly long kaon lifetime with its observed production cross section. Strangeness was postulated to be conserved by the strong and electromagnetic interactions and violated by the weak interaction. Early studies of kaon decays suggested that there were two types of K^+, the ϑ and the τ. The particles could be differentiated only by their assigned intrinsic parity. Based on this, Lee and Yang [13] proposed that parity was not necessarily conserved in weak interactions. The discovery of parity violation by Wu *et al.* [14] was a surprise; however, it could be incorporated into the theory in a straight forward manner. Feynman and Gell-Mann [15] proposed that weak processes were described by a point-like current-current interaction of the form:

$$\mathcal{H}_{\text{weak}} = \frac{4G_F}{\sqrt{2}} \mathcal{J}_\lambda \mathcal{J}^{\lambda\dagger}, \tag{1}$$

where $\mathcal{J}^\dagger$ and $\mathcal{J}$ represented the charge lowering and charge raising currents for hadronic and leptonic decays. For leptons, the charged currents were of the form:

$$\mathcal{J}_\lambda = \bar{\nu}\gamma_\lambda(1-\gamma_5)e,$$

where $\bar{\nu}$, e were 4 component Dirac spinors and $\gamma_\lambda(1-\gamma_5)$ represented the $V-A$ Lorentz structure of the theory. The $\gamma_\lambda\gamma_5$ term was responsible for parity violation.

Soon after the parity party concluded and the $V-A$ structure of the weak current was established [16], it was observed that the different weak interactions did not proceed with the same coupling strength. Based on the comparison of $\Delta S = 0$ and $\Delta S = 1$ weak decay rates with the benchmark muon decay rate, Cabbibo [17] proposed that weak interaction universality could be maintained by modifying the hadronic currents entering equation 1. The modified hadronic current was given by,

$$\mathcal{J}_{\text{hadronic}} = \mathcal{J}_{\Delta S=0}\cos\theta_c + \mathcal{J}_{\Delta S=1}\sin\theta_c,$$

where $\theta_c \sim 13°$ was the Cabbibo angle.

In 1964, shortly after the Cabbibo theory was introduced, the physics world was stunned by the announcement of CP violation [18]. A BNL experiment designed to study K_L^0 decays observed that the K_L^0 decayed to a two pion final state with a branching ratio of 2×10^{-3}. The two pion decay was forbidden by the combined symmetry of charge conjugation and parity implicit in the $V - A$ structure of the weak interaction.

1.2.2 Standard Model

In the original version of the Standard Model, proposed by Glashow, Weinberg and Salam [19], electromagnetic and weak interactions were unified by introducing a gauge theory based on $SU(2)_L \times U(1)$ symmetry.[2] The theory replaced the Fermi current-current point interaction by introducing massive gauge bosons, the W^+, W^- and Z^0, which coupled to the fermion currents. The theory grouped the fundamental leptons into left handed doublets:

$$\begin{pmatrix} \nu_e \\ e^- \end{pmatrix}_L, \begin{pmatrix} \nu_\mu \\ \mu^- \end{pmatrix}_L,$$

with the $W^\pm$ coupling to the fermion currents given by:

$$\mathcal{J}_\lambda^{(\pm)} = \bar{\chi_L} \tau_\pm \gamma_\lambda (1 - \gamma_5) \chi_L,$$

where χ_L represented a lefthanded weak isospin doublet and $\tau_\pm$ were the Pauli isospin matrices. The $SU(2)$ structure of the theory required weak neutral currents coupled to the Z^0 of the form:

$$\mathcal{J}_\lambda^{NC} = \bar{\chi} \tau_3 \gamma_\lambda (1 - \gamma_5) \chi,$$

which predicted $\bar{\nu}_\mu + e^- \rightarrow e^- + \bar{\nu}_\mu$ scattering.

For the quark sector, in accordance with the Cabbibo ansantz, the weak isospin doublet was (u, d_θ) with $d_\theta = d \cos\theta_c + s \sin\theta_c$. The corresponding charged current, when expanded had the desired form (only the $\mathcal{J}_\lambda^+$ term is shown),

$$\mathcal{J}_\lambda^+ = \bar{u} \gamma_\lambda (1 - \gamma_5) d \cos\theta_C + \bar{u} \gamma_\lambda (1 - \gamma_5) s \sin\theta_C,$$

reproducing the effective $\Delta S = 0$ and $\Delta S = 1$ coupling strengths. However, evaluating the corresponding neutral current led to (neglecting the γ matrices):

$$\begin{aligned} \mathcal{J}^{NC} &= \bar{u}u + \bar{d}_\theta d_\theta \\ &= \bar{u}u + \bar{d}d \cos^2\theta_c + \bar{s}s \sin^2\theta_c + (\bar{d}s + \bar{s}d) \cos\theta_c \sin\theta_c, \end{aligned}$$

[2] An excellent presentation of the Standard Model is given by Quigg [20].

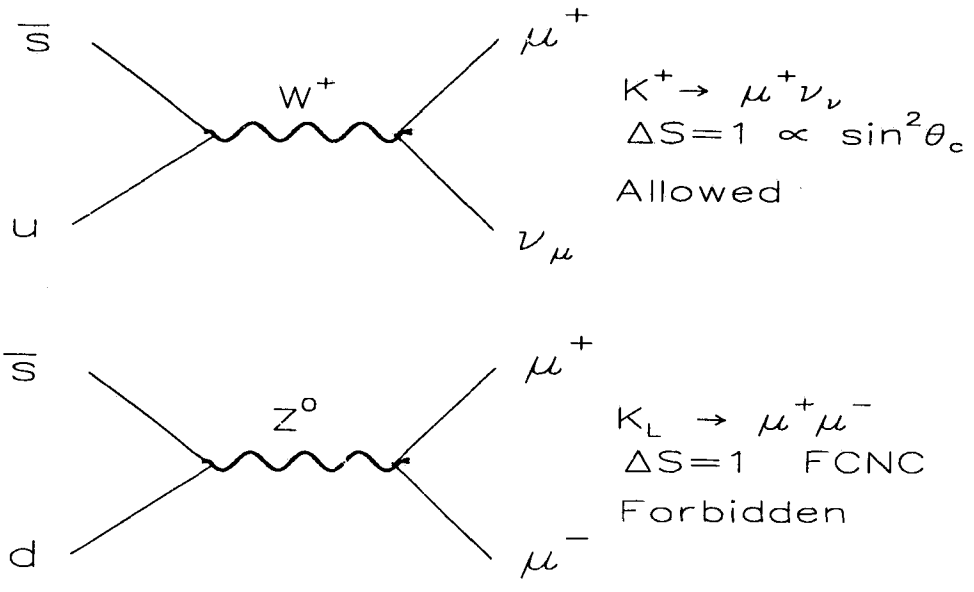

Figure 1.1: Feynman diagrams for the allowed decay $K_{\mu 2}$ and the forbidden first order flavour changing neutral current decay $K_L^0 \to \mu^+\mu^-$.

which predicted a non-zero amplitude proportional to $\cos\theta_c \sin\theta_c$ for $(s \to d)$ transitions. This was slightly embarrassing, as FCNC processes were known to be highly suppressed. At the time, branching ratio upper limits of $O(10^{-6})$ existed for the decays $K_L^0 \to \mu^+\mu^-$ and $K^+ \to \pi^+\nu\overline{\nu}$.

1.2.3 GIM Mechanism

Along with the non-observation of the predicted flavour changing neutral currents, the embryonic Standard Model had an additional problem; the perfectly valid orthogonal combination of $s_\theta = s\cos\theta_c - d\sin\theta_c$ did not fit in anywhere. It was somewhat unnatural that only the linear combination giving the correct charged current strength was used. In 1970, motivated by the existence of two doublets in the lepton sector, Glashow, Iliopoulos and Maiani postulated a fourth quark, *charm*, to complete the second quark doublet (c, s_θ) [1]. The weak isospin $I_3 = -1/2$ eigenstates were now related to the strong interaction mass eigenstates by a rotation matrix,

$$\begin{pmatrix} d_\theta \\ s_\theta \end{pmatrix} = \underbrace{\begin{pmatrix} \cos\theta_c & \sin\theta_c \\ -\sin\theta_c & \cos\theta_c \end{pmatrix}}_{U_C} \begin{pmatrix} d \\ s \end{pmatrix}.$$

The quark level neutral current was now:

$$\begin{aligned}
\mathcal{J}^{NC} &= \bar{u}u + \bar{c}c + \bar{d}_\theta d_\theta + \bar{s}_\theta s_\theta \\
&= \bar{u}u + \bar{c}c + \begin{pmatrix} \bar{d}_\theta & \bar{s}_\theta \end{pmatrix} \begin{pmatrix} d_\theta \\ s_\theta \end{pmatrix} \\
&= \bar{u}u + \bar{c}c + \begin{pmatrix} \bar{d} & \bar{s} \end{pmatrix} U_c^\dagger U_c \begin{pmatrix} d \\ s \end{pmatrix} \\
&= \bar{u}u + \bar{c}c + \bar{d}d + \bar{s}s.
\end{aligned}$$

Not only did the addition of the charm quark solve the FCNC problem, it also elegantly incorporated the "extra" orthogonal combination of s and d quarks. The simultaneous discovery of the charm quark in 1974 by groups working at BNL and SLAC was a striking vindication of the Standard Model [21].

1.2.4 The CKM Matrix

The four quark Standard Model was incomplete as there was still the question of CP violation. In 1973 Kobayashi and Maskawa demonstrated that the addition of a third quark doublet, (t, b), enabled the introduction of a CP violating phase into the expanded quark mixing matrix [22].[3] The mixing of $I_3 = -1/2$ or down type quarks was now given by:

$$\begin{pmatrix} d' \\ s' \\ b' \end{pmatrix} = \underbrace{\begin{pmatrix} V_{ud} & V_{us} & V_{ub} \\ V_{cd} & V_{cs} & V_{cb} \\ V_{td} & V_{ts} & V_{tb} \end{pmatrix}}_{V} \begin{pmatrix} d \\ s \\ b \end{pmatrix}, \tag{2}$$

where the matrix V is called the Cabibbo-Kobayashi-Maskawa (CKM) matrix. The CKM matrix has 4 independent parameters: 3 mixing angles that describe the couplings of quarks and 1 global complex phase which generates CP violation. The unitarity of V implies that the GIM mechanism of FCNC suppression remains intact. Wolfenstien [24] has proposed a parameterization of the CKM matrix based on powers of $\sin\theta_c \approx \lambda = 0.22$, which enables a geometrical interpretation of the matrix. In this parameterization, V is given by:

$$\begin{pmatrix} V_{ud} & V_{us} & V_{ub} \\ V_{cd} & V_{cs} & V_{cb} \\ V_{td} & V_{ts} & V_{tb} \end{pmatrix} = \begin{pmatrix} 1 - \frac{\lambda^2}{2} & \lambda & A\lambda^3(\rho - i\eta) \\ -\lambda & 1 - \frac{\lambda^2}{2} & A\lambda^2 \\ A\lambda^3(1 - \rho - i\eta) & -A\lambda^2 & 1 \end{pmatrix} + O(\lambda^4). \tag{3}$$

[3] It is noteworthy to point out that only *three* quarks had been "observed" at the time. The first evidence of a third generation was the discovery of the τ lepton in 1975 [23].

1.3 $K^+ \to \pi^+\nu\overline{\nu}$ and the Standard Model

Figure 1.2 shows the second order Feynman diagrams responsible for $K^+ \to \pi^+\nu\overline{\nu}$. The amplitude is a sum over the contributions of the three up-type quarks (charge = +2/3) and the different leptons for the case of the "Box" diagram. The hadronic aspects of the decay can be factored out of the $K^+ \to \pi^+\nu\overline{\nu}$ amplitude and are related by isospin to the well known matrix element $\langle\pi^0|(\bar{s}u)_{V-A}|K^+\rangle$ measured in $K^+ \to \pi^0 e^+\nu$ decays [2]. Precise knowledge of this matrix element is a major reason why $K^+ \to \pi^+\nu\overline{\nu}$ is so attractive for determining $|V_{td}|$. If QCD corrections (gluon exchanges between the quark lines in figure 1.2) and tau mass effects are ignored, the $K^+ \to \pi^+\nu\overline{\nu}$ branching for three generations is given by [3]:

$$\frac{\mathrm{BR}(K^+ \to \pi^+\nu\overline{\nu})}{\mathrm{BR}(K^+ \to \pi^0 e^+\nu)} = \frac{3\alpha^2}{8\pi^2 \sin^4\theta_W} \frac{1}{|V_{us}|^2} |\sum_{i=u,c,t} V_{qs}^* V_{qd} X(x_q)|^2, \tag{4}$$

where

$$X(x) = \frac{x}{8}\left[\frac{x+2}{(x-1)^2} + \frac{(3x-6)}{(x-1)^2}\ln x\right],$$

is a monotonically increasing function of the quark mass with $x_q = m_q^2/M_W^2$.

The sum over the u, c, t quarks is proportional to $\Sigma V_{qs}^* V_{qd}$, which, in the limit of equal quark masses vanishes due to the unitarity of the CKM matrix. Since the quark masses are different, the GIM cancellation of the second order $K^+ \to \pi^+\nu\overline{\nu}$ amplitude is only partially realized. The ratio of $X(x_c)$ to $X(x_t)$ is $O(10^{-4})$, suggesting that the top quark contribution completely dominates the amplitude; however, the kinematic enhancement from the large top quark mass is in turn suppressed by the smaller CKM couplings, V_{td} and V_{ts}. QCD corrections and τ mass effects reduce the charm contribution by about 30% [5, 25]. The net result is that the charm contribution to $K^+ \to \pi^+\nu\overline{\nu}$ decay rate is approximately 30% that of the top quark. The fact that the decay rate is primarily due to the top quark makes $K^+ \to \pi^+\nu\overline{\nu}$ an excellent top quark "laboratory". There are also potential "long distance" contributions of the form $K^+ \to \pi^+ Z^0$ with the Z^0 off-shell. These have been shown to be $O(10^{-3})$ times smaller than the short distance contribution and therefore do not cause a problem in interpreting the decay rate [26].

The $K^+ \to \pi^+\nu\overline{\nu}$ branching ratio for three neutrino generations has been estimated to be [4, 5, 6],

$$\mathrm{BR}(K^+ \to \pi^+\nu\overline{\nu}) \sim 0.6 \to 6 \times 10^{-10}.$$

Figure 1.3, taken from reference [6], shows the maximum and minimum allowed branching ratio as a function of top quark mass using constraints from two possible solutions for the CP violation parameter ϵ in the neutral kaon system.

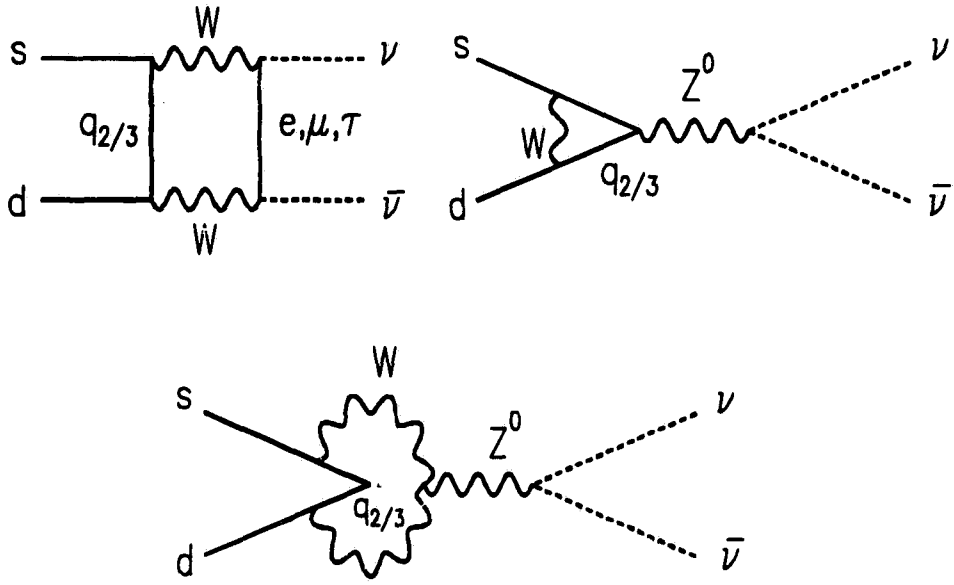

Figure 1.2: Second order Feynman diagrams for $K^+ \to \pi^+ \nu\bar{\nu}$. The $q_{2/3}$ lines represent the u, c, t quarks. The GIM suppression of the $s \to d$ transition is only approximate because of the different values of the quark masses.

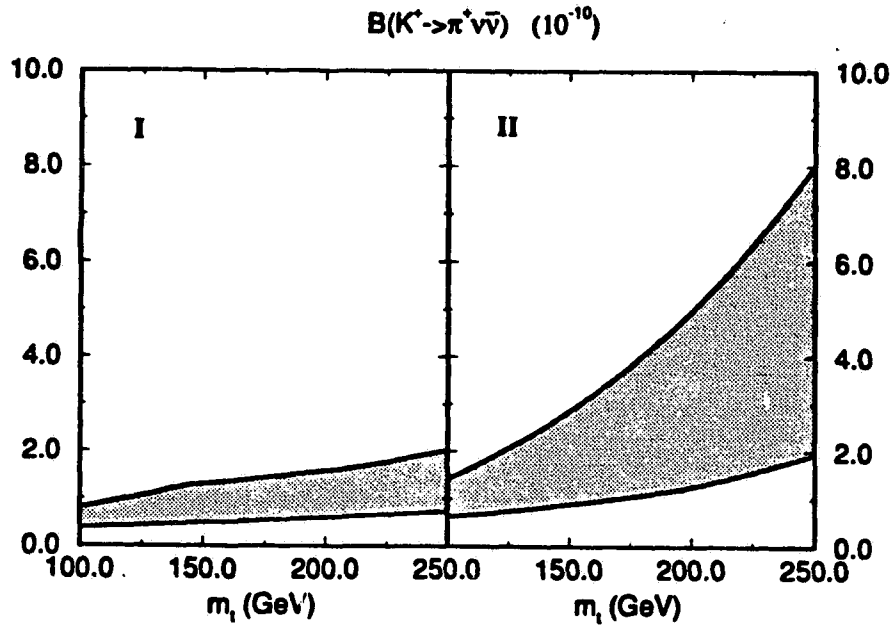

Figure 1.3: Allowed range of BR($K^+ \to \pi^+ \nu\bar{\nu}$) for top quark mass $100 < m_t < 250$ GeV from reference 6. The shaded regions denote allowed regions with the constraints determined from allowed solutions for the CP violation parameter ϵ in the neutral kaon system. The labels I and II refer to $\delta < \pi/2$ and $\delta > \pi/2$, respectively where δ is the CP violating phase in the CKM matrix.

The uncertainty is due to the imprecise knowledge of the following Standard Model parameters:

- The top quark mass, m_t, which is presently estimated to be 164^{+18}_{-21} GeV/c^2 from analysis of LEP data [27]. The CDF collaboration has recently announced evidence for a top quark of $174 \pm 10^{+13}_{-12}$ GeV/c^2 [28]. The published upper limit from the D0 collaboration is $m_t \geq 131$ GeV/c^2 [29].
- The value of $|V_{td}|$ is estimated to be in the range $0.006 \leq |V_{td}| \leq 0.018$ from $B^0\bar{B}^0$ mixing and CKM unitarity [6].
- The value of $|V_{ts}|$ which is set equal to $|V_{cb}|$.[4] From measurement of the B meson lifetime, $|V_{cb}| = 0.041 \pm 0.006$ yielding $A = 0.85 \pm 0.12$ [6].
- The charm quark mass, $1.2 \leq m_c \leq 1.4$ GeV/c^2.

The central values of the above parameters correspond to a $K^+ \rightarrow \pi^+\nu\overline{\nu}$ branching ratio of approximately 1×10^{-10}.

1.3.1 $|V_{td}|$ from BR($K^+ \rightarrow \pi^+\nu\overline{\nu}$)

A detailed discussion on the determination of $|V_{td}|$ is beyond the scope of this thesis; nonetheless, a brief discussion is merited.[5] It was first noted by Haggerty [30] that the $K^+ \rightarrow \pi^+\nu\overline{\nu}$ branching ratio given by equation 4 can be manipulated to yield the equation of a circle in the (ρ, η) plane. Substituting for the well known quantities in equation 4 and using the approximation $X(x_t) = 0.650x_t^{0.59}$ gives

$$\mathrm{BR}(K^+ \rightarrow \pi^+\nu\overline{\nu}) = 1.97 \times 10^{-11} A^4 x_t^{1.18}(\eta^2 + (\rho_0 - \rho)^2).$$

This defines a circle of radius r_{BR}, given by

$$r_{BR} = \frac{1}{A^2 x_t^{0.59}} \sqrt{\frac{\mathrm{BR}(K^+ \rightarrow \pi^+\nu\overline{\nu})}{1.97 \times 10^{-11}}},$$

centered at $(\rho_0, 0)$ with ρ_0 given by

$$\rho_0 = 1 - \frac{1}{A^2 0.650 x_t^{0.59}} \left[\frac{\eta_{QCD} X(x_c)}{\lambda^5}\right],$$

where $\eta_{QCD} \approx 0.70$ represents the QCD correction for the charm contribution. The effect of the charm contribution is to displace the center of the circle from $(1, 0)$. The effect of the τ mass in the charm loop modifies the above equation slightly.

[4] The equality of $|V_{ts}|$ and $|V_{cb}|$ implied in equation 3 is good to about 4%.

[5] An exhaustive review of top quark and CKM phenomenology from FCNC processes is found in reference [6].

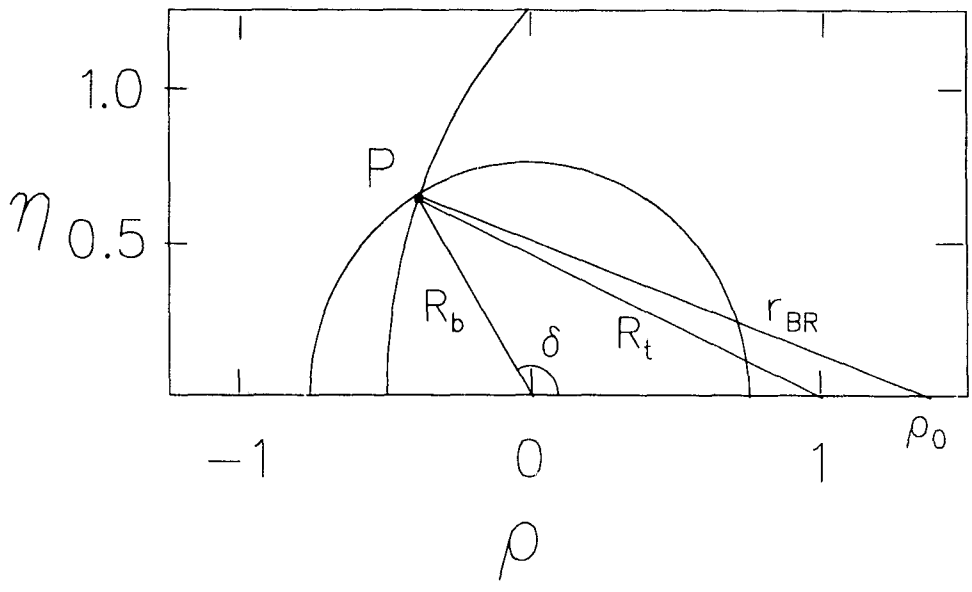

Figure 1.4: Relationship of BR($K^+ \to \pi^+\nu\overline{\nu}$) to $|V_{td}|$ in the (ρ, η) plane. See text for a description of symbols.

Measurement of $|V_{td}|$ from the $K^+ \to \pi^+\nu\overline{\nu}$ branching ratio requires an independent measurement of A (equivalently $|V_{cb}|$), $|V_{ub}/V_{cb}|$, and a knowledge of m_t. The relationship is schematically shown in figure 1.4. The point of intersection, P, of the circle defined by the $K^+ \to \pi^+\nu\overline{\nu}$ branching ratio, with the circle centered at $(0,0)$ having radius R_b, where,

$$R_b = \frac{1}{\lambda}\left|\frac{V_{ub}}{V_{cb}}\right| = \sqrt{\rho^2 + \eta^2}$$

defines a unique distance, R_t, to point $(\rho = 1, \eta = 0)$ given by,

$$R_t = (1 + R_b^2 + \frac{r_{BR}^2 - R_b^2}{\rho_0} - \rho_0)^{\frac{1}{2}}.$$

This distance is directly related to $|V_{td}|$ by $|V_{td}| = A\lambda^3 R_t$. The relationship between the CP violating phase angle δ and the point P is also shown in figure 1.4. The experimental value R_b is 0.45 ± 0.14 [31]. The present error in R_b corresponds to a $3-4\%$ error in $|V_{td}|$ when all other input parameters are fixed at their central values. In contrast, the existing error in A corresponds to a 17% error in $|V_{td}|$ [25].

Presently $|V_{td}|$ is determined from $B^0\bar{B}^0$ mixing. The error on the extracted value of $|V_{td}|$ is dominated by the purely theoretical uncertainty in the $\Delta B = 2$ hadronic matrix element.[6] Recently, the QCD corrections to $K^+ \to \pi^+\nu\overline{\nu}$ at the "next-to-leading log"

[6] Unlike $K^+ \to \pi^+\nu\overline{\nu}$ there is no directly measurable hadronic matrix element available.

order have been evaluated by Buchalla and Buras [25]. The calculation removes the large dependence of BR($K^+ \to \pi^+\nu\bar{\nu}$) on the assumed value of m_c. The calculation has reduced the theoretical uncertainty in the extraction of $|V_{td}|$ to the level of 7% compared to 30% for earlier QCD corrections performed in the "leading log approximation" [5, 32]. Buchalla and Buras argue that, given the difficulty in reducing the theoretical error in the $B^0\bar{B}^0$ based value of $|V_{td}|$, the most reliable estimate of $|V_{td}|$ will come from a measurement of $K^+ \to \pi^+\nu\bar{\nu}$.

For a known $K^+ \to \pi^+\nu\bar{\nu}$ branching ratio, the existing uncertainties in A and m_t dominate the error on the extracted value of $|V_{td}|$. This defines a near term goal for E-787 to measure the branching ratio with a 20-30% precision. However, once the top quark mass is known, an effort should be made to measure the branching ratio as precisely as possible.

1.3.2 The Unitarity Triangle

The triangle defined by the points $(0,0)$, $(1,0)$ and the point P in figure 1.4 is equivalent to the so-called unitarity triangle defined by

$$V_{ud}V_{ub}^* + V_{cd}V_{cb}^* + V_{td}V_{tb}^* = 0.$$

At present, there is intense interest in the study of CP violation in B meson decays as a means of determining this triangle. An alternative method of probing the unitarity triangle is the measurement of the branching ratios for $K^+ \to \pi^+\nu\bar{\nu}$ and the closely related CP violating decay $K_L^0 \to \pi^0\nu\bar{\nu}$. [7] The $K_L^0 \to \pi^0\nu\bar{\nu}$ decay rate does not depend on ρ and is proportional to η^2. Given the exceptionally clean theoretical situation that exists in the $K \to \pi\nu\bar{\nu}$ system, the measurement of their branching ratios offers a highly competitive and perhaps superior means of evaluating the unitarity triangle and testing the origin of CP violation in the Standard Model.

[7] For $K_L^0 \to \pi^0\nu\bar{\nu}$ the theoretical situation is even cleaner than $K^+ \to \pi^+\nu\bar{\nu}$. The uncertainty in the charm quark contribution is not present since it is highly suppressed by CP considerations. The decay is also of interest because it an example of "direct" CP violation.

Chapter 2

The Experiment

Night is when graduate students take shifts, and they don't lie.
They don't know how, they haven't learned yet.

- L. Lederman

In this chapter, the experimental method will be described. The experimental challenges confronting a measurement of $K^+ \to \pi^+\nu\overline{\nu}$ will be discussed and the detector requirements will be outlined. The E-787 spectrometer will be presented and the qualitative features of the potential backgrounds to $K^+ \to \pi^+\nu\overline{\nu}$ and their means of suppression will be introduced. Finally, the on-line event selection and data sets will be described.

2.1 Experimental Considerations

The $K^+ \to \pi^+\nu\overline{\nu}$ decay signature is a poor one. The topology of a single charged track with neutrals occurs in 94% of all charged kaon decays. Furthermore, the $K^+ \to \pi^+\nu\overline{\nu}$ decay does not yield a peak in a kinematic distribution; it is a three body decay with two of the three particles, the neutrino and anti-neutrino, unobservable

Table 2.1 lists the top 7 charged kaon decay modes and their respective momentum spectrum endpoints. It can be seen that of the primary K^+ decay modes containing a π^+, the $K_{\pi 2}$ decay has the largest momentum at 205 MeV/c. The charged track momentum distributions for the primary K^+ decay modes containing a muon or pion and the Standard Model $K^+ \to \pi^+\nu\overline{\nu}$ spectrum [33] is shown in figure 2.1. The end point of the momentum spectrum for $K^+ \to \pi^+\nu\overline{\nu}$ is 227 MeV/c. From figure 2.1, it is apparent that by studying kaons decaying at rest and limiting the search to the region between the $K_{\pi 2}$ and $K_{\mu 2}$ peaks, corresponding to approximately 20% of the $K^+ \to \pi^+\nu\overline{\nu}$ spectrum, a large degree of background suppression can be achieved.

The kinematic region between the $K_{\pi 2}$ and $K_{\mu 2}$ peaks is referred to as "above the

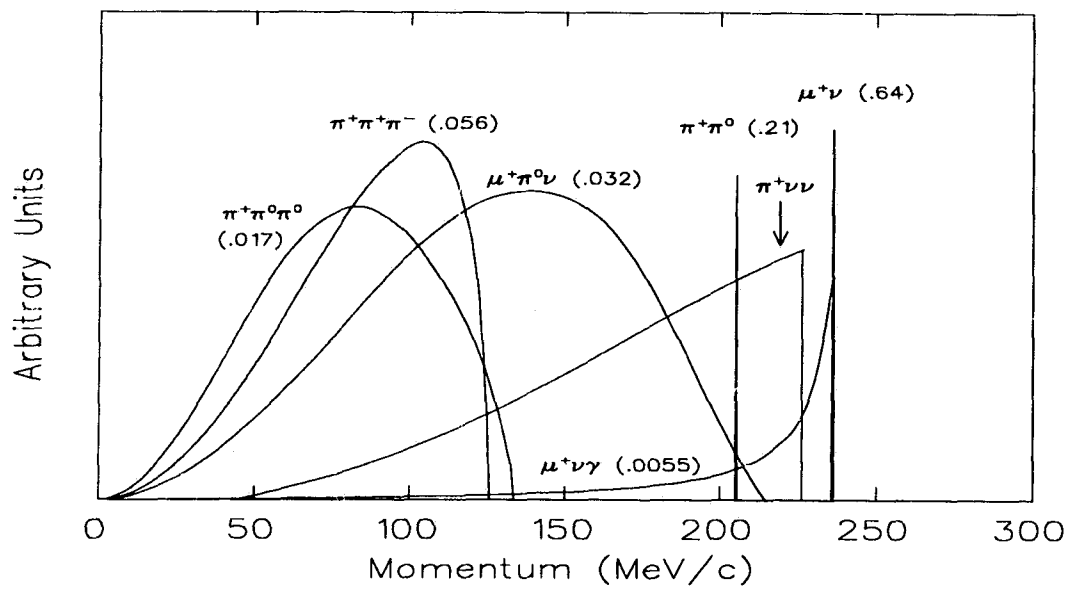

Figure 2.1: Charged particle momentum distributions for common kaon decays with a charged pion or muon in the final state.

Primary Decay Modes of the K^+			
Decay Mode	Symbol	Branching Ratio	P_{Max} (MeV/c)
$K^+ \to \mu^+\nu_\mu$	$K_{\mu 2}$	0.6351 ± 0.0019	236
$K^+ \to \pi^+\pi^0$	$K_{\pi 2}$	0.2117 ± 0.0016	205
$K^+ \to \pi^+\pi^+\pi^-$	Tau	0.0559 ± 0.0005	125
$K^+ \to e^+\pi^0\nu_\mu$	K_{e3}	0.0482 ± 0.0006	228
$K^+ \to \mu^+\pi^0\nu_\mu$	$K_{\mu 3}$	0.0318 ± 0.0008	215
$K^+ \to \pi^+\pi^0\pi^0$	$K_{\pi 3}$	0.0173 ± 0.0004	133
$K^+ \to \mu^+\nu_\mu\gamma$	$K_{\mu 2\gamma}$	0.0055 ± 0.0003	236

Table 2.1: Primary decay modes of the K^+.

$K_{\pi 2}$ peak". [1] The potential backgrounds to $K^+ \to \pi^+\nu\overline{\nu}$ in this region are:

- $K_{\mu 2}$ and $K_{\mu 2\gamma}$ decays with the muon misidentified as a pion,
- $K_{\pi 2}$ decays with the photons from the π^0 decay missed,
- $K_{\mu 3}$ decays with muon the misidentified *and* the π^0 photons missed,
- scattered beam pions misidentified as kaon decays, and,
- semi-leptonic K_L^0 decays from kaon charge exchange.

Figure 2.2 shows the total range, kinetic energy and momentum distributions for $K^+ \to \pi^+\nu\overline{\nu}$ compared with those for the $K_{\pi 2}$ and $K_{\mu 2}$ backgrounds. The kinematic variables are shown for a realistic dectector response. The kinematics of the hypothetical two-body decay $K^+ \to \pi^+ X^0$ for massless X^0 are also shown. From figure 2.2, it is apparent that the total range variable exhibits the largest relative separation between the $K_{\pi 2}$ and $K_{\mu 2}$ peaks.

Kinematics alone are not able to suppress backgrounds to the 10^{-10} level required for unambiguous identification of a $K^+ \to \pi^+\nu\overline{\nu}$ signal. To obtain further background suppression, the signature of a single π^+ track with no other observed energy must be utilized. A candidate $K^+ \to \pi^+\nu\overline{\nu}$ event would have to satisfy the following criteria:

1. The event has a single charged track from the decay of a tagged kaon with no other activity, *i.e.* photons in the detector at the kaon decay time.
2. The charged track being positively identified as a pion by observation of the characteristic decay sequence $\pi \to \mu \to e$ *and* by requiring consistency of the kinematic variables with a pion hypothesis.
3. Each of the pion's energy, momentum and range lie in the region allowed by the kinematics of the $K^+ \to \pi^+\nu\overline{\nu}$ decay.

Given the small $K^+ \to \pi^+\nu\overline{\nu}$ branching ratio, the detector must be able to suppress the above backgrounds to the level of 10^{-10} per event. To achieve this level of background rejection and reach the requisite sensitivity for $K^+ \to \pi^+\nu\overline{\nu}$, the detector must be able to perform the following in a high beam rate environment:

- accurately measure the range, energy and momentum of charged tracks to identify the mono-chromatic $K_{\pi 2}$ and $K_{\mu 2}$ backgrounds,

[1] The experiment is also able to search for $K^+ \to \pi^+\nu\overline{\nu}$ "below the $K_{\pi 2}$ peak". The search is more difficult due to the nature of the backgrounds but it has the potential to double the sensitivity. The nature of the "below the peak" search is fundamentally different; therefore, it will not be discussed extensively. The results of the "below the peak" search based on the 1989 data set are reported on in reference [34].

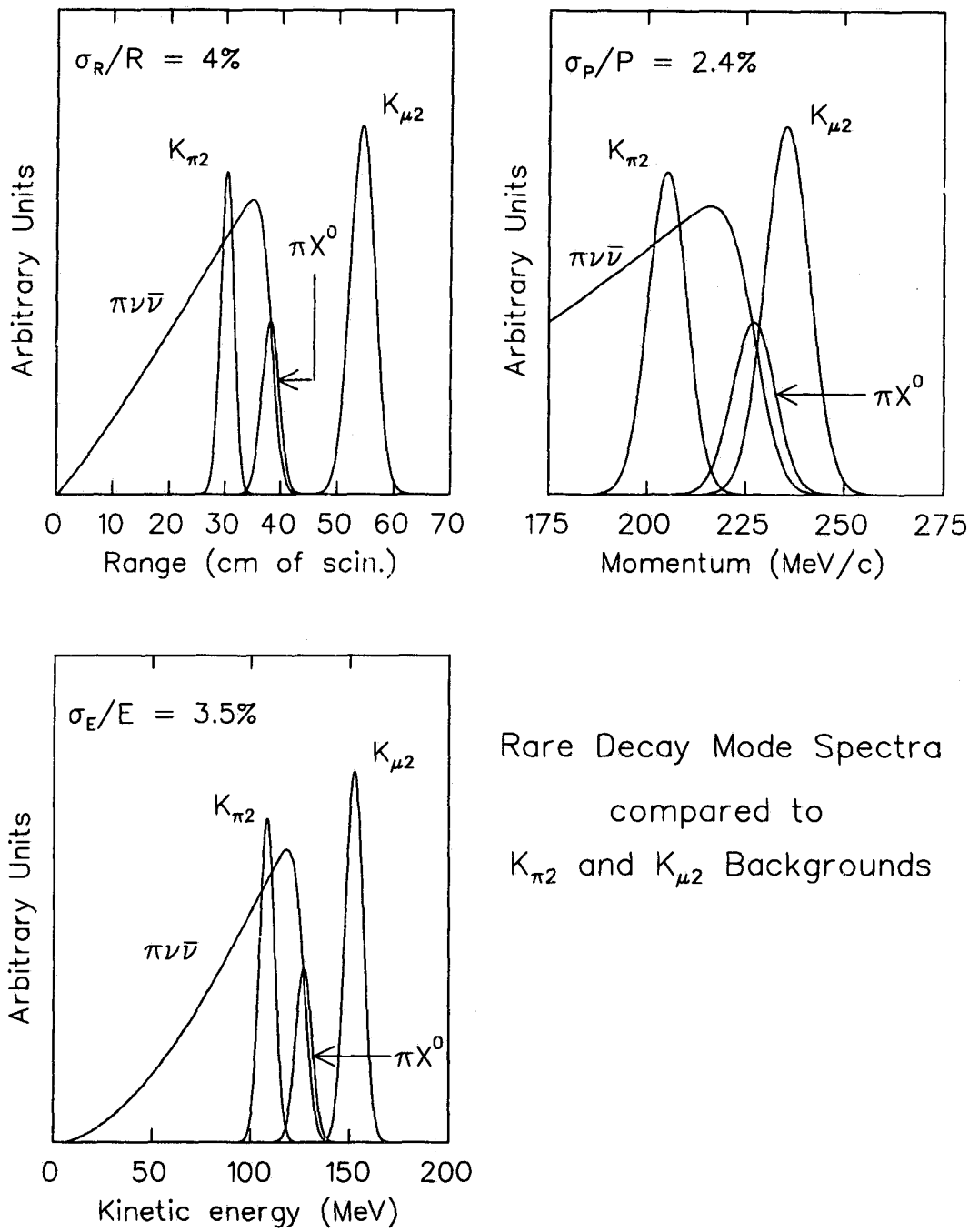

Figure 2.2: Kinematic distributions for $K^+ \to \pi^+\nu\bar{\nu}$ and the mono-chromatic $K_{\pi 2}$ and $K_{\mu 2}$ backgrounds Also shown are the kinematics for the hypothetical two-body decay $K^+ \to \pi^+ X^0$ with massless X^0. The kinematic quantities have been smeared using typical detector resolutions.

- positively identify charged pions by detection of the complete $\pi \rightarrow \mu \rightarrow e$ decay sequence to suppress muon type backgrounds,
- detect photons with high efficiency so as to veto $K_{\pi 2}$, $K_{\mu 3}$ and $K_{\mu 2\gamma}$ decays,
- identify stopped kaons with a low probability of error to suppress backgrounds from scattered beam pion and kaon charge exchange, and,
- veto low momentum secondary tracks originating from the kaon decay vertex to suppress semi-leptonic K_L^0 decays.

The detector must have a minimum of dead material in which energy from photons or charged tracks can be missed. The detector must also have a fast triggering system that can quickly evaluate the topology of a kaon decay and reject obvious background events. A high speed data acquisition system to process and transfer data to tape is also essential.

2.2 The E-787 Spectrometer

2.2.1 Overview

In this section the E-787 spectrometer will be presented with a focus on how the detector sub-systems are optimized for background suppression. Detailed descriptions of the various detector sub-systems may be found in reference [35]. Design considerations favoured a detector with cylindrical symmetry. The experiment was designed to study kaons at rest; therefore, by virtue of working in the center-of-mass system, the E-787 detector resembles a colliding beam experiment. A side view of the E-787 detector drawn to scale is shown in figure 2.3. A end-on view of the detector which emphasizes the large degree of segmentation necessary to deal with high counter rates and to identify backgrounds is shown in figure 2.4.

Kaons of momentum 800 MeV/c were selected by the LESB-I beam line and identified by a Čerenkov counter located downstream of the last beam line element. Kaons were slowed by passage through a degrader and were stopped in a highly segmented active target located [36] at the center of a solenoid magnet which produced a uniform 1.0 T field along the beam direction. The charged kaon decay products were momentum analysed in a cylindrical drift chamber [37] surrounding the target. Charged tracks were stopped and had their energy and range measured in a cylindrical array of scintillator counters which comprise the range stack. Pulse shape information for each counter of the range stack was recorded in a system of transient digitizers [38] to enable detection of pion and muon decays and provide track timing information. Surrounding the range stack and drift chamber, covering 97% of 4π solid angle, was the photon veto system which consisted of the barrel veto and endcaps. The

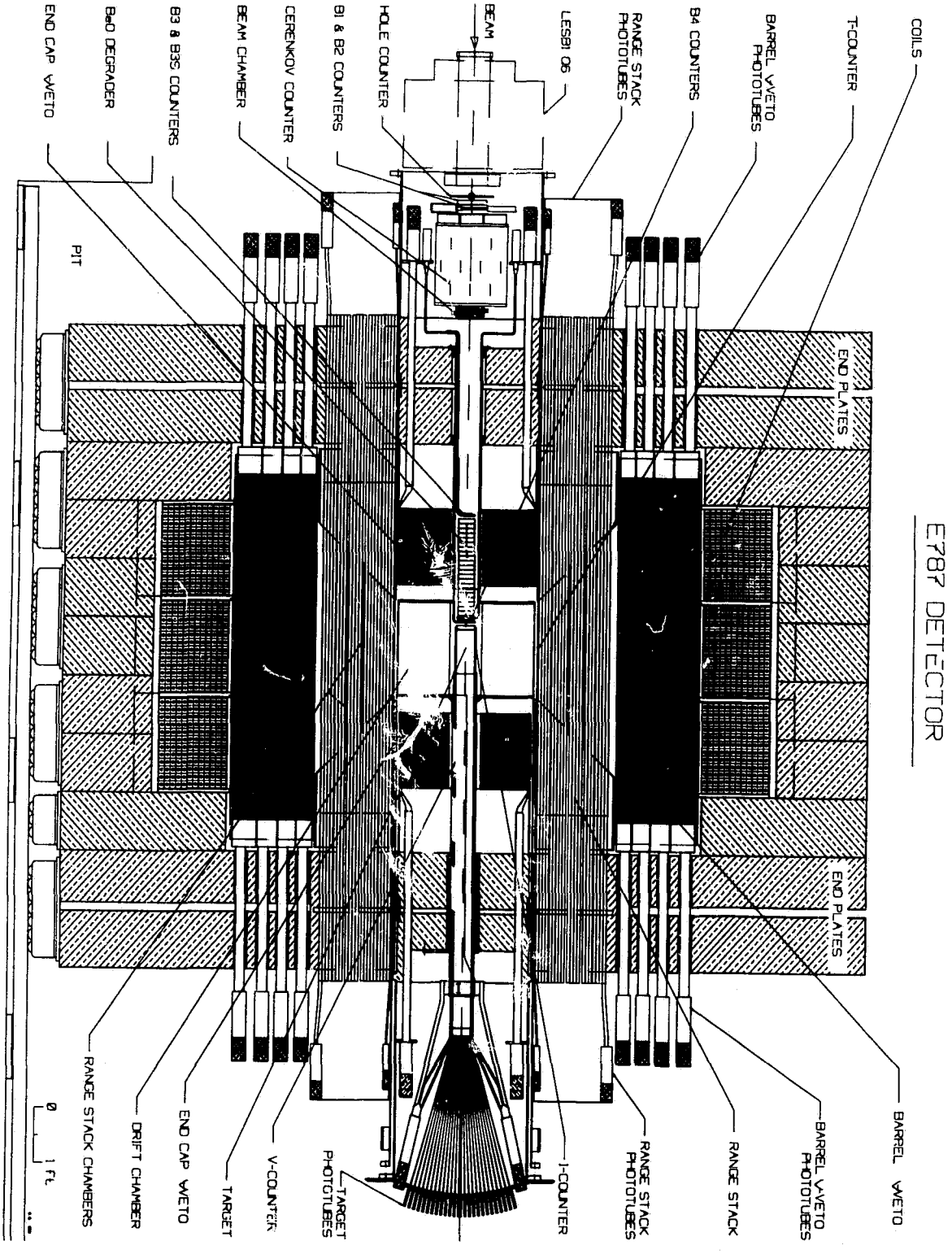

Figure 2.3: A side view of the the E-787 detector. The subsystems are drawn to scale.

barrel veto was located in the central region outside the range stack and the endcaps covered regions upstream and downstream of the drift chamber. The magnet, located outside the barrel veto, was the main support structure for the detector. The endplates, which acted as the magnetic flux return, were located outside the endcaps. An event display showing a $K_{\pi 2}$ event is presented in figure 2.5.

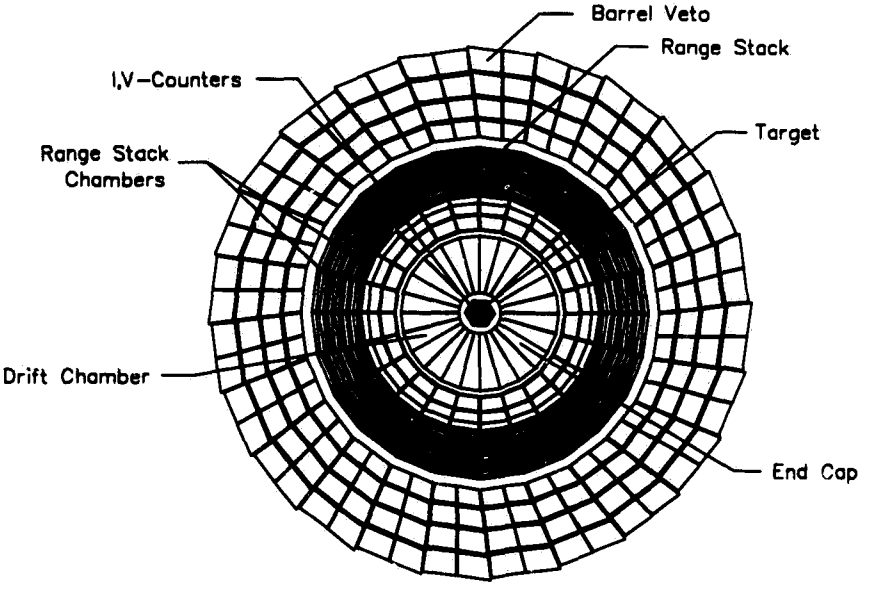

Figure 2.4: An endview of the E-787 detector showing the detector subsystems and the degree of azimuthal and radial segmentation.

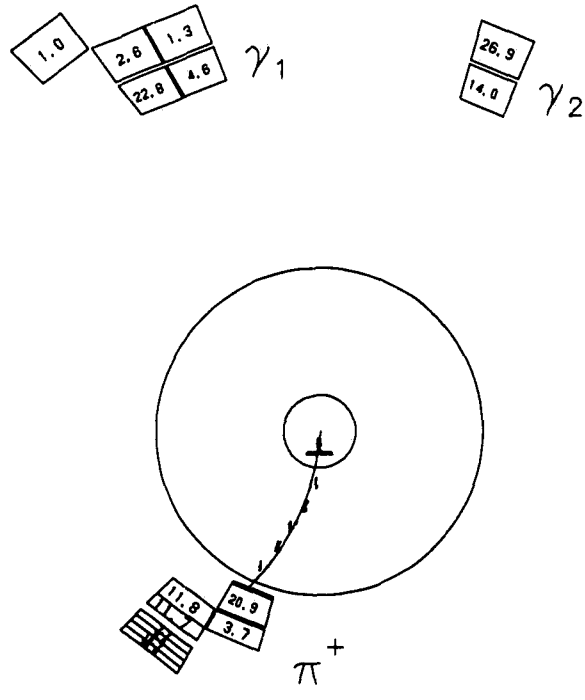

Figure 2.5: An event display showing a $K_{\pi 2}$ decay. The π^+ stopped in the range stack. The arc is the track fit from the drift chamber information. The associated π^0 decayed into 2 photons, labeled γ_1 and γ_2, which were detected in the barrel veto. The numbers inside the counters denote the energy deposited in MeV. The visible energy is shown for the barrel.

2.2.2 The LESB-I Beam Line

The source of kaons for the experiment was the LESB-I beam line [2] located at the Alternating Gradient Synchrotron (AGS) at Brookhaven National Laboratory. A schematic of the LESB-I beam line is shown in figure 2.6. Kaons produced at 10.5° relative to the 28 GeV C1 proton beam were selected by the D1 septum magnet and focused by two quadrapole magnets (Q1 and Q2) onto a momentum dispersing dipole magnet (D2). The electrostatic separator, consisting of crossed E and B fields, and mass slit were used to select the kaon band in velocity-momentum space to reduce the non-kaon beam contamination. A second pair of quadrapoles (Q3 and Q4) were used to adjust the focus of the beam at the mass slit to improve the $\pi - K$ separation. Downstream of the mass-slit were the Q5 quadrapole, a final momentum selection dipole (D3) and focusing quadrapole Q6.

For rare kaon decay experiments, the AGS produces a slow extracted 28 GeV proton beam. During the typical AGS beam spill of 1.4 s, $\sim 6 \times 10^{12}$ protons were directed onto the 89 mm thick platinum C1 kaon production target producing a nominal kaon Čerenkov rate of $\sim 10^6$ kaons per beam spill. On average, the AGS provided 1100 beam spills per hour, which corresponds to a kaon rate of 1.1×10^9 per hour. Only a small fraction of kaons firing the Čerenkov stop in the target; the majority decay in-flight upstream of the target or are lost via nuclear interactions in the degrader. The kaon flux was typically one quarter of the total beam flux entering the detector. The ratio of kaons, pions and protons was typically 1:2:1. The usable kaon flux represented only 6% of the total beam flux entering the detector. The unusable beam flux contributed to the accidental losses incurred when requiring the detector to be silent at the kaon decay time. [3] The pion contamination in the beam was responsible for a component of the pion scattering background.

2.2.3 The Beam Counters

The purpose of the beam counters was to provide redundant identification of a single kaon entering the target and to monitor the beam profile for optimization of the kaon flux. The beam counter system, shown in figure 2.7, consisted of a set of scintillator hodoscopes, (B1 and B2), followed by a Čerenkov counter and a hole counter (BH). The hole in the BH counter corresponded to the active area of the Čerenkov. Downstream of the Čerenkov was a multi-wire proportional counter (BWPC) followed by the B3 counter and a Beryllium Oxide (BeO) degrader. Located at the front face of the target were 2 planes of segmented scintillator counters rotated 90° with respect to each other, forming the B4 hodoscope. The B4 hodoscope was a 4×4 array for the 1989 and 1990 data runs. For the 1991 run, it was

[2] LESB is an acronym for Low-Energy-Separated-Beam

[3] It will be shown that accidentals result in false vetoing of approximately a third of the events.

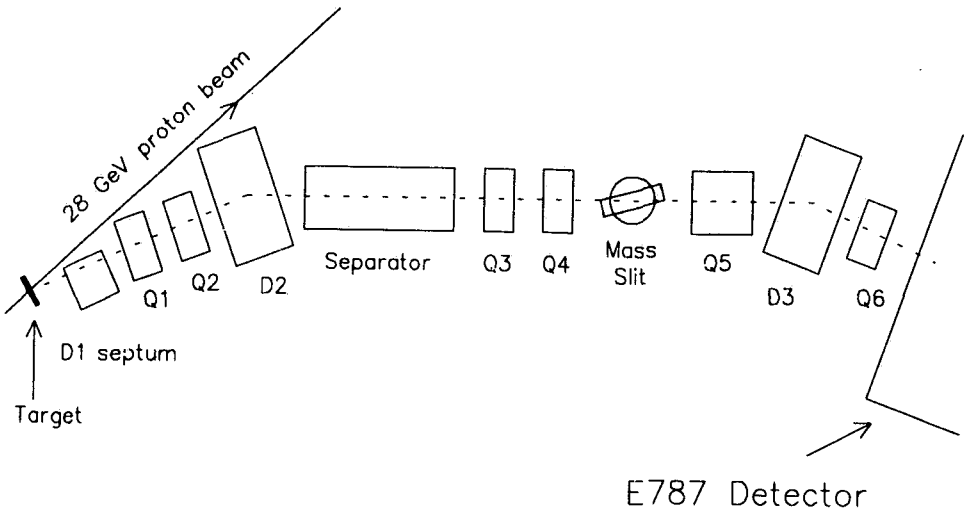

Figure 2.6: The LESB-I beam line located off of the 28 GeV C1 proton beam line at the AGS at Brookhaven National Laboratory.

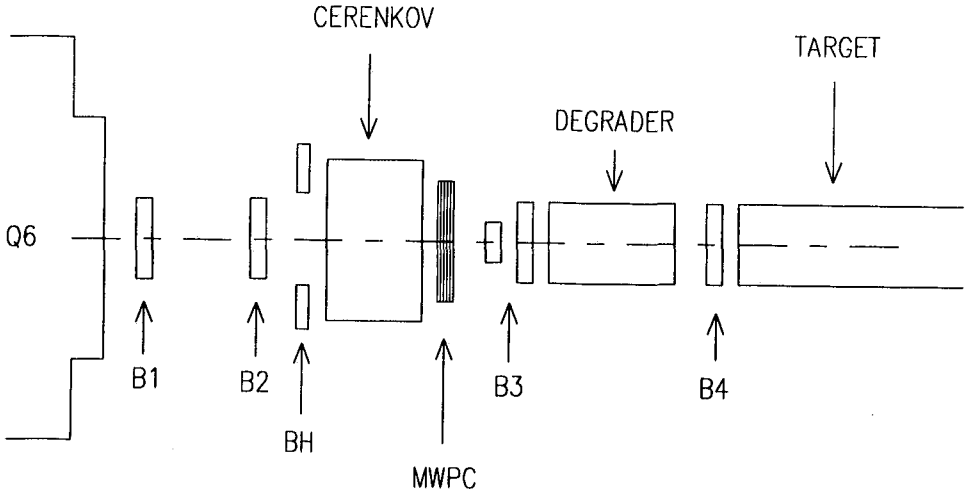

Figure 2.7: The beam counter system. Q6 is the last element of the LESB-I beam line

upgraded to a 6×6 array. For 1989 and 1990, an additional counter, B4T, was located downstream of the B4 hodoscope. The B4T counter was shaped like a hexagon to match the transverse profile of the target. The B4 hodoscope was used to identify kaons entering the target by use of dE/dx information. The B4 hodoscope was also used to provide a redundant measure of the kaon time. The B4T counter, present for the 1989 and 1990 runs, was used to define a reference time for the detector. For the 1991 run, part of the BeO degrader was removed and replaced with an active 3.6 radiation length lead glass degrader.

The first level trigger used beam information to require a kaon in the detector. The trigger signal K_T was defined as the coincidence,

$$K_T = \check{C}_K \cdot B4 \cdot E_{TG},$$

where $\check{C}_K$, $B4$ denote hits in the kaon Čerenkov and B4 hodoscope, respectively. The E_{TG} signal required 5 MeV deposited in the target. The coincidence timing was determined by $\check{C}_K$.

The Čerenkov counter, shown in figure 2.8, was used to identify kaons and pions entering the detector. The Čerenkov counter exploited the fact that at ~ 800 MeV/c, the light produced in a lucite radiator by pions and kaons can be easily distinguished. The pion produced light will be internally reflected at the lucite-air boundary, whereas the light from kaons will be transmitted with very high efficiency since the Čerenkov light is polarized in the plane of the beam and the angle of incidence is near to Brewster's angle. The light from the kaons was refracted at the lucite-air interface and was focused by a parabolic mirror onto a ring of 10 photomultiplier tubes (PMT). Each PMT was equipped with a Winston cone (a non-imaging aluminized reflector) to enhance the light collection. The light from the pions which emerges out the sides of the lucite radiator was focused onto a second ring of 10 PMTs, also equipped with Winston cones, located at a smaller radius. The pion Čerenkov counter ($\check{C}_\pi$) was used off-line to veto events with beam pions in coincidence with the charged track. The kaon Čerenkov detection efficiency for kaons was 98% for PMT multiplicity requirement of 7 or more phototubes fired. The pion Čerenkov detection inefficiency for pions was 10^{-4} for a multiplicity requirement of 5 or more phototubes fired.

The beam multi-wire proportional chamber (BWPC) was used to monitor the beam profile and to tag secondary beam particles that passed outside the Čerenkov radiator or were "missed" due to beam particle pile-up. The beam wire chamber was used to reject events from scattered beam pions that were not detected by the Čerenkov or beam hole counter. The BH counter was used to reject events from scattered beam pions in the beam halo that were not detectable by the Čerenkov or beam wire chamber.

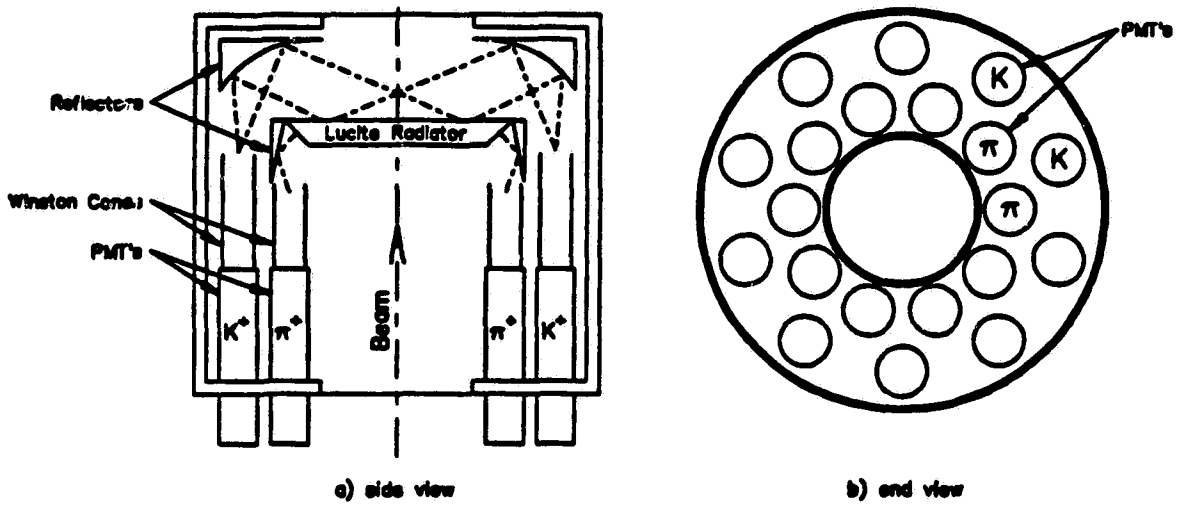

Figure 2.8: The Čerenkov counter. Figure a) is a side view showing the different paths for pion and kaon produced light. Figure b) shows the arrangement of the photomultiplier tubes. The figures are not to scale.

2.2.4 The Target

The target served a dual purpose; the first was to stop kaons exiting the degrader and the second was to enable identification of the kaon decay vertex from timing and energy information. The target was a highly segmented hexagonal array of plastic scintillating fibers. A transverse view of the target is shown in figure 2.9. The target contained a total of 379 channels; 378 triangles and one central fiber. Each triangle was comprised of 6 individual scintillating fibers epoxied together in a triangular mold. The epoxy and individual fiber claddings introduced dead material in the target corresponding to 25% of the target volume. The total length of the target fibers was approximately 3 m long. Each individual channel was read out by a PMT located outside the magnet at the downstream end of the detector as shown in figure 2.3.

The target fiducial volume was defined by 2 sets of 6 scintillators which outlined the hexagonal shape of the target. The I-counters, 24 cm long by 0.64 cm thick were positioned at the upstream end of the target. They defined the target fiducial region by tagging charged kaon decay products before they entered the drift chamber. The V-counters were located downstream of the I-counters outside the I-counter light guides. At the trigger level, the I-counters helped to define the fiducial acceptance and were used to select stopped kaons by demanding a "delayed coincidence" with the K_T signal. The V-counters were used off-line

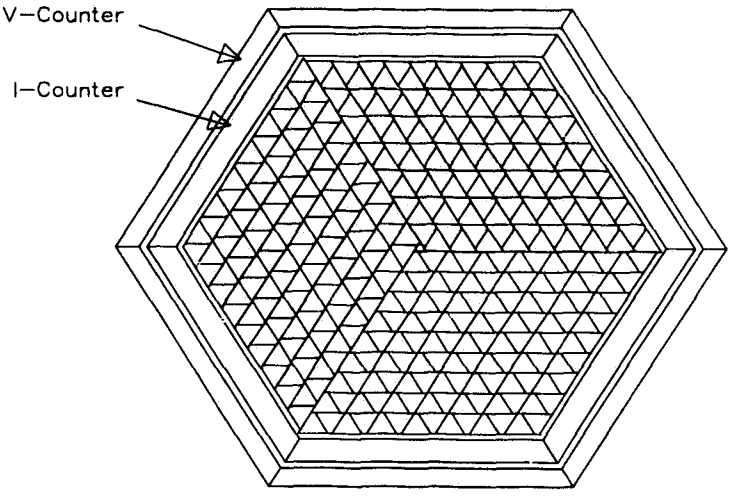

Figure 2.9: Side view of the target showing the individual triangles. The inner and outer 6 flat counters defining a hexagon are the I-counters and V-counters, respectively.

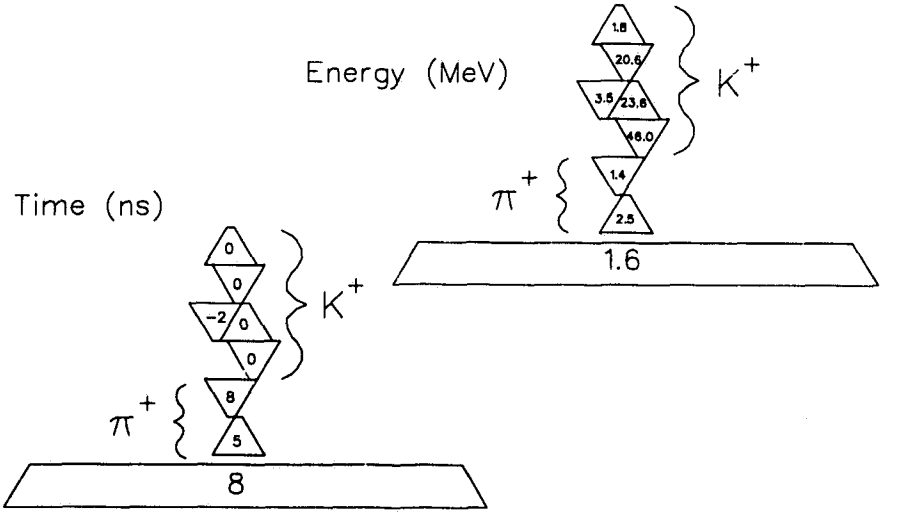

Figure 2.10: Target energy (ADC) and timing (TDC) information for the $K_{\pi 2}$ event shown in figure 2.5. Note the ability to distinguish between kaon and pion fibers when the energy and timing information is combined.

as part of the photon veto.

In the target, triangles belonging to the kaon were identified by the large energy, > 5 MeV, deposited. The kaon is highly ionizing and is travelling along the fibers. A typical stopping kaon would excite about 4 fibers. The charged kaon decay products typically deposited 1 MeV per fiber and were delayed relative to the kaon. This can be seen in figure 2.10 where the target event display is shown for the same $K_{\pi 2}$ event shown in figure 2.5. The range and energy of the charged track in the target are used to calculate the track's total range, total energy and total momentum. It is therefore important to cleanly identify the target triangles belonging to the charged track.

Rejection of the pion scattering background and kaon charge exchange background relies on use of the target information to identify the kaon decay vertex and to spot anomalous energy depositions inconsistent with a stopped kaon decay. The target is also used as part of the photon veto system. For a kaon stopping at the center of the fiducial region in the target, the surrounding target material corresponds to $\sim 0.25X_0$ in the upstream direction and $\sim 5X_0$ in the downstream direction.

2.2.5 The Drift Chamber

The cylindrical drift chamber (DC), which subtended a solid angle of 2π sr, served two primary purposes: one, to measure the charged track momentum, and two, to provide track position information for off-line selection of candidates.

The chamber wires were arranged in 5 superlayers of 36, 40, 50, 60 and 70 cells, respectively. An expanded view of a typical cell is shown in figure 2.11. The cells within a given superlayer were identical; the cell half width varied from 12 mm to 17 mm depending on the radial position. The cathode-wire plane, shared by neighboring cells, consisted of 19 Be-Cu wires strung 2.54 mm apart at a tension of 150 g. The sense-wire plane, strung at 50 g tension, consisted of two Be-Cu guard wires and eight 20 μm diameter gold-plated tungsten anode wires spaced 5.08 mm apart. The in-cell left-right ambiguity was resolved by staggering alternating anode wires by $\pm 254\mu$m with respect to the cell mid-plane. The Al endplates were supported in position by 2 graphite epoxy fiber cylinders located at the inner and outer radii, having thicknesses of 80 mg-cm^{-2} and 94 mg-cm^{-2}, respectively.

The chamber occupied the radial region between 95 mm and 432 mm with a total length, including pre-amplifiers, connectors, and cables of 650 mm. The superlayer and drift cell boundaries are shown in figure 2.12; the event display information is from the $K_{\pi 2}$ event shown in figure 2.5. The chamber was operated with a 50:50 mixture of Argon and Ethane at atmospheric pressure. To suppress aging effects, the Argon was bubbled through ethanol at 0° C . Superlayers 2 to 5 were nominally operated with an applied voltage of -4500 V with the innermost superlayer, 1, at -4000 V.

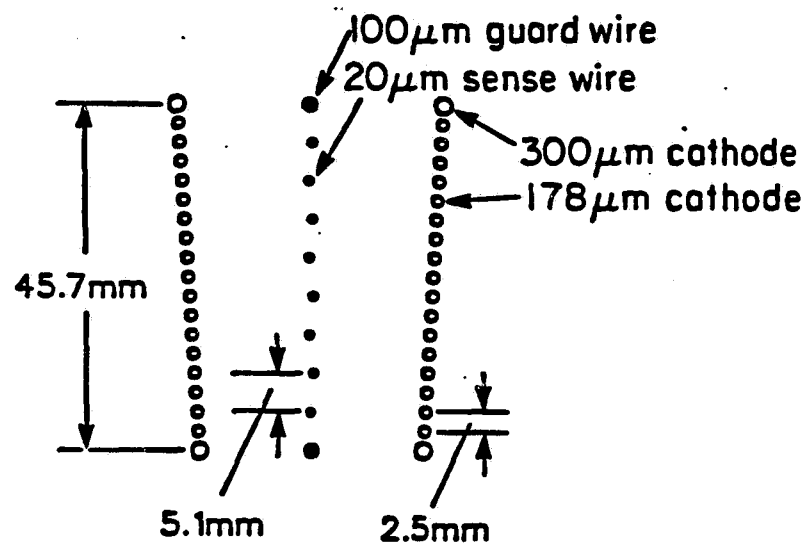

Figure 2.11: Expanded view of a drift chamber cell.

Superlayers 1,3 and 5 were strung axially and provided $x - y$ coordinates. Layers 2 and 4 were strung between feedthroughs offset by one cell. The offset in the stringing resulted in stereo angles of approximately $\pm 3.5°$ enabling measurement of z coordinates for the track. Only the inner six anode wires (out of 8) were read out; therefore up to 18 axial hits and 12 stereo hits were available for track reconstruction. Each anode read out was instrumented with a 500 MHz pipeline TDC channel (Lecroy 1879) which allowed up to 10 hits in 1024 ns. The TDC stop signal was the 24-fold OR of the individual $(T \cdot A)$ trigger signals (described in section 2.2.6).

The drift velocities, nominally 52 mm-μs^{-1}, for each of the 30 different radial positions were determined using $K_{\mu 2}$ events with the magnetic field turned off. Individual timing offsets were determined for each wire by iterative minimization of the average fit residual for tracks on the left and right hand side of a given cell using $K_{\mu 2}$ events taken with $B = 0$ kG. Calibrated wire positions for the axial layers were obtained in a similar manner. The Lorentz angle, 25°, was determined by iterative minimization of track χ^2 using $B = 10$ kG $K_{\mu 2}$ data. A second order calibration to correct for the sector to sector variation of the TDC stop signal was also performed in the same manner. The position resolution as a function of drift distance is shown in figure 2.13. The resolution was limited by multiple scattering in the drift chamber gas and cathode wires.

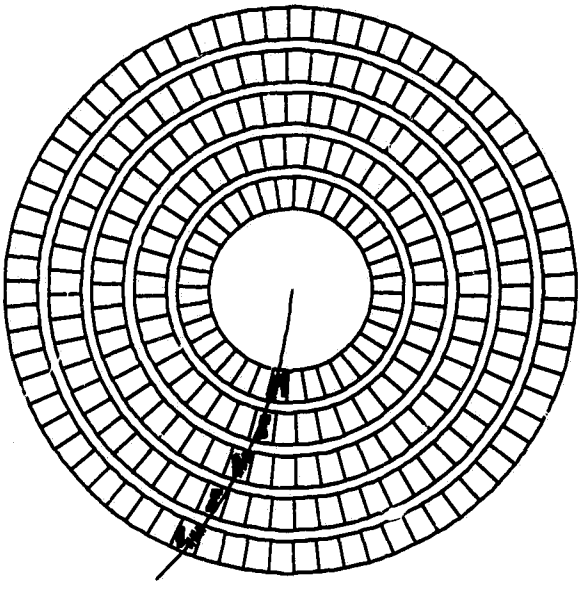

Figure 2.12: Event display of the drift chamber information for the $K_{\pi 2}$ event shown in figure 2.5.

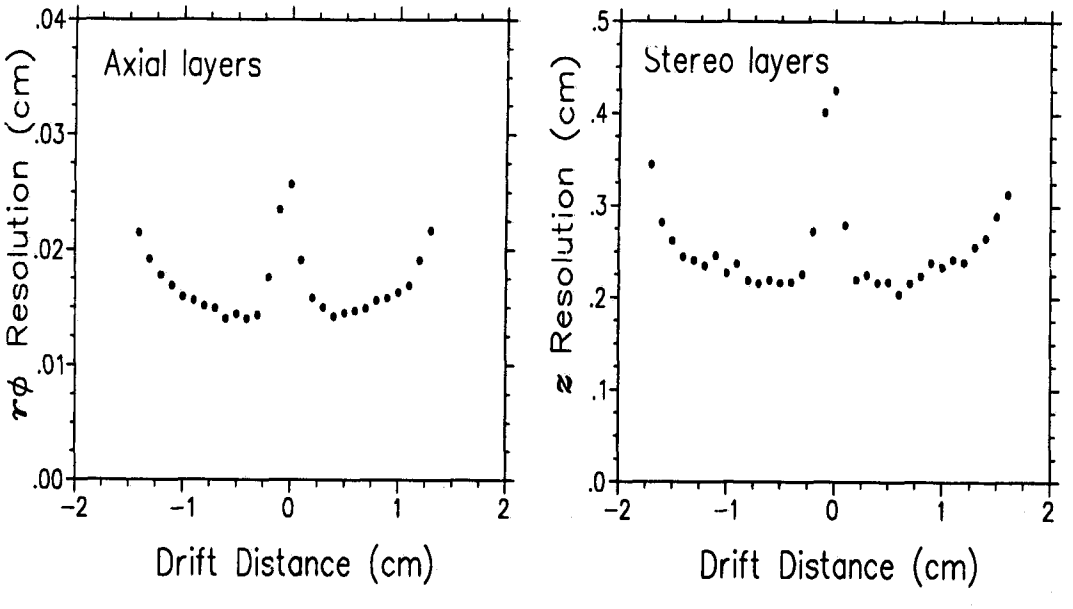

Figure 2.13: Drift chamber position resolution versus drift distance for axial and stereo layers.

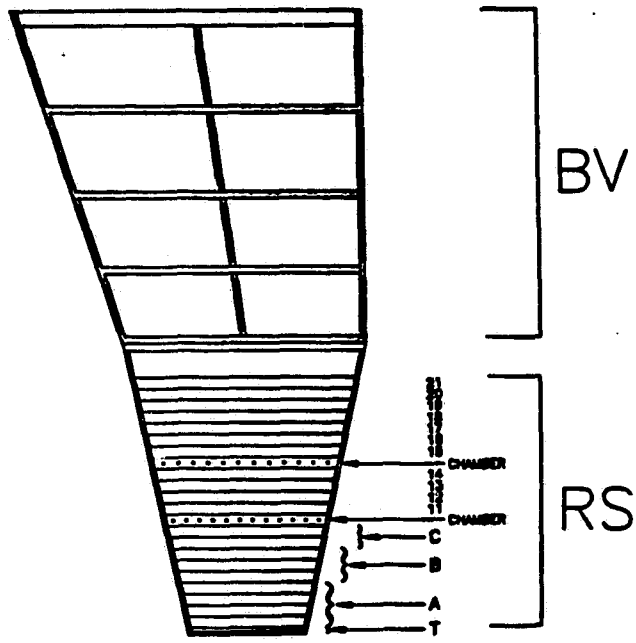

Figure 2.14: An expanded end on view of a range stack sector. The corresponding barrel veto sectors are also shown.

2.2.6 The Range Stack

The range stack was used to measure the energy and range of charged tracks. It also served as the detection medium for observation of the $\pi \rightarrow \mu \rightarrow e$ decay sequence and as an element in the photon veto system. The range stack was a cylindrical array of layers of plastic scintillators divided into 24 sectors in azimuth. Each sector consisted of 20 1.82 m long $\times$ 19.05 mm thick plastic scintillator counters and an innermost 52 cm long $\times$ 0.635 cm thick counter called the T counter. A range stack sector is shown in figure 2.14. Light from each end of the counters was read out using lightguides passing through the spokes of the magnet end plates coupled to PMTs. The range stack also performs as a photon veto. The total thickness of scintillator corresponds to roughly 0.9 radiations lengths of an essentially completely active material. Figure 2.15 demonstrates how the T counter was used in combination with the I-counter to define the fiducial acceptance at the trigger level.

The range stack counters were supported within the magnet by a pair of welded stainless-steel frames located upstream and downstream. Each end of the support structure

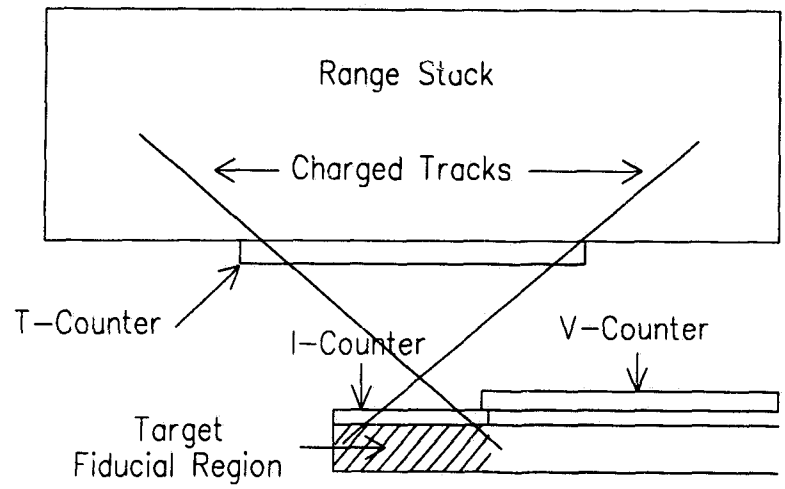

Figure 2.15: The definition of the fiducial volume by the I, V and T-counters. Charge tracks passing through the I and T-counters are constrained to the shaded region in the target. The lines originating in the target and entering the range stack represent charged tracks from kaon decays. For clarity, only one half of the detector is shown and the individual layers in the range stack are not drawn. The dimensions are not to scale.

or "web" (so-called because of its end-on appearance) was conically shaped and centered along the beam axis. The inner diameter of the web extends inward almost to the edge (within 3.5 cm) of the T-counter and tapers back towards the outer diameter. The support structure can be seen in figure 2.3. The amount of inert material introduced into the fiducial volume by the support structure is minimal except for $K_{\mu 2}$ decays at large polar angles. Muons stopping in the web are a source of background because the large energy loss near the end of their range enables them to mimic a pion kinematically.

The inner nine layers of 19 mm thick counters were ganged together into 3 superlayers referred to as the A, B and C having 4, 3 and 2 layers of scintillator, respectively. For the $K^+ \rightarrow \pi^+ \nu\overline{\nu}$ search above the $K_{\pi 2}$ peak, the minimum required charged track range is > 30 cm equivalent in scintillator; therefore, the "multiplexing" of the inner ~ 18 cm of the range stack did not degrade the quality of the range measurement.

For the purpose of reading out the pulse shape information, the signals from 4 adjacent range stack counters (in azimuth) were summed together. Each grouping of 4 sectors was referred to as a "hextant". The counter in which the charged track stopped was referred to as the "stopping counter"; similarly, the "stopping layer", "stopping sector" and "stopping hextant" were defined. Signals from the phototubes at each end were fed into a splitter with three outputs. One output was sent to an ADC for energy information and a second output was summed with the other counter ends within the hextant and read out with a

transient digitizer. The third output was sent to a discriminator for use in the trigger and in the transient digitizer system for decoding the within hextant hit pattern in the off-line analysis.

At the heart of the E-787 experiment was a system of transient digitizers (TDs) which provided pulse shape information in the range stack to be used in identification of the $\pi \rightarrow \mu \rightarrow e$ decay sequence. The TDs sampled the phototube output every 2 ns over a period of 10 μs. Since the average pion lifetime (26 ns) is comparable to the width of the PMT pulses, a high sampling frequency was necessary to detect $\pi \rightarrow \mu$ decays. The requirement of a long memory was a consequence of the muon lifetime (2.2 μs). An example of a $\pi \rightarrow \mu \rightarrow e$ decay sequence showing the TD information is presented in figure 2.16. Off-line, the TD information in the stopping hextant was fit for one and two pulse hypotheses to identify $\pi \rightarrow \mu$ decays. The TDs were also used to provide timing information for the range stack hits. The hit timing was determined from the rising or "leading" edge of the digitized pulses.

In each sector, following range stack layers 10 and 14, there was a multi-wire proportional counter (RSPC). The radial positions of the inner and outer RSPCs roughly coincided with the stopping distribution peaks for the $K_{\pi 2}$ and $K^+ \rightarrow \pi^+ X^0$ decays, respectively. The purpose of the RSPCs was to provide additional information to track the charged tracks through the range stack. Azimuthal or $x - y$ information was obtained from the position of the struck anode wire. The z position was determined from the end-to-end time difference of signals from the serpentine cathode strip. On-line, z information from the inner layer of chambers was used to provide dip-angle information in a refined range cut at the second level trigger.

2.2.7 The Photon Veto: Barrel and Endcaps

The ability to reject π^0's depends primarily on the solid angle coverage and number of radiation lengths afforded by the photon veto system. The barrel veto (BV) and endcap (EC) photon veto systems combine to cover approximately 97% of the 4π solid angle.[4] Both systems consisted of alternating layers of 1 mm thick lead and 5 mm thick scintillator and had a visible energy fraction (ratio of energy deposited in scintillator to the total energy) of 0.29.

The active region of the barrel veto was 1.9 m long and covered approximately two-thirds of the solid angle corresponding to the central 90 degrees of the polar angle. For photons at normal incidence, the barrel veto thickness corresponded to 14.3 radiation lengths.

[4]The detector provides at least 12 radiation lengths for the central 79% of the 4π sr. For small polar angles, the number of radiation lengths falls off rapidly, however, there are at least 2 radiation lengths for 99% of the 4π sr.

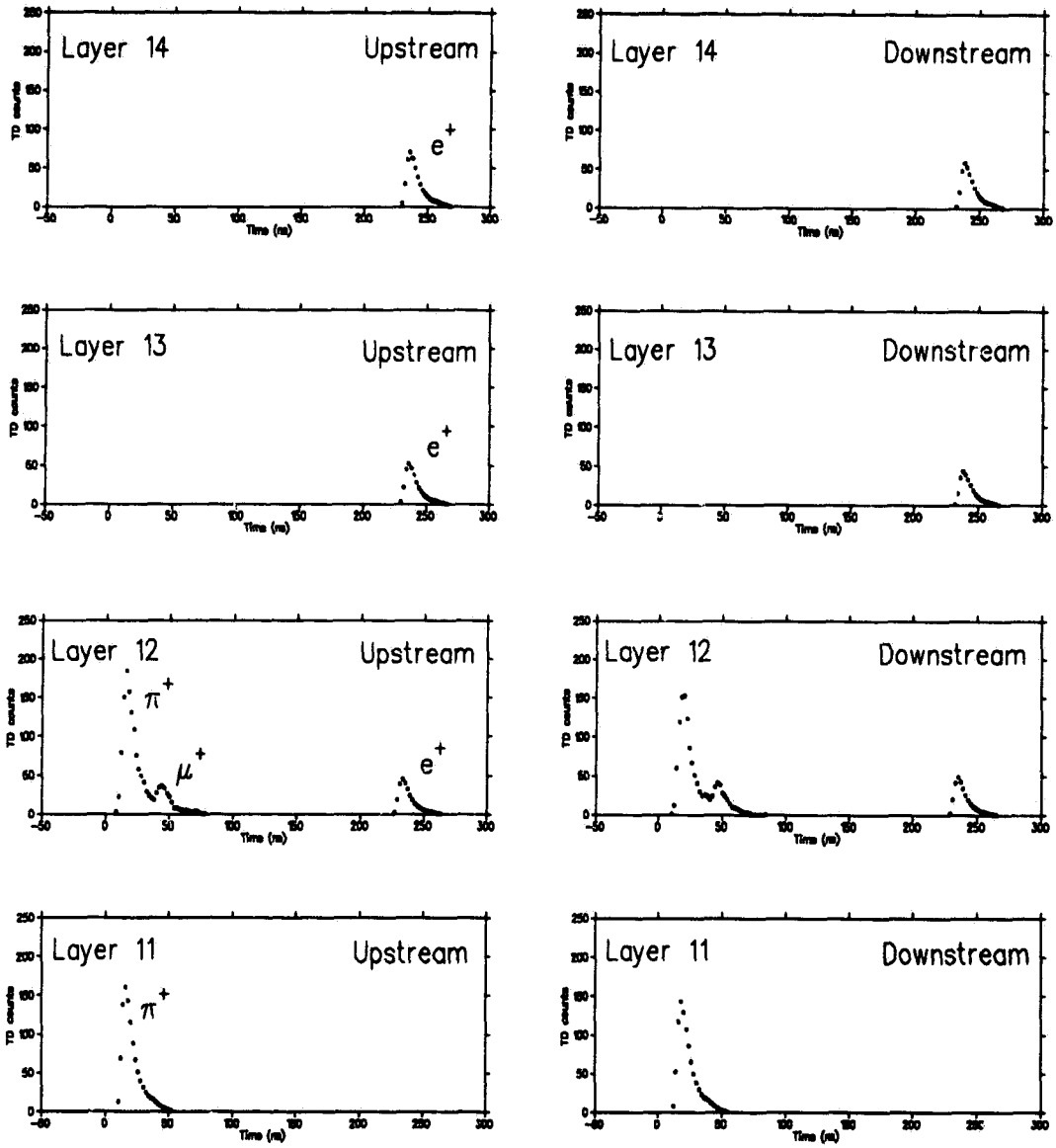

Figure 2.16: Transient digitizer information showing the $\pi \rightarrow \mu \rightarrow e$ decay sequence. The pion passed through layer 11 and stopped in layer 12. Approximately 40 ns later it decayed to a muon which in turn decayed to an electron 220 ns later.

The barrel veto was segmented into 48 azimuthal sectors with each sector further segmented into 4 radial layers. The azimuthal boundaries were tilted so that the inter-sector gaps did not project back to any part of the target.[5]. Each end of the 48×4 modules was read out using a mixer block scheme coupled to a light guide which was read by a phototube located outside the magnet endplate. Each module end was instrumented with individual ADC and TDC channels. For off-line photon vetoing, the mean time of the end-to-end coincidences was used to eliminate z dependent timing effects.

The endcaps covered the region upstream and downstream of the drift chamber. Each endcap was segmented into 24 azimuthal modules. The lead- scintillator layers were oriented perpendicular to the detector axis. The total thickness was 12.4 radiation lengths. The endcaps surrounded a 20 cm hole on the beam axis through which the beam entered the detector (upstream) and through which the target was read out (downstream). Light from the end caps was read out using a wavelength shifter bar located on the EC outer radius. The bar was coupled to a light guide which was read by a phototube located outside the magnet endplug. Each azimuthal module was instrumented with individual TDC and ADC channels.

The trigger used barrel veto and endcap information to perform a fast veto of events with photons activity. The analog sum of the individual channels in the barrel veto, upstream and downstream endcaps were discriminated. For the barrel, the on-line threshold applied to the energy sum was equivalent approximately 5 MeV visible. For each endcap, the threshold was approximately 10 MeV visible; the higher threshold was necessary due to the proximity to the beam where the accidental rates are highest.

An additional advantage to performing the experiment in the center of mass system is the strong correlation between the direction of the photons from the π^0 decay and that of the π^+ emitted in $K_{\pi 2}$ decay. The angle subtended by the barrel and definition of the fiducial volume ensures that in every $K_{\pi 2}$ decay there is at least one photon that heads directly into the barrel. [6] The minimum opening angle between the π^0 decay photons, given by $2\tan^{-1}(m_{\pi^0}/p_{\pi^0}) = 67$ degrees, implies that there is one photon of at least 122 MeV (required by momentum conservation) with angular separation greater than $180-32.5 \approx 147$ degrees with respect to the π^+. Given that the barrel veto covers the central 90 degrees of polar angle and the fiducial volume is limited to central 60 degrees, the high energy photon is contained within the solid angle subtended by the barrel.

[5]This can be seen in figures 2.4 and 2.14

[6]This assumes, of course, that the pion does not scatter in the target and ruin the correlation between the measured and initial π^+ direction. It is precisely this effect that makes the search for $K^+ \to \pi^+\nu\bar{\nu}$ below the peak more difficult. A scatter in the target can degrade the $K_{\pi 2}$ pion energy and enable the high energy photon to escape along the beam axis.

2.3 On-line Event Selection

2.3.1 Overview

The on-line event selection or trigger was divided into four stages or levels, with each level having increased complexity and required decision time. The trigger exploited the basic $K^+ \rightarrow \pi^+\nu\overline{\nu}$ signature: a single pion track with no associated photons in the kinematic region between the $K_{\pi 2}$ and $K_{\mu 2}$ peaks. The trigger levels for $K^+ \rightarrow \pi^+\nu\overline{\nu}$ can be summarized as follows:

- Level 0:
  - Require a delayed decay of a stopped kaon in the target.
  - Require a charged track within the fiducial volume defined by the I and T counters.
  - Require the charged track in the range stack to reach layer B and stop before layer 19.
  - Veto events with photon activity in the barrel veto or endcaps.
- Level 1:
  - Require the charged track to reach layer 11.
  - Require that there be no more than 2 adjacent RS hextants hit.
  - Veto long range tracks using stopping layer, target range and RSPC based dip-angle information.
- Level 1.5:
  - Require the charged track energy to be less than 133 MeV.
- Level 2:
  - Require $\pi \rightarrow \mu$ decay signature in the stopping hextant.

At the trigger level, the most serious background is $K_{\mu 2}$ due to the large branching ratio and similar signature of a single charged track with unobservable neutral. The $K_{\pi 2}$ background is highly suppressed by the photon veto; after the fast Level 0 trigger, the ratio of $K_{\mu 2}$ to $K_{\pi 2}$ is a factor of 13. After Level 1, the ratio of $K_{\mu 2}$ to $K_{\pi 2}$ worsens to a factor of 70. The complexity of the trigger is a consequence of the difficulty in separating muons and pions in the momentum range 200-240 MeV/c. Until the Level 1.5 trigger; rejection of $K_{\mu 2}$ events relies solely on the 16 cm difference in charged track range between a pion at

the endpoint of the $K^+ \to \pi^+\nu\overline{\nu}$ spectrum and the $K_{\mu 2}$ muon. Overall the trigger achieves a rejection factor of almost 10^5 for $K_{\pi 2}$ and $K_{\mu 2}$ decays.

The E-787 trigger was set up so that different physics and calibration triggers could be implemented and taken simultaneously. Other physics triggers included:

- A second type of $K^+ \to \pi^+\nu\overline{\nu}$ trigger designed to select events in the kinematic region below the $K_{\pi 2}$ peak.
- A trigger designed to select $K^+ \to \pi^+\mu^+\mu^-$ decays.
- Two triggers for $K^+ \to \pi^+\gamma\gamma$ optimized for low and high invariant mass photon pairs, respectively.

The rate of each of the above triggers was sufficiently reduced to allow them to be acquired simultaneously with $K^+ \to \pi^+\nu\overline{\nu}$. Along with the physics triggers, a number of different calibration or "monitor" triggers were taken at a preselected rate. As their name implies, the monitor triggers were used to evaluate the detector performance: by definition, the variation in the detector performance, beam characteristics and rate is accounted for and properly sampled. The monitor triggers were used extensively when evaluating the detector sensitivity for $K^+ \to \pi^+\nu\overline{\nu}$. Since the monitor triggers typically required only simple Level 0 requirements, it was necessary to prescale the rate at which they were accepted by a fixed factor lest the data acquisition system be flooded. Every trigger recorded to tape included the information on the status of each trigger level for each physics trigger. This enabled off-line evaluation of the trigger using real data and greatly facilitated the measurement of the acceptance and background.

2.3.2 Level 0 Trigger

The first stage, Level 0, used fast combinational logic to identify stopped kaon decay in the target with a single charged track in the range stack satisfying a rough range cut without associated photons. The $K^+ \to \pi^+\nu\overline{\nu}$ Level 0 trigger logic was,

$$\pi\nu\bar{\nu}L0 = K_T \cdot IC \cdot DC \cdot (T \cdot A) \cdot B_{CT} \cdot \overline{(19_{CT} + 20_{CT} + 21_{CT})} \cdot \overline{(BV + ECM + ECP)} \quad (5)$$

where:

- K_T was the coincidence $(\check{C}_K \cdot B4 \cdot E_{TG})$,
- IC was a struck I-counter,
- DC was a delayed coincidence ($\sim$ 2 ns) between IC and K_T,
- $(T \cdot A)$ was a coincidence within a range stack sector,

- X_{CT} defines a charge track in layer CT, and,
- BV, ECM, ECP were the barrel veto, upstream and downstream endcap energy sums, respectively.

The subscript CT denotes a struck counter within 3 sectors (assuming a positively charged track) of the $(T \cdot A)$ sector. The $\overline{(19_{CT} + 20_{CT} + 21_{CT})}$ requirement was a range cut designed to reject muons.

The $K_{\pi 2}$ and $K_{\mu 2}$ monitor triggers used extensively in the analysis were selected with following Level 0 requirements:

$$K_{\pi 2}(1) = K_T \cdot (T \cdot A) \cdot B_{CT} \cdot \overline{(19_{CT} + 20_{CT} + 21_{CT})} \quad (6)$$

$$K_{\mu 2} = K_T \cdot (T \cdot A) \cdot B_{CT} \cdot (19_{CT} + 20_{CT} + 21_{CT}). \quad (7)$$

A third type of monitor trigger used to evaluate the detector performance was the pion scattering trigger:

$$\pi-\text{scat} = \check{C}_\pi \cdot B4 \cdot E_{TG} \cdot IC \cdot \overline{DC} \cdot (T \cdot A) \cdot B_{CT} \cdot \overline{(19_{CT} + 20_{CT} + 21_{CT})} \cdot \overline{(BV + ECM + ECP)}, \quad (8)$$

with the $\check{C}_\pi$ replacing the normal $\check{C}_K$ requirement used to select kaons. The $\overline{DC}$ requirement selected events that immediately scattered in the target. Beam pions scattering in the target are the only significant source of pions with a range greater than that of the $K_{\pi 2}$ pion.

2.3.3 The Level 1 Trigger

The Level 1 trigger consisted of two parts; a refined range cut and an extension of the photon veto to include the range stack. The Level 1 refined range trigger used the stopping layer, target and RSPC z information to compute a dip-angle corrected range. The refined range trigger required the charged track to reach layer 11 with a unique RSPC z hit. The inner layer RSPC z position was determined from the end-to-end time difference. The time difference was converted into an amplitude and digitized to form a 4 bit word proportional to the z position. The range in the target was estimated from the number of target triangles above threshold. A 4-bit word proportional to the target range was obtained by digitizing the multiplicity sum of the target discriminator pulses. The encoded target and RSPC information was combined with the 4-bits giving the stopping layer in the range stack. The resulting 12-bit word was then used to address a memory-lookup-unit (MLU) which was programmed to reject the long range tracks at large dip-angles from $K_{\mu 2}$ decays.

The Level 1 photon veto cut required that no more than 2 adjacent hextants have more than 10 MeV. The 15×4 counters within each hextant were summed and the output

discriminated. The resulting 6-bits of information were input to an MLU programmed to accept events with an allowed pattern of hit hextants. The hextant pattern was also used to determine the hextant used in the on-line $\pi \rightarrow \mu$ cut. The Level 1 trigger provided a rejection factor of $12 - 15$.

2.3.4 Data Acquisition

The higher level triggers required certain subsystems of the detector to be read out; therefore, before proceeding to describe the Level 1.5 and Level 2 triggers, the data acquisition system needs to be described. The E-787 data acquisition system was a hybrid of FASTBUS [39] and CAMAC [40] computer-control standards. The data acquisition system is shown in figure 2.17. During the beam spill, the TD and TDC data in individual FASTBUS crates were processed and stored by a SLAC Scanner Processor (SSP) [41]. The ADC information was read out over a high speed CAMAC serial line for use in the Level 1.5 trigger. Individual SSPs were connected by the FASTBUS cable segment and controlled by the Master SSP which enabled event synchronization. At the end of the beam spill, the Master SSP collected and assembled the events which were then sent to an available node in a farm of VME based micro-processors (ACP) [42]. The primary purpose of the ACP system was to act as a data buffer. The ACP system also performed compaction of the TD data thereby reducing the event size by a factor of 2. It was also possible to run high level off-line analysis in the ACP system.[7] Events processed by the ACP system were transferred to the host data acquisition computer and were then copied to tape.

The data acquisition system was designed to have a high transfer rate; typically, the data was transferred to tape at a rate of 180 kbytes/s. During typical AGS beam spill, approximately 30 events of 10 kbytes each, roughly broken down as 20 $K^+ \rightarrow \pi^+\nu\overline{\nu}$ triggers, 8 events from other physics triggers and 2 or so monitor events, could be recorded to tape. The trigger and data acquisition systems could operate at $3 - 5 \times 10^5$ K_T per spill with roughly 30% deadtime depending on the trigger mix. The quality of the data was monitored on-line by a dedicated program. Quantities such as the channel occupancies in the various detector subsystems, event size, and trigger rates and data acquisition performance were continuously monitored to enable prompt identification of problems in the detector, trigger or data acquisition systems.

2.3.5 The Level 1.5 Trigger

The Level 1.5 trigger reduced the trigger rate by a factor of 2 by rejecting events where the charged track energy was greater than 133 MeV. The on-line definition of the charged track

[7] For example, the Level 3 trigger for $K \rightarrow \pi\gamma\gamma$ performed an invariant mass cut on photon pairs in the barrel veto. No cuts were applied at Level 3 to the $K^+ \rightarrow \pi^+\nu\overline{\nu}$ trigger.

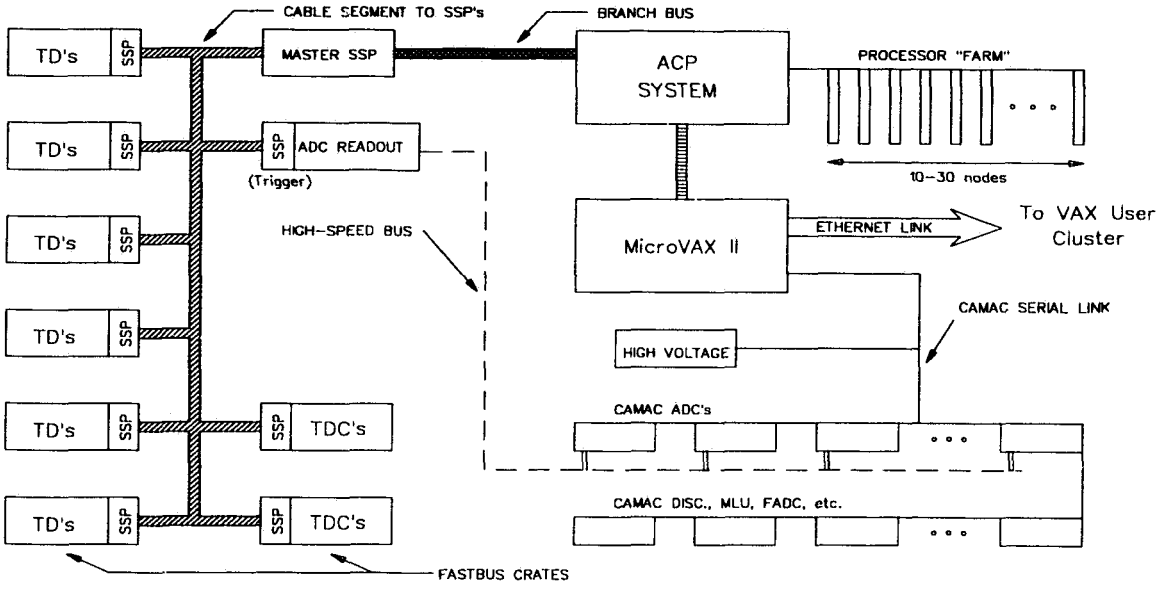

Figure 2.17: The E-787 data acquisition system.

energy was sum of the raw range stack and target ADC information. The Level 1.5 algorithm was performed by the trigger SSP. The algorithm summed the range stack energy in a 3 sector wide swath starting with Level 0 ($T \cdot A$) sector. The algorithm assumed a positively charged track and required that the ($T \cdot A$) address to be unique; events with multiple ($T \cdot A$) coincidences were vetoed. A calibration of 32 ADC counts/MeV was assumed for the detector. Corrections were made for the T ($\div 4$) and A ($\times 2$) counters as their gains differed significantly from the other RS layers. The target triangles included in the sum were required to have less than 2 MeV equivalent exclude the kaon fibers. The 133 MeV cut appears to be quite close to the kinematic limit for $K^+ \rightarrow \pi^+ \nu\overline{\nu}$ (127 MeV); however, the Level 1.5 energy calculation systematically underestimates the track energy. The I-counter energy is not included and saturation effects are ignored; furthermore, the actual target calibration is closer to 22 counts per MeV.

2.3.6 The Level 2 Trigger

The Level 2 trigger utilized the stopping hextant pulses recorded in the TD system to search for evidence of a $\pi \rightarrow \mu$ decay. The on-line stopping hextant was determined from the Level 1 hextant and the Level 0 stopping layer information. The Level 2 algorithm compared the peak pulse height to the total area of the pulse to determine whether an extra muon pulse was present. The peak pulse height and total area are quantities that can be quickly calculated from the raw data, and the ratio of the two does not depend strongly on the

pulse size. The Level 2 trigger used this relationship to require the presence of extra pulse area or equivalently, the extra energy from the $\pi \rightarrow \mu$ decay muon. For the case where the second pulse was detached, the algorithm required the second pulse to have an integrated area greater than the minimum threshold. The upstream and downstream pulses were examined sequentially; failure at either end would immediately veto the event. Events with large stopping hextant energies resulting in an overflow in the TD system were rejected. The rejection and acceptance of the Level 2 trigger varied slightly from year-to-year. On average, the Level 2 trigger provided a reduction factor of 20 for $K^+ \rightarrow \pi^+\nu\overline{\nu}$ triggers.

For the 1989 data run, the Level 2 algorithm was performed by the TD crate SSP which first read out the TD information. Improvements were made to the Level 2 trigger for the 1990 and 1991 data runs. For the 1990 data run, the pulse area calculation was performed in a specially designed FASTBUS crate controller before being read out by the SSP. For 1991, improvements were made to the algorithm used to determine the peak pulse height and individual counter calibrations were installed.

2.4 The Data

The data analysed in this thesis was amassed over three separate running periods. A summary of the data sets with the corresponding raw kaon flux is presented in table 2.2. The experiment took roughly 40 million triggers, of which approximately two-thirds were $K^+ \rightarrow \pi^+\nu\overline{\nu}$. Aside from minor differences, the data were taken under similar conditions. One exception was a broken drift chamber wire during the 1989 run. The wire break occurred approximately two-thirds of the way through the run and resulted in a reduced drift chamber tracking efficiency for the balance of the 1989 run. The data were, however, sufficiently different that it was necessary to evaluate the backgrounds and the $K^+ \rightarrow \pi^+\nu\overline{\nu}$ acceptance for each data set individually.

The $K^+ \rightarrow \pi^+\nu\overline{\nu}$ Data Samples		
Year	Running Period	K_{Tlive}
1989	March 17 to May 26	1.75×10^{11}
1990	February 2 to April 18	1.98×10^{11}
1991	April 12 to June 10	1.45×10^{11}
Sum		5.18×10^{11}

Table 2.2: K_{Tlive} was the unit of kaon flux derived from the scaler sum of the trigger K_T signals with the detector "live". The detector was "live" if the trigger and data acquisition were not already processing a previous kaon decay.

Chapter 3

The Off-line Analysis

The probability of a kaon decaying as $K^+ \to \pi^+\nu\overline{\nu}$ is about the same as that for your house to be hit by a meteor (sic) this year.

- P. Meyers

3.1 Overview

The upper limit for $K^+ \to \pi^+\nu\overline{\nu}$ based on the 1989 data set [11] has all but ruled out a large signal for the combined 1989-1991 data set. The single track $K^+ \to \pi^+\nu\overline{\nu}$ signature and 3 body phase space, coupled with the size of the potential signal, suggested that a "blind" analysis would be advantageous. In a blind analysis, the event selection criteria or "cuts" are devised without inspection of the candidate events. The primary advantage of this approach is that once the number of candidates is small, one is not influenced by the properties of the remaining candidates in determining additional cuts.

A prerequisite to a blind analysis is a detailed understanding of the backgrounds. The only possible way to extract a small signal is to have *a priori* knowledge of the backgrounds. The major component of the off-line analysis was the study of the backgrounds to the measurement of $K^+ \to \pi^+\nu\overline{\nu}$. The background processes studied were: $K_{\mu 2}$, $K_{\pi 2}$, the beam related pion scattering backgrounds and semi-leptonic K_L^0 decays from kaon charge exchange. The contribution from each of these backgrounds was evaluated and cuts were devised for their efficient elimination; each background was suppressed to the few tenths of an event level.

3.1.1 Analysis Method: Background Studies

For some experiments, it is possible to adequately simulate the primary backgrounds by Monte Carlo methods; however, for $K^+ \to \pi^+\nu\overline{\nu}$, this is not feasible. For $K^+ \to \pi^+\nu\overline{\nu}$ it is not possible to simulate the experiment to the required degree of accuracy; therefore, real

data was used to estimate the backgrounds. There are numerous advantages to using real data compared to a Monte Carlo simulation:

- The actual detector response is utilized and not simulated.
- Systematic uncertainties arising from the true geometry of the detector are eliminated.
- Hardware problems and the rate at which they occur are accounted for.
- Poorly known or measured physical processes do not have to be modeled.
- Systematic effects arising from unknown deficiencies or errors in the Monte Carlo simulation are eliminated.

The analysis was structured to enable study of the major background types using real data where possible. The selection criteria applied at the earlier stages of the analysis were chosen so that adequate reduction of the sample size could be achieved while simultaneously retaining enough events of a given background type for detailed study.

The statistical sensitivity of the background samples were enhanced beyond that of the $K^+ \to \pi^+\nu\overline{\nu}$ data sample by using two methods:

- "Inverting" a cut or group of cuts to select backgrounds with a well defined signature.
- Relaxing or not applying cuts with a large ($\sim 10^5$) rejection for the background under study.

By selecting the events that fail (or would have failed) certain cuts it is possible to select a sample representative of the background under study. This tagged sample can then be used to evaluate/design other cuts for that background. If the correlation between the tagging [1] cuts and the remaining cuts applied to the tagged sample is known, then the overall rejection can be calculated and the background contribution estimated.

There are a number of factors to consider when applying this technique. Implicit in this approach is the assumption that the rejection of the tagging cuts can be reliably evaluated. The correlation between the rejection of the tagging cut with the other cuts employed must be understood or small. An unknown correlation could lead to a systematic mismeasurement of the background. The cuts used to tag backgrounds were chosen to minimize the known correlations. Another potential problem is that the data set used to evaluate a given background may not be representative of the background in question. For example, detector resolutions may not be the same for the derived background samples as

[1] The remarks regarding the tagging cuts also apply to cuts that are relaxed.

for the actual background. This can arise from inherent differences in the data and/or the effect of relaxing cuts to improve the sensitivity of the sample.

The probability distribution that describes a discrete process when the expected outcome is a small number of events is the Poisson distribution,

$$P(n;\mu) = \frac{\mu^n}{n!}e^{-\mu},$$

where $P(n;\mu)$ is the probability of observing n events when μ is the expected number of events. The requisite background level can be determined by defining that 2 signal events constitute a $K^+ \to \pi^+\nu\overline{\nu}$ signal and that the probability of observing 2 background events be less than 5%. This corresponds to a background level from all sources of ~ 0.4 events. It is noteworthy to point out that for a $K^+ \to \pi^+\nu\overline{\nu}$ sensitivity of 1×10^{-9}, there is a 16% chance of observing a $K^+ \to \pi^+\nu\overline{\nu}$ event for an actual branching ratio of 2×10^{-10}.

3.1.2 Analysis Method: $K^+ \to \pi^+\nu\overline{\nu}$

$K^+ \to \pi^+\nu\overline{\nu}$ and $K^+ \to \pi^+X^0$ candidates were selected from stopped kaon decays using a combination of kinematic particle identification techniques, event timing, reconstruction and veto type cuts, and by requiring the characteristic $\pi \to \mu \to e$ decay sequence. The final cut on the event kinematics defined the rare decay signal region. A "blind" analysis was performed; all cuts and their positions, except for the final range cut position were devised, without inspection of the $K^+ \to \pi^+\nu\overline{\nu}$ candidates.

The acceptances for the rare decay modes were evaluated for stopped kaons using $K_{\mu 2}$, $K_{\pi 2}$, $\pi-$scattering and Monte Carlo generated rare decay data samples. The stopping kaon flux was normalized using the known $K_{\mu 2}$ branching ratio. The calculations of the rare decay acceptances and flux normalization were tested by measuring the $K_{\pi 2}$ branching ratio.

The potential systematic uncertainties in the true background level and the blind analysis philosophy suggested that a pre-defined method for dealing with background events in the signal region be developed. In this analysis, it was decided that the cut on the minimum total range of the charged track be allowed to vary from the nominal cut at 33 cm to a cut of 34 cm. The choice and limits of the total range cut were motivated by the uncertainties of the $K_{\pi 2}$ background measurement and the $K_{\pi 2}$ total range spectrum determined from the background studies. After the final analysis pass, candidate events satisfying the energy and momentum components of the signal region cut having total range between these two limits would be examined. Based on the other detector information, a decision would be made on the likelihood of the event(s) being a background or a $K^+ \to \pi^+\nu\overline{\nu}$ signal. Events consistent with being background would be removed by moving the

range cut only if they could be unambiguously identified as such. Events with total range greater than 34 cm were required to be accepted as $K^+ \to \pi^+\nu\overline{\nu}$ candidates.

3.2 The Backgrounds to $K^+ \to \pi^+\nu\overline{\nu}$

Before proceeding with a detailed description of the analysis, a review of the backgrounds and the basic strategies in dealing with them will be given. The calculations of the expected level of background presented in this section were all done before the final stage of $K^+ \to \pi^+\nu\overline{\nu}$ candidate selection was performed.

3.2.1 $K_{\mu 2}$ Type Backgrounds

There are two components to the $K_{\mu 2}$ type background, *i)* the monochromatic $K_{\mu 2}$ decay and *ii)* the radiative mode $K^+ \to \mu^+\nu_\mu\gamma$ ($K_{\mu 2\gamma}$). The rejection of $K_{\mu 2}$ type backgrounds relies on three factors:

- The ability to identify the mono-energetic muon using momentum, range and energy measurements for $K_{\mu 2}$ backgrounds or to identify the associated photon for $K_{\mu 2\gamma}$ decays.
- Consistency of the correlations between the energy, range, momentum and dE/dx with a pion hypothesis.
- Requirement of the $\pi \to \mu \to e$ decay signature.

The $K_{\mu 2}$ type background was estimated using real data. The estimated background level and associated statistical error was 0.08 ± 0.02 events for the combined 1989-1991 data set. The estimate was based on the assumption that the rejection obtained from the kinematic type quantities was independent of the rejection from requirement of the $\pi \to \mu \to e$ decay sequence. The kinematic type cuts included the final spectrum cut, which defined the $K^+ \to \pi^+\nu\overline{\nu}$ acceptance region, and cuts requiring consistency of the range-energy-momentum correlation with a pion mass hypothesis. For convenience in estimating the background rate, kinematic type cuts also included all off-line cuts excluding those aimed at identifying the $\pi \to \mu \to e$ decay chain.

Requirement of the complete $\pi \to \mu \to e$ decay sequence in the range stack using the TD system provides the largest rejection factor for $K_{\mu 2}$ type backgrounds. The empirically determined rejection was greater than 10^6. The key component is identification of the mono-energetic 4.1 MeV muon from the decay $\pi^+ \to \mu^+\nu_\mu$. The majority of muon backgrounds occur when an uncorrelated hit in the stopping counter fakes the $\pi \to \mu$ decay muon pulse and the initial muon decays as $\mu^+ \to e^+\nu_e\bar{\nu}_\mu$ to complete the $\pi \to \mu \to e$ sequence. A

related background is due to early muon decays, where the decay electron has the requisite energy to fake a muon from pion decay[2] and an uncorrelated hit fakes the decay electron to complete the chain. A third class of muon backgrounds, "tail fluctuations", arises when fluctuations in the pulse shape of the stopping muon mimic a second pulse.

3.2.2 $K_{\pi 2}$ Backgrounds

Elimination of the $K_{\pi 2}$ background relies on detection of the associated π^0 and identification of the mono-energetic π^+. For a $K_{\pi 2}$ event to mimic a $K^+ \to \pi^+ \nu\bar{\nu}$ event, the kinematic quantities must be misconstructed and the photons from the π^0 decay missed. The π^0 decay products were identified by examining the timing and energy of hits in the detector not associated with the pion or initial kaon tracks. Cuts were applied on the maximum allowed energy observed to be in coincidence with the pion track.

The rejection of π^0s is a delicate balancing act between rejection and acceptance loss. The ability to reject π^0s is a function of the width of the time window used to define a coincidence with the charged track and the threshold for the maximum allowable energy. The rate of accidental hits scales linearly with the window width and rises sharply for small hit energy. The accidentals are from beam particles and decays of "stale" muons and pions remaining in the detector from previous kaon decays. The coincidence criteria were determined from comparison of the detection rate of the π^0 decay products with the rate of ambient detector noise accidentally vetoing events.

The π^0 rejection inefficiency is limited by physics processes such as photo-nuclear absorption, and by the detector herniticity (from construction constraints) to a factor of approximately 10^{-6} per π^0. It may seem surprising that π^0s can be rejected with such a high efficiency; however, the design of the detector and the constraint of operating in the center of mass system, coupled with the fact that only one of the 2 photons involved needs to be detected, enables such a high rejection.

Any measurement of $K^+ \to \pi^+ \nu\bar{\nu}$ with a sensitivity greater than the π^0 rejection will observe residual $K_{\pi 2}$ events with no associated photons.[3] Rejection of these events is achieved by the final kinematic cuts which define the lower edge of the signal region. The level of rejection depends on the quality of the kinematic measurements; therefore, cuts designed to suppress tails in the kinematic distributions were applied.

To reliably estimate the $K_{\pi 2}$ background, the kinematic lineshapes must be well understood. The $K_{\pi 2}$ background was estimated using real data. To increase the statistical

[2]The observed rate of this process, $\sim 10^{-5}$ per muon, is consistent with the estimate from the integration of the Michel spectrum and a timing cut at 75 ns. It is for this reason that requirement of the complete $\pi \to \mu \to e$ decay sequence is necessary.

[3]The $K_{\pi 2}$ decay is source of tagged π^0s. Using the the 1988 data set, E-787 has established BR($\pi^0 \to \nu\bar{\nu}$) $\leq 8.3 \times 10^{-7}$ 90% C.L. [43]. This result is the best direct measurement of this process.

sensitivity of the background study sample, the $K_{\pi 2}$ monitor triggers were analysed without the full set of photon veto cuts. The estimate was based on the assumption that the photon veto cuts were not correlated with the final kinematic cut. For the combined data set, the estimated background and associated statistical error from $K_{\pi 2}$ decays was 0.13 ± 0.05 events.

3.2.3 Beam Related Backgrounds

There are three types of beam related backgrounds; all involve pion scattering (π-scat).

- Type I π-scat backgrounds, where a primary beam pion and kaon enter the detector with the beam pion scattering in the target into the fiducial volume. Either the kaon decay products are not detected or the kaon is absorbed and lost.
- Type II π-scat backgrounds, where a kaon enters the detector and produces a pion upstream of the target either by decaying or by strong interaction scattering. The pion subsequently scatters in the target into the fiducial region.
- Type IIa π-scat backgrounds (also referred to as kaon pileup) occur when a kaon has entered the target and a subsequent beam kaon produces a pion upstream of or in the target.

The three types of beam related backgrounds are shown in figure 3.1. The classification of the π-scat backgrounds reflects the ability to unambiguously identify the different backgrounds in the data.

The beam related backgrounds are recognizable by one or more of the following features:

- Activity in the pion Čerenkov or beam-hole counters coincident with the pion track time in the detector.
- An additional track in the BWPC coincident with the pion track time.
- The event will be "prompt". Prompt events have a small delay between the reconstructed target pion and kaon times.
- Irregular energy deposition in the B4 counter, target or I-counters.
- Timing and tracking mismatches between detector subsystems.
- Gaps between the kaon and pion track in the target track segment.

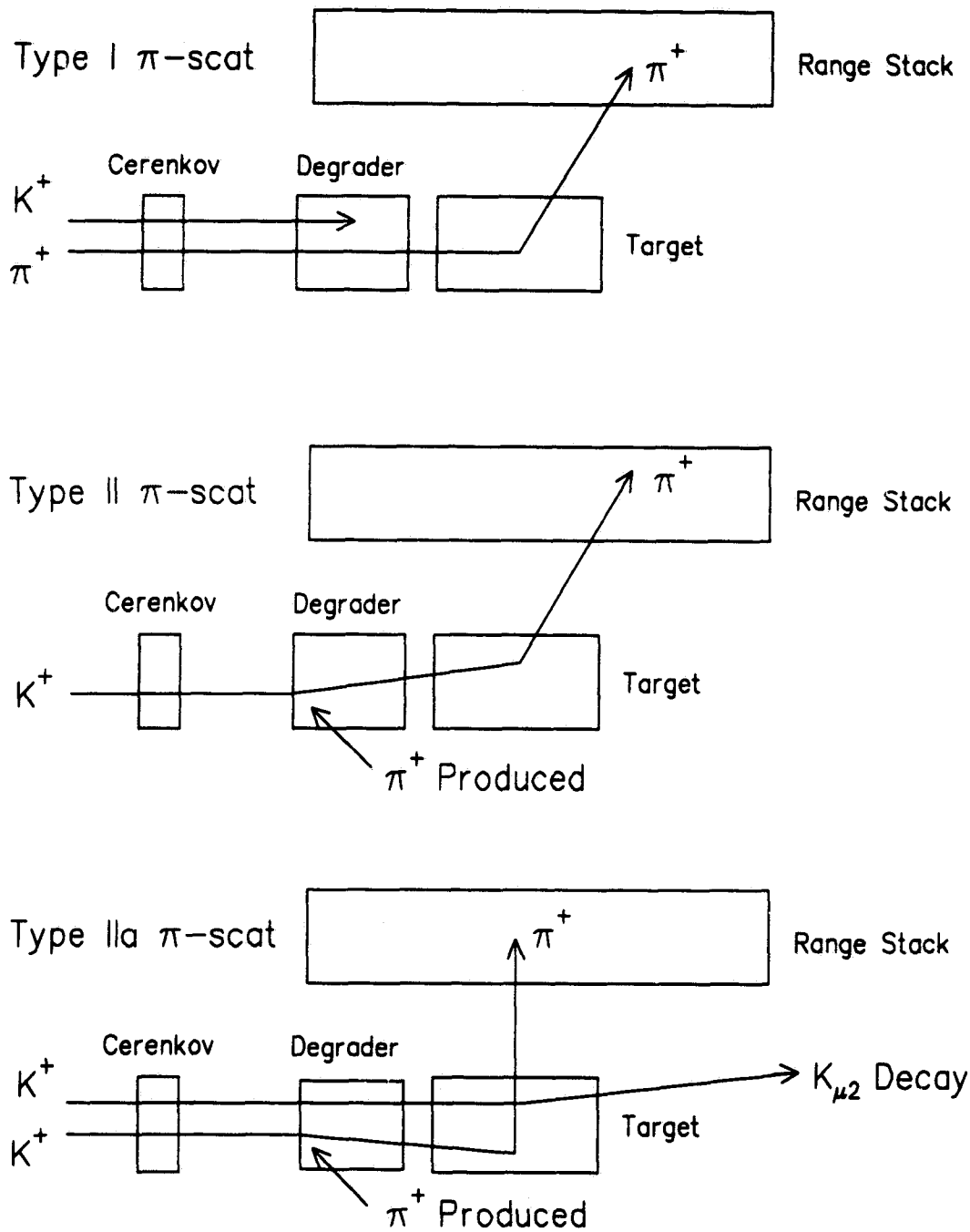

Figure 3.1: The three types of pion scattering (π-scat) backgrounds. The Type I background is due to pion contamination in the primary beam. The Type I background with the kaon entering the target is not shown. In the Type II and IIa backgrounds, the π^+ is produced by kaon decay-in-flight or by strong interaction scattering. Each type of background was estimated separately. The figure is not drawn to scale.

The beam related backgrounds were estimated using real data. The distinct signatures of the beam related backgrounds were used to tag events in the data set by inverting cuts to study the effect of the remaining cuts. The estimated background from all beam related sources was 0.21 ± 0.05 events where the error is purely statistical.

3.2.4 Charge Exchange Backgrounds

A potential background to $K^+ \to \pi^+\nu\bar{\nu}$ is the charge-exchange (CEX) background from semi-leptonic K_L^0 decays. This can occur when the K^+ enters the target and interacts with a neutron in a nucleus to produce a proton and a K^0. The CEX background process is illustrated in equation 9 where l denotes either a muon or an electron.

$$\begin{array}{rcl} K^+ + n \to & K^0 & + \; p \\ & \downarrow & \\ & K_L^0 & \to \pi^+ \; l^- \; \nu_l. \end{array} \tag{9}$$

Suppression of this background mode relies upon identification of the associated lepton and requiring decay vertex consistency. The proton associated with the K^0 is indistinguishable from the initial K^+ in the target. The neutral K_L^0 does not deposit energy along its trajectory; therefore, there will be a gap between the production and the decay vertices. Additional background suppression is achieved through the $K^+ \to \pi^+\nu\bar{\nu}$ spectrum cut and requiring a delayed coincidence between the target pion and kaon times.

Of all the backgrounds, charge exchange was the only one evaluated using a Monte Carlo simulation. The use of Monte Carlo was necessitated by an inability to cleanly tag a sufficiently large sample of CEX events for general background studies in real data. Components of the beam related backgrounds have similar target topologies making it difficult to extract and normalize the CEX background. Summing over the semi-leptonic decay modes, the estimated background and associated statistical error was 0.08 ± 0.05 events for the complete 1989-1991 data set.

3.2.5 Other Kaon Decay Modes

There are other K^+ decay modes with charged particle spectra which overlap the $K^+ \to \pi^+\nu\bar{\nu}$ signal region. The most common of these are the semi-leptonic decays, $K^+ \to l^+\pi^0\nu_l$, where l is a muon or an electron. Only the muonic mode needs to be considered. For a $K^+ \to \mu^+\pi^0\nu_\mu$ to mimic a $K^+ \to \pi^+\nu\bar{\nu}$ event, both photons from the π^0 have to be missed and the $\pi \to \mu \to e$ decay sequence has to be faked. The rejection of these two factors combined is greater than 10^{10}. The small phase space and the lower branching ratio provide additional suppression.

There are two rare kaon decay modes with a charged pion present and having $P_{\rm Max}$ = 227 MeV/c. They are $K^+ \to \pi^+e^+e^-$ and $K^+ \to \pi^+\gamma\gamma$. The rare decay $K^+ \to \pi^+e^+e^-$ has a branching ratio of $(2.7 \pm 0.5) \times 10^{-7}$ and is highly suppressed as a background by the presence of 2 additional charged tracks. From Monte Carlo, the rejection of electronic decay mode of the CEX background using only the detection of the electron in the final state was estimated to be a factor of 150. For $K^+ \to \pi^+e^+e^-$ which has an e^+e^- pair, the rejection should be at least the order of $150^2 = 22500$. This factor combined with the low branching ratio implies that $K^+ \to \pi^+e^+e^-$ is not a potential background.

The $K^+ \to \pi^+\gamma\gamma$ decay has been studied by E-787. Based on an earlier data run, an upper limit of 1×10^{-6} at the 90% confidence level has been set for the branching ratio for the kinematic region $P_\pi > 215$ MeV/c [44]. The requirement that both photons be missed provides a factor of at least $\sim 10^5$ further suppression which effectively eliminates this background. Predictions of the $K^+ \to \pi^+\gamma\gamma$ branching ratio and photon spectrum using chiral perturbation theory suggest that the branching ratio is $O(10^{-7})$ with large invariant mass photon pairs heavily favoured [45]. For the 1991 run, a trigger designed to accept events with this topology was implemented. It is anticipated that the data will reveal the first observation of this decay mode.

3.2.6 Summary of Estimated Background Levels

A summary of the number of estimated background events for the sources discussed are presented in table 3.1. All errors quoted are purely statistical. The total number of expected background events from all sources studied was 0.50 ± 0.09. The error was obtained by summing the individual errors in quadrature. The levels quoted in table 3.1 correspond to those computed before the final analysis pass on the $K^+ \to \pi^+\nu\overline{\nu}$ data set.

3.3 Summary of the Off-line Analysis

This section summarizes the analyses of the $K^+ \to \pi^+\nu\overline{\nu}$ data sets. Discussion of the results will be postponed until after the selection criteria and background estimates have been described in detail.

In order to unambiguously identify an exceedingly rare process like $K^+ \to \pi^+\nu\overline{\nu}$ in the presence of enormous backgrounds, one is forced to use virtually every bit of information that the detector provides. The reduction of the diverse forms of background, by approximately 10 orders of magnitude, necessitated a somewhat large of number of selection criteria. In all, there were 57 different off-line cuts applied which utilized close to 70 different variables.[4] An

[4]Figures showing the relevant distribution for the majority of the selection criteria are presented. The cut positions are denoted by lines. Unless otherwise stated, the side of the line that an arrow appears is the

Estimated Background Levels	
Background	Combined 1989-1991
$K_{\mu 2}$ Type	0.08 ± 0.02
$K_{\pi 2}$	0.13 ± 0.05
Type I $\pi-$scat	0.05 ± 0.04
Type II $\pi-$scat	0.10 ± 0.03
Type IIa $\pi-$scat	0.06 ± 0.02
CEX $K_{\mu 3}$	0.07 ± 0.05
CEX K_{e3}	0.005 ± 0.005
Total	0.50 ± 0.09

Table 3.1: The estimated number of background events from the sources studied. The values correspond to those computed before the final analysis pass. All errors quoted are purely statistical.

attempt has been made to reduce the reference to individual cuts by their potentially cryptic names; however, this was not feasible for the tabulation of the different analysis summaries. A complete list of the selection criteria giving a brief description which references the sections where the cut is described in detail is included in Appendix D; the section where the acceptance of the cut was measured is also cross-referenced.

The analysis was divided into 3 passes for the 1989 data set and into 4 passes for the 1990 and 1991 samples. For the 1989 data, the PASS1 analysis included most of the PASS2 selection criteria applied to the 1990 and 1991 data. Table 3.2 summarizes the selection criteria and the background sample preparation for the different passes through the data. Figure 3.2 shows the kinematic distributions at various stages of the analysis for the 1989 data. It should be noted that at each stage of the analysis, the events passing the selection criteria were not "compressed". All information from the various detector subsystems was skimmed off with the event. The results of the CPU intensive event reconstruction was saved and written out with the event.

3.3.1 PASS0

The first pass through the data was PASS0. The PASS0 procedure was a sorting stage where calibration and monitor triggers were sorted and skimmed out to different data streams. The 1989 PASS0 was performed on the BNL CCD IBM 3090. The subsequent tape copying and consolidation was done at BNL and Princeton. For the 1990 and 1991 data, the initial tape copying phase of the 300 or so 8mm tapes was done on the BNL IBM or on the E-787

region rejected by the cut. For arrows labled with "veto" instead of "cut", the region rejected is enclosed by the cut position lines.

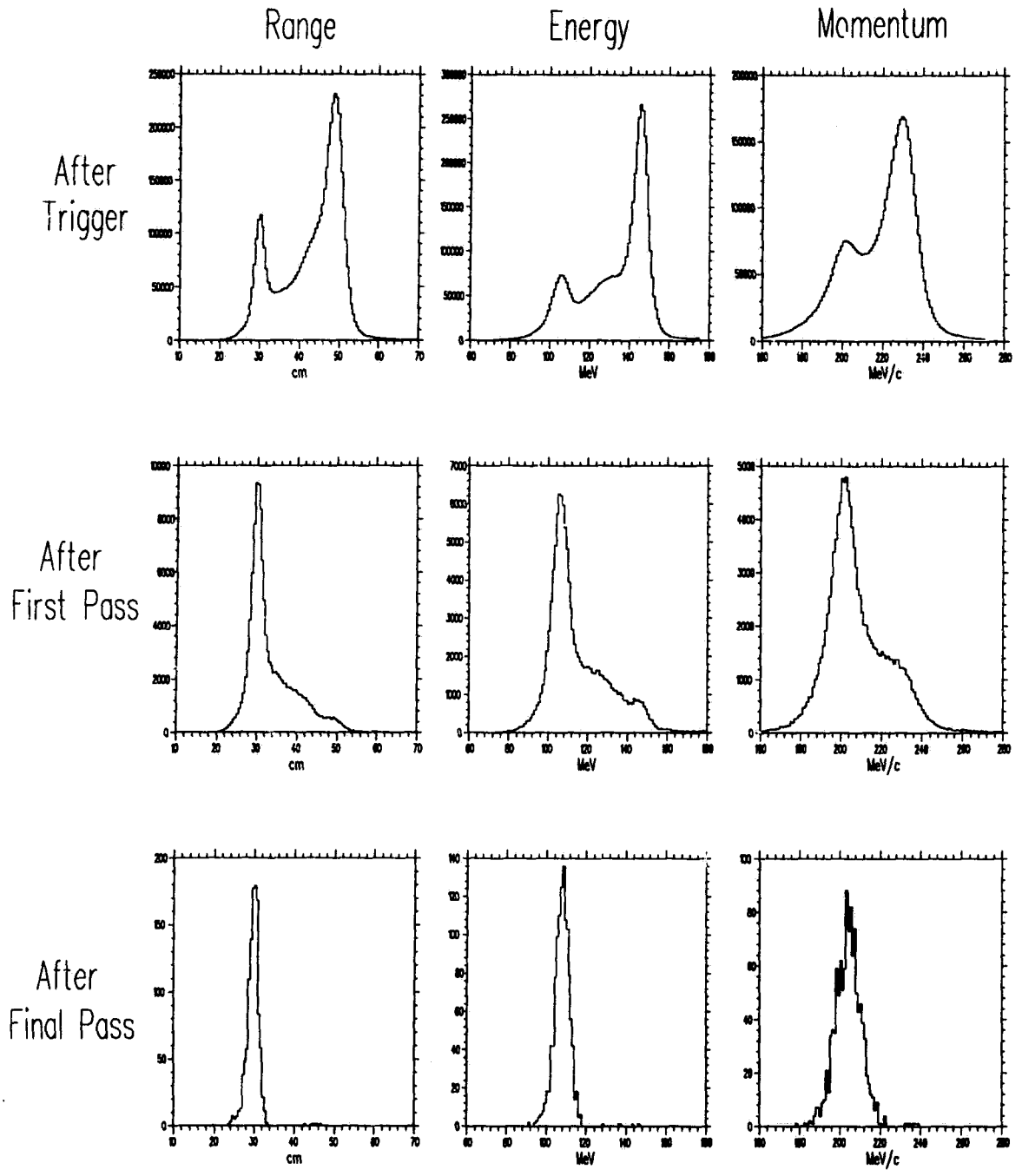

Figure 3.2: Kinematic distributions for the 1989 $K^+ \rightarrow \pi^+\nu\overline{\nu}$ data set shown for different stages of the analysis. The suppression of the $K_{\mu 2}$ peak from requirement of $\pi \rightarrow \mu \rightarrow e$ decay sequence is clearly evident. Also evident is the effect on the $K_{\pi 2}$ peak of the off-line photon veto cuts. The events having range, energy and momentum greater than the $K_{\pi 2}$ peak after the first pass on the data are predominately pion scattering background events. The row denoted "After Trigger" has had only the track reconstruction cuts applied.

Analysis Passes	
PASS0	Sort triggers, select $K_{\pi 2}$ and $K_{\mu 2}$ monitor events for detector studies and calibration
PASS1	Apply track reconstruction, photon veto and $\pi \rightarrow \mu$ cuts Select samples for muon type background studies
PASS2	Tighten photon veto cuts and require a $\pi \rightarrow \mu \rightarrow e$ sequence Prepare samples for beam related background studies
PASS3	Delayed coincidence and event quality cuts Kinematic particle ID cuts Final photon veto and $\pi \rightarrow \mu \rightarrow e$ cuts $K^+ \rightarrow \pi^+ \nu\overline{\nu}$ signal region cut

Table 3.2: Description of data analysis passes. There were minor differences between the three data sets.

counting house computer cluster. The tape copies were then divided into roughly three equal sets. Each institution, BNL, Princeton and TRIUMF was responsible for a share of the PASS0 and PASS1 processing.

3.3.2 PASS1

The goal of the PASS1 analysis was to reduce the data using only those cuts that would allow high statistics study of the major $K^+ \rightarrow \pi^+ \nu\overline{\nu}$ backgrounds. The selection criteria that were applied included:

- Charged track reconstruction in the target, drift chamber and range stack.
- Requirement of $\pi \rightarrow \mu$ two pulse signature in the stopping counter.
- Photon veto cuts in the range stack, barrel veto and endcaps.

The chronological sequence of the PASS1 analysis did not follow that of the data taking. The 1990 PASS1 was performed first, followed by 1991 and 1989. With the exception of 1989, the PASS1 analysis was performed at BNL, Princeton and TRIUMF. Each institution ran identical software which was first cross-checked and tested on a common set of data tapes. A parallel PASS1 analysis of other physics triggers was performed.

It was realized after the 1990 PASS1 had been performed that careful attention must be paid to the cut selection to ensure that the samples required for background studies could be derived from the PASS1 output. The 1989 and 1991 PASS1 analyses produced two output data streams: the regular $K^+ \rightarrow \pi^+ \nu\overline{\nu}$ data stream and a second stream called MUBG for muon type background studies. The MUBG data stream was a prescaled sample

of $K^+ \rightarrow \pi^+\nu\overline{\nu}$ triggers which were subjected to identical reconstruction and photon veto cuts as the regular $K^+ \rightarrow \pi^+\nu\overline{\nu}$ stream but had no TD based $\pi - \mu$ particle identification cuts applied. The use of the MUBG sample will be discussed in detail in section 5.1 where the $K_{\mu 2}$ type background is estimated. The prescale for the MUBG samples was a factor of 50 for both 1989 and 1991.

The 1989 PASS1 was performed at TRIUMF. The data set corresponded to 69 8mm tapes. Approximately 8×10^6 $K^+ \rightarrow \pi^+\nu\overline{\nu}$ triggers were analysed. A total of 137845 events passed the $K^+ \rightarrow \pi^+\nu\overline{\nu}$ selection criteria. The MUBG analysis resulted in 71328 events. The 1989 data had been previously analysed and its inherent subtleties were well understood. Therefore, the PASS1 analysis applied tighter selection criteria than would normally be applied at the first stage of the analysis. A summary of the PASS1 analysis for the $K^+ \rightarrow \pi^+\nu\overline{\nu}$ and MUBG streams is presented in table 3.4. The INTIME photon veto cut parameters are described in section 4.5.

The 1990 PASS1 is summarized in table 3.5. The raw data set corresponded to approximately 10×10^6 $\pi\nu\overline{\nu}$ (1) triggers. The selection criteria were not as stringent as in the the 1989 analysis. A total of 503291 events survived the analysis. The 1990 PASS1 analysis was performed before a systematic approach to background studies had been developed. Consequently, the MUBG sample was not produced. To further complicate the background studies, a particle identification cut based on the range-momentum correlation, was applied. As a safety measure, the photon veto cuts were applied only if the target and range stack track time difference satisfied $|\Delta t| < 5$ ns.

The 1991 PASS1 is summarized in table 3.6. The raw data set corresponded to approximately 8×10^6 $\pi\nu\overline{\nu}$ (1) triggers. The number of $K^+ \rightarrow \pi^+\nu\overline{\nu}$ events passing the selection criteria was 667945. The selected MUBG sample corresponded to 106950 events. The target reconstruction was performed but was not required to be successful. Similar to 1990, the photon veto cuts were applied only if the target pion time was within 10 ns of the range stack pion time.

3.3.3 PASS2

The PASS2 analysis was designed to reduce the data set to a more manageable size consistent with the requirements of background sample selection. There was no PASS2 analysis of 1989 data set. The PASS2 analysis for 1990 and 1991 primarily consisted of tighter cuts on the TD based $\pi \rightarrow \mu \rightarrow e$ identification and photon veto cuts.

The PASS2 analyses are summarized in table 3.7. The parameters used in the photon veto cuts, INTIME and TGVET, are given in section 4.5. The ELCTRN cut required a delayed $\mu \rightarrow e$ decay signature. As a monitor of the analysis, the PASS1 target reconstruction and single track requirements were re-applied. Events cut at PASS2 by the target and drift

chamber-range stack track matching requirements in 1990 reflect updates in the calibration files or minor modifications to the reconstruction software. The target reconstruction requirement was imposed on the 1991 data set.

3.3.4 Final Analysis Pass: PASS3

All the analysis cuts were determined *a priori*; hence, there existed the possibility of discovering a new background that had not been considered or observed in the background studies. To guard against this possibility, the PASS3 analysis was divided into six stages. At each stage, one-half of a given year's data set was run upon. The prescaling was performed by skipping every second event. If a stage resulted in no candidate events, the analysis proceeded to the next stage.[5] The 1989 data was analysed first, followed by the 1990 and 1991 data sets. Detailed descriptions of the PASS3 cuts will be addressed in next chapter.

Analysis of the 1989 data resulted in no $K^+ \to \pi^+\nu\overline{\nu}$ candidates in the signal region. The analyses of the 1990 and 1991 data sets each resulted in one candidate event surviving all cuts. The final spectra are shown in figure 3.3 and a summary of the remaining number of events below, above and in the $K^+ \to \pi^+\nu\overline{\nu}$ signal region is given in table 3.3. The PASS3 analyses are summarized in tables 3.8, 3.9, 3.10 for 1989, 1990 and 1991, respectively. Discussion of the candidate events will be postponed until chapter 6.

Distribution of Remaining Events				
Spectral Region	1989	1990	1991	Sum
Below Signal Region	1142	1117	768	3027
Above Signal Region	5	0	4	9
In Signal Region	0	1	1	2

Table 3.3: Distribution of remaining events with respect to rare decay mode signal region.

[5]The experience of "opening the BOX" was strikingly similar to my recollections of Christmas morning as a child. The reader is left to infer the connection.

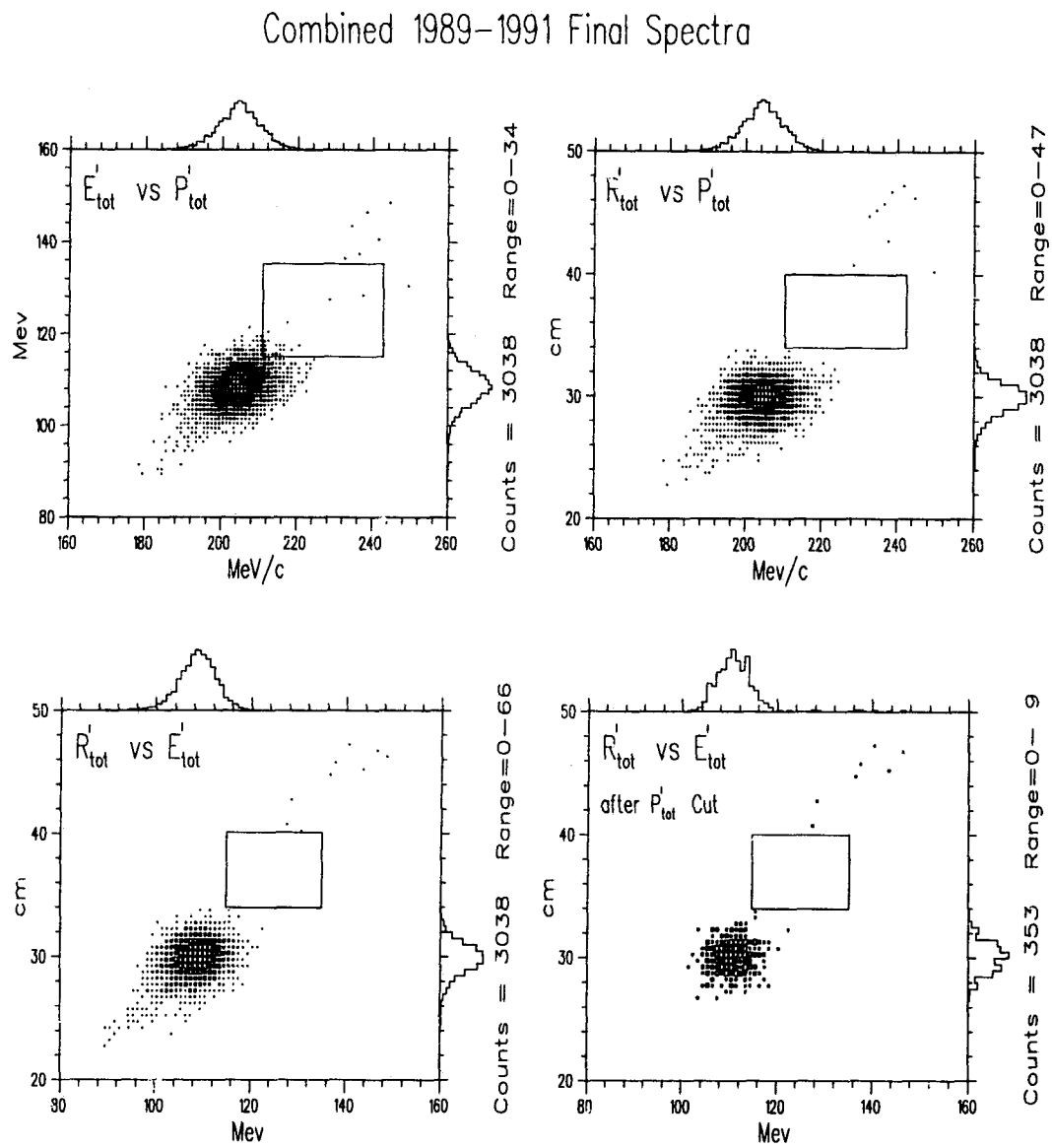

Figure 3.3: Final kinematic distributions for the combined $K^+ \to \pi^+\nu\bar{\nu}$ data set. A total of 3038 events remained before application of the final kinematic cut. The kinematic or BOX cut is denoted.

1989 PASS1 Analysis			
Cut	Rejection		Comment
	$\pi\nu\bar{\nu}$	MUBG	
PRESCALE	-	50	Prescale factor for MUBG
TARGET	1.02	1.02	Target reconstruction
DC_FIT	1.19	1.19	Drift chamber reconstruction
NTRK_RS	1.04	1.04	One and only one DC/RS track match
P_DC	1.02	1.02	Require $P_{DC} < 270$ MeV/c
TRKTIM	1.00	1.00	Find range stack track time
TICTG	1.01	1.01	Find target or I-counter time
DIPANG	1.04	1.04	Dip-angle cut: Require $\lvert\cos\theta_D\rvert < 0.55$
PREFIT	2.69	-	Single pulse TD fit, require CHIMU > 1.8
INTIME	2.06	1.48	RS,BV,EC PASS1 photon veto
DCTG_XY	1.17	1.09	Target-DC $x - y$ match < 3 cm
TRSTG	1.06	1.03	TGT-RS track time match $\lvert\Delta t\rvert < 8$ ns
FITPI	2.35	-	Require 2 pulse $\pi \rightarrow \mu$ signature
TMUAV	1.06	-	Pion lifetime cut $t_\mu^{av} > 8$ ns
CHITD	1.28	-	1% Confidence level cut for TD fit results
ELVETO	1.94	-	Veto events from early $\mu \rightarrow e$ decays
Total $\pi\nu\bar{\nu}$	58.8	-	137845 events, 2.8 Gbytes
Total MUBG	-	2.28	71328 events, 1.9 Gbytes ($\text{Rej}_{\text{tot}} = 114$)

Table 3.4: Summary of the 1989 PASS1 cut rejections. The PREFIT cut examined the quality of fit for a single pulse hypothesis in the stopping counter; an event was passed if the single pulse was a poor description of the data.

1990 PASS1 Analysis		
Cut	Rej.	Comment
PREFIT	1.56	Single pulse TD fit, require CHIMU > 1.6
TARGET	1.02	Target reconstruction
DC_FIT	1.07	Drift chamber reconstruction
NTRK_RS	1.02	One and only one DC/RS track match
P_DC	1.01	Require $P_{DC} < 270$ MeV/c
DCTG_XY	1.10	Target-DC $x - y$ match < 3 cm
DIPANG	1.01	Dip-angle cut: Require $\lvert\cos\theta_D\rvert < 0.60$
RNGMOMC	2.62	Range-momentum mass hypothesis: $\text{CL}_\pi > 0.01$ for RS tracks with longer than expected range
INTIME	1.37	RS,BV,EC PASS1 photon veto if Target-RS track time match $\Delta t < 5$ ns
FITPI	4.33	Require 2 pulse $\pi \rightarrow \mu$ signature
Total	29.8	503291 events, $\sim$ 10 Gbytes

Table 3.5: Summary of the 1990 PASS1 cut rejections. Due to availability, the statistics shown represent only a fraction of the data.

1991 PASS1 Analysis			
Cut	Rejection		Comment
	$\pi\nu\bar{\nu}$	MUBG	
PRESCALE	-	50	Prescale factor for MUBG
DC_FIT	1.09	1.09	Drift chamber reconstruction
NTRK_RS	1.04	1.04	One and only one DC/RS track match
DIPANG	1.02	1.02	Dip-angle cut: Require $\lvert\cos\theta_D\rvert < 0.60$
P_DC	1.02	1.02	Require $P_{DC} < 270$ MeV/c
TRKTIM	1.00	1.00	Find RS time
INTIME	1.36	1.36	RS,BV,EC PASS1 photon veto if Target-RS track time match $\Delta t < 10$ ns
FITPI	4.69	-	Require 2 pulse $\pi \rightarrow \mu$ signature
CHITD	1.30	-	1% Confidence level cut for TD fit results
Total $\pi\nu\bar{\nu}$	11.7	-	667945 events, $\sim$ 13 Gbytes
Total MUBG	-	1.83	106950 events, $\sim$ 2 Gbytes, ($\text{Rej}_{tot} = 92$)

Table 3.6: Summary of the 1991 PASS1 cut rejections. The target reconstruction and $\pi \rightarrow \mu$ PREFIT cuts were not applied.

PASS2 Analyses						
Cut	1990			1991		
	N_{ex}	N_{cut}	Rej.	N_{ex}	N_{cut}	Rej.
TRIG_BIT	503291	4	1.00	667945	4	1.00
TARGET	503287	28	1.00	667941	37977	1.06
NTRK_RS	503259	2	1.00	629964	0	1.00
TRKTIM	503257	146	1.00	629964	0	1.00
TICTG	503111	1008	1.00	667941	20203	1.03
DIPANG	502103	25153	1.05	609761	23218	1.04
INTIME	476950	182425	1.62	586543	233191	1.66
DCTG_XY	294525	155	1.00	353352	77507	1.28
TRSTG	294370	14520	1.05	275845	14771	1.06
TGVET	279850	63220	1.29	261074	57513	1.28
FITPI	216630	3002	1.01	-	-	-
TMUAV	213628	39034	1.22	203561	2321	1.01
CHITD	174594	38655	1.28	201240	113	1.00
ELVETO	135939	82118	2.53	201127	150793	3.99
ELCTRN	53821	21551	1.67	50354	27427	2.20
Summary	32270		15.6	22927		29.1

Table 3.7: The PASS2 analyses. "N_{ex}" and "N_{cut}" denote the number of events examined by and failing the cut, respectively. "Rej." is the cut rejection defined by the ratio of events examined to events passing. The TRIG_BIT cut required the trigger bit pattern to match the $K^+ \to \pi^+\nu\overline{\nu}$ trigger. The ELCTRN cut required an electron to complete $\pi \to \mu \to e$ sequence. For 1990, the $\pi \to \mu$ fit in the stopping counter was redone using an improved version of the algorithm.

1989 PASS3 Analysis							
Cut	N_{ex}	N_{cut}	Rej.	Cut	N_{ex}	N_{cut}	Rej.
STLAY_RS	137845	158	1.00	BHTRS	7231	115	1.02
INTIME	137687	83417	2.54	B4DEDX	7116	63	1.01
ENERK	54270	7270	1.16	PISCUT	7053	245	1.04
NTRIK	47000	3088	1.07	TGVET	6808	4011	2.43
TIMEKS	43912	1269	1.03	TGPCA	2797	381	1.16
DPIK	42643	2259	1.06	EPIMAX	2416	7	1.00
KROAD	40384	2115	1.06	EPIBAR	2409	24	1.01
RTDIF	38269	1550	1.04	EKMAX	2385	2	1.00
DCTG_XY	36719	1323	1.04	EKBAR	2383	12	1.01
TGT_Z	35396	907	1.03	IC_E	2371	37	1.02
RS_Z1	34489	2372	1.07	RSHEX	2334	49	1.02
RS_Z2_D	32117	1638	1.05	ELVETO	2285	21	1.01
LAYER14	30479	5465	1.22	ELVETO2	2264	314	1.16
RNGMOM0	25014	7127	1.40	ELCTRN	1950	402	1.26
PHOTOV	17874	1642	1.10	TDFOOL	1548	28	1.02
KINPCA	16232	1625	1.11	TMUBM	1520	29	1.02
RS_DEDX	14607	875	1.06	TMUBV	1491	15	1.01
4SEC	13745	33	1.00	TD_PCA	1476	44	1.03
DC_Z	13712	19	1.00	TD_ANAL	1432	235	1.20
PIKTIME	13693	5167	1.61	TMUADC	1197	50	1.04
PIKTIME2	8526	172	1.02	BOX_P	1147	993	7.45
B4DELC	8354	235	1.03	BOX_E	1147	1117	38.2
TRS	8119	93	1.01	BOX_R	1147	1145	574
KBEAM	8026	166	1.02	BOX	1147	1147	-
PIBEAM	7860	629	1.09	Candidates	0		

Table 3.8: Summary of the 1989 PASS3 analysis. The rejection of the individual components, (range, R, energy, E, and momentum, P), of the final kinematic or BOX cut are given.

1990 PASS3 Analysis							
Cut	N_{ex}	N_{cut}	Rej.	Cut	N_{ex}	N_{cut}	Rej.
TARGET	32270	37	1.00	PIBEAM	2797	208	1.08
STLAY_RS	32233	144	1.00	BHTRS	2589	12	1.01
INTIME	32089	15679	1.96	B4DEDX	2577	18	1.01
ENERK	16410	2541	1.18	PISCUT	2559	171	1.07
NTRIK	13869	808	1.06	TGVET	2388	223	1.10
TIMEKS	13061	339	1.03	TGPCA	2165	328	1.18
DPIK	12722	758	1.06	EPIMAX	1837	12	1.01
KROAD	11964	286	1.02	EPIBAR	1825	31	1.02
RTDIF	11678	793	1.07	EKMAX	1794	0	1.00
DCTG_XY	10885	539	1.05	EKBAR	1794	7	1.00
TGT_Z	10346	315	1.03	IC_E	1787	8	1.00
RS_Z1	10031	555	1.06	RSHEX	1779	33	1.02
RS_Z2_D	9476	171	1.02	ELVETO	1746	0	1.00
LAYER14	9305	601	1.07	ELVETO2	1746	158	1.10
RNGMOM0	8704	4	1.00	ELCTRN	1588	3	1.00
PHOTOV	8692	691	1.09	TDFOOL	1585	16	1.01
KINPCA	8001	1203	1.18	TMUBM	1569	84	1.06
RS_DEDX	6798	384	1.06	TMUBV	1485	17	1.01
4SEC	6422	4	1.00	TD_PCA	1468	54	1.04
DC_Z	6418	2	1.00	TD_ANAL	1414	248	1.21
PIKTIME	6416	3438	2.15	TMUADC	1166	48	1.04
PIKTIME2	2978	57	1.02	BOX_P	1118	1015	10.9
B4DELC	2921	92	1.03	BOX_E	1118	1055	17.7
TRS	2829	11	1.00	BOX_R	1118	1113	224
KBEAM	2818	21	1.01	BOX	1118	1117	1118.
				Candidates	1		

Table 3.9: Summary of the 1990 PASS3 analysis. The rejection of the individual components, (range, R, energy, E, and momentum, P), of the final kinematic or BOX cut are given.

1991 PASS3 Analysis							
Cut	N_{ex}	N_{cut}	Rej.	Cut	N_{ex}	N_{cut}	Rej.
STLAY_RS	22927	114	1.01	BHTRS	1574	11	1.01
INTIME	22813	10434	1.84	B4DEDX	1563	5	1.00
ENERK	12379	1418	1.13	PISCUT	1558	51	1.03
NTRIK	10961	481	1.05	TGVET	1507	118	1.09
TIMEKS	10480	154	1.02	TGPCA	1389	179	1.15
DPIK	10326	742	1.08	EPIMAX	1210	13	1.01
KROAD	9584	157	1.02	EPIBAR	1197	25	1.02
RTDIF	9584	657	1.07	EKMAX	1172	1	1.00
DCTG_XY	8927	386	1.04	EKBAR	1171	5	1.00
TGT_Z	8541	199	1.02	IC_E	1166	11	1.01
RS_Z1	8342	867	1.12	RSHEX	1155	20	1.02
RS_Z2_D	7475	134	1.02	ELVETO	1135	0	1.00
LAYER14	7341	446	1.07	ELVETO2	1135	109	1.11
RNGMOM0	6895	1089	1.19	ELCTRN	1026	3	1.00
PHOTOV	5799	376	1.07	TDFOOL	1023	10	1.01
KINPCA	5423	879	1.19	TMUBM	1013	32	1.03
RS_DEDX	4544	249	1.06	TMUBV	981	10	1.01
4SEC	4302	9	1.00	TD_PCA	971	22	1.02
DC_Z	4293	7	1.00	TD_ANAL	949	143	1.18
PIKTIME	4286	2338	2.20	TMUADC	806	33	1.04
PIKTIME2	1948	95	1.05	BOX_P	773	677	8.05
B4DELC	1853	35	1.02	BOX_E	773	746	28.6
TRS	1818	0	1.00	BOX_R	773	769	193.
KBEAM	1818	11	1.01	BOX	773	772	773.
PIBEAM	1807	233	1.148	Candidates	1		

Table 3.10: Summary of 1991 PASS3 analysis. The rejection of the individual components, (range, R, energy, E, and momentum, P), of the final kinematic or BOX cut are given.

Chapter 4

The Off-line Analysis: Event Selection

Any sufficiently developed technology is indistinguishable from magic.
- Clarke's Third Law

This chapter describes the individual cuts or selection criteria applied in the off-line analysis. The off-line event selection can be classified into eight categories:

- charged track reconstruction and event reconstruction quality cuts,
- delayed coincidence or kaon decay timing cuts,
- fiducial volume cuts,
- photon veto cuts,
- beam counter cuts,
- particle identification cuts using kinematic quantities,
- particle identification cuts using TD information, and,
- $K^+ \to \pi^+ \nu\overline{\nu}$ signal region cuts.

The off-line analysis was controlled using an analysis shell called KOFIA [46] developed for the E-787 experiment. KOFIA[1] controlled data input/output and performed scaler record and calibration file management and was the interface to the event display software and histogramming package FIOWA [47]. The KOFIA package included standard software libraries for target, drift chamber and range stack event reconstruction and accessing calibrated energy and timing information in the other detector subsystems. Off-line analysis of

[1]KOFIA is an acronym for Kaon OFfline Interactive Analysis.

the data was performed via a user-provided DPLOT subroutine. KOFIA allowed complete control over the analysis; lists of cuts to be applied and analysis parameters could be passed on to the DPLOT routine. With the exception of the specialized code used at PASS1, the analysis utilized one multi-purpose DPLOT routine. The purpose of this was to perform the $K^+ \to \pi^+\nu\overline{\nu}$ analysis, background estimates and acceptance measurements using identical code thereby avoiding potential errors and differences between DPLOTs written for specific purposes.[2]

4.1 Track Reconstruction

There are 3 separate track segments that must be reconstructed. They are the target (TGT), drift chamber (DC) and range stack (RS).

4.1.1 Target

The target reconstruction utilized the timing and energy information of the target fibers and I-counters to reconstruct kaon and pion clusters. The target pion time, t_π^{tgt}, was determined from the energy weighted mean value of the fibers assigned to the pion. The kaon time was defined similarly. If no pion fibers were found or if the R.M.S. deviation of the target time, $\sigma_t^{\bar{}}$, greater than 2 ns, the I-counter time was used. The I-counter assigned to the pion track used was determined from the intersection of the drift chamber track with a cylinder of radius 6.85 cm. The range of the track in the I-counter, R_{IC}, was determined from the direction cosines of the DC track at the I-counter radius and the I-counter thickness. Events with the DC track failing to intersect the 6.85 cm radius cylinder were removed. The TICTG cut required that a target or I-counter based pion time be found. The target pion range in the transverse plane, R_{tgt}^{x-y}, was defined as the distance between the pion track coordinates at the target periphery $(x_{tgt}^{ex}, y_{tgt}^{ex})$ and the point of closest approach to the kaon decay vertex.

4.1.2 Drift Chamber

The reconstruction process of the track segment in the drift chamber can be summarized as follows:

- Track finding in the $x - y$ plane:

  1. Convert leading edge TDC times to $x-y$ coordinates with radial layer dependent drift velocities using calibrated time pedestals and wire positions (axial layers

[2]One drawback of this is that the resulting DPLOT grew to 4760 lines of code!

Target Variables	
Variable	Description
R_{tgt}^{x-y}	Transverse pion target range
x_{vtx}, y_{vtx}	Kaon decay vertex
t_{π}^{tgt}	Target pion time
t_{K}^{tgt}	Target kaon time
σ_t^{π}	R.M.S. deviation of target pion triangles times
σ_t^{K}	R.M.S. deviation of target kaon triangles times
$N_{\triangle}^{\pi}$	Number of pion fibers (triangles)
$N_{\triangle}^{K}$	Number of kaon fibers (triangles)
$\delta_{tgt}^{K-\pi}$	Distance between kaon cluster and pion cluster
$x_{tgt}^{ex}, y_{tgt}^{ex}$	coordinates of pion track at target periphery
E_{tgt}	Charged track energy in target
E_K	Kaon energy in target
$t_{K-\pi}$	Kaon decay time, $t_{\pi}^{tgt} - t_{K}^{tgt}$
E_{IC}	Charged track energy in I-counter
R_{IC}	Charged track range in I-counter

Table 4.1: List of target variables utilized in the analysis.

only) for individual wires. Correct for sector-to-sector variation in the $T \cdot A$ stop signal and Lorentz angle.

2. For axial layer cells (super-layers 1,3 and 5), combine in-cell hits to form vectors defining track segments. Search for inter-axial layer vector matches and "connect" the cells.

3. For all possible cell combinations, perform a three parameter circle fit using the corresponding $x - y$ hits with individual hits weighted by their position dependent resolution. Test χ^2 for the fit and examine effect of including additional hits. Select tracks satisfying minimum χ^2 and number-of-hits-used requirements. Reject secondary tracks with hits used by "good" tracks.

- Track finding in the $r - z$ plane:

1. Using the constraint of the $x-y$ track fit parameters, calculate initial z positions from the $x - y$ stereo hits.

2. Select z hits with similar slopes in $r-z$ plane. Fit z hits to a straight line and test χ^2; examine effect of including additional hits. Select tracks satisfying minimum χ^2 and number of hits used requirements. Apply residual cut eliminating points with large residuals and iterate the z fit.

- Correct initial $x-y$ fit for the dip-angle dependent time-of-flight effects. Apply azimuthal angle dependent drift time correction. Iterate the $x-y$ and z fits.

- Apply $x-y$ residual cut and iterate the $x-y$ and z fits.

The DC reconstruction required at least one reconstructed track. The DC track matching the reconstructed RS track (see below) was required to have $P_{DC} < 270$ MeV/c. The track dip-angle, θ_D, was defined as the angle of the DC track with respect to the $+z$ axis. Aside from the momentum measurement, the drift chamber track information was used to estimate the track coordinates as a function of radial position in the range stack and target.

Drift Chamber Variables	
Variable	Description
P_{DC}	Drift chamber momentum
$\cos\theta_D$	Cosine of DC track dip-angle
dr	Sine of DC track dip-angle
R_C	DC track radius-of-curvature
x_c, y_c	DC track center-of-curvature
z_{ow}	DC based track z position at DC outer wall
z_{vtx}	DC based z position of kaon decay vertex
z^i_{DC}	DC based track z position at RSPC radii ($i = 1,2$)

Table 4.2: List of drift chamber variables utilized in the analysis.

4.1.3 Range Stack

The range stack tracking used ADC information to find contiguous hits in the range stack counters starting with $T \cdot A$ hits in the same sector. The algorithm gave preference to positively charged tracks. Candidate tracks were required to have a drift chamber track consistent with the $T \cdot A$ sector. The NTRK_RS cut required that there be only one DC track matching a $T \cdot A$ per event. The raw range stack energy, E^{raw}_{RS}, was the sum of energies in the individual counters where the geometric mean of the two ends was used to eliminate z dependent effects.

The range stack range, R_{RS}, was calculated using the available $x-y$ and z RSPC information. Valid RSPC hits were required to have the anode based $x-y$ hit coincident with a cathode based z hit. This requirement suppressed hits due to noise in the chambers, which for the z measurement, will lead to large tracking errors. A further requirement on the hit quality was imposed; z hits with differing by greater than 20 cm from the expected

value using the extrapolated DC track were not used. For the case of multiple coincidences, the $x-y, z$ pair with the smallest z residual was chosen.

Range Stack Variables	
Variable	Description
R_{RS}	Range of track in range stack
E_{RS}^{raw}	Energy of track in range stack
S_L'	Stopping layer in $T, A, B, C, 11 \ldots 21$ convention
S_L	Stopping layer in $T, 2 \ldots 21$ convention
S_S	Stopping sector
z_{RS}^i	z coordinate of inner ($i=1$) and outer ($i=2$) RSPC hit
E_{SL}	Energy deposited in stopping layer
t_{RS}	Time of track in range stack

Table 4.3: List of range stack variables utilized in the analysis.

The range stack range was computed from linking segments defined by the $x-y$ and z coordinates calculated from the DC track fit at the RS entrance and RSPC anode and cathode hits. The radius-of-curvature of the DC track, R_C, was rescaled by a constant factor to account for energy loss in the segment and used to compute the segment path lengths in the $x-y$ plane. The path lengths were then corrected for the track dip-angle using z information. If no RSPC information was available, the coordinates computed using an extrapolation of the DC track at the appropriate RSPC radius were used. The range to the front face of the stopping layer, beyond the last layer of RSPCs traversed, was determined from an extrapolation of the DC track using a rescaled R_C. The path length in the stopping layer was determined from the unsaturated stopping layer energy corrected for the decay muon using lookup tables. [3] Corrections were made for the azimuthal and radial gaps traversed. The equivalent path length in scintillator for the material traversed in the RSPCs was accounted for. Track energy dependent corrections for dead material energy losses were computed. Dead material included the RSPC frames and scintillator log wrappings. The range stack tracking also computed the range in the individual layers; this information was utilized in the dE/dx analysis of the range stack track.

The TRKTIM cut required that a valid RS track time be found. The time of the charged track in the range stack, t_{RS}, was determined by averaging the mean times of the individual counters found in the ADC based tracking. Counter times with large residuals or suspect timing were excluded.

[3] The stopping counter energy analysis is discussed in detail in section 4.2.2.

4.2 Calculation of the Kinematic Quantities

This section describes how the total momentum, total kinetic energy and total range were calculated. The charged track was assumed to be a pion except where noted. The data samples used to compute the peak positions and resolutions were monitor triggers spanning the entire range of runs for the year in question. The resolutions quoted were obtained without kinematic cuts requiring consistency with either a muon or a pion mass hypothesis. The $K_{\mu 2}$ based measurements assumed a muon mass.

4.2.1 Momentum

The total momentum was calculated from the raw DC momentum using

$$E = \sqrt{(P_{DC}^2 + m^2)} + E_{tgt} + E_{IC} + (R_{wall} \times dE/dx_{DC}),$$

$$P_{tot} = \sqrt{E^2 - m^2},$$

where m was the pion (muon) mass. The R_{wall} term was a small correction for the DC inner carbon fiber wall, where R_{wall} was the range in the DC inner wall, and dE/dx_{DC} was the dE/dx for a pion or a muon of momentum P_{DC} determined from interpolation of the NASA dE/dx tables [48].

The fitted peak positions for the $K_{\pi 2}$ and $K_{\mu 2}$ momentum distributions exhibited a discrepancy with the accepted values for each year for both real data and Monte Carlo data. A constant scaling factor was used to align the peaks with the accepted $K_{\pi 2}$ and $K_{\mu 2}$ values. To properly simulate the observed detector response, it was necessary to smear the momentum for Monte Carlo data. The corrections applied to real data raw momenta were

$$P'_{tot} = a_P \times P_{tot},$$

and to simulated data,

$$P'_{tot} = a_P^u \times P_{tot} \times (1 + G \times \frac{P_{smr}}{100}),$$

where a_P and a_P^u were scaling factors for data and Monte Carlo respectively, G was a Gaussian random number, and P_{smr} was the approximate difference in quadrature of the relative error between data and Monte Carlo at the $K_{\pi 2}$ and $K_{\mu 2}$ peak positions. A summary of corrections applied to the total momentum is given in table 4.4. The differences between the parameters was a consequence of the refinements made in the drift chamber tracking and improvements in the calibration procedure. The peak positions and resolutions obtained after applying the above corrections are shown in table 4.5.

Kinematic Correction Factors				
Data Type	Variable	1989	1990	1991
Momentum				
Data	a_P	1.022	1.018	1.0097
Monte Carlo	P_{smr}	1.95	1.35	1.45
	a_P^u	1.0051		
Range				
Data	b_R	0	0	0.10
Monte Carlo	R_{smr}	0.40	0	0.40
	a_R^u	1.0309		
	b_R^u	-1.1402		
Energy				
Data	a_E	0.9270	0.9389	0.9125
	b_E	10.845	9.5549	10.9308
Monte Carlo	a_s	1.00×10^{-3}	0.93×10^{-3}	1.96×10^{-3}
	b_s	-0.047	0.025	-0.096
	a_E^u	1.0092		

Table 4.4: Correction factors applied to raw kinematic quantities.

4.2.2 Energy

The total energy[4] was calculated in a four step procedure. The raw range stack energy E_{RS}^{raw} was first rescaled by a factor of 1.95/1.905 to correct for a discrepancy between the actual RS layer thickness and the thickness used in the Monte Carlo simulation employed in the ADC calibration [49]. For stopping pions, the ADC gate included the 4.12 MeV muon energy from the $\pi^+ \rightarrow \mu^+\nu_\mu$ decay. A cut on the maximum allowed pion lifetime constrained the decay to occur within the ADC gate. This excess muon energy was corrected for by subtracting the saturated energy equivalent, 3.05 MeV. Saturation effects occur when a particle dE/dx is large (equivalently, the ionization density); the scintillation mechanism is less efficient because of light quenching by damaged molecules. The saturation model used was,

$$\frac{dL}{dx} = \frac{dE/dx}{1 + K_B(dE/dx)},$$

where L was the visible energy deposited with K_B, Birks' constant, equal to 0.01 [50]. The dE/dx was calculated using the Bethe-Bloch equation. The sum of the range stack, target and I-counter energies were then unsaturated using the same model. The total track energy

[4] Unless otherwise stated, energy refers to kinetic energy.

was calculated as,

$$E_{tot} = F_{\rm unsat}(\frac{1.95}{1.905} \times E_{RS}^{raw} - 3.05 + E_{tgt} + E_{IC}) + E_{dead},$$

where $F_{\rm unsat}$ represented the unsaturation correction function and E_{dead} was a correction made for known dead material in the DC and RS. For the RS, the path length in the RSPC chambers and scintillator log wrappings were converted into an equivalent energy using a dE/dx determined from the track energy integrated inwards from the stopping counter. The typical correction was 1.8 MeV and 3.2 MeV for $K_{\pi 2}$ and $K_{\mu 2}$ events, respectively. The DC dead material correction was for the inner and outer carbon fiber support tube walls. The correction for each wall was typically 0.2 MeV. For the kinematic particle identification cuts, the range stack energy was defined as,

$$E_{RS} = F_{\rm unsat}(\frac{1.95}{1.905} \times E_{RS}^{raw} - 3.05) + E'_{dead},$$

where E'_{dead} represented the RS and DC outer wall dead material corrections. As in the case of the total momentum, there remained systematic differences between the observed and accepted values for the $K_{\pi 2}$ and $K_{\mu 2}$ energies. Monte Carlo generated data also required additional smearing to properly simulate real data. [5] The scaling correction applied to real data was,

$$E'_{tot} = a_E \times E_{tot} + b_E,$$

where a_E and b_E were determined by constraining E'_{tot} to the accepted $K_{\pi 2}$ and $K_{\mu 2}$ values. For Monte Carlo data, the total energy was rescaled using

$$E'_{tot} = a_E^u \times (E_{tot} + G \times F(E; a_s, b_s)),$$

where a_E^u was a scaling factor, G was a Gaussian random number and $F(E; a_s, b_s)$ was an energy dependent smearing factor of the form $(a_s E + b_s)\sqrt{E}$. For Monte Carlo data, a constant value for a_E^u was sufficient for all three data sets. A summary of the final kinematic corrections applied to the data set is given in table 4.4. The year-to-year differences are possibly due to rate effects and aging of the RS scintillator. The peak positions and resolutions obtained after application of the above corrections is shown in table 4.5.

4.2.3 Range

The total track range was determined using the relation,

$$R_{tot} = R_{RS} + R_{tgt} + R_{IC} + R_{walls} + R_{gas},$$

[5] This was necessary even though the energies in individual counters were smeared using realistic photoelectron statistics for the range stack and target.

where $R_{tgt} = R_{tgt}^{x-y}/dr$ was the dip-angle corrected target range, R_{walls} and R_{gas} were the equivalent thickness in scintillator of the DC carbon fiber walls and DC gas, respectively. The R_{walls} and R_{gas} corrections were typically 0.2 cm and 0.06 cm, respectively. The value of R_{RS} used in the kinematic particle identification cuts was corrected for the equivalent range in the DC outer wall. The measured mean ranges for the $K_{\pi 2}$ and $K_{\mu 2}$ were in good agreement for 1989 and 1990. A small correction, $b_R = 0.10$ cm, was applied to the total range for the 1991 data set to correct for a systematic difference between the $K_{\pi 2}$ and $K_{\mu 2}$ peak positions when compared to the 1989 and 1990 data. The source of the shift is unknown. Rescaling and additional smearing was required to simulate the observed peak positions and resolutions for Monte Carlo data. The corrections applied to the Monte Carlo data were,

$$R'_{tot} = a_R^u \times (R_{tot} + G \times R_{smr}) + b_R^u,$$

where G was a gaussian random number and R_{smr} was a range independent smearing factor. The correction factors are summarized in table 4.4. The total range measurements for each year and species are summarized in table 4.5.

Summary of Kinematic Quantities							
Quantity	Year	$K_{\pi 2}$			$K_{\mu 2}$		
		Peak	σ	%	Peak	σ	%
Momentum (MeV/c)	1989 Data	205.03	5.80	2.83	235.18	6.64	2.82
	MC	205.06	5.93	2.89	235.43	6.65	2.82
	1990 Data	205.10	5.01	2.44	235.52	5.70	2.42
	MC	205.19	5.14	2.50	235.40	5.70	2.42
	1991 Data	204.95	5.33	2.60	235.15	5.78	2.46
	MC	205.06	5.29	2.58	235.46	5.86	2.49
Accepted Value		205.14			235.53		
Energy (MeV)	1989 Data	108.43	3.46	3.19	152.43	4.09	2.68
	MC	108.39	3.59	3.31	152.50	3.95	2.59
	1990 Data	108.54	3.74	3.44	152.43	4.25	2.78
	MC	108.46	3.83	3.53	152.47	4.21	2.76
	1991 Data	108.43	3.73	3.44	152.53	4.47	2.93
	MC	108.39	3.76	3.47	152.52	4.45	2.92
Accepted Value		108.55			152.48		
Range (cm)	1989 Data	30.27	1.12	3.70	53.25	2.26	4.24
	MC	30.19	1.14	3.78	53.16	2.41	4.53
	1990 Data	30.17	1.07	3.57	53.25	2.21	4.15
	MC	30.21	1.08	3.57	53.18	2.30	4.32
	1991 Data	30.23	1.14	3.77	53.15	2.22	4.17
	MC	30.20	1.14	3.78	53.20	2.41	4.53
Accepted Value		30.34			54.62		

Table 4.5: Summary of the kinematic quantities for $K_{\pi 2}$ and $K_{\mu 2}$ monitor triggers and Monte Carlo (MC) generated data.

4.3 Delayed Coincidence Cuts

The purpose of the delayed coincidence cuts was to ensure that the kaon decayed at rest thereby preserving the mono-chromaticity of the $K_{\pi 2}$ and $K_{\mu 2}$ backgrounds. Furthermore, requiring that the target pion and kaon clusters have clear temporal separation discriminates against backgrounds due to beam pions scattering in the target and kaon charge exchange. Two sets of delayed coincidence cuts were used which are summarized in table 4.6. The standard cut on target pion-kaon time difference, PIKTIME, required $t_{K-\pi} > 2$ ns. The PIKTIME2 cut tightened this to 4 ns for events where the target pion time was based on the I-counter to compensate for the slightly poorer timing resolution. The delayed coincidence distributions for $K_{\pi 2}$ events passing the Level 0 delayed coincidence cut for target and I-counter based pion times are shown in figure 4.1.

To provide a redundant measure of the kaon decay time independent of the target, two additional cuts were devised. The B4DELC and TRS were designed to reject events passing the standard target or I-counter based cuts due to timing fluctuations or misconstructed kaon and pion clusters. The B4DELC cut compared t_{RS} to the kaon time determined from the average time of the two B4 hodoscope planes, t_K^{B4}, and required $t_{RS} > t_K^{B4}$. The distributions for $t_{RS} - t_K^{B4}$ are shown in figure 4.2 for pion scattering background and $K_{\pi 2}$ events after application of the PIKTIME and PIKTIME2 delayed coincidence cuts. The TRS cut compared t_{RS} to a third measure of the kaon time. For 1990 and 1991, the TRS cut required that $t_{RS} > t_K^{BM}$, where t_{BM} was the beam strobe time [6] determined by the kaon Čerenkov. For the 1989 data set, the TRS cut used the B4T counter TD time since the beam strobe signal was not instrumented with a TD channel.

Delayed Coincidence Cuts	
Cut	Description
PIKTIME	$t_\pi^{tgt} - t_K^{tgt} > 2$ ns for triangle based t_π^{tgt}
PIKTIME2	$t_\pi^{tgt} - t_K^{tgt} > 4$ ns for I-counter based t_π^{tgt}
B4DELC	$t_{RS} > t_K^{B4}$: t_K^{B4} was the average B4 time
TRS	$t_{RS} > t_K^{BM}$: where t_{BM} was the beam strobe time

Table 4.6:

4.4 Fiducial Volume Cuts

Fiducial volume cuts served to ensure that the event was contained within the active volume of the detector. The fiducial volume cuts applied are summarized in table 4.7. The STLAY_RS cut required the off-line stopping layer to satisfy $11 \leq S_L \leq 18$. The cut was the same as the on-line requirement. Events with $S_L < 11$ were from $K_{\pi 2}$ events where the on-line stopping layer algorithm was fooled by a non-contiguous photon shower lengthening the track. For $S_L > 18$, the $K^+ \to \pi^+ \nu \overline{\nu}$ acceptance is negligible. The DIPANG cut required the dip-angle measured in the drift chamber to satisfy $|\cos\theta_D| < 0.55$. The LAYER14 and DC_Z cuts were tuned using the events in the $K^+ \to \pi^+ \nu \overline{\nu}$ signal region derived from the MUBG samples. Discussion of these cuts will resume when the $K_{\mu 2}$ type backgrounds are evaluated in section 5.1. The TGT_Z cut examined the DC based z position of the kaon decay vertex, z_{vtx}, the lower limit for the cut corresponds to the front face of the target. The cut addressed beam-related backgrounds from pions scattering upstream of the target. The maximum z_{vtx} cut position was determined from inspection of $K_{\pi 2}$ and $K_{\mu 2}$ monitor

[6] The beam strobe was the K_T trigger signal associated with the event.

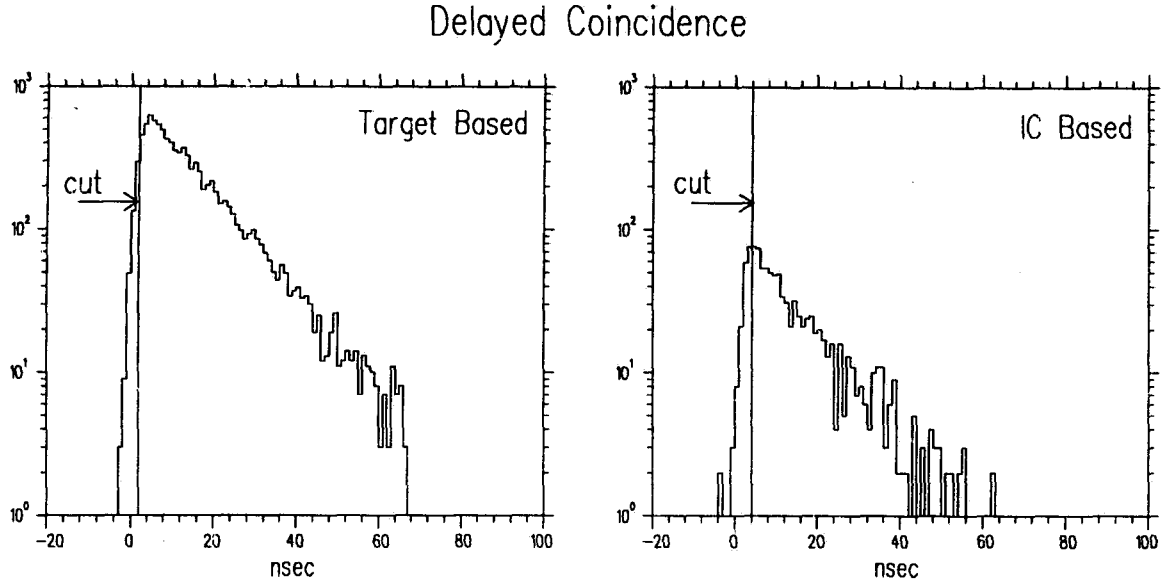

Figure 4.1: Delayed coincidence cut distributions showing $t_{K-\pi}$ for $K_{\pi 2}$ events. The PIKTIME and PIKTIME2 cut positions are shown. The on-line cut has already been applied.

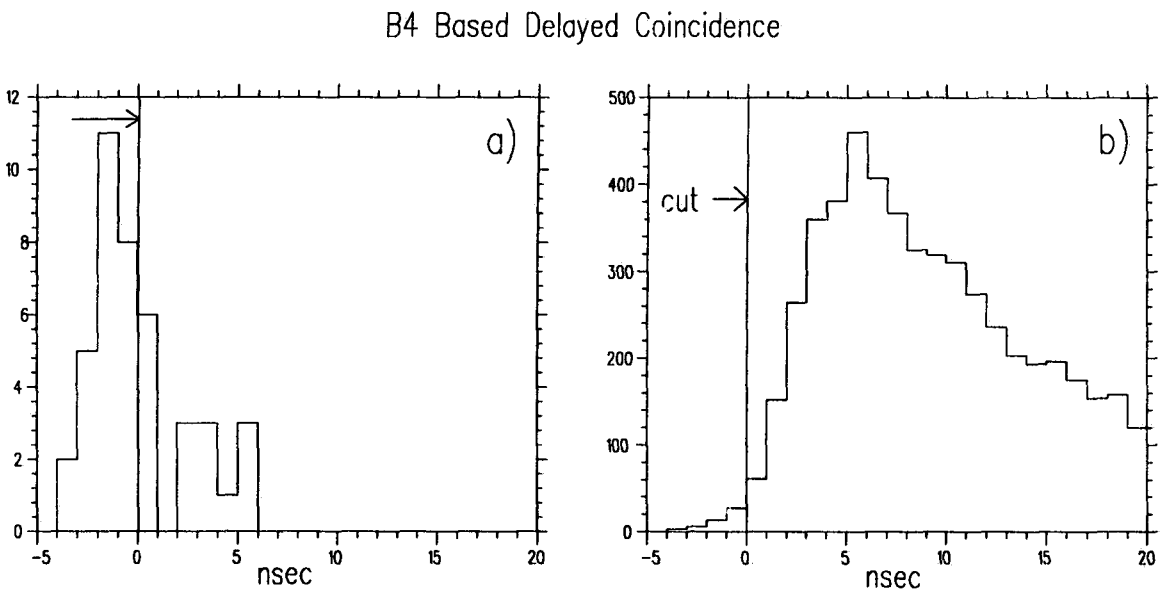

Figure 4.2: B4 hodoscope TDC based delayed coincidence times, $t_{RS}-t_K^{B4}$. The distributions are from events passing the on-line and the standard target based cuts for a) pion scattering events and b) $K_{\pi 2}$ events.

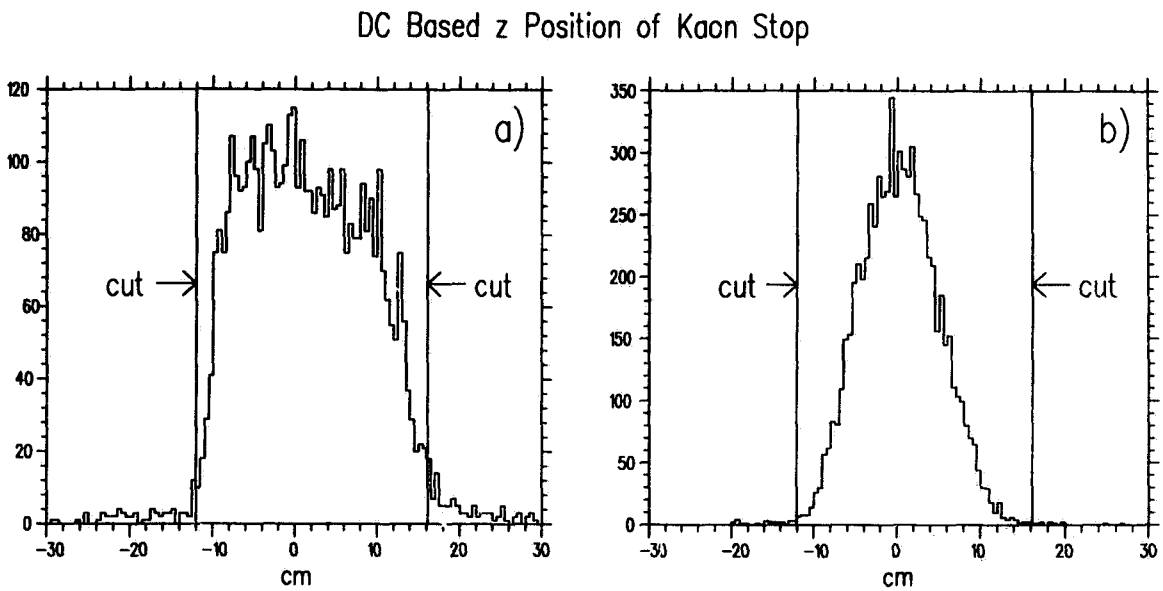

Figure 4.3: Drift chamber based z position of the decay vertex, z_{vtx}, for a) pion scattering events and b) $K_{\pi 2}$ events.

data. The z_{vtx} distribution for pion scattering backgrounds and $K_{\mu 2}$ events from the 1990 data is shown in figure 4.3.

Fiducial Volume Cuts	
Cut	Description
STLAY_RS	Off-line stopping layer cut: $11 \leq S_L \leq 18$
DIPANG	DC track dip-angle cut: $\lvert\cos\theta_D\rvert < 0.55$
LAYER14	For events with $S_L = 14$, DC track dip-angle cut: $-0.35 < \cos\theta_D < 0.50$ Veto on outer layer RSPC in the S_S or $S_S + 1$ sector
DC_Z	DC based z position at DC outer wall: $\lvert z_{ow}\rvert < 25$ cm
TGT_Z	DC based z position of the decay vertex: $-12 < z_{vtx} < 16$ cm

Table 4.7:

4.5 Photon Veto Cuts

The off-line photon vetoing in subsystems other than the target was performed using the general purpose routine INTIME. For a given detector subsystem (or subset of subsystem channels), the routine determined the energy sum of hits in coincidence with an input

reference time for a given set of coincidence windows. A veto hit in coincidence satisfied

$$|t_{hit} - (t_0 + t_{off})| < t_{win},$$

where t_{hit} was the time of the veto hit, t_0 was the reference time, t_{off} was the timing offset and t_{win} the coincidence window. Veto hits in the barrel and range stack were defined as end-to-end coincidences with associated ADC information and mean-times falling in the coincidence window. For the range stack, the list of counters associated with the pion track were excluded from the search. Veto hits in the endcaps, I-counters and V-counters were required to have ADC information and leading edge TDC times within the coincidence window. The I-counter assigned to the pion track was excluded. [7]

The photon veto cuts were applied in three stages. At PASS1, relatively narrow coincidence windows were used to allow flexibility in the later stages of the analysis. No corrections were made for the visible energy fraction in the sampling based detectors and no cuts were applied to the sum of the individual subsystem veto energies. The PASS1 cuts are tabulated in table 4.8. No subsystem timing offsets were employed. For 1990 and 1991, the PASS2 analysis tightened the photon veto cuts to be consistent with the PASS1 cuts of 1989.

PASS1 Photon Veto Cuts						
Subsystem	1989		1990		1991	
	Window	E_{cut}	Window	E_{cut}	Window	E_{cut}
RS	1 ns	1 MeV	1 ns	2 MeV	1 ns	1 MeV
BV	3 ns	1 MeV	2 ns	2 MeV	2 ns	1 MeV
EC	3 ns	3 MeV	2.5 ns	5 MeV	2 ns	3 MeV

Table 4.8: Summary of the PASS1 photon veto cuts.

The final photon veto cuts are tabulated in table 4.9. The final offsets, thresholds and veto windows were determined from an optimization of the relative veto rate between tagged $K_{\mu 2}$ monitor trigger events and tagged $K_{\pi 2}$ events from the PASS2 $K^+ \to \pi^+ \nu\bar{\nu}$ output for the range stack, barrel veto and endcap subsystems. The scatterplot of the timing difference of hits relative to the range stack time and their associated energy was used to perform a bin-by-bin search for the choice of veto window width, timing offset and energy threshold giving the largest ratio. The $K_{\pi 2}$ events were selected by requiring the confidence level for a $K_{\pi 2}$ hypothesis to be greater than 10%. The confidence level was based on the total range, energy and momentum of the track. The veto hit timing and

[7] The INTIME routine calculated different classes of energy sums based on the quality of the detector information. Other searches such as $\pi^0 \to \nu\bar{\nu}$ and $K^+ \to \pi^+ \nu\bar{\nu}$ below the $K_{\pi 2}$ peak require tighter photon vetoing criteria.

energy distributions for $K_{\mu 2}$ and $K_{\pi 2}$ data from the 1989 data set are shown in figure 4.4. The events examined had the PASS2 photon veto cuts already applied. Trivial solutions were suppressed by comparing the number of $K_{\pi 2}$ events vetoed after the PASS2 cuts to the number of $K_{\mu 2}$ events rejected. The number of $K_{\mu 2}$ events included the losses incurred by the looser PASS1 and PASS2 cuts.

PASS2 and PASS3 Photon Veto Cuts					
Subsystem	PASS2		PASS3		
	Window	E_{cut}	Offset	Window	E_{cut}
RS	1 ns	1 MeV	4.0 ns	4.0 ns	0.5 MeV
BV	3 ns	1 MeV	5.5 ns	7.0 ns	0.5 MeV
EC	3 ns	3 MeV	2.0 ns	3.0 ns	1.0 MeV
IC	3 ns	1 MeV	-0.2 ns	6.0 ns	1.0 MeV
VC	3 ns	1 MeV	0 ns	6.0 ns	1.0 MeV
Target	3 ns	see text	0 ns	6.0 ns	see text

Table 4.9: Summary of PASS2 and PASS3 photon veto cuts. The PASS2 cuts for the range stack, barrel veto and endcaps were the same as the 1989 PASS1 cuts.

4.5.1 Target Photon Veto: TGVET

The target photon veto analysis combined information from the drift chamber tracking and the target reconstruction. The DC track was extrapolated back into the target defining a 2 cm wide road whose end-points were defined by the point of closest approach to the decay vertex and the target periphery. The energy of the triangles outside the road or those inside the road not explicitly assigned to the pion or kaon tracks within the coincidence window was summed. Figure 4.5a shows the timing distribution for target hits outside the road for $K_{\pi 2}$ events after the PASS2 photon veto cuts. Figure 4.5b shows the distance from the center of the road for triangles not assigned to the kaon for $K_{\mu 2}$ events. The sum of the unused energy within the road was defined as E_{tgt}^{NU} and the number of veto triangles was N_{Δ}^{vet}. The veto window was a function of the target pion time, with $[t_{lo}, t_{hi}]$ defined according to

$$\left[\max(t_K^{tgt} - 2, t_\pi^{tgt} - t_{win}), t_\pi^{tgt} + t_{win})\right] \text{ ns},$$

where t_{win} was 3 ns and 6 ns for PASS2 and PASS3 respectively. The PASS2 cut rejected events with target veto energy sum $E_{vet} > 5$ MeV or $E_{vet} > 2$ MeV for events with $N_{\Delta}^{vet} > 1$. The final cut required that for the veto energy sum, $E_{vet} > 1$ MeV,

$$E_{vet} < 2.5 - N_{\Delta}^{vet} \times 0.5 \text{ MeV}.$$

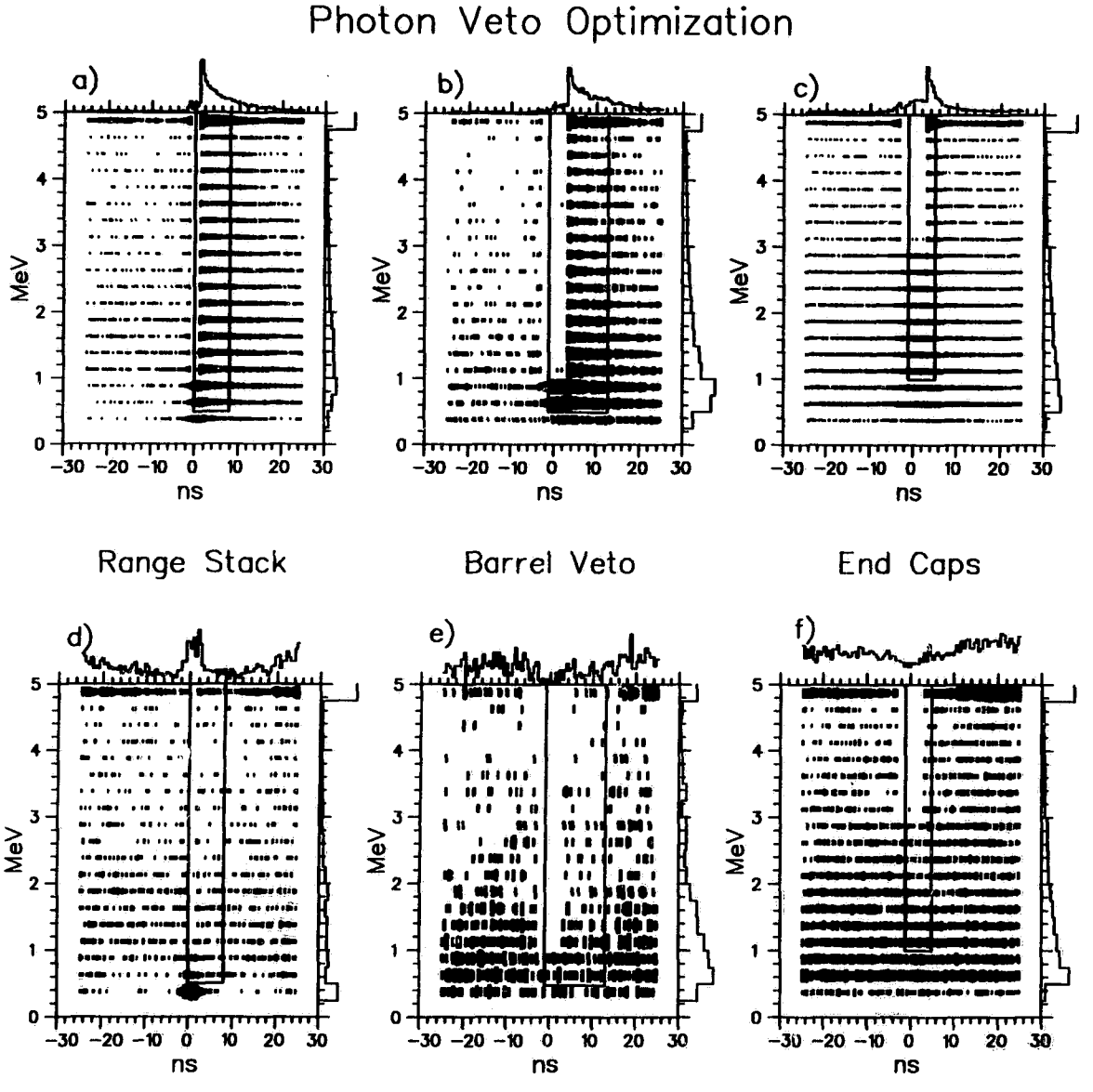

Figure 4.4: Energy versus time distributions used to optimize the PASS3 photon veto cuts. Figures a), b) and c) show the RS, BV and EC subsystems for tagged $K_{\pi 2}$ events from the $K^+ \rightarrow \pi^+ \nu\overline{\nu}$ data set. Similarly, figures d), e) and f) show $K_{\mu 2}$ monitor trigger events. The PASS2 photon veto cuts have been applied and are responsible for the depleted regions centered about 0 ns. The boxes denote the regions rejected by the PASS3 photon veto cuts.

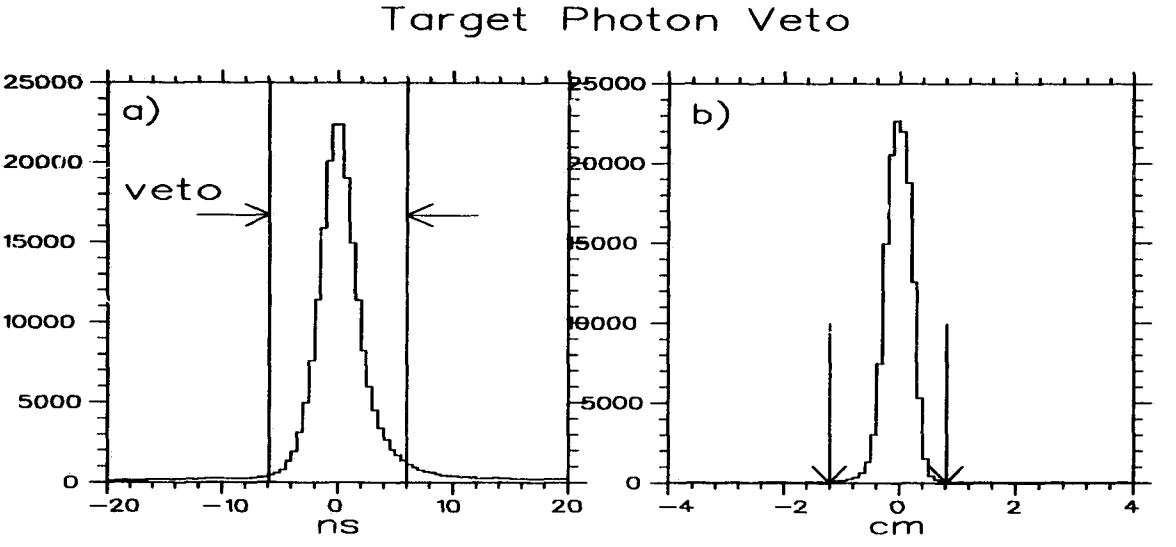

Figure 4.5: Target photon veto distributions. Figure a) shows the timing distribution relative to the pion track time for triangles outside the road defined by the DC track for $K_{\pi 2}$ events after the PASS2 photon veto. The final timing cut position is denoted. Figure b) shows the distance from the extrapolated DC track to the triangle center for fibers not assigned to kaon for $K_{\mu 2}$ events. Energy from triangles lying outside the range denoted by arrows was used to compute the target veto energy.

4.6 Event Quality Cuts

The basic track reconstruction cuts were designed to reconstruct the track segments in the individual detector subsystems with as high an efficiency as possible; failure was symptomatic of a "complete disaster". To achieve adequate background suppression, further requirements on the quality of the event reconstruction were necessary. The event quality cuts fall into two basic categories, kaon type and pion type. The event quality cuts applied are summarized in table 4.10 . Detailed descriptions follow below.

4.6.1 Energy and Timing Correlation: TGPCA

The TGPCA cut simultaneously examined 8 variables describing the overall consistency of the target pion and kaon energy distributions and the inter-subsystem timing. The variables utilized are tabulated in table 4.11. A principal component analysis (PCA) [8] of the dispersion matrix calculated using tagged $K_{\pi 2}$ monitor events from each data set was performed. The confidence level for an 8 D.O.F χ^2 sum was required to satisfy $\log(\mathrm{CL_{tgt}}) > -1.8$. The $\log(\mathrm{CL_{tgt}})$ distribution for $K_{\pi 2}$ events and tagged pion scattering background

[8] See Appendix B for a description of multivariate analysis, of which PCA is a type.

events denoting the cut position is shown in figure 4.7. A related cut, TRSTG, which required $|t_\pi^{tgt} - t_{RS}| < 8$ ns, was applied at PASS2 (PASS1 for 1989). Events failing this cut would also fail the TGPCA cut applied at PASS3.

Event Quality Cuts	
Cut	Description
TGPCA	8 variable PCA based confidence level of target timing and energy distributions: $\log(\mathrm{CL}_{\mathrm{tgt}}) > -1.8$
TIMEKS	RMS deviation of t_K^{tgt}, $\sigma_t^K < 2$ ns
NTRIK	Number of kaon triangles: $N_\Delta^K < 11$
ENERK	Target kaon energy: $20 \leq E_K \leq 140$ MeV
EKMAX	Maximum kaon fiber energy: $\max(E_\Delta^K) \geq 8$ MeV
EKBAR	Average kaon fiber excluding maximum kaon fiber > 3 MeV for $N_\Delta^K > 2$
KROAD	Extrapolated DC track intersects at least one kaon fiber
DCTG_XY	Require match in $x-y$ plane of drift chamber-target tracks at target periphery to within 1.5 cm
DPIK	Cut on minimum pion-kaon separation in the target in the $x-y$ plane
RTDIF	Maximum K-π target cluster overlap of 2 cm
EPIBAR	Dip-angle corrected average pion triangle energy: $\langle E_\Delta^\pi \rangle < 2.0$ MeV
EPIMAX	Dip-angle corrected maximum pion triangle energy: $\max(E_\Delta^\pi) < 5.0$ MeV
IC_E	I-counter energy $E_{IC} < 5$ MeV
RS_Z1	Require an inner RSPC z hit with $\lvert z_{RS}^1 - z_{DC}^1 \rvert < 12$ cm
RS_Z2_D	For $S_L > 14$ and $\lvert \cos\theta_D \rvert > 0.30$, require outer RSPC z hit with $\lvert z_{RS2}^2 - z_{DC}^2 \rvert < 12$ cm
4SEC	Veto range stack tracks crossing 3 sector boundaries

Table 4.10:

4.6.2 Kaon-Type Cuts

The TIMEKS cut was designed to reject events where the within kaon cluster timing was suspect. Large R.M.S deviations can arise from fiber misassignment, overlapping target tracks and hardware problems. The NTRIK cut removed events with an abnormally large number of kaon fibers. The cut required that $N_\Delta^K < 11$. The distribution of N_Δ^K was well described by a Poisson distribution with mean values of 4.1, 3.8 and 4.8 triangles for 1989, 1990 and 1991, respectively. The wider distribution for 1991 may have been due to the implementation of the active lead glass degrader. The mean N_Δ^K for beam pion scattering

Quantities used in the TGPCA Cut	
Quantity	Comment
E_K	Target kaon energy
z_{vtx}	DC based z position of kaon decay vertex
t_π^{tgt}	Target kaon time
$t_\pi^{tgt} - t_{RS}$	Target-Range Stack track time difference
$t_\pi^{tgt} - t_{IC}$	Target I-Counter track time difference
$\log(E_{IC}/E_{IC}^{cal})$	Logarithm of ratio of measured to expected I-counter energies
R_{tgt}	Pion range in the target
$E_{tgt} + E_{tgt}^{NU}$	Sum of pion target and unclassified energy consistent with a pion origin

Table 4.11:

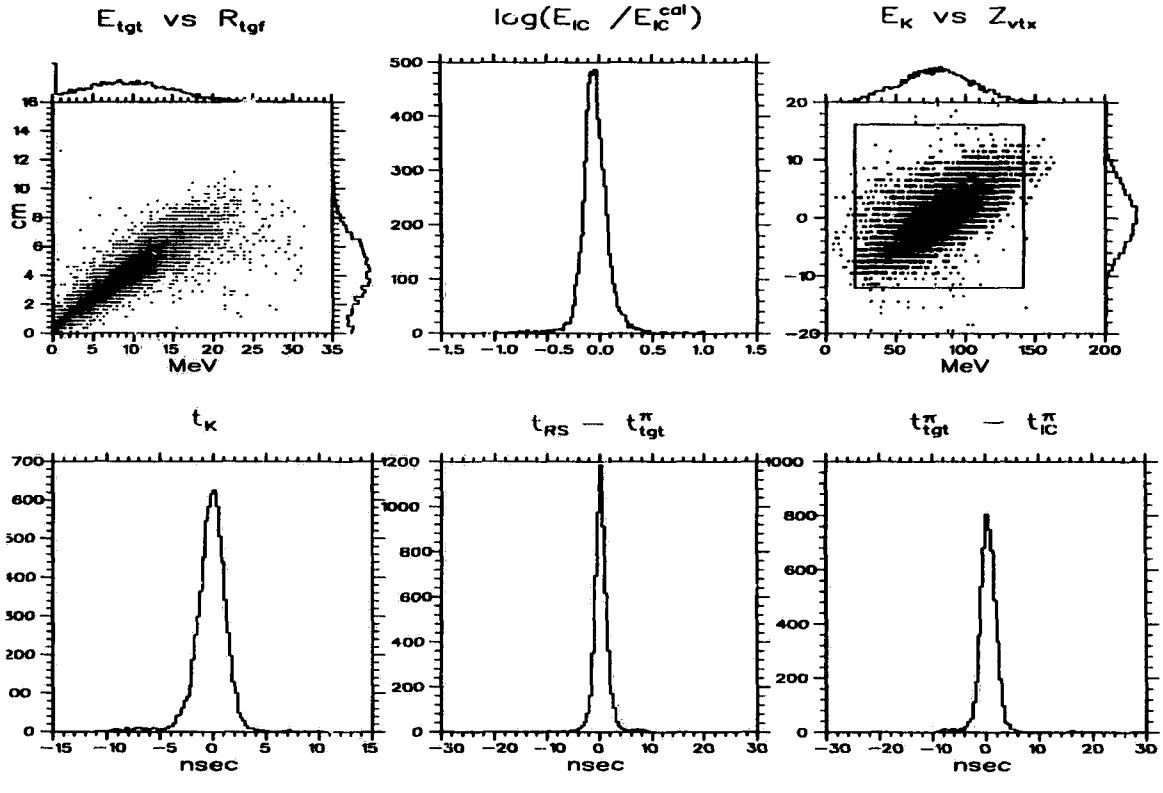

Figure 4.6: Variables used in the principal component analysis of the target information or TGPCA cut. The box in the E_K vs. z_{vtx} distribution denotes the ENERK and TGT_Z cuts. The data shown are $K_{\pi 2}$ events.

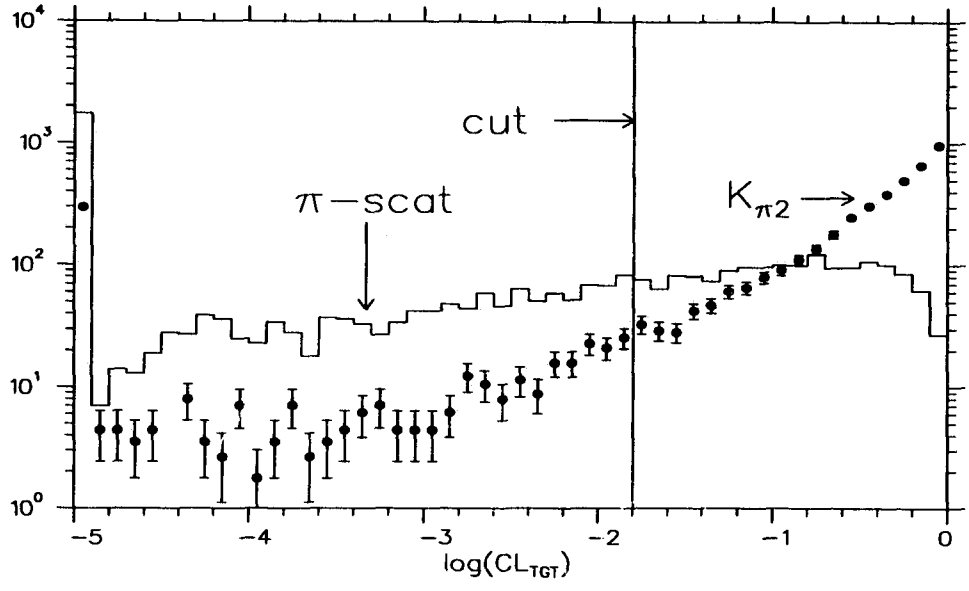

Figure 4.7: Logarithm of the TGPCA cut confidence level distributions, log(CL_{tgt}) for pion scattering events and $K_{\pi 2}$ events.

backgrounds in the 1991 data was 6.8. The distributions for σ_t^K and N_Δ^K for $K_{\mu 2}$ monitor triggers and $\pi-$scat background events are shown in figure 4.8 for 1991 data.

The cuts on the kaon energy distributions, ENERK, EKMAX and EKBAR were designed to reduce two types of backgrounds. The ENERK cut required $20 < E_K < 140$ MeV. The E_K distribution for $K_{\mu 2}$ data and $\pi-$scat events is shown in figure 4.8. Large kaon energies are associated with scattered beam pions, whereas small energies are symptomatic of kaon charge exchange. The EKMAX cut required the maximum kaon fiber energy to satisfy $\max(E_\Delta^K) \geq 8$ MeV. The EKBAR cut examined the average kaon fiber energy excluding $\max(E_\Delta^K)$. The mean value was required to be greater than 3 MeV. These cuts were based on the kaon CEX background studies. The distributions for the EKBAR and EKMAX cuts are presented in figure 4.9.

4.6.3 Pion Track Cuts

The pion tracking cuts were designed to remove the following types of events:

- photon conversions from π^0 decay with the π^+ track misidentified;
- discontinuous pion and kaon clusters symptomatic of beam pion scattering or kaon charge exchange;
- unusual target topologies leading to mismeasurement of kinematic quantities;

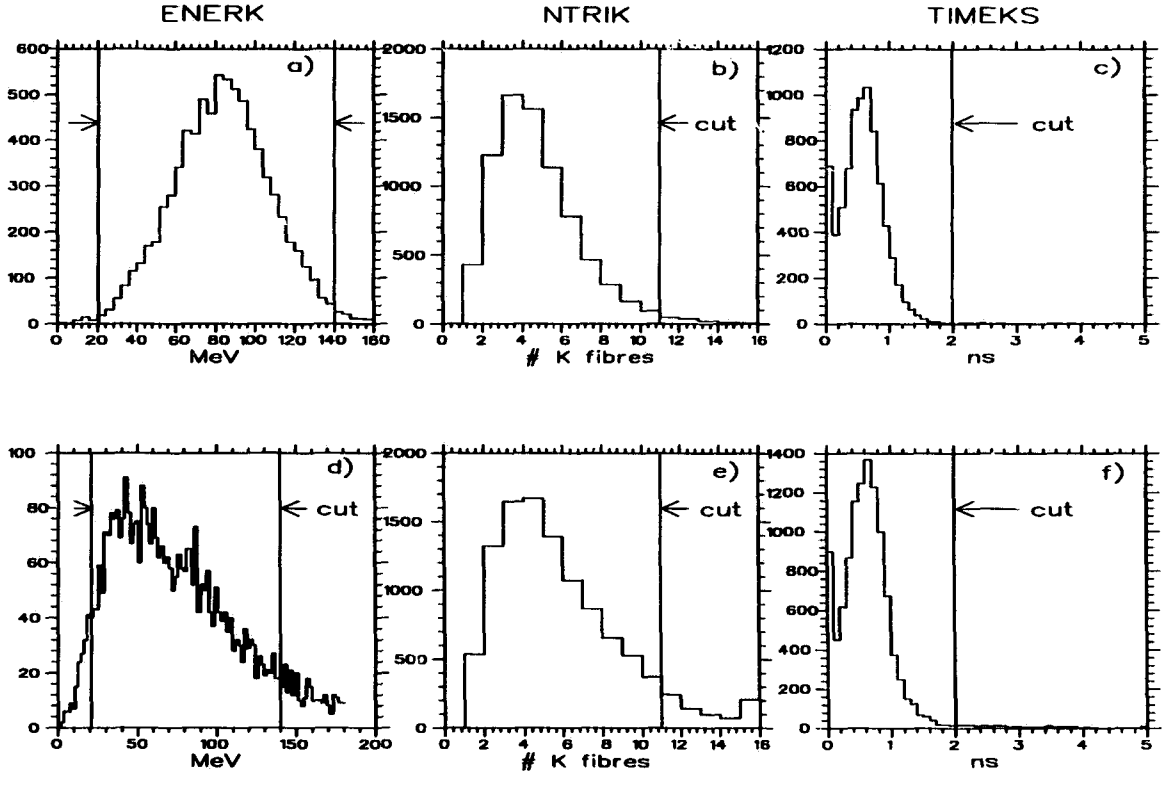

Figure 4.8: ENERK, NTRIK and TIMEKS cut distributions for 1991 data. Figures a), b) and c) show the kaon target energy, E_K, the number of kaon triangles, N_Δ^K, and R.M.S deviation for the target kaon time, σ_t^K for $K_{\mu 2}$ events, respectively. Figures d), e), f) show the same distributions for pion scattering events. The cut positions are denoted.

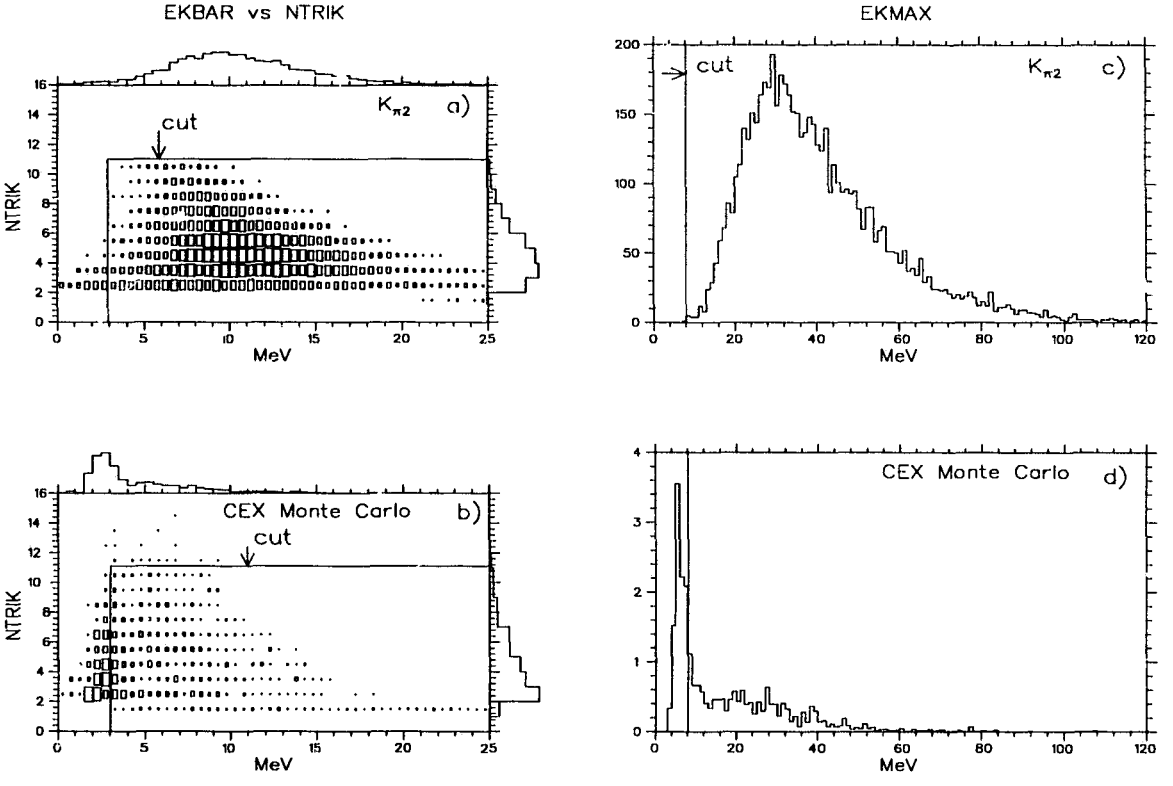

Figure 4.9: Kaon energy topology cuts. Figures a) and b) are the EKBAR vs N_{Δ}^{K} distributions for $K_{\pi 2}$ and CEX Monte Carlo data respectively. The NTRIK cut has not been applied to the CEX data. Figures c) and d) are the maximum kaon fiber energies, $\max(E_{\Delta}^{K})$, for $K_{\pi 2}$ and CEX Monte Carlo data, respectively. The cut positions are denoted. The TGPCA cut has been applied to the $K_{\pi 2}$ data.

- pion elastic scattering in the target or range stack leading to non-gaussian effects in range measurement.

The DCTG_XY cut examined the match between the pion track segments in the target and drift chamber in the $x-y$ plane at the target periphery. The cut required that the difference be less than 1.5 cm. The DCTG_XY cut applied at PASS1 was a looser version requiring the difference to be less than 3 cm. The DPIK cut looked for disconnected pion and kaon clusters. Three separate measures of the $\pi - K$ separation were cut upon. The distance of closest approach of the pion track to the kaon decay vertex was required to satisfy $\delta_{tgt}^{K-\pi} < 1.2$ cm. All possible combinations of $K-\pi$ fiber pairs were then examined, the minimum separation was required to satisfy $\delta_{min}^{K-\pi} < 1.5$ cm. The average value of $\delta_{min}^{K-\pi}$ and $\delta_{tgt}^{K-\pi}$ was then required to be less than 1.0 cm.

There were two cuts which used the DC based extrapolation of the pion track into the target. The KROAD cut required that at least one kaon fiber lie on a 2 cm wide road defined by the extrapolated pion track. The KROAD cut was motivated by the CEX background studies where it was observed that 30% of the events failed this criterion before application of the DCTG_XY cut. The RTDIF cut examined the length of the kaon cluster along the DC based road. The length was required to be less than 2 cm. The RTDIF distributions for $K_{\pi 2}$ and pion scattering data are shown in figure 4.12. The RTDIF cut was designed to remove events where ambiguity in the kaon decay vertex existed. Misassigning the vertex can artificially lengthen the pion target range, thereby pushing a $K_{\pi 2}$ event into the $K^+ \to \pi^+ \nu\bar{\nu}$ signal region.

The RS_Z1 cut required an inner layer RSPC z hit to satisfy $|z_{RS}^1 - z_{DC}^1| < 12$ cm where z_{DC}^1 was the expected z position determined from the extrapolated drift chamber track. The distribution for $K_{\pi 2}$ data is shown in figure 4.13. The cut was designed to remove events where reconstruction errors or large angle scatters in the range stack resulted in tracking errors and undesirable tails in the range distribution. At one point in the 1989 $K_{\pi 2}$ background study, 6 of the 8 remaining events in the $K^+ \to \pi^+ \nu\bar{\nu}$ signal region failed this requirement. The cut was also effective against $K_{\mu 2}$ type background events where noise in the RSPC generated a fake z hit to satisfy the Level 1 trigger with the track passing through the dead material of the chamber frame.

The RS_Z2_D cut addressed events where the track may have passed through the dead material in or around the outer layer RSPC. The cut required events stopping beyond layer 14 with large dip-angles, $|\cos\theta_D| > 0.30$, to have a z hit satisfying $|z_{RS}^2 - z_{DC}^2| < 12$ cm.

The 4SEC cut removed $K_{\mu 2}$ type events where the RS track crossed three sector boundaries. The cut was based on a Monte Carlo simulation of $K^+ \to \pi^+ \nu\bar{\nu}$ decays, where no events were observed to fail out of 10^5 triggers.

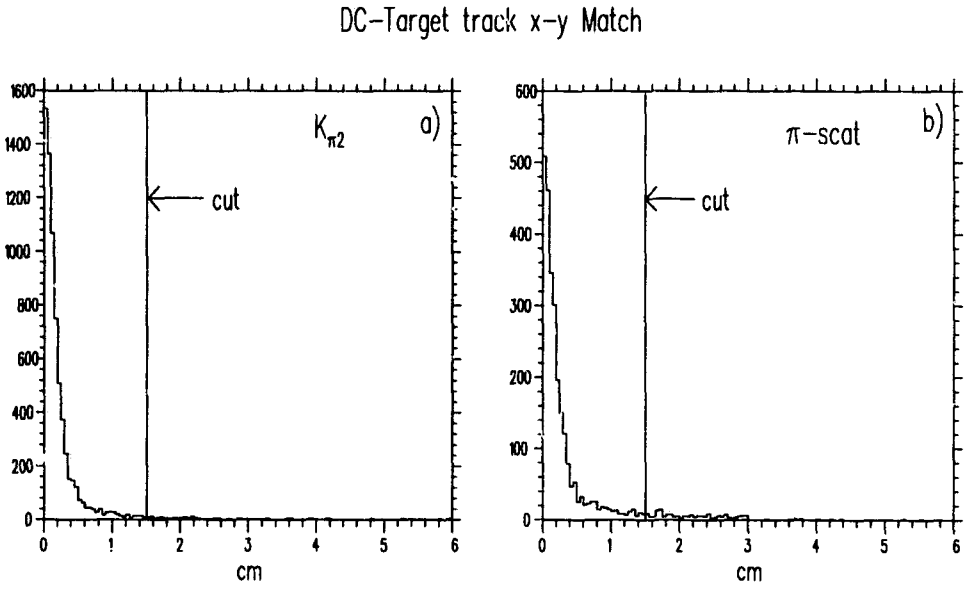

Figure 4.10: Drift chamber-target track matching in the $x - y$ plane for a) $K_{\pi 2}$ events and b) pion scattering background events. The DCTG_XY cut position is denoted.

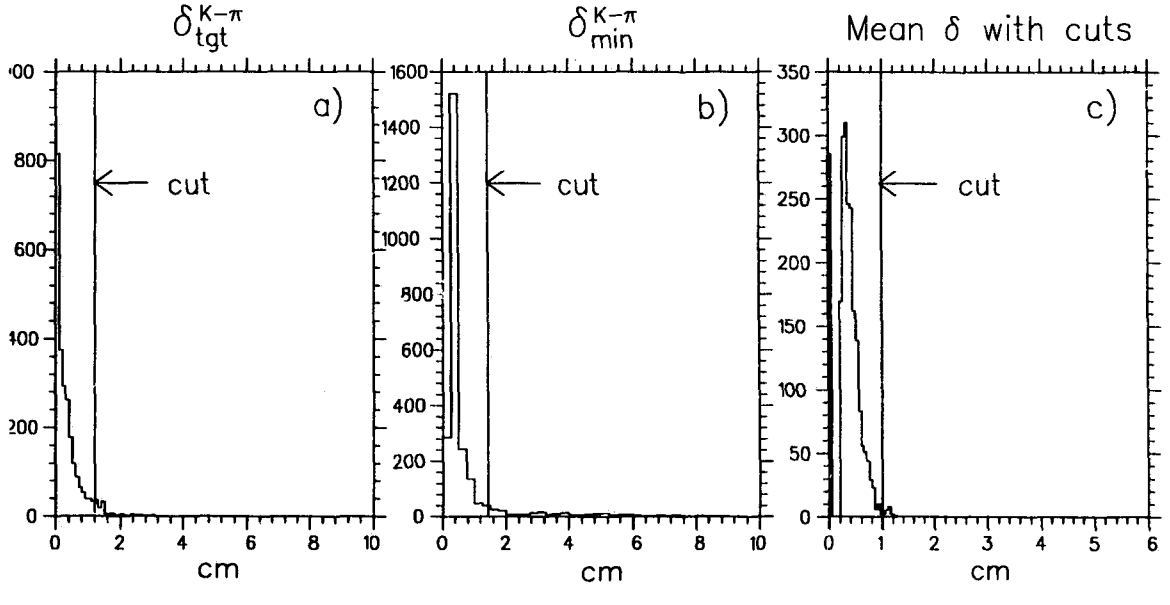

Figure 4.11: Kaon-pion proximity cuts shown for Type I $\pi-$scat backgrounds. Figure a) shows $\delta^{K-\pi}_{tgt}$, the distance of closest approach of the pion track to the assigned kaon decay vertex. Figure b) shows $\delta^{K-\pi}_{min}$, the minimum distance between any $(K - \pi)$ fiber pair. Figure c) is the average value of the two measures after their respective cuts. The DPIK cut positions are denoted.

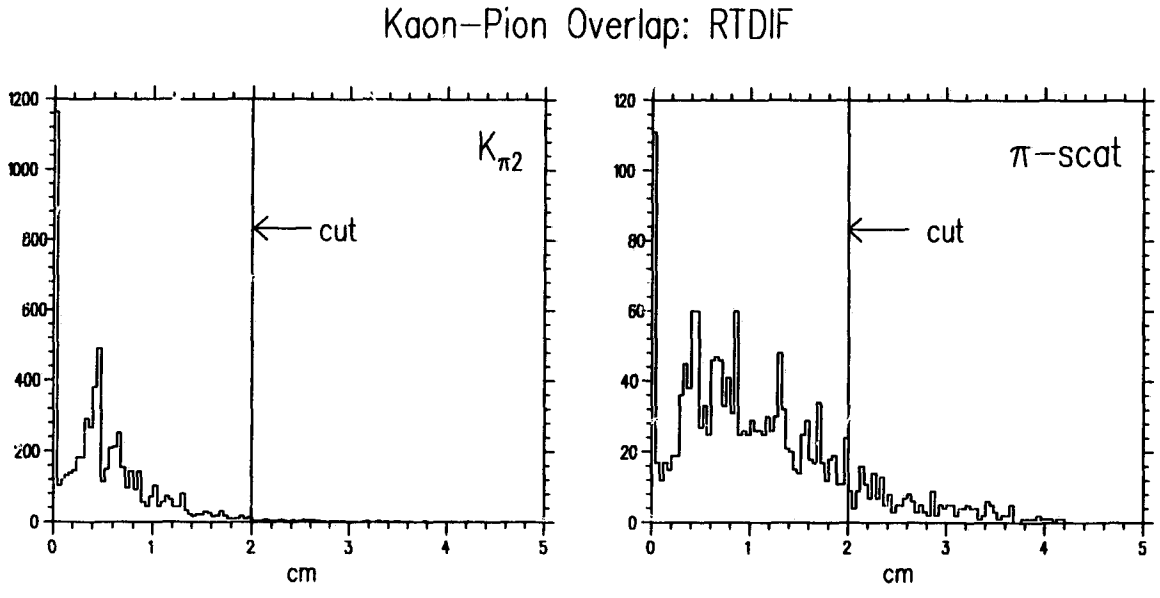

Figure 4.12: RTDIF cut distributions showing the kaon-pion cluster overlap determined from the DC track for $K_{\pi 2}$ events and pion scattering backgrounds. The cut is denoted.

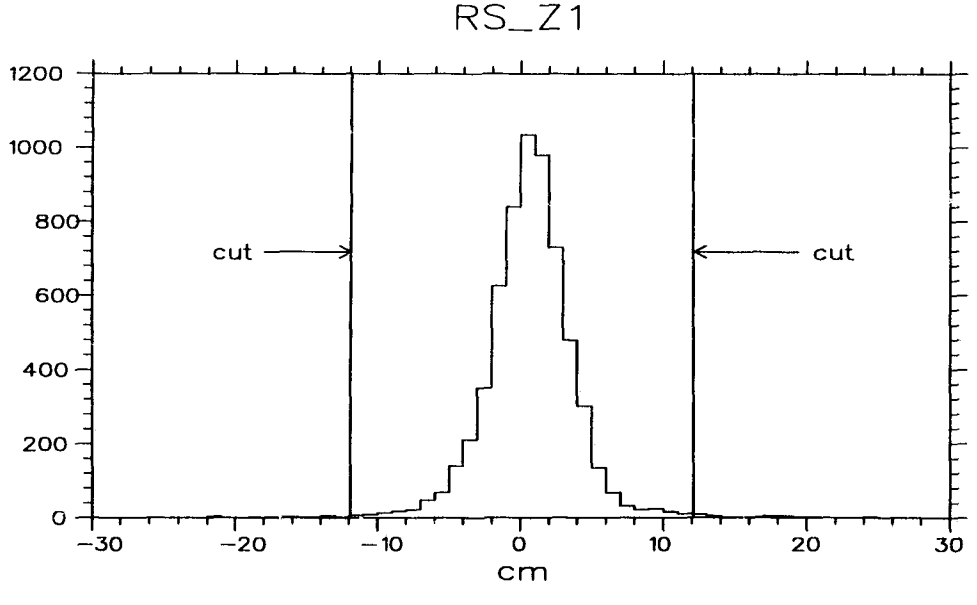

Figure 4.13: Measured minus expected inner layer RSPC z position, $z^1_{RS} - z^1_{DC}$, for $K_{\pi 2}$ data. Events without a valid RSPC z hit are not shown. The RS_Z1 cut position is denoted.

The EPIMAX cut required that the dip-angle corrected maximum pion fiber energy be less than 5 MeV. The EPIBAR cut required that the dip-angle corrected average pion fiber energy be less than 2 MeV. The IC_E cut required that the I-counter energy be less than 5 MeV. These cuts were an additional consistency test of the pion dE/dx in the target and I-counters; the TGPCA cut is less sensitive to irregular energy depositions for events with extreme values of N_{Δ}^{π} because of target resolution effects. The IC_E cut was aimed at events where an error in the I-counter range enabled an overlaying photon conversion to satisfy the dE/dx cut. The distributions for the EPIMAX, EPIBAR and IC_E cut are shown in figure 4.14.

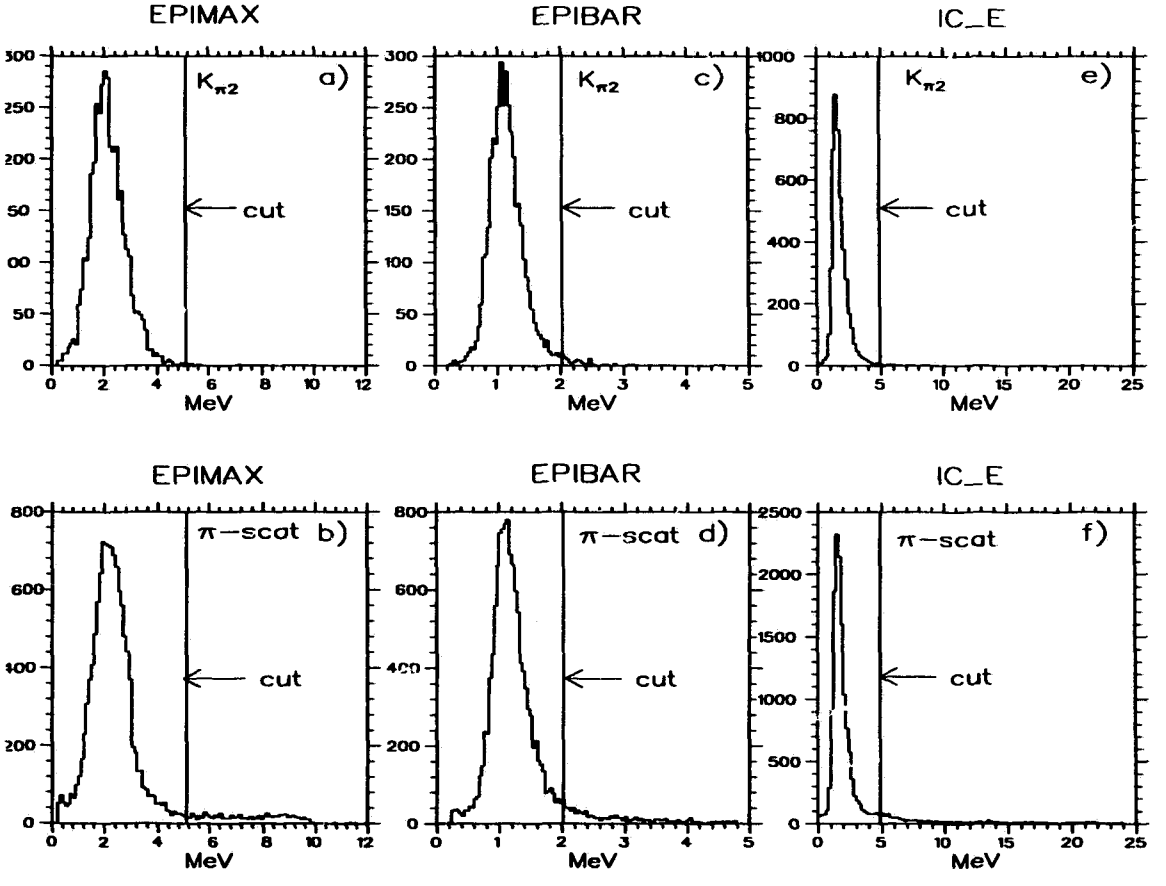

Figure 4.14: EPIMAX, EPIBAR and IC_E cut distributions. Figures a) and b) are for $K_{\pi 2}$ and pion scattering events respectively. Similarly, figures c) and d) are for the EPIBAR cut, and figures e) and f) are for the IC_E cut. The cut positions are shown. The $K_{\pi 2}$ events are shown after application of the TGPCA cut. The pion scattering events have not had the TGPCA cut applied.

4.7 Beam Counter Cuts

The purpose of the beam counter cuts was to insure that an event was due to a single kaon entering the target. The cuts are summarized in table 4.12. Detailed descriptions follow below.

Beam Counter Cuts	
Cut	Description
PIBEAM	Veto on $\check{C}_\pi$ hits coincident with t_{RS}
KBEAM	Require a coincidence between $\check{C}_K$ and target kaon time
B4DEDX	B4 hodoscope dE/dx consistent with a single kaon
PISCUT	Veto on secondary BWPC tracks coincident with t_{RS}
BHTRS	Veto on beam hole-counter hits coincident with t_{RS}

Table 4.12:

The pion Čerenkov was used to veto beam pions entering the detector and scattering into fiducial volume (Type I π-scat background). The timing windows for the cuts applied are summarized in table 4.13. The run-to-run differences reflect improvements made in timing resolution and modifications to the $\check{C}_\pi$ counting house electronics. The $\check{C}_\pi$ timing distributions for the individual data sets are shown in figure 4.15 before application of the cut.

Pion Čerenkov Cuts	
Run	Cut (ns)
1989	$\lvert t_{C\pi} - t_{RS} + 1.0\rvert < 7.0$
1990	$\lvert t_{C\pi} - t_{RS} + 1.0\rvert < 7.0$
1991	$\lvert t_{C\pi} - t_{RS} - 2.5\rvert < 6.5$

Table 4.13: Summary of the $\check{C}_\pi$ cut (PIBEAM) timing windows.

There was a class of beam related backgrounds where the kaon firing the $\check{C}_K$ was "lost" upstream of the target and a subsequent beam particle was responsible for the event. This background was suppressed by requiring a coincidence between the kaon Čerenkov and target kaon time. The KBEAM cut required $|t_{CK} - t_K^{tgt}| < 18$ ns. The cut was aimed at removing events with gross timing mismatches. The $t_{CK} - t_K^{tgt}$ distribution for $K_{\pi 2}$ and Type II pion scattering events is shown in figure 4.16.

The B4DEDX cut required a B4 hodoscope dE/dx signature consistent with a highly-ionizing particle. The B4 hodoscope energy sum (in MeV) was required to satisfy $0.5 < \log(E_{B4}) < 1.2$. The $\log(E_{B4})$ distributions for $K_{\pi 2}$ and pion scattering background data

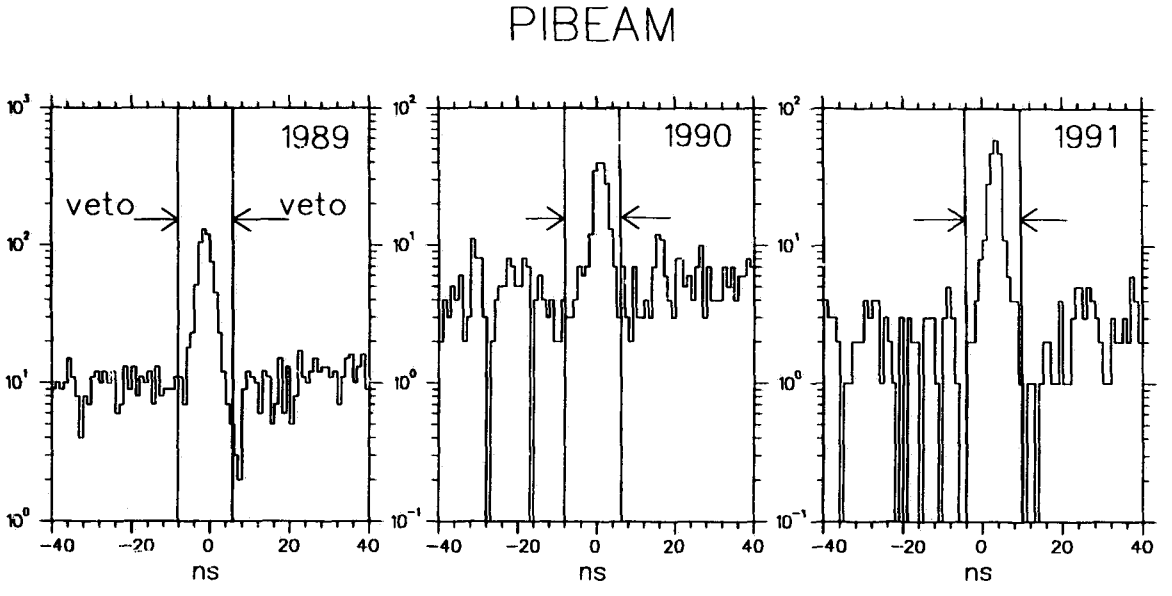

Figure 4.15: Pion Čerenkov hit timing with respect to the range stack track time for 1989, 1990 and 1991 data sets. The data shown are the $K^+ \to \pi^+\nu\overline{\nu}$ samples before the application of the cut at PASS3. The cut positions are denoted.

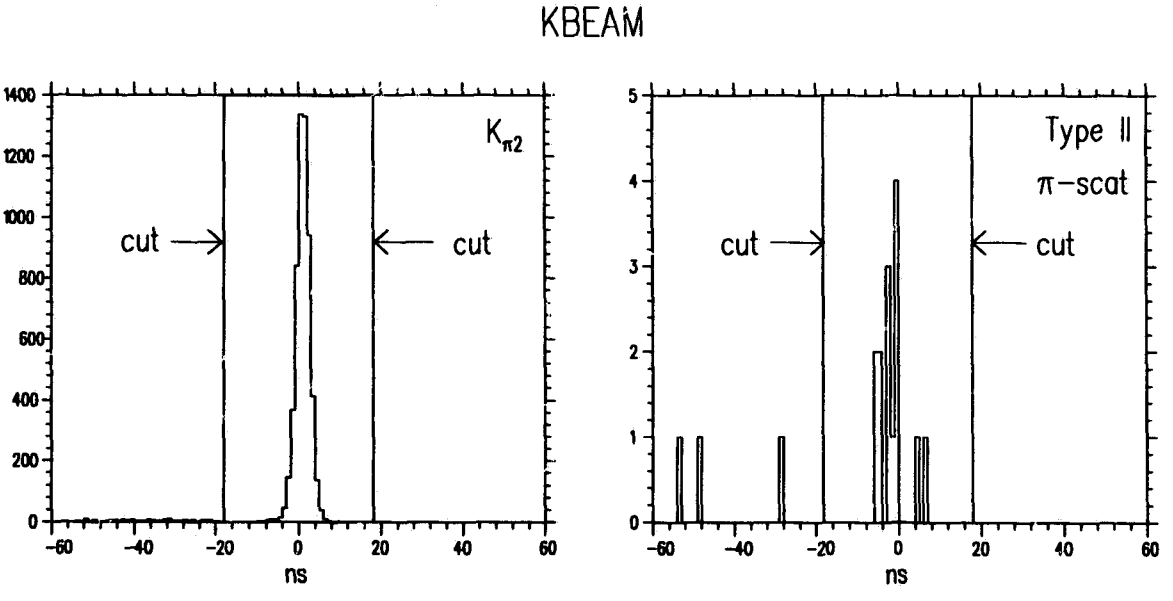

Figure 4.16: Time difference between the kaon Čerenkov and target time, $t_{CK} - t_K^{tgt}$ for $K_{\pi 2}$ and Type II pion scattering backgrounds for 1989 data. The cut position is denoted.

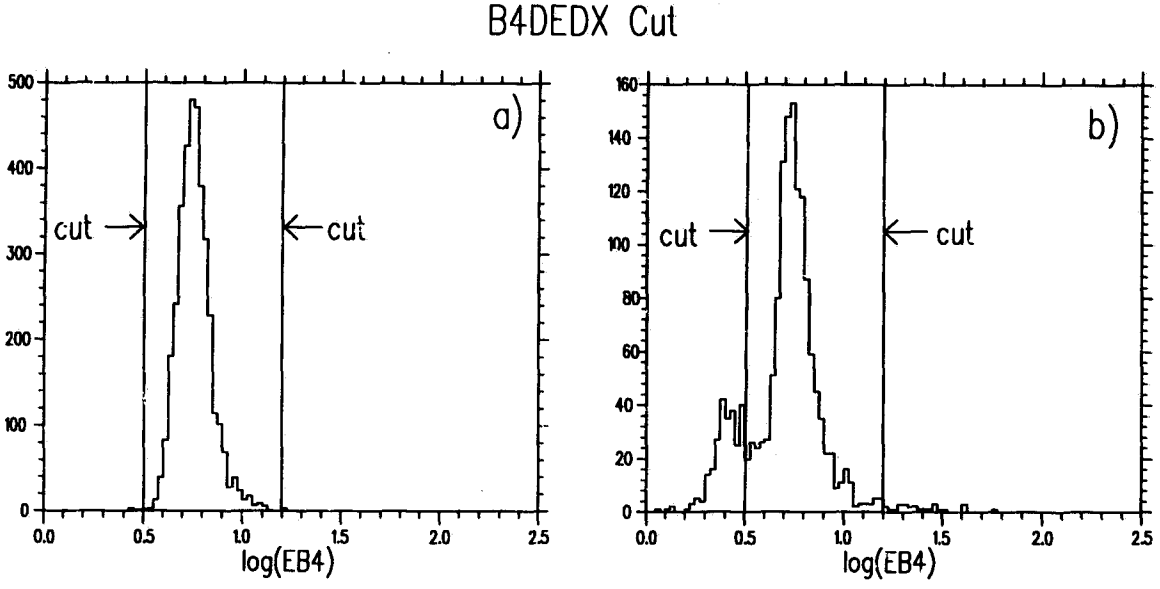

Figure 4.17: Logarithm of B4 hodoscope energy, $\log(E_{B4})$ for events with $t_{K-\pi} < 8$ ns for a) $K_{\pi 2}$ data and b) pion scattering background data. Events from the 1991 data set are shown before the application of the delayed coincidence cuts. The B4DEDX cut positions are denoted.

for 1991 data is shown in figure 4.17. For 1990, a problem with fingers 1 and 2 of the x hodoscope plane resulted in a large tail; the maximum energy cut was relaxed to 1.4. The maximum energy cut helped to suppress multiple B4 tracks and acted as an additional photon veto.

The background due to beam halo particles and the intrinsic $\check{C}_\pi$ inefficiency was suppressed by two cuts: the PISCUT cut which used BWPC information and the BHTRS cut which looked at the beam-hole counter. The PISCUT cut rejected events with a BWPC track coincident with the $\check{C}_K$ and a second BWPC track coincident with t_{RS}. Kaon tracks were identified by satisfying $|t_{Ck} - t^1_{BW}| < T^1_{win}$. A second track satisfying $|t_{RS} - t^2_{BW} - \Delta| < T^2_{win}$, where Δ was an empirically determined offset, vetoed the event. A summary of the coincidence windows and offsets is given table 4.14. The BHTRS cut vetoed events with a beam-hole counter hit satisfying $|t_{RS} - t_{BH}| < 3$ ns for pedestal subtracted BH hits greater than 50 counts.

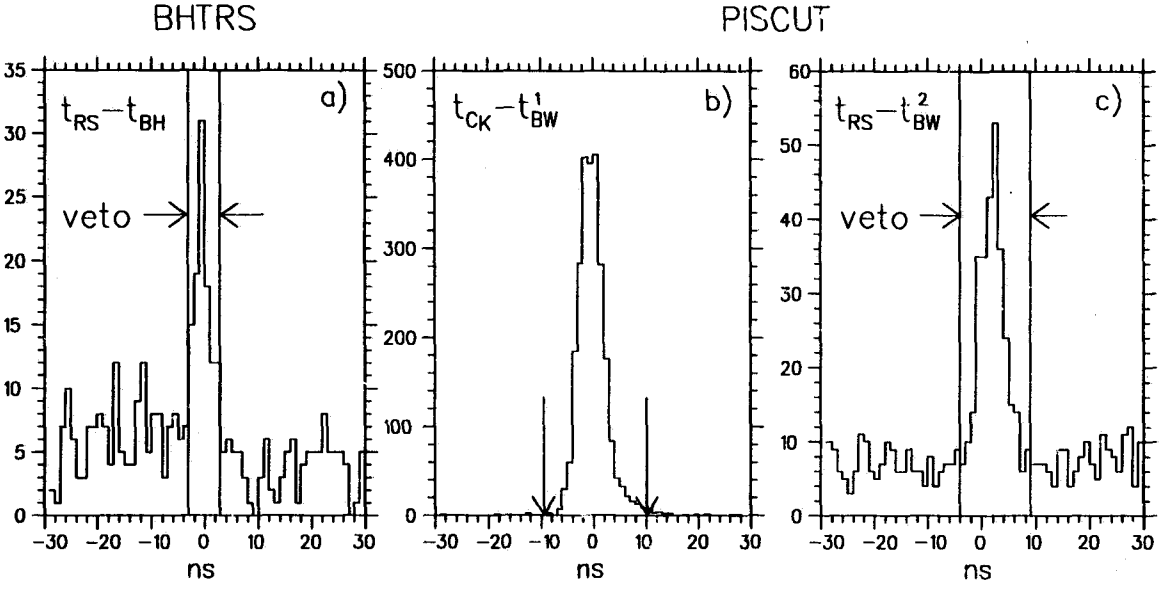

Figure 4.18: The BHTRS and PISCUT cut distributions. Figure a) shows the time difference between a hit in the beam hole counter and the range stack track. The PISCUT cut distributions are shown in figure b) and c). Figure b) shows the time difference between BWPC track and the kaon Čerenkov hit showing the window used to tag the kaon track. Figure c) shows the time difference between a second BWPC track and the range stack track. The cut position for the second track is shown. The distributions are shown for 1991 $K^+ \to \pi^+\nu\overline{\nu}$ data at PASS3 before the application of the delayed coincidence cuts and after the pion Čerenkov cut.

BWPC Track Cut Parameters			
Run	T^1_{win} (ns)	T^2_{win} (ns)	Δ (ns)
1989	16	10	6
1990	12	10	0
1991	10	6.5	2.5

Table 4.14: Summary of the PISCUT cut timing windows for BWPC tracks. T^1_{win} was the coincidence window used to select kaon tracks associated with $\check{C}_K$ hits. T^2_{win} was the timing window used to find secondary tracks in coincidence with the range stack track time with an offset Δ.

4.8 Kinematic Particle ID Cuts

The mass difference between pions and muons enables them to be distinguished by the correlations between the energy, momentum and range of the track. For example, the difference in range for muons and pions of momentum 227 MeV/c is approximately 12 cm. A series of cuts requiring that the track kinematics be consistent with a pion were applied. The cuts applied are summarized in table 4.15. Two of the cuts utilize a χ^2 probability test requiring the confidence level for a pion hypothesis, CL_π, to greater than a certain minimum.

Kinematic Particle ID Cuts	
Cut	Description
RNGMOM0	Range-momentum mass hypothesis: $CL_\pi > 0.01$ for RS tracks with longer than expected range
KINPCA	Overall energy-momentum-range correlation: $CL_{kin} > 0.20$
RS_DEDX	RS energy deposition topology consistent with a pion
PHOTOV	Require that maximum excess of energy in a given RS layer be less than 4σ.

Table 4.15:

4.8.1 Range-Momentum: RNGMOM0

The range-momentum cut examined the consistency of the measured range stack range, R_{RS}, with that expected for a pion of P_{DC}. The cut used a linear interpolation of a lookup table of ranges calculated as a function of momentum using an integration of the Bethe-Bloch equation. The cut required that the χ^2 defined as

$$\chi^2_{P/R} = \frac{(R_{RS} - R(m_\pi; P_{DC}) - \Delta_{P/R})^2}{\sigma^2}$$

have a greater than a 1% probability, where $R(m_\pi; P_{DC})$ was the expected pion range for P_{DC}, $\Delta_{P/R}$ was an empirical offset used to center the distribution and σ was the measured range momentum resolution. The cut was applied only to events with $R_{RS} - R(m_\pi; P_{DC}) > 0$ cm. Table 4.16 summarizes the RNGMOM0 cut parameters.

4.8.2 Pion Kinematic Consistency: KINPCA

The KINPCA cut examined the overall consistency of the range stack track with a pion hypothesis. A principal component analysis (PCA) using the following variables was per-

Range-Momentum Cut				
Definition	Symbol	1989	1990	1991
Offset (cm)	Δ	0.	0.	-0.38
Resolution (cm)	σ	2.50		

Table 4.16: Summary of the RNGMOM0 cut parameters.

formed:

$$\delta_{PR} = R_{RS} - R(m_\pi; P_{DC}),$$

$$\delta_{EP} = m_\pi + E_{RS} - \sqrt{P_{DC}^2 + m_\pi^2},$$

$$\delta_{ER} = R_{RS} - R(m_\pi; E_{RS}),$$

where $R(m_\pi; E_{RS})$ was the expected range for a pion of energy E_{RS}. The distributions for δ_{PR}, δ_{EP} and δ_{ER} plotted versus the stopping layer, S_L, are shown in figure 4.19 for the 1991 data set for pions. For comparison the muon distributions are also shown, note that the muon data has had the RNGMOM0 cut already applied. The PCA was performed using tagged pions from the pion scattering background analysis. [9] The kinematic dependence of the resolutions was accounted for by performing the PCA for each of the 8 layers of the $K^+ \to \pi^+\nu\bar{\nu}$ acceptance. The muon data shown in figure 4.19 corresponds to the 1991 MUBG data set. The KINPCA cut required that the kinematic confidence level $\mathrm{CL_{kin}} > 0.2$. Figure 4.20 shows the confidence level for tagged pions compared to the residual signal region muons for the 1991 MUBG data.

4.8.3 Range Stack dE/dx: RS_DEDX

The radial segmentation in the range stack provided a number of independent samples with which to measure the dE/dx evolution of the track. Since the range in the stopping counter was determined from the energy, there are $S'_L - 2$ (ignoring the T counter) samples that may be used test the consistency of a pion hypothesis. The RS_DEDX cut required $\mathcal{F} < 1.1$, where $\mathcal{F}$ was defined as,

$$\mathcal{F} = \ln\left(\frac{1}{S'_L - 2}\sum_{i=2}^{S'_L-1}\left[\ln\left(\frac{(dE/dx_{exp})_i}{(dE/dx_{obs})_i}\right) - \Delta_i(S'_L)\right]^2\right) + 4.2,$$

[9] The pion event tagging will be discussed in section 5.3.1.

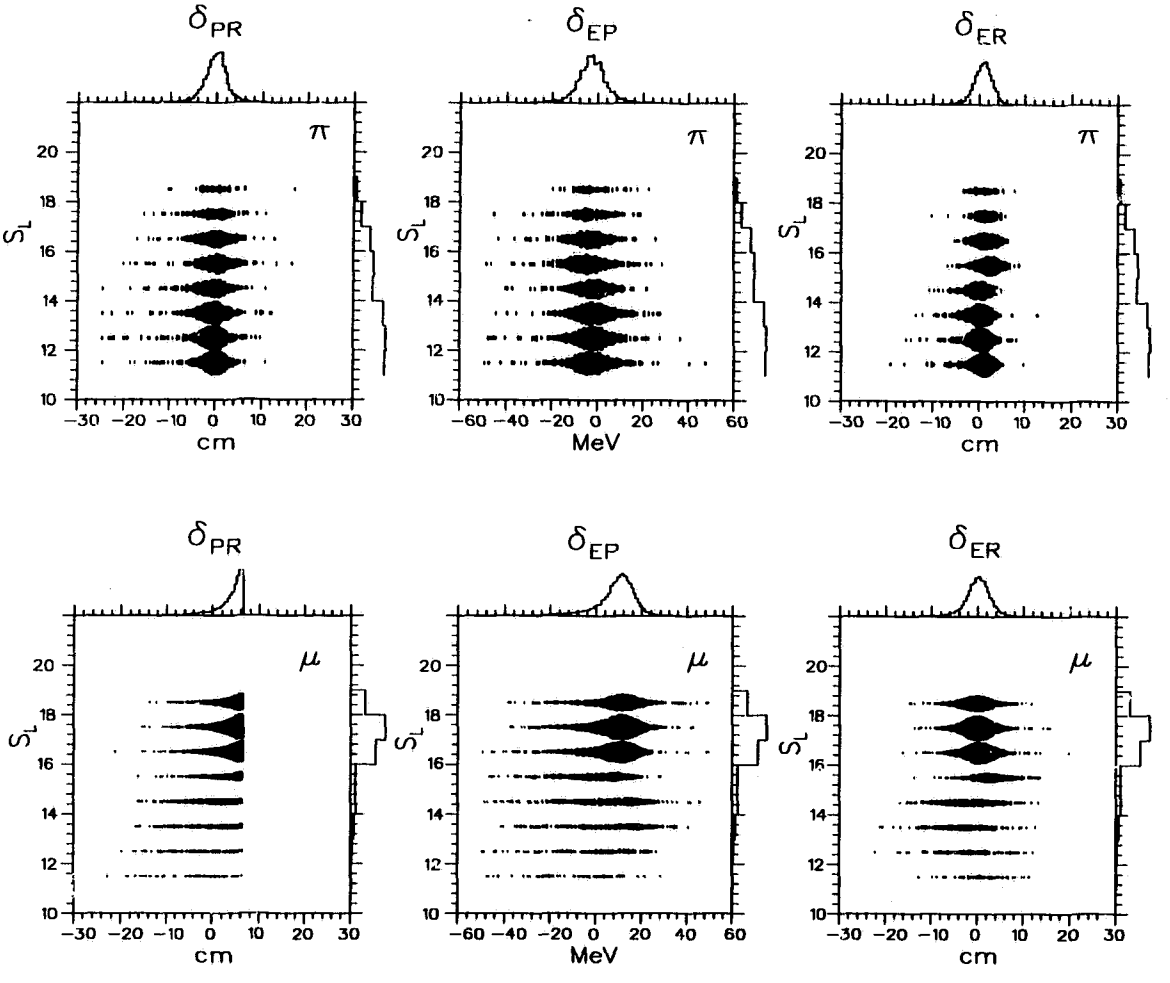

Figure 4.19: Distribution for variables used in the KINPCA cuts showing the stopping layer dependence of δ_{PR}, δ_{EP} and δ_{ER} for tagged pions (π) and $K_{\mu 2}$ type background data (μ). The muon distributions are shown after the RNGMOM0 cut has been applied.

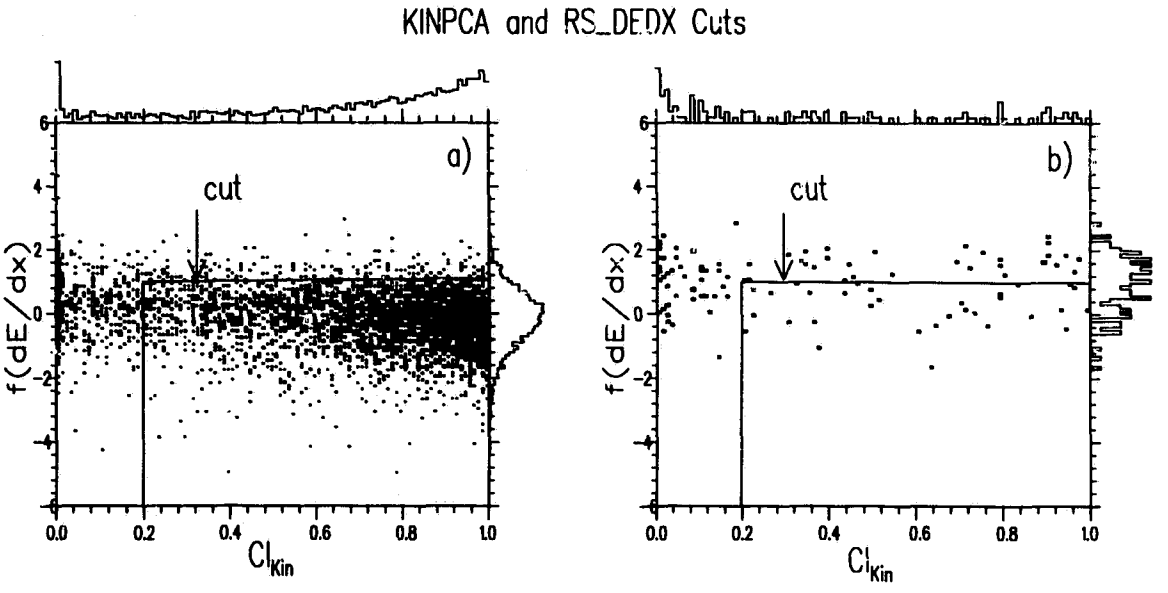

Figure 4.20: The KINPCA and RS_DEDX cut distributions, CL_{kin} vs. $\mathcal{F}(dE/dx)$. Figure a) shows the distribution for tagged pions and figure b) shows the distribution for $K_{\mu 2}$ type background events in the signal region. The cut positions are denoted.

where $(dE/dx_{exp})_i$ and $(dE/dx_{obs})_i$ were the expected and observed dE/dx in the ith layer, respectively, $\Delta_i(S'_L)$ was the calibrated difference between the calculated and mean dE/dx for pions stopping in the S'_Lth layer for the ith range stack layer. The constant factor of 4.2 was used to center the distributions for pions. $\mathcal{F}$ can be interpreted as being the average squared dE/dx residual of the track when compared to the pion expectation. [10]

The observed dE/dx was determined from the energy of the range stack layer and the corresponding layer range calculated in the range stack tracking. The expected dE/dx values were determined using Bethe-Bloch and the individual layer ranges. Corrections for in-layer sector crossings were made. The starting point for the calculation was the stopping counter, where, by definition, the kinetic energy is zero, the track length was then integrated inwards towards the target. This exploited the fact that the dE/dx separation between pions and muons is largest near the end of their range and that the initial momentum is reasonably well defined by the stopping counter energy.

The dE/dx analysis also enabled tagging of photons which converted and overlapped the charged track. The PHOTOV cut looked for anomalously large energies in individual

[10]The functional form of $\mathcal{F}$ arose from studies comparing the rejection and acceptance for different usages of the dE/dx information and from the desirability of a variable suitable for multivariate analysis (MVA). The use of logarithms in dE/dx analysis is a standard method of simulating a Gaussian response function. The dE/dx information was eventually not used in the kinematic MVA; however, the function $\mathcal{F}$ was retained.

range stack layers. The maximum normalized dE/dx residual of layers up to $S'_L - 1$ was required to be less than 4. The maximum residual was defined as,

$$\delta_{max} = \max\left[\frac{\ln(dE/dx_{exp})_i - \ln(dE/dx_{obs})_i - \Delta_i(S'_L)}{\sigma_i(S'_L)}\right],$$

where $\sigma_i(S'_L)$ was the observed width of the calibrated difference between the measured and expected dE/dx in the ith layer for pions stopping in layer S'_L. The PHOTOV cut was also effective against large angle scatters.

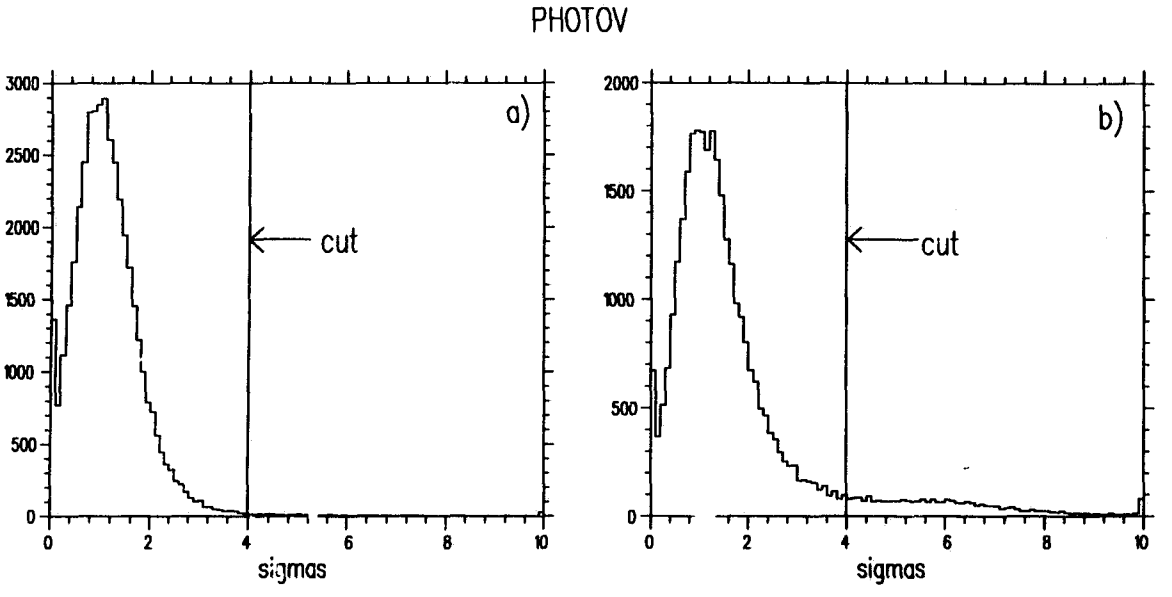

Figure 4.21: The PHOTOV cut distribution. The maximum residual, δ_{max} is plotted for a) the 1989 $K_{\pi 2}$ background sample and b) the $K^+ \to \pi^+\nu\overline{\nu}$ data set before application of the cut. The cut position is denoted.

4.9 TD Particle ID Cuts

The TD based pion identification cuts can be divided into two categories: cuts on the quality of the $\pi \rightarrow \mu \rightarrow e$ signature and veto type cuts. The cuts applied are summarized in table 4.17.

TD Particle ID Cuts	
Cut	Description
FITPI	Stopping counter $\pi \rightarrow \mu$ pulse fitting
PREFIT	Single pulse fit quality, $C_\mu > 1.8(1.6)$ for 1989 (1990)
TMUAV	Require pion decay time $t_\mu^{av} > 8$ ns
TMUADC	Require $t_\mu^{av} < 75$ ns
CHITD	Require a 1% C.L. for FITPI quantities (see text)
RSHEX	Require $4 < E_{SL} < 35$ MeV, < 3 counters hit in S_H and no unused ADC hits
ELVETO	Veto on "local region" RS activity at pion decay time
ELVETO2	Expansion of local region of ELVETO cut
TDFOOL	Veto on double pulse signature in $S_L - 1$ or $S_L - 2$ counters
ELCTRN	Require electron signature to complete $\pi \rightarrow \mu \rightarrow e$ decay sequence
TMUBM	Veto on $\check{C}_\pi$ and $\check{C}_K$ activity at pion decay time
TMUBV	Veto on BV activity in proximity to S_S at pion decay time
TD_PCA	6 variable PCA based confidence level cut $CL_{TD} > 0.01$
TD_ANAL	Combined PCA CL_{TD} and Fisher variable cut (see text)

Table 4.17:

4.9.1 The $\pi \rightarrow \mu$ Fitter: FITPI

The identification of the $\pi \rightarrow \mu$ decay sequence was performed by fitting the pulse information recorded in the stopping counter for the characteristic two pulse signature [49]. Using the average pulse shape as a template, an arbitrary pulse can be described by two parameters, the leading edge time and the total pulse area. For each end of the stopping counter, the observed pulse shape was fitted for two hypotheses; a single pulse and a double pulse fit were tested. The time of the first pulse to be fitted was required to agree with the range stack track time. Events not meeting this criteria were removed from further consideration.[11]

The quality-of-fit variables, defined as the sum of the fit residuals squared, for the one and two pulse fits were defined as C_μ^i and C_π^i respectively, where $i = 1, 2$ and refers to the

[11] For 1990, the pulse shape fits performed at PASS1 did not examine the relative timing of the range stack track and the first pulse. A small loss of acceptance (2-3%) resulted from early accidentals in the stopping hextant being mistaken for the primary pion pulse.

upstream and downstream counter ends. The C_μ^i and C_π^i variables are not true χ^2 variables; however, their behaviour is similar in that C_μ^i will have small values for single pulses and large values for double pulses. The converse applies to C_π^i. It was observed that events with a good fit to a single pulse hypothesis are poor candidates for the more CPU intensive double pulse fit. The 1989 and 1990 PASS1 PREFIT cut required $C_\mu < 1.8(1.6)$ for 1989 and 1990, respectively. The different cut was motivated by the observed C_μ distributions for pion data which exhibited a shift for the 1990 data. The difference between the fitted times of the first and second pulse defined the decay time, the average of the two counter ends was defined as t_μ^{av}. The fitting procedure is illustrated in figure 4.22.

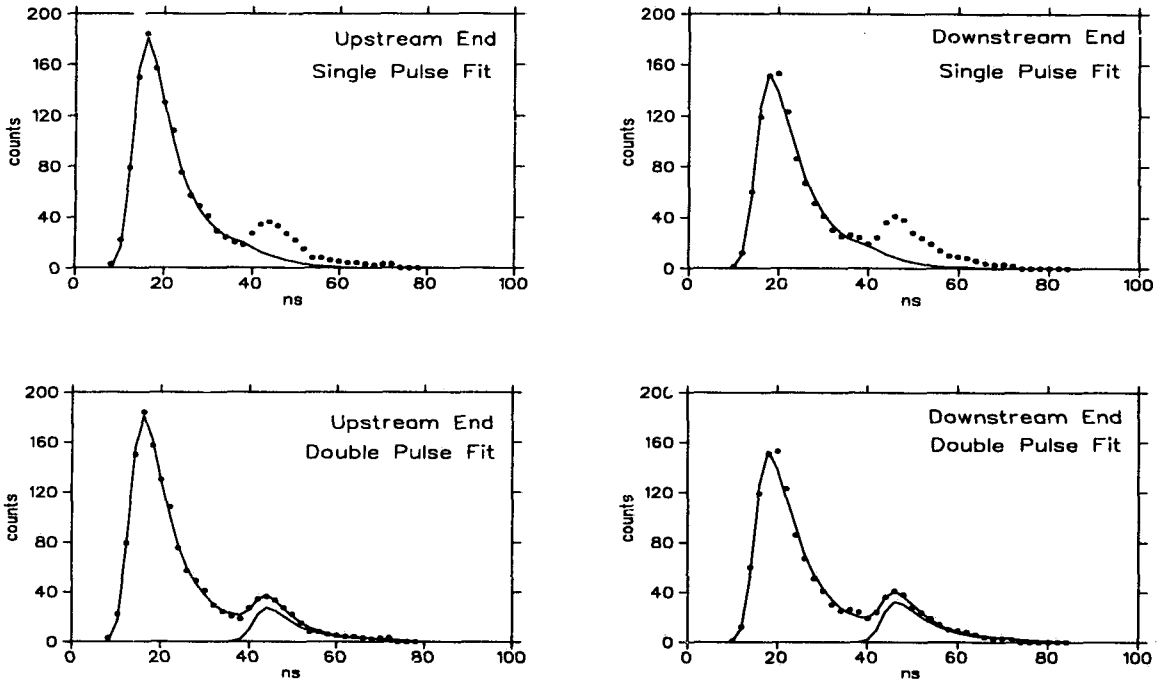

Figure 4.22: Example of a pulse fit for $\pi \rightarrow \mu$ decay showing the two ends of the counter. The upper two figures show the raw data and single pulse fit for the upstream and downstream end of the RS counter. The lower two figures show the double pulse fit. The fitted secondary muon pulse is also shown. It can be seen that the single pulse hypothesis is a poor description of the data.

Once the double pulse nature was established, a series of cuts on the consistency of the second pulse with a $\pi \rightarrow \mu$ hypothesis were applied. A true $\pi \rightarrow \mu$ decay should have the same decay time in each end, and the geometric mean of the fitted second pulse areas should be consistent with the 4.12 MeV mono-energetic muon pulse expected from pion decay. The default TD fitter cuts are summarized in table 4.18. The fitted pion lifetime distribution for the 1991 data is shown in figure 4.23. Muons passing the $\pi \rightarrow \mu$ fitter were

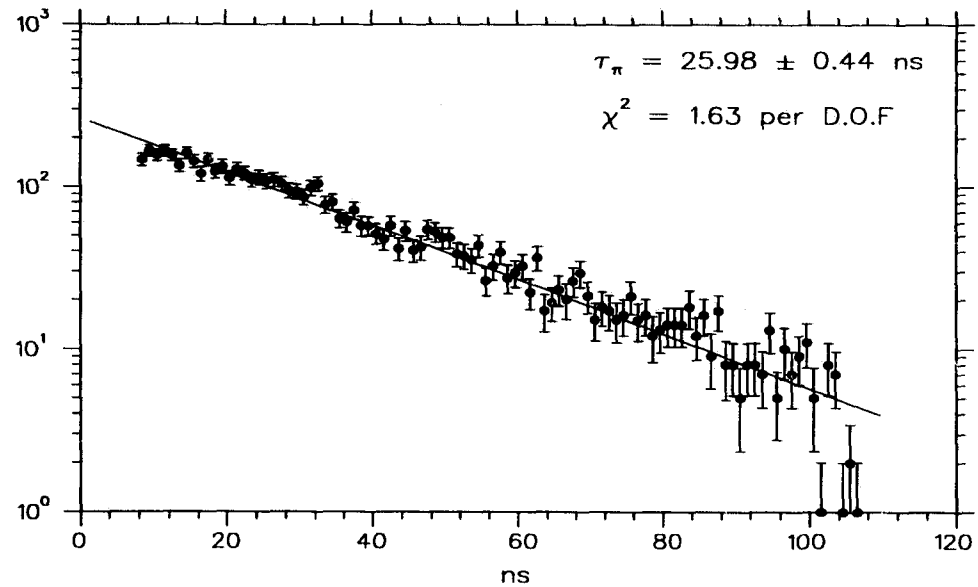

Figure 4.23: Pion lifetime distribution for 1991 data showing the fitted average pion lifetime.

biased to short lifetimes which are symptomatic of fluctuations in the pulse shape.

TD Fitter Quantities and Cuts	
Quantity	Description
C_μ^i	Quality of single pulse fit in end i, $i = 1, 2$
C_π^i	Quality of double pulse fit in end i
$C_{\pi\,i}^{\mu}$	Combined quality of fit for end i
	Require $C_\mu^i/C_\pi^i > 1.5$ for each end
C_μ	Overall quality of single pulse fit, $\log_{10}(\sqrt{C_\mu^1 C_\mu^2})$
	Require $C_\mu > 1.8$ (1989), $C_\mu > 1.6$ (1990)
P_π^μ	Combined quality of fit product
	Require $P_\pi^\mu = (C_\mu^1 C_\mu^2) \times (C_\pi^1 C_\pi^2)^{-1}) > 3$
t_μ^i	Time of second fitted pulse for end i, (decay time)
t_μ^{av}	Average decay time, $\frac{1}{2}(t_\mu^1 + t_\mu^2)$, $2 < t_\mu^{av} < 120$ ns
δt_μ	End-to-end muon time difference, $t_\mu^1 - t_\mu^2$, $\lvert\delta t_\mu\rvert < 5$ ns
E_μ^i	Fitted second pulse energy in end i, $60 < E_\mu^i < 360$ TD counts
E_μ^{tot}	Total muon energy, $\sqrt{E_\mu^1 E_\mu^2}$, $70 < E_\mu^{tot} < 270$ TD counts

Table 4.18: TD fitter variables used in the analysis and the default FITPI cuts.

4.9.2 Pion Decay Time Cuts

Cuts were imposed to restrict the pion decay time, t_μ^{av}, to lie in the region $[8, 75]$ ns. For shorter pion decay times, the second pulse merges with the primary pulse and becomes difficult to distinguish from fluctuations in the TD pulse shape. The TMUAV cut required $t_\mu^{av} > 8$ ns. The cut on long decay times, TMUADC, was motivated by the timing distribution of the muon background. Accidentals faking the decay muon pulse will have a flat timing distribution, whereas pion decays will be exponentially distributed. The TMUADC cut position coincided with the trailing edge of the range stack ADC gate.

4.9.3 Electron Tagging: ELCTRN

The range stack TD system was used to find the decay electron from the $\pi \rightarrow \mu \rightarrow e$ decay sequence. The long memory of the TD system enables a search for the muon decay up to 6 μs after the pion decay. This corresponds to 2.7 muon lifetimes, or approximately 93% of all muon decays. Cuts on the electron energy spectrum further reduced the acceptance. The electron tagging algorithm examined end-to-end coincidences in the range stack delayed relative to the pion track time. A candidate electron was required to satisfy the following criteria:

- At least 2 hits within a 3 by 5 counter volume centered by the stopping counter, ± 2 layers, ± 1 sector.
- At least one hit with pulse area greater than 100 TD counts in each end.
- At least one hit in the same sector as the stopping counter within ± 1 layer.
- Total RS energy less than 7000 TD counts ($\sim$ 60 MeV).
- Electron energy greater than 750 TD counts ($\sim$ 7 MeV).
- End-to-end timing match with the pion pulse satisfying $|z_\pi^t - z_e^t| < 3.5$ ns, where z_π^t was determined from the FITPI results.

The $\mu \rightarrow e$ decay time distribution for pions passing the FITPI, TMUAV and CHITD cuts is shown in figure 4.24; the fitted muon lifetime of 2170 ± 35 ns is in agreement of the accepted value of 2197 ns. The accidental rate for the electron signature varied from 2-4% depending on the instantaneous beam rate and the pion stopping layer.

4.9.4 Multivariate Analysis Cuts

The default $\pi \rightarrow \mu$ fitter and electron cuts were not adequate to reduce the muon background to an acceptable level. Further muon suppression was achieved by cutting on three different

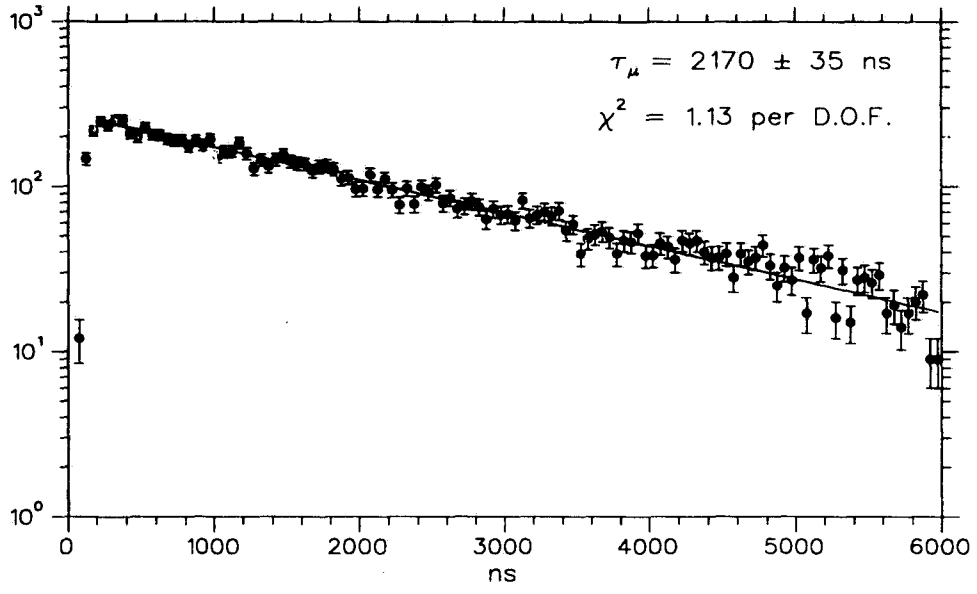

Figure 4.24: Muon lifetime distribution for the combined data set showing the fitted average muon lifetime.

measures of the probability of a pion hypothesis using the TD fitter and track information. The cuts were: a χ^2 test for a pion hypothesis using FITPI variables, an expanded χ^2 test based on a principal component analysis (PCA) of $\pi \to \mu \to e$ variables from tagged pions, and a discriminant function analysis (DFA) Fischer variable cut based on direct comparison of muon backgrounds with tagged pions.[12] The variables used in the multivariate analysis (MVA) cuts are tabulated in table 4.19 and are shown for muon backgrounds and pions in figure 4.25. The pion and muon samples shown have already had $\pi \to \mu \to e$ cuts with a measured rejection of 2.5×10^4 per muon applied.

The CHITD cut used variables calculated by FITPI to form a confidence level for a pion hypothesis. A 1% confidence level was applied to the χ^2 sum; inclusion of terms in the χ^2 depended on the characteristics of the fit. Consider the quantity,

$$\chi_0^2 = \left(\frac{\delta t_\mu}{\sigma_{\delta t_\mu}}\right)^2 + \left(\frac{E_\mu^{tot} - \overline{E_\mu^{tot}}}{\sigma_{E_\mu^{tot}}}\right)^2,$$

where overlined quantities denote mean values. For events with $\log(P_\pi^\mu) < (\overline{\log(P_\pi^\mu)} - 0.17)$, the $\chi^2 = \chi_0^2 + \chi_1^2$, where

$$\chi_1^2 = \left(\frac{\log(P_\pi^\mu) - \overline{\log(P_\pi^\mu)}}{\sigma_{\log(P_\pi^\mu)}}\right)^2.$$

[12] An introduction to discriminant function analysis is given in appendix B.

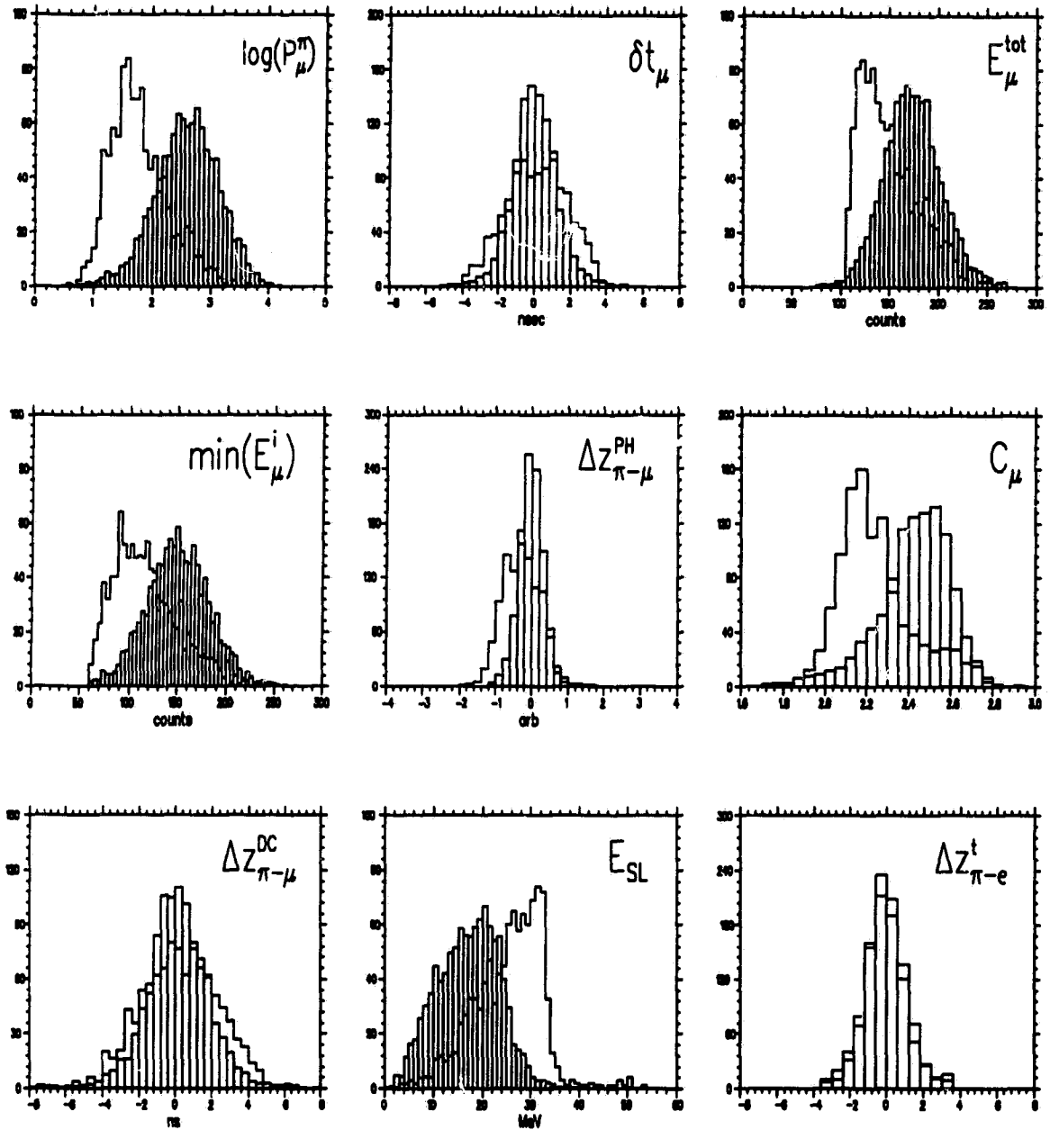

Figure 4.25: MVA variables for tagged muon backgrounds and pions from the 1989 data set. Pions are displayed as filled in histograms. The distributions have been normalized to the same number of counts.

TD Confidence Level Cut Variables		
Quantity	Analysis	Description
C_μ	CHITD, PCA, DFA	Overall quality of single pulse fit
$\log(P_\pi^\mu)$	CHITD, DFA	Logarithm of the combined TD fit quality product
δt_μ	CHITD, PCA	End-to-end muon time difference
E_μ^{tot}	CHITD, PCA, DFA	Total muon energy
$\min(E_\mu^i)$	PCA, DFA	Minimum of single end muon pulse heights
$\Delta z_{\pi-\mu}^{PH}$	PCA	Difference in z from fitted pulse areas $\ln(E_\pi^1/E_\pi^2) - \ln(E_\mu^1/E_\mu^2)$
$\Delta z_{\pi-\mu}^{DC}$	PCA	DC based Δz between π and μ $z_\pi^{DC} - z_\mu^t$
$\Delta z_{\pi-e}^t$	PCA	Timing based Δz between π and e
E_{SL}	DFA	Stopping layer energy

Table 4.19: Variables used in TD confidence level and discriminant function analysis (DFA) cuts.

CHITD Cut Parameters						
Quantity	1989		1990		1991	
	Mean	Sigma	Mean	Sigma	Mean	Sigma
E_μ^{tot} (cnts.)	175.8	28.1	158.4	29.1	165.1	28.8
δt_μ (ns)	-	1.22	-	1.10	-	1.13
$\log(P_\pi^\mu)$	2.47	0.56	2.17	0.48	2.06	0.53
C_μ	2.44	0.16	2.35	0.16	2.40	0.16

Table 4.20: The CHITD cut parameters. The measurements are based on pion scattering monitor data passing the default FITPI cuts with a 10% pion C.L. range-momentum requirement.

For events that have $C_\mu < \overline{C_\mu}$, $\chi^2 = \chi_0^2 + \chi_2^2$, where

$$\chi_2^2 = \left(\frac{C_\mu - \overline{C_\mu}}{\sigma_{C_\mu}}\right)^2.$$

For events that simultaneously have low C_μ and low $\log(P_\pi^\mu)$, $\chi^2 = \chi_0^2 + \chi_1^2 + \chi_2^2$. The criteria for inclusion of the $\log(P_\pi^\mu)$ and C_μ terms is rooted in the "directionality problem" of the χ^2 test. This is where the distribution of a variable shows separation between two species in only one direction. The means and sigmas for the quantities entering the χ^2 were determined from Gaussian fits to the respective distributions and are presented in table 4.20.

An additional measure of the pion likelihood was obtained by using a PCA of $\pi \rightarrow \mu \rightarrow e$ decay variables. The variables utilized were E_μ^{tot}, δt_μ, $\min(E_\mu^i)$, $\Delta z_{\pi-\mu}^{PH}$, $\Delta z_{\pi-\mu}^{DC}$ and $\Delta z_{\pi-e}^t$.

The TD_PCA cut required a pion confidence level of, $CL_{TD} > 1\%$. To achieve further muon rejection, a discriminant function analysis (DFA) was performed. The variables used in the DFA were $\log(P_\pi^\mu)$, E_μ^{tot}, $\min(E_\mu^i)$, C_μ, and E_{SL}. The fundamental differences between tail fluctuation and accidental type muon backgrounds required that separate discriminant functions be utilized to optimize the rejection. The pion and muon dispersion matrices were calculated for two ranges of t_μ^{av} for each data set. The tail fluctuation analysis used events with $8 < t_\mu^{av} < 22$ ns whereas accidental type events were selected by requiring $t_\mu^{av} > 22$. A summary of the discriminant functions weights is given in table 4.21. The mean value of the Fischer Variable, $< F_\pi >$, for tagged pions was subtracted from F to center the distributions at the origin to facilitate comparison of the different runs. The TD_ANAL cut utilized a linear combination of CL_{TD} and F to improve the muon rejection. The run-to-run difference in the Fischer variable cuts for $t_\mu^{av} < 22$ ns was due to the different on-line TD $\pi \rightarrow \mu$ cuts applied. A summary of F cuts is given in table 4.22. Figure 4.26 shows the pion and muon distributions for the Fischer variable versus the PCA based confidence level for the two ranges of t_μ^{av} for the 1991 data after all cuts except the pion lifetime cut at 75 ns.

Discriminant Function Weights							
Run		$\log(P_\pi^\mu)$	E_μ^{tot}	C_μ	E_{SL}	$\min(E_\mu^i)$	$< F_\pi >$
1989	$t_\mu^{av} < 22$ ns	0.90966	0.00284	0.40975	-0.06772	0.00607	3.6664
	$t_\mu^{av} > 22$ ns	0.20711	-0.00406	0.97827	-0.00824	0.00231	2.4566
1990	$t_\mu^{av} < 22$ ns	0.10855	-0.00672	0.99395	-0.01481	0.00324	1.6539
	$t_\mu^{av} > 22$ ns	0.26514	-0.00577	0.96411	-0.01295	0.00180	2.0303
1991	$t_\mu^{av} < 22$ ns	0.24112	-0.01291	0.96841	-0.06141	0.00975	0.9460
	$t_\mu^{av} > 22$ ns	0.18069	-0.00606	0.98337	-0.01677	0.00388	2.0716

Table 4.21: The discriminant function weights used to calculate the Fischer variable.

Summary of Fischer Variable Cuts		
Run	$t_\mu^{av} < 22$ ns	$t_\mu^{av} > 22$ ns
1989	$F > -1.0, F > -4.167 \times CL_{TD}$	$F > -0.2, F > -2.083 \times CL_{TD} + 0.3$
1990	$F > -0.25, F > -1.042 \times CL_{TD}$	
1991	$F > -0.65, F > -2.708 \times CL_{TD}$	

Table 4.22: Summary of cuts applied to the Fischer variable F in the TD_ANAL cut.

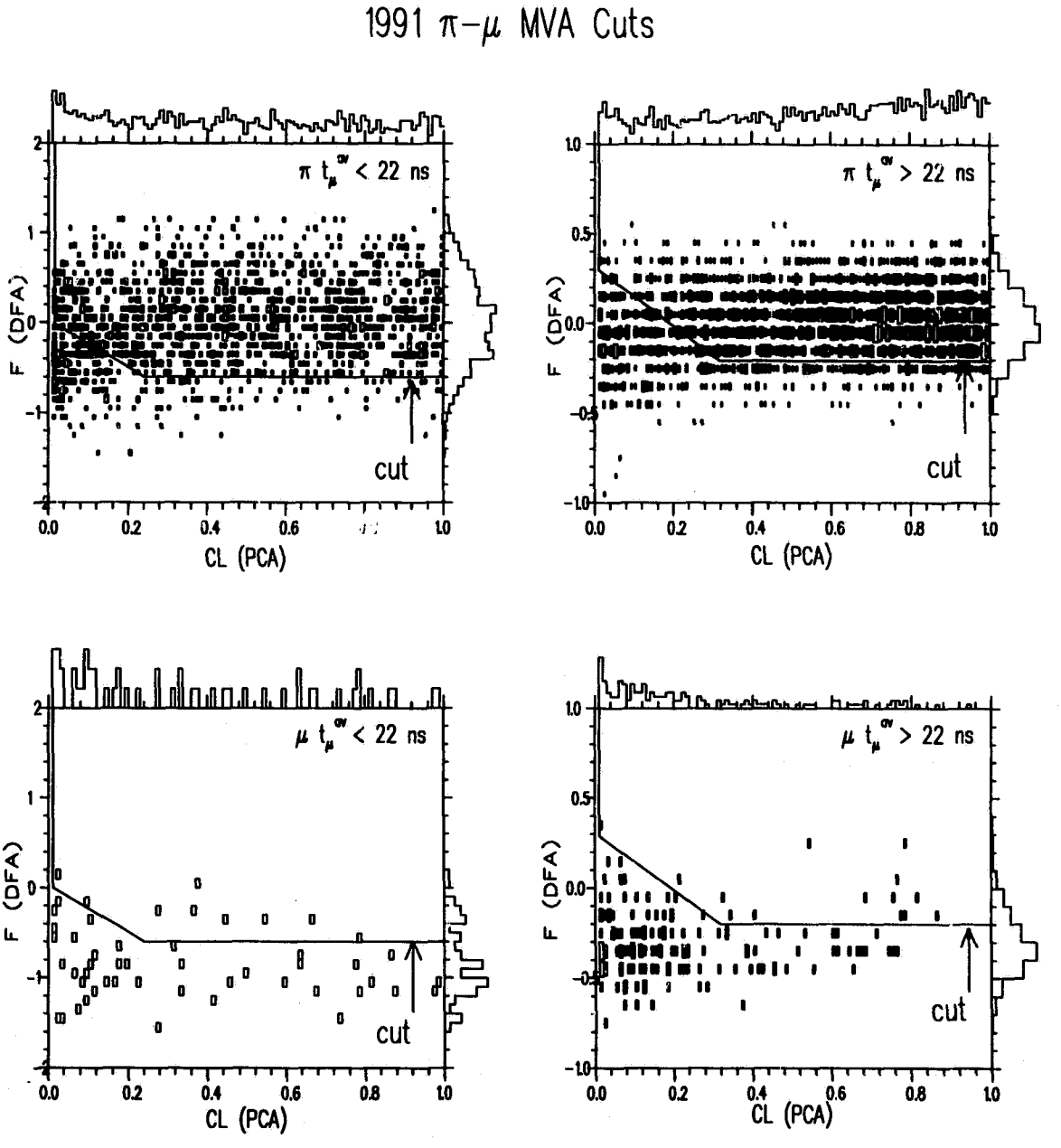

Figure 4.26: DFA Fischer Variable F versus PCA based Confidence level CL_{TD} for 1991 data showing position of MVA cuts for muon backgrounds and tagged pions. All $\pi \rightarrow \mu \rightarrow e$ cuts except the 75 ns pion lifetime cut have been applied.

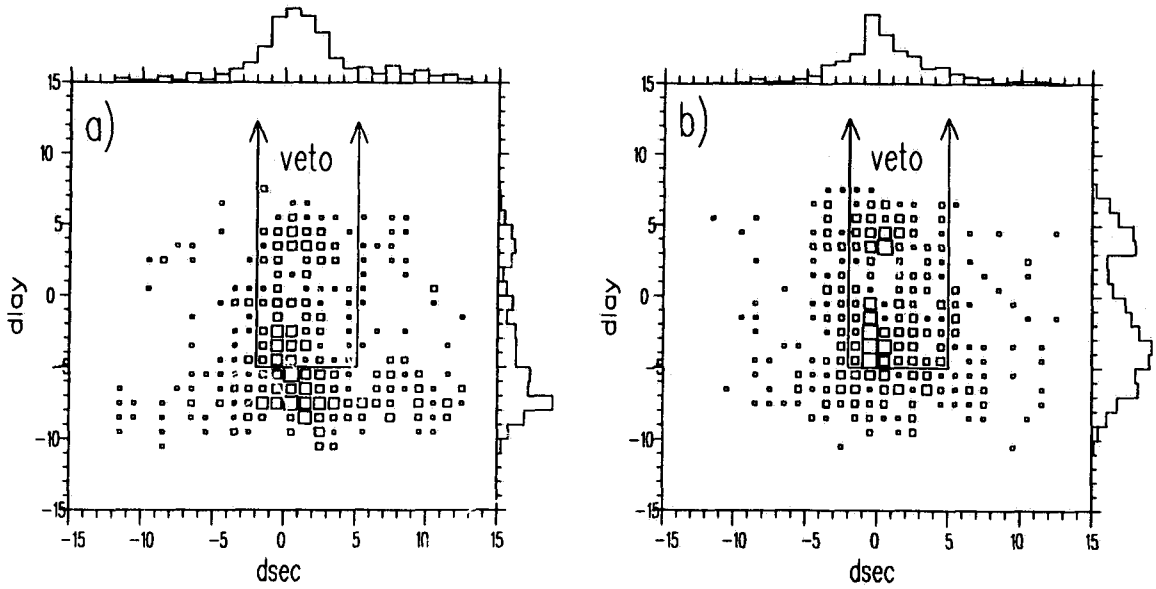

Figure 4.27: Range Stack activity at the apparent $\pi \rightarrow \mu$ decay time. The difference in the RS sector is plotted versus the difference in the RS layer for hits coincident with the apparent pion decay time with respect to the stopping counter. Figure a) is for muons with an associated electron, figure b) is for muons failing the electron cut.

4.9.5 Early $\mu \rightarrow e$ Veto Cuts

The ELVETO class of cuts rejected events where an early $\mu \rightarrow e$ decay faked the $\pi \rightarrow \mu$ decay signature with the electron depositing energy outside the stopping counter. The ELVETO cuts also rejected events where an accidental hit elsewhere in the range stack produced a "4 MeV" pulse in the stopping hextant. The ELVETO cut looked for coincidences in the "local region" surrounding the stopping counter. The local region was defined as ± 2 layers within the same hextant or within the same layer in sectors adjacent to the stopping hextant. Coincidence windows were ± 5 ns for double ended hits which could be assigned unambiguously to a given counter[13] and ± 7 ns for ambiguous or single end hits. In the final analysis pass, the ELVETO cut was tightened (ELVETO2) by expanding the search region. Events with a hit within -2 to $+4$ sectors and -5 to $+12$ layers of the stopping counter were vetoed. Figure 4.27 shows the cut position for two samples of muons; 4.27a) is for muons passing the electron tagging and 4.27b) is for events that have failed the electron cut.

The TDFOOL cut looked for secondary pulses in the next to last two RS layers before

[13]Recall that the within-hextant TD multiplexing can result in ambiguity in the actual counter hit, if the associated discriminator data is not present.

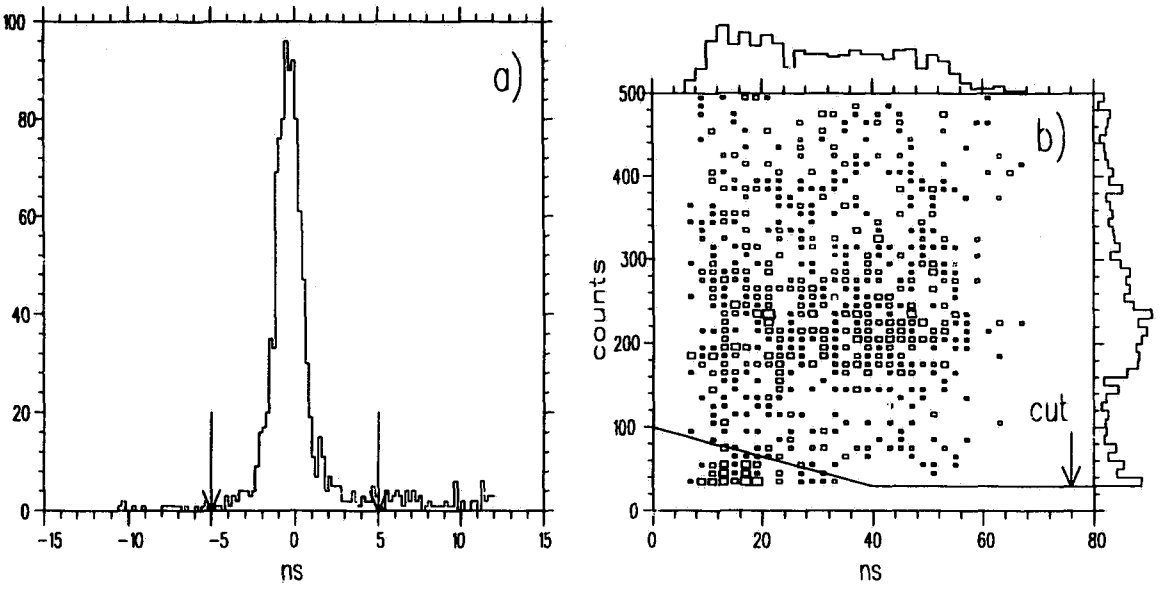

Figure 4.28: Timing and energy distributions for fitted secondary pulses in the inner layer of the range stack at the apparent $\pi \rightarrow \mu$ decay time. Figure a) shows the mean-time difference with respect to the stopping counter; the coincidence window was ± 5 ns. Figure b) shows the energy distribution of the second pulse versus t_μ^{av}. The cut applied is shown. The events shown have failed the electron tagging cut.

the stopping layer. Early $\mu \rightarrow e$ decays with the electron heading inward and overlapping the RS track can have the electron TD pulse obscured by the primary muon pulse. The FITPI fitting procedure was used to determine whether a second pulse was present. A combination of timing and energy cuts were applied. Secondary pulses were required to have mean-times within ± 5 ns of the decay time in the stopping counter. For events with $t_\mu^{av} < 40$ ns, events with second pulse energy $E_2^{tot} > 100 - 1.67 \times t_\mu^{av}$ counts were cut. For events with $t_\mu^{av} > 40$ ns, the cut on E_2^{tot} was 30 counts. The mean-time difference and the second pulse energy versus t_μ^{av} for events passing the mean-time cut are shown in figure 4.28 for muons failing the electron requirement.

4.9.6 Other Veto Type Cuts

The RSHEX cut examined the stopping hextant and layer ADC information. This cut was designed to reject events where the TD multiplexing led to hit assignment ambiguity in the stopping hextant. A cut on the stopping layer energy requiring $4 < E_{\mathrm{SLAY}} < 35$ MeV was applied. The pion decay muon will deposit 3.05 MeV of visible energy; any events with less than 4 MeV would therefore be suspect. The RSHEX cut also required that there be less than 3 hit counters within the stopping hextant and that there were no unused ADC hits.

The hit threshold was 0.5 MeV, single end hits were included.

The TMUBM cut vetoed events with $\check{C}_\pi$ or $\check{C}_K$ activity coincident with the pion decay time. The coincidence windows for each counter were $\pm$8ns. The timing distributions for muon backgrounds are shown in figure 4.29. TMUBV removed events with activity in the barrel veto within $\pm$8 ns of the pion decay time and $\pm$3 sectors (with respect to the RS) of the stopping sector. The TMUBV cut addressed early $\mu \rightarrow e$ decays with radiated photons missed by the range stack and beam related photons which Compton scattered in the stopping counter. Figures 4.30a) and 4.30b) show the barrel veto activity for events failing and passing the electron tagging, respectively.

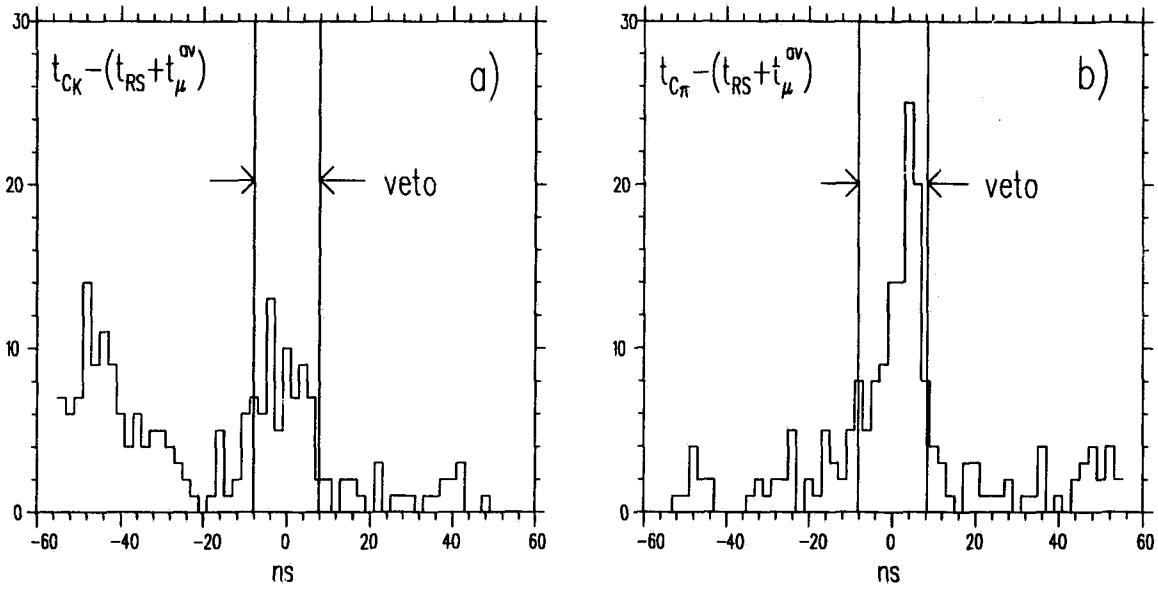

Figure 4.29: Čerenkov counter activity at the apparent $\pi \rightarrow \mu$ decay time; a) kaon Čerenkov and b) pion Čerenkov.

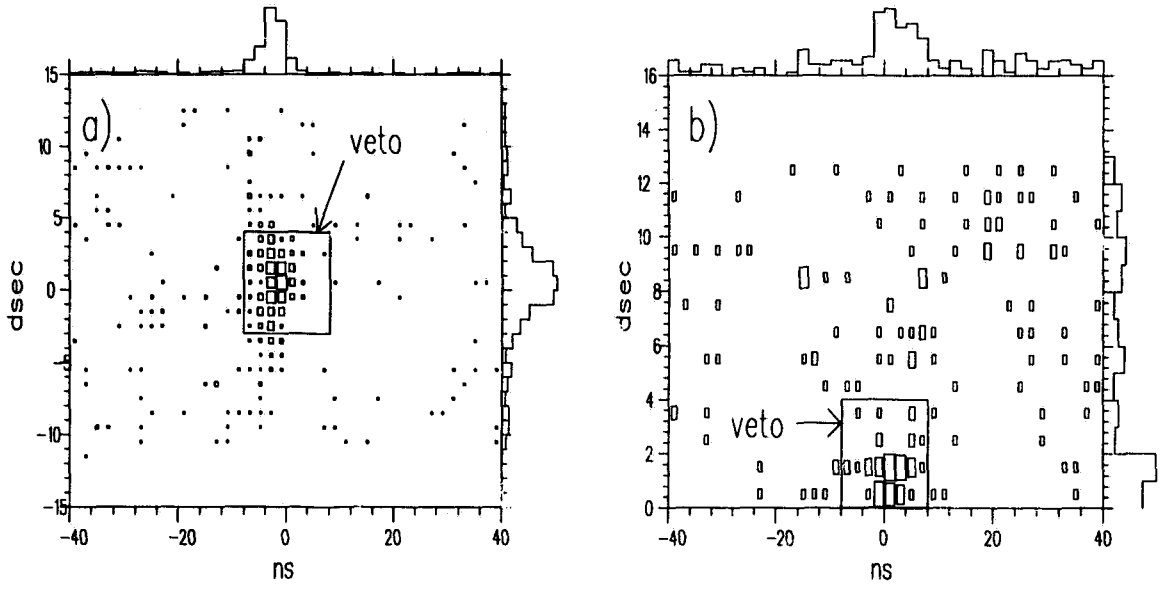

Figure 4.30: Barrel veto activity at the apparent $\pi \rightarrow \mu$ decay time. The ordinate is the number of sectors between the stopping sector and the BV hit. The BV has been multiplexed by a factor of two in azimuth. The abscissa is $t_{BV} - (t_{RS} + t_{\mu}^{av})$. Figure a) is for muons failing the electron requirement, b) is with an electron requirement. Note that for figure b), the absolute value of the sector difference is plotted.

4.10 Kinematic Signal Region: BOX Cut

The kinematic region of acceptance for $K^+ \rightarrow \pi^+\nu\bar{\nu}$ defined by the *a priori* background studies was:

$$33 < R'_{tot} < 40 \text{ cm},$$

$$115 < E'_{tot} < 135 \text{ MeV},$$

$$211 < P'_{tot} < 242 \text{ MeV}/c,$$

where the primes denote the rescaled kinematic variables. The lower edge of the energy box corresponds to a pion range of 33.0 cm. The lower edge of the momentum cut is equivalent to a pion range of 32.4 cm. The Monte Carlo generated rare decay spectra are shown in figures 4.31 and 4.32 before application of the BOX cut.

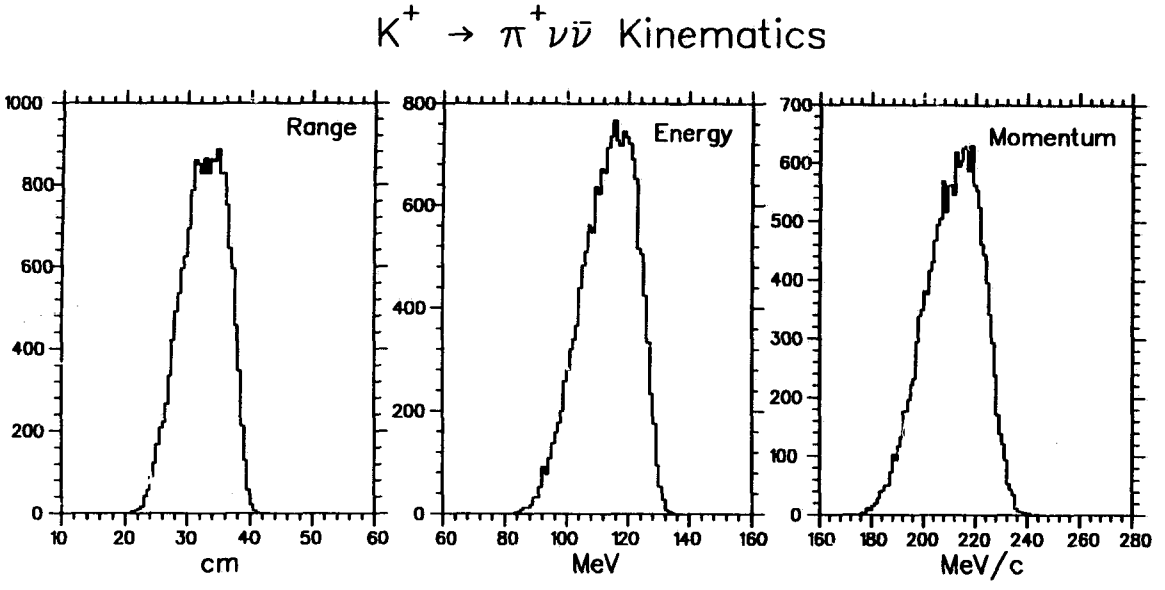

Figure 4.31: $K^+ \to \pi^+\nu\bar{\nu}$ kinematic distributions before application of the BOX cut.

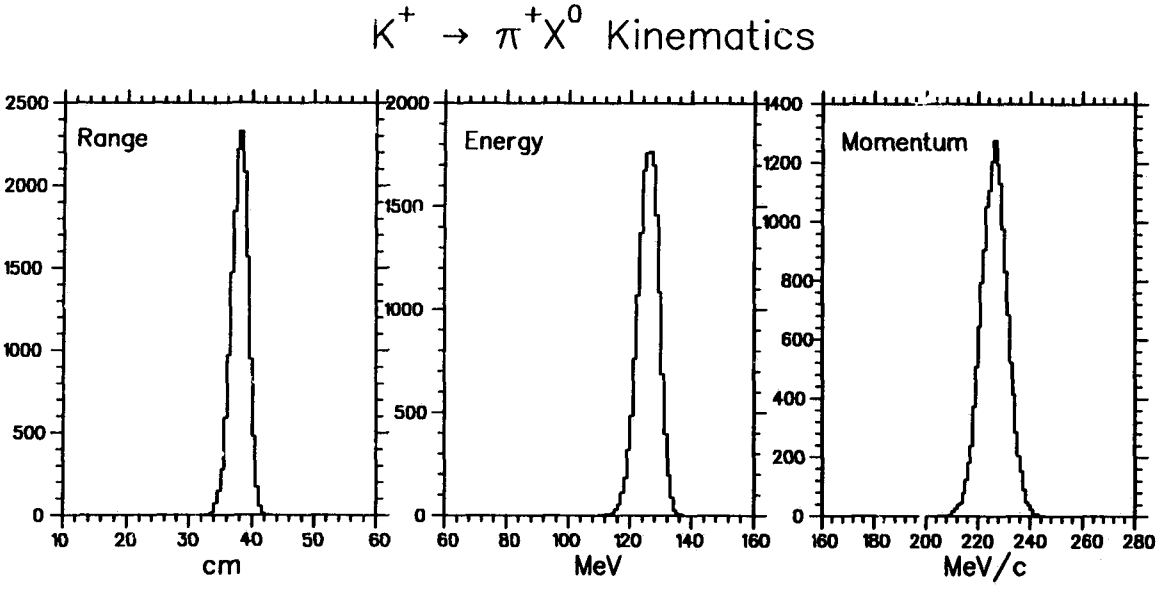

Figure 4.32: $K^+ \to \pi^+X^0$ kinematic distributions before application of the BOX cut for massless X^0.

Chapter 5

Calculation of the Background

If you torture the data long enough, it will confess.

- Dr. Jane Orient

5.1 $K_{\mu 2}$ Type Backgrounds

Estimates of the $K_{\mu 2}$ type background are based on the assumption that it can be factored into two independent components: *i)* the rate of kinematic misidentification of the $K_{\mu 2}$ muon as a $K^+ \to \pi^+ \nu\bar{\nu}$ pion and *ii)* the TD factor or the probability for the $\mu \to e$ decay to be misidentified as $\pi \to \mu \to e$. In this section the technique used to estimate the $K_{\mu 2}$ background rate is presented, followed by descriptions of the mechanisms by which $K_{\mu 2}$ type backgrounds fake the $K^+ \to \pi^+ \nu\bar{\nu}$ signature.

The 1989 and 1991 Data Sets

The expected number $K_{\mu 2}$ type background events for the 1989 and 1991 data sets estimated using,

$$N_{bgd} = f_{ps}^{\mathrm{bgd}} \times N_{box} \times \bar{\epsilon}_{TD}, \tag{10}$$

where $f_{ps}^{\mathrm{bgd}} = 50$ was the prescale factor used to define the MUBG sample at PASS1, N_{box} was the number of events in the MUBG sample passing the full analysis except for the TD based particle identification cuts, and $\bar{\epsilon}_{TD}$ was the probability per muon of satisfying the off-line $\pi \to \mu \to e$ cuts. There is no available sample of muons with sufficient sensitivity that have not already has the on-line TD cut applied; therefore, rejection of the trigger $\pi \to \mu$ requirement was included in the measurement of N_{box} for the MUBG samples.

The MUBG samples from the 1989 and 1991 PASS1 were used to measure two factors: the kinematic rejection (equivalently N_{box}) and the rejection of a subset of the off-line $\pi \to \mu \to e$ identification cuts. The definition of the MUBG samples ensured that hardware

failure related backgrounds and run-to-run dependencies in the detector resolutions were sampled uniformly. Furthermore, the acceptance correction for reconstruction failures, event quality cuts and accidental vetoes was automatically accounted for.

The 1990 Data Set

The $K_{\mu 2}$ type background for the 1990 data run was estimated using the $\pi\nu\overline{\nu}$ Level 0 and $K_{\pi 2}(1)$ monitor triggers spanning the same data runs as the $K^+ \to \pi^+\nu\overline{\nu}$ data set.[1] A first pass analysis similar to the MUBG PASS1 was run on the 1990 monitor data set. The Level 0 and Level 1 photon veto cuts were applied by requiring the appropriate trigger bits to be set. The 1990 $K_{\mu 2}$ type background was estimated using the following relation,

$$N_{bgd} = f_{ps}^{90} \times N_{box} \times \frac{1}{R_{TD}^{on-line}} \times \bar{\epsilon}_{TD}, \tag{11}$$

where $f_{ps}^{90} = 21845.3$ was the trigger prescale for the sum of the $K_{\pi 2}(1)$ and $\pi\nu\overline{\nu}$ Level 0 triggers and, $R_{TD}^{on-line}$ was the rejection of the trigger $\pi \to \mu$ requirement. The on-line TD rejection was measured using the $K_{\pi 2}(1)$ and $\pi\nu\overline{\nu}$ Level 0 data set. The value of the off-line TD muon rejection inefficiency determined from the 1991 data set was used.

5.1.1 TD Muon Backgrounds

There are three different types of muon backgrounds to consider. They are:

- tail fluctuations, where the tail of the primary pulse has correlated fluctuations that fake a decay muon.
- fake muon backgrounds, where a localized random "4 MeV" accidental hit is mistaken for the decay μ, and,
- random electrons, where an extended accidental fakes the e in the $\pi \to \mu \to e$ decay sequence with an early $\mu \to e$ decay faking the $\pi \to \mu$ decay.

The tail fluctuation component is associated with short pion decay times. It arises from fluctuations in the pulse shape of the stopping particle and is usually correlated with large stopping counter energy. A sub-category of this background is due to malfunctioning electronics which lead to pulse irregularities and/or phototubes with unstable pulse shapes. Both ends of the counter must have fluctuations in their pulse shapes for an event to satisfy the default FITPI $\pi \to \mu$ cuts and the fluctuations must exhibit enough correlation to reproduce the correct z position and muon energy.

[1] Recall that the muon background study sample was not produced at the PASS1 stage.

The random "4 MeV" component has a flat timing distribution. It is more difficult to remove because unlike tail fluctuations, there is a real secondary pulse in the stopping hextant. A significant fraction, 25%, is related to beam activity detectable in the Čerenkov counters. The source of the remaining isolated accidentals is not known but it is beam rate dependent. Accidentals of $2-4$ MeV will satisfy the muon energy cut because of the finite resolution. Rejection of the accidental induced background relies on two factors: The first is multiple and redundant measurements of the μ and π z position using pulse area and timing information and the second is vetoing on extra activity in the detector at the π decay time.

The random electron background occurs when the primary muon decays to a low energy electron which is contained in the stopping counter and a subsequent accidental completes the $\pi \rightarrow \mu \rightarrow e$ decay sequence. Because of the similar stopping counter topology, rejection of this background relies predominantly on veto type cuts at the muon time and requirement of the muon decay electron.

Evaluation of the TD Rejection for Muons

The probability per muon of satisfying the off-line $\pi \rightarrow \mu \rightarrow e$ cuts can be expressed as the product of two factors,

$$\bar{\epsilon}_{TD} = \bar{\epsilon}_{TD}^{p1} \times \bar{\epsilon}_{TD}^{p2}, \tag{12}$$

where $\bar{\epsilon}_{TD}^{p1}$ is the rejection inefficiency of the standard $\pi \rightarrow \mu \rightarrow e$ cuts (defined below) and $\bar{\epsilon}_{TD}^{p2}$ is the rejection of the remaining $\pi \rightarrow \mu \rightarrow e$ cuts, which include tighter vetoing of detector activity at the pion decay time and the multivariate analysis based cuts.

It was necessary to divide the measurement of the TD rejection into two stages. To insure a proper normalization of the number of muons, the pion background has to be eliminated before any offline $\pi \rightarrow \mu \rightarrow e$ cuts are applied. This is clearly not feasible at the PASS1 analysis stage. A second complication arises from the required orthogonality of the final muon background data with the residual events from the main $K^+ \rightarrow \pi^+\nu\bar{\nu}$ analysis.

The standard $\pi \rightarrow \mu \rightarrow e$ cuts were FITPI, TMUAV, CHITD, ELVETO and ELCTRN. The muons used to evaluate their rejection were selected from the MUBG samples derived at the PASS1 stage as described in section 3.3.2. Cuts designed to eliminate pion scattering backgrounds and the tighter PASS2 photon veto cuts were applied. To ensure that the events selected were not in the final data sample, the range-momentum test of a pion hypothesis was reversed. Events with less than a 10% probability of satisfying a pion hypothesis while simultaneously having measured ranges longer than expected were selected. No requirement of consistency with a muon hypothesis was imposed. Further kinematic cuts requiring $P'_{tot} > 205$ MeV/c and $E'_{tot} > 120$ MeV were required to remove residual

$K_{\pi 2}$ events with poorly measured range. The standard $\pi \to \mu \to e$ cuts were then applied to the remaining events. The results for $\bar{\epsilon}_{TD}^{p1}$ for the 1989 and 1991 data are tabulated in table 5.1. The basic requirements of a localized three pulse signature, combined with the Level 2 $\pi \to \mu$ trigger cut provides a muon rejection factor of 2.5×10^4 per muon.

Muon Rejection for Offline $\pi \to \mu \to e$ Cuts						
Cut	1989			1991		
	N_{ex}	N_{cut}	Rej.	N_{ex}	N_{cut}	Rej.
FITPI	34148	30976	10.76	40920	38117	14.92
TMUAV	3172	1101	1.53	2743	353	1.15
CHITD	2071	911	1.79	2390	711	1.42
ELVETO	1160	1024	8.53	1679	1484	8.61
ELCTRN	(see text)		5.02	195	172	8.48
N_{pass}	136			23		
$\bar{\epsilon}_{TD}^{p1}$	$(7.9 \pm 0.7) \times 10^{-4}$			$(5.6 \pm 1.2) \times 10^{-4}$		
RSHEX	1034	157	1.18	888	205	1.30
ELVETO2	877	180	1.26	683	275	1.67
ELCTRN	697	0	1.00	408	8	1.02
TDFOOL	697	25	1.04	400	40	1.11
TMUBM	672	41	1.07	360	78	1.28
TMUBV	631	12	1.02	282	27	1.11
TD_PCA	619	147	1.31	255	53	1.26
TD_ANAL	472	438	13.88	202	175	7.48
TMUADC	34	10	1.42	27	7	1.35
N_{pass}	24			20		
$\bar{\epsilon}_{TD}^{p2}$	$(2.3 \pm 0.5) \times 10^{-2}$			$(2.3 \pm 0.5) \times 10^{-2}$		
$\bar{\epsilon}_{TD}$	$(1.8 \pm 0.4) \times 10^{-5}$			$(1.3 \pm 0.4) \times 10^{-5}$		

Table 5.1: Summary of $\pi \to \mu \to e$ cut rejections for tagged muon data. The table shows the separate measurements of $\bar{\epsilon}_{TD}^{p1}$ and $\bar{\epsilon}_{TD}^{p2}$. The product $\bar{\epsilon}_{TD}^{p1} \times \bar{\epsilon}_{TD}^{p2}$ gives the overall off-line muon rejection inefficiency, $\bar{\epsilon}_{TD}$. For 1989, the ELCTRN rejection was measured separately. The events removed at the second stage by the ELCTRN cut in the 1991 analysis were due to a tightening of the $\mu \to e$ tagging which was already included in the 1989 measurement.

The remaining TD cuts were investigated using the muon samples derived from the 1989 and 1991 $K^+ \to \pi^+ \nu \bar{\nu}$ PASS1 outputs. The muon selection criteria were the same; the standard set of $\pi \to \mu \to e$ cuts were first applied. A summary of the rejections for the final set of $\pi \to \mu \to e$ cuts is shown in table 5.1. The product of the two TD cut factors is the off-line muon rejection inefficiency, $\bar{\epsilon}_{TD}$, which is also given in table 5.1. This factor combined with the kinematic rejection factor computed using the MUBG sample is used to evaluate the muon background rate.

The estimate of the 1990 muon background required the rejection of the on-line $\pi \rightarrow \mu$ cut, $R_{TD}^{\text{on-line}}$. Measurement of the on-line TD cut rejection utilized muons selected from $\pi\nu\overline{\nu}$ Level 0 monitor trigger samples. The muon tagging was similar except that the range-momentum cut was not reversed. A summary of the on-line TD rejections is given in table 5.2. The measured 1989 and 1991 values are also shown. The overall TD rejection can be computed for the 1989 and 1991 data sets using the measured value of the on-line cut rejection; the combination of the on and off-line cuts provides a factor of 10^6 rejection per muon for each year.

On-Line $\pi \rightarrow \mu$ Cut Rejection		
1989	1990	1991
17.0 ± 0.6	21.4 ± 0.9	22.5 ± 2.5

Table 5.2: Summary of on-line TD cut rejections for muons.

5.1.2 Kinematic Background

For a $K_{\mu 2}$ event to kinematically mimic a $K^+ \rightarrow \pi^+\nu\overline{\nu}$ event, some form of non-Gaussian process is required. From table 4.5 it can be seen that the upper edge of the $K^+ \rightarrow \pi^+\nu\overline{\nu}$ signal region is approximately 5σ and 3σ below the $K_{\mu 2}$ peak for range and energy, respectively. Gaussian statistics would imply a rejection of 10^9 based on these cuts alone; needless to say, this is not observed. $K_{\mu 2}$ events that have had their kinematic quantities affected by only Gaussian measurement errors are not a background because the final kinematic cut will remove them. Possible non-Gaussian effects are due to reconstruction errors, muon interactions such as large angle Coulomb scattering, or interaction with dead material in the detector. The $K_{\mu 2}$ type background studies were tailored to extract these non-Gaussian events for detailed study.

By the definition of the background study sample, the $K_{\mu 2\gamma}$ background was evaluated simultaneously. The branching ratio of $K_{\mu 2\gamma}$ decay mode is a factor of 100 lower than $K_{\mu 2}$. Studies using Monte Carlo simulation and the observed properties of $K_{\mu 2}$ type background events suggest that the dominant background is due to mono-chromatic $K_{\mu 2}$ events.

The muon background was estimated using a modified treatment of the stopping layer energy (section 4.2.2) to account for a known correlation between the kinematic and TD rejections The standard practice of subtracting the "4 MeV" pion-decay muon energy was not performed. The MUBG sample muons are predominately tail fluctuation type events with a small fraction of events having a real second pulse in the RS ADC gate.

The measurement of N_{box} was performed in three stages to facilitate detailed study of

the $K_{\mu 2}$ type background signature. The PASS1 analysis, where the MUBG samples were selected, defined the first stage. The second pass analysis consisted of the final set of photon veto cuts for systems other than the target, a loose range-momentum requirement and a subset of the cuts designed to suppress the beam related backgrounds. Application of the range-momentum cut RNGMOM0 removed most of the uninteresting Gaussian component. The second pass for the 1990 data included the off-line application of the on-line Level 1 refined range and Level 1.5 energy cuts.

Signal Region Events

The events in the $K^+ \to \pi^+\nu\bar{\nu}$ signal region after the second pass were skimmed off and the remaining cuts not related to fiducial volume or kinematic particle identification were applied. The stopping layer distribution for the 1991 MUBG signal region events is shown in figure 5.1. The distributions for the 1989 and 1990 data were similar. The majority, 75%, of the residual events in the $K^+ \to \pi^+\nu\bar{\nu}$ signal region are tracks ending in layer 14. The "Layer 14" effect is due to muons stopping in dead material in the RSPC frames and the range-stack support structure. Layer 14 backgrounds are biased to larger values of z_{vtx} and dip-angles of $\cos\theta_D < -0.2$. The asymmetry is due to the target; muons from kaon decays with large z_{vtx} can have large negative dip-angles and still pass through the T counter and intersect with the dead material. The front face of the target and the downstream edge of the T counter constrain tracks to smaller dip-angles which define trajectories that do not intersect with the dead material in the support structure. This can be seen in figure 2.15.

Approximately 50% of the layer 14 events have a hit in an outer layer RSPC. Recall that the RSPCs are located immediately beyond layer 14. Monte Carlo simulation supports the interpretation that the muons stopped in the RSPC frame or RS support structure. Layer 14 events with either an RSPC anode or cathode hit in the stopping sector or adjacent sector (S_S+1) were vetoed. Based on the dip-angle distribution of the Layer 14 background events, shown in figure 5.1 for the 1991 data set, $K^+ \to \pi^+\nu\bar{\nu}$ candidate events in layer 14 were required to have $-0.35 < \cos\theta_D < 0.50$.

An cut on the z position of the DC track at the DC outer-wall radius was found to be effective against tracks which passed through the DC end plates or had their dip-angle grossly mismeasured. Tracks were required to have $|z_{ow}| < 25$ cm; the cut position corresponds to edge of the DC active volume. The z_{ow} distributions for $K_{\mu 2}$ monitor data and $K_{\mu 2}$ type signal region events are shown in figure 5.2.

The RS_Z2_D cut required an outer layer RSPC z hit within 12 cm of the expected position estimated using the DC track extrapolation for tracks stopping in layer 15 and beyond with $|\cos\theta_D| > 0.30$. The cut targeted backgrounds from muons scattering in the

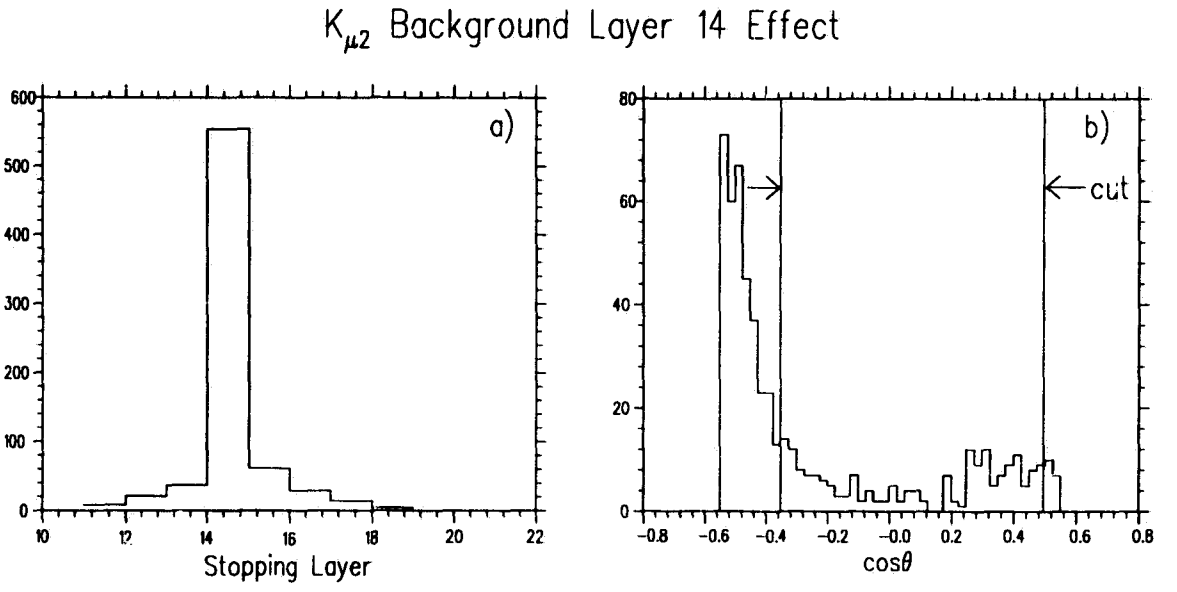

Figure 5.1: The "Layer 14" effect. Figure a) is the stopping layer distribution for the signal region $K_{\mu 2}$ type events before application of the fiducial volume cuts. Figure b) is the dip-angle distribution for the events stopping in layer 14 with the cut position denoted.

range stack towards larger dip-angles. The range calculation can be fooled into assigning the track a shorter range and furthermore, the muon may stop in the dead material in the RS periphery. The RS_Z1 cut which required an inner layer RSPC z hit within 12 cm of the expected position was also effective against this background. The dip-angle distributions for $K_{\mu 2}$ type background events without a valid outer layer RSPC z hit are shown in figure 5.3; also shown is the dip-angle distribution for $K^+ \rightarrow \pi^+ \nu \overline{\nu}$ Monte Carlo data for events stopping in layers 15 to 18.

The range, energy and momentum spectra for the muon type backgrounds are shown in figure 5.4 for the 1991 data set after application of the complete set of analysis cuts. The energy versus range distributions, before and after the BOX momentum cut, are shown in figure 5.5. The events below the box are $K_{\pi 2}$ events that have passed the complete set of photon veto cuts. A summary of the rejections of the fiducial volume and kinematic particle identification cuts for events in the signal region is given in table 5.3. The values of N_{box} for 1989 and 1991 are consistent, once the relative flux and acceptance is accounted for.

5.1.3 Estimate of the $K_{\mu 2}$ Type Background

The $K_{\mu 2}$ type background was evaluated using equation 10. The factors entering the calculation and the estimated background levels are summarized in table 5.4. The expected

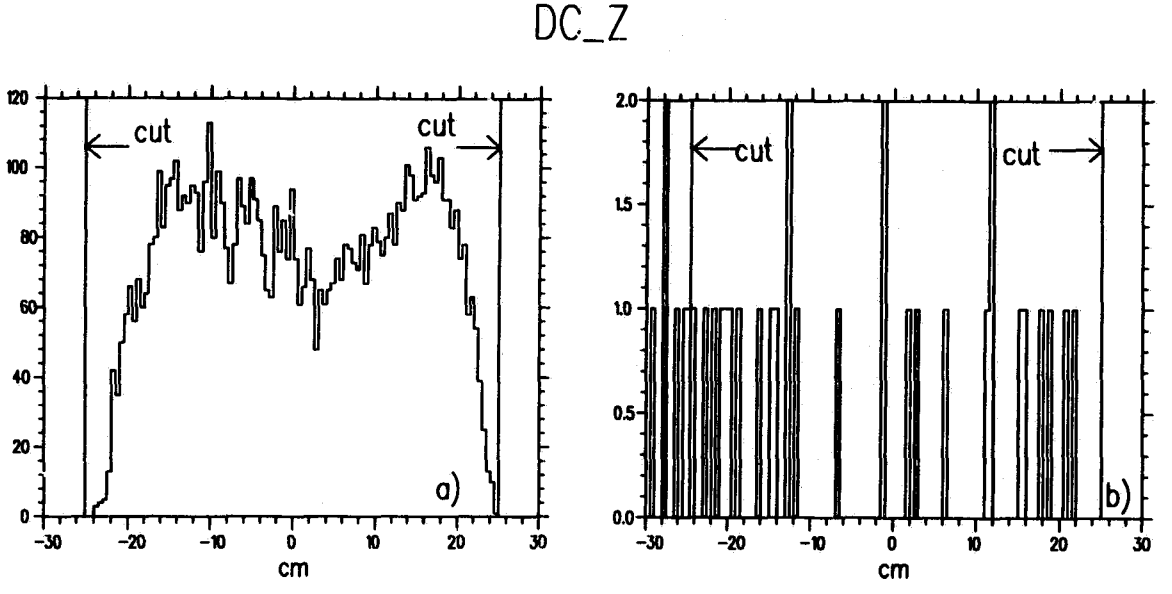

Figure 5.2: The DC based z position at the DC outer wall, z_{ow} for a) $K_{\mu 2}$ monitor events and b) $K_{\mu 2}$ type background events. Note that the convention used to show the cut is reversed.

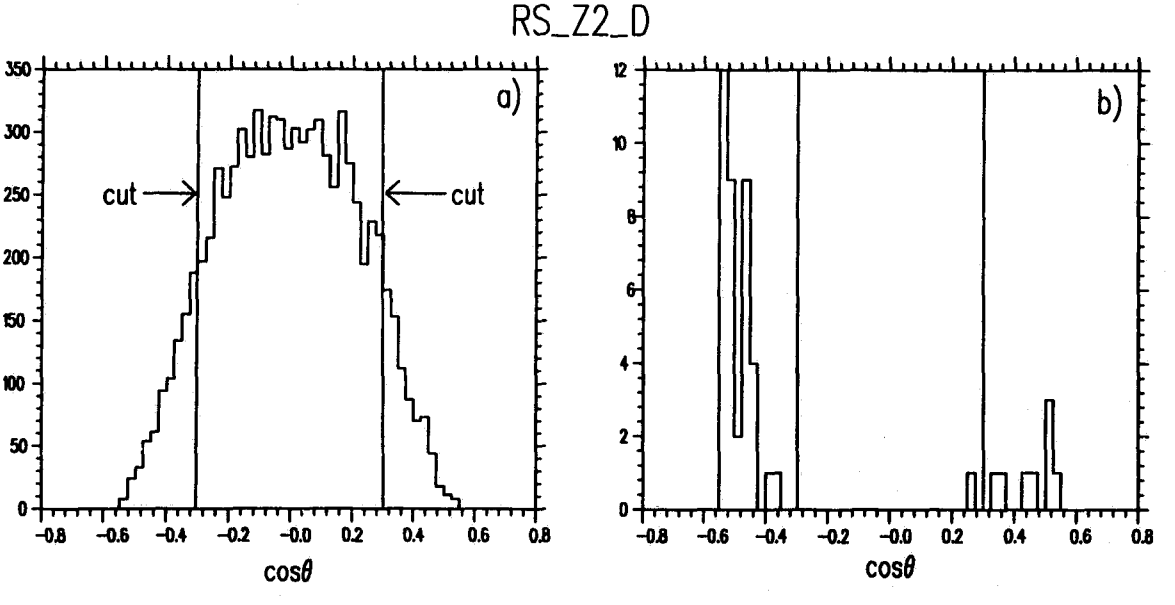

Figure 5.3: The RS_Z2_D cut distributions. Figure a) shows the dip-angle distribution for $K^+ \to \pi^+ \nu\bar{\nu}$ events stopping beyond layer 14. The requirement of the RSPC z hit applies only to the events with $|\cos\theta_D| > 0.3$ as shown by the cut positions. Figure b) is the dip-angle distribution for $K_{\mu 2}$ type background events which have failed the RSPC z hit requirement. The cut positions are shown.

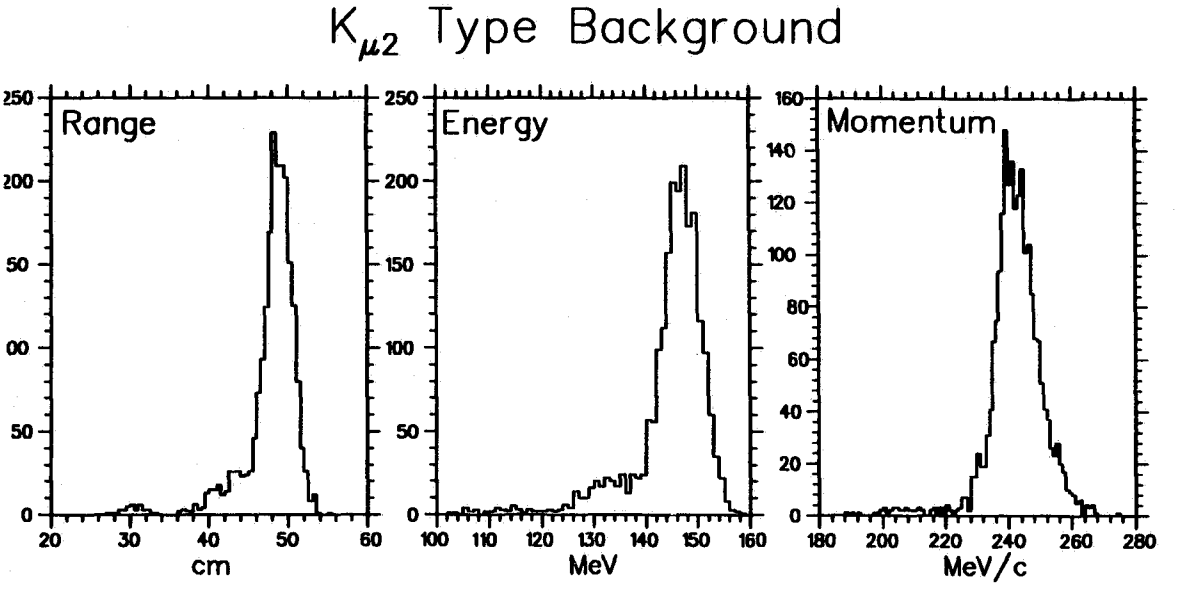

Figure 5.4: Kinematic distributions for the $K_{\mu 2}$ type backgrounds before application of the BOX cut for 1991 data. The events at 30 cm in the total range distribution are $K_{\pi 2}$ events that passed the full set of photon veto cuts.

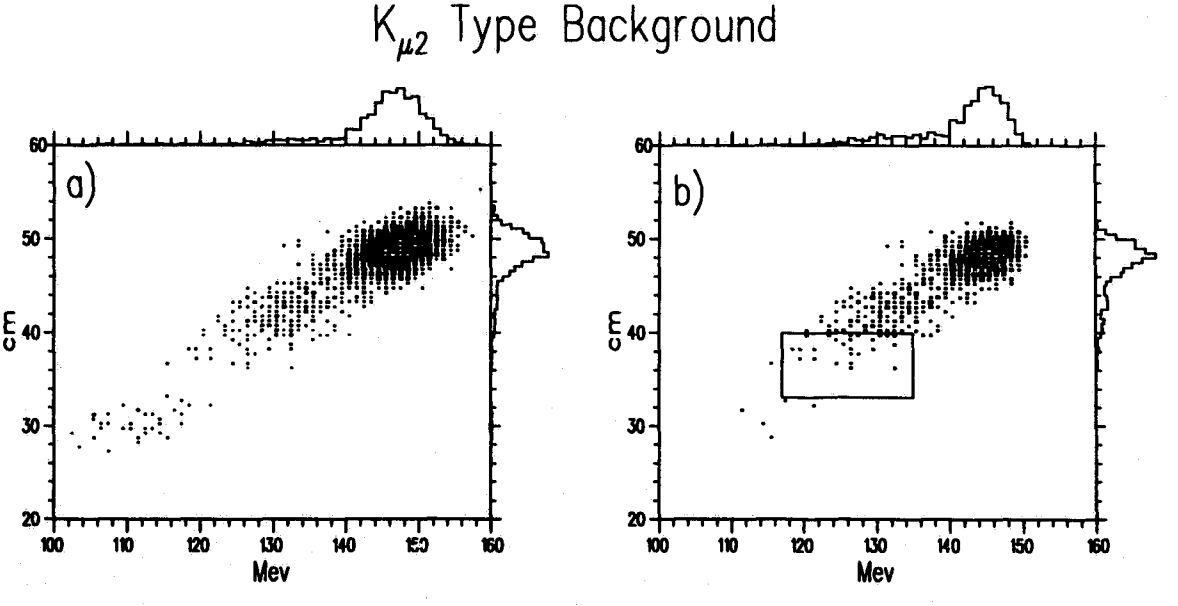

Figure 5.5: Energy versus range distributions for $K_{\mu 2}$ type backgrounds for a) before application of the momentum BOX cut and b) after the momentum cut. The energy-range BOX is shown in b). Data from 1991 is shown. The number of counts in figures a) and b) are 2095 and 969, respectively. The events clustered at 30 cm in range and 110 MeV in energy are consistent with $K_{\pi 2}$ events that have passed photon veto cuts.

$K_{\mu 2}$ Type Background Signal Region Events									
	1989			1990			1991		
Cut	$N_{\rm ex}$	$N_{\rm cut}$	Rej.	$N_{\rm ex}$	$N_{\rm cut}$	Rej.	$N_{\rm ex}$	$N_{\rm cut}$	Rej.
RS_Z1	587	58	1.11	59	1	1.02	728	97	1.15
RS_Z2_D	529	20	1.04	58	5	1.09	631	46	1.08
LAYER14	509	367	3.59	53	45	6.63	585	422	3.59
PHOTOV	142	39	1.38	8	1	1.14	163	53	1.48
KINPCA	103	22	1.27	7	6	7.00	110	48	1.77
RS_DEDX	81	30	1.59	1	0	1.00	62	28	1.82
DC_Z	51	2	1.04	1	0	1.00	34	5	1.17
N_{box}	49			1			29		

Table 5.3: Fiducial volume and kinematic particle ID cut rejections for $K_{\mu 2}$ type events in the $K^+ \to \pi^+ \nu\overline{\nu}$ signal region.

number of $K_{\mu 2}$ type background events for the combined data set was 0.08 ± 0.02. The expected number of events remaining in the final spectrum above the $K^+ \to \pi^+ \nu\overline{\nu}$ signal region, denoted as N_{bgd}^{above} in table 5.4, was 4.6 ± 0.7. The errors quoted for the expected number of events are purely statistical.

$K_{\mu 2}$ Type Background Estimates			
Factor	1989	1990	1991
$f_{ps}^{\rm bgd,90}$	50	21845.3	50
$\bar{\epsilon}_{TD}$	$(1.8 \pm 0.4) \times 10^{-5}$	$(1.3 \pm 0.4) \times 10^{-5}$	$(1.3 \pm 0.4) \times 10^{-5}$
$R_{TD}^{\rm on-line}$	-	$21.4 \pm 0.9.$	-
N_{box}	49	1	29
N_{above}	2440	83	2030
N_{bgd}	0.045 ± 0.012	0.013 ± 0.013	0.018 ± 0.007
Sum 1989-1991	0.08 ± 0.02		
N_{bgd}^{above}	2.25 ± 0.50	1.07 ± 0.33	1.28 ± 0.39
Sum 1989-1991	4.6 ± 0.7		

Table 5.4: Summary of $K_{\mu 2}$ type background factors and estimates. N_{bgd} gives the expected number of events in the $K^+ \to \pi^+ \nu\overline{\nu}$ signal region. N_{above} refers to the measured number of events remaining above the signal region in the background studies and N_{bgd}^{above} corresponds to the estimated number of residual $K_{\mu 2}$ type events above the $K^+ \to \pi^+ \nu\overline{\nu}$ signal region after the full analysis. All errors are purely statistical.

5.2 $K_{\pi 2}$ Background

5.2.1 Outline

Elimination of the $K_{\pi 2}$ background relies on detection of the associated π^0 and identification of the mono-energetic π^+. The photon veto aspect of the $K_{\pi 2}$ rejection has been described in section 4.5. The physics limitations to the photon veto rejection imply that there will be a class of $K_{\pi 2}$ events with unobserved photons remaining after all photon veto cuts have been applied. Since, the photon veto cuts are not sufficient to remove all $K_{\pi 2}$ backgrounds, ultimately the rejection of $K_{\pi 2}$ events relies on the final kinematic cut. This section focuses on the kinematic rejection of $K_{\pi 2}$ events.

The $K_{\pi 2}$ background was estimated using the following relation:

$$N_{bgd} = N_{K\pi 2}^{\pi\nu\nu} \times \frac{N_{BOX}}{N_{K\pi 2}}, \tag{13}$$

where $N_{K\pi 2}^{\pi\nu\nu}$ was the number of residual $K_{\pi 2}$ events in the $K^+ \to \pi^+\nu\overline{\nu}$ data set, and $N_{K\pi 2}$ and N_{BOX} were the number of $K_{\pi 2}$ events in the background study sample and $K^+ \to \pi^+\nu\overline{\nu}$ signal region, respectively. The value of $N_{K\pi 2}^{\pi\nu\nu}$ used to normalize the $K_{\pi 2}$ background estimate was determined by applying the final analysis cuts to the $K^+ \to \pi^+\nu\overline{\nu}$ data set with events having energy and range in the signal region first removed. The values of $N_{K\pi 2}$ and N_{BOX} were determined from the $K_{\pi 2}$ background samples by applying all the cuts except for a subset of the photon veto cuts.

5.2.2 Correlations

The measurement of the $K_{\pi 2}$ background assumed that the fraction of $K_{\pi 2}$ events in the $K^+ \to \pi^+\nu\overline{\nu}$ signal region was independent of the photon veto cuts. There are three potential correlations to consider.

If the π^+ scatters in the target into the fiducial acceptance, the collinearity between the π^+ and π^0 directions is lost. The high energy π^0 decay photon is no longer constrained to intersect the barrel veto and can now escape the detector along the beam axis. This scattering introduces a low side tail in the $K_{\pi 2}$ spectrum that can result in an overestimate of the true background.

If the π^0 decays with the photons back-to-back in the lab frame, hence collinear with the π^+, the low energy photon (20.2 MeV) can convert and overlap the π^+ track. This additional energy can boost the $K_{\pi 2}$ into the signal region. Measurement of the single photon veto inefficiency [51] suggests that this process is enhanced by tight photon veto cuts.

The previous $K^+ \to \pi^+\nu\overline{\nu}$ analyses had observed that target reconstruction errors due to converted photons were a significant source of $K_{\pi 2}$ events in the signal region. The tight

photon veto cuts in the full $K^+ \to \pi^+\nu\overline{\nu}$ analysis enhance the rate of photon conversions in the target relative to that in the $K_{\pi 2}$ monitor samples. The $K_{\pi 2}$ samples used in this study may not have sufficient sensitivity for these types of events to accurately determine their contribution.

The correlation resulting in the low side kinematic tail described above will cancel out to some degree the correlations which tend to push events into the signal region. The simulation of the photon veto at the 10^{-6} level of π^0 inefficiency is not reliable enough to use Monte Carlo techniques to estimate the correlation. The primary source of the uncertainty is in the contribution of the photo-nuclear process to the π^0 inefficiency. Given the large and unknown uncertainty in the effect of the photon veto upon the $K_{\pi 2}$ kinematic rejection, the background estimate assumed there was no net effect.

5.2.3 Kinematic Rejection of $K_{\pi 2}$

The $K_{\pi 2}$ background was the last one estimated using real data and therefore benefitted from the study of the other backgrounds. The cuts developed for the pion scattering backgrounds were effective against reconstruction errors and converted photons in the target. Similarly, the kinematic particle identification cuts studied in the $K_{\mu 2}$ background analysis were found to be effective against kinematic tails. Therefore, for brevity, only $K^+ \to \pi^+\nu\overline{\nu}$ signal region cut results will be discussed.

The $K_{\pi 2}$ background studies utilized the $K_{\pi 2}(1)$ and $K_{\pi 2}(2)$ monitor triggers for the 1989 and 1990 data sets. The $K_{\pi 2}(2)$ trigger differed from the $K_{\pi 2}(1)$ trigger in that the Level 0 delayed coincidence (DC), Level 1 hextant cut and on-line $\pi \to \mu$ trigger requirements were applied on-line. Off-line the full Level 0 and Level 1 $K^+ \to \pi^+\nu\overline{\nu}$ trigger cuts (excluding photon veto) were imposed. The 1991 background study sample was taken from a series of special runs optimized for the $\pi^0 \to \gamma X^0$ decay mode.[2] The trigger requirements were the same as $K^+ \to \pi^+\nu\overline{\nu}$ except the Level 0 barrel veto requirement was not applied.

The analyses of the $K_{\pi 2}$ background data was the same as the full $K^+ \to \pi^+\nu\overline{\nu}$ analysis except for a subset of the photon veto cuts. For the 1989 and 1990 $K_{\pi 2}$ monitor samples, the final target, I-counter and V-counter photon veto cuts were applied. To investigate potential correlations between the photon veto and kinematics, the 1991 background analysis included all the photon veto analysis except for the barrel veto.

The $K_{\pi 2}$ kinematic distributions, before application of the target principal component analysis (TGPCA) and kinematic particle identification cuts for the 1991 background study data, is shown in figure 5.6. Note the hump in the energy distribution arising from the 20

[2] E-787 has established the first upper limit for this process, BR($\pi^0 \to \gamma X^0$) $\leq 5 \times 10^{-4}$ 90% C.L. for a massless X^0 [52].

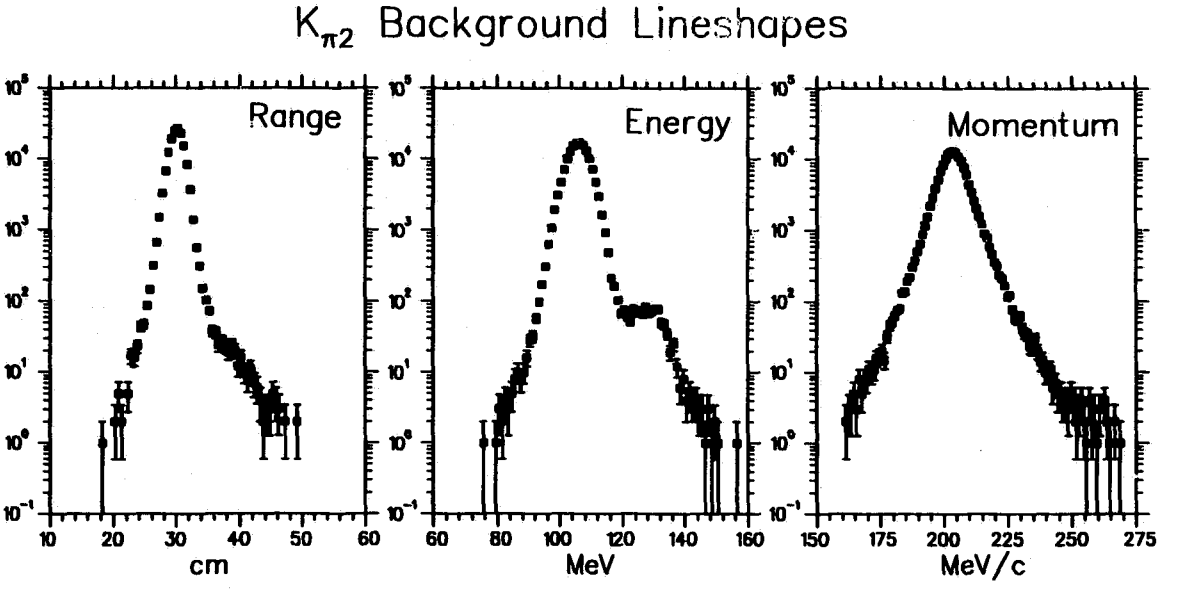

Figure 5.6: Kinematic distributions for the 1991 $K_{\pi 2}$ background study sample before application of the kinematic particle identification and TGPCA cuts. Note the hump in the energy distribution at 130 MeV due to the 20 MeV overlapping π^0 photon.

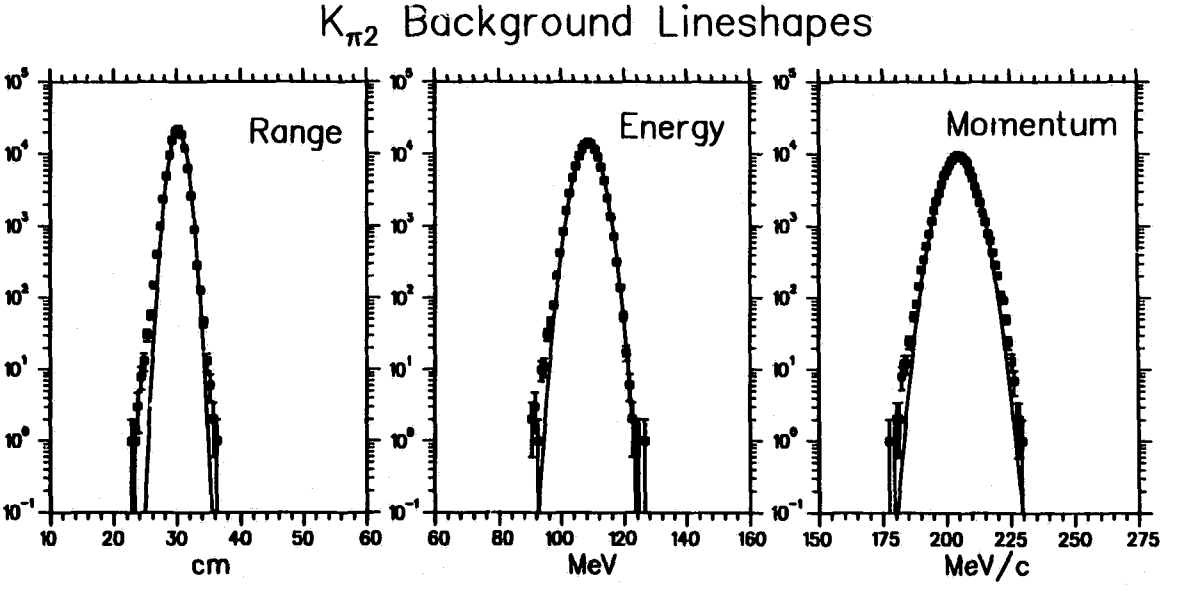

Figure 5.7: Final kinematic distributions for the 1991 $K_{\pi 2}$ background study data before application of the signal region BOX cut. The solid line is a Gaussian fit to the distribution.

MeV photon overlapping the pion track. The final spectrum before application of the signal region BOX cut is shown in figure 5.7. The large tails have been suppressed, most notably, the hump in the energy distribution.

5.2.4 Estimate of the $K_{\pi 2}$ Background

The $K_{\pi 2}$ background measurements are summarized in table 5.5. The $K_{\pi 2}$ background study was limited by statistics; therefore, the background was estimated by summing over the three samples. Summing over all three data sets, a total of 7 events out of 167569 remained in the $K^+ \to \pi^+ \nu\bar{\nu}$ signal region after all cuts. The expected $K_{\pi 2}$ background for the combined data set was 0.13 ± 0.05 events. This estimate assumed that the photon veto and kinematic rejection of the $K_{\pi 2}$ background were not correlated.

$K_{\pi 2}$ Background Analysis				
Factor	1989	1990	1991	Sum
$N_{K\pi 2}$	27766	22012	117791	167569
N_{BOX}	0	1	6	7
$K^+ \to \pi^+ \nu\bar{\nu}$ data: E, R BOX Removed				
$N_{K\pi 2}^{\pi\nu\nu}$	1142	1117	768	3026
N_{bgd} (90%)	< 0.09	< 0.20	< 0.07	< 0.21
	0.05 ± 0.02	0.05 ± 0.02	0.03 ± 0.01	0.13 ± 0.05

Table 5.5: Summary of $K_{\pi 2}$ background estimates. The upper limits for N_{bgd} were determined using the rejection measured for the year in question. The N_{bgd} figures were estimated using the rejection determined from combining the 1989-1991 samples. All errors are purely statistical.

The uncertainty in the $K_{\pi 2}$ background estimates, due to unknown correlations and poor sensitivity of the background sample, suggested that a cut be left in reserve to deal with unexpected events. It was decided *a priori* that the total range cut be allowed to vary up to 34 cm to remove residual signal region events consistent with a $K_{\pi 2}$ origin only if other evidence in the detector supported that conclusion. The choice of the range variable was motivated by the total range distribution. Figure 5.8 shows the total range for $K_{\pi 2}$ events before and after the energy and momentum BOX cuts for the combined 1989-91 $K_{\pi 2}$ background data. Of the 7 remaining signal region events, 6 can be removed by tightening the range cut to 34 cm.

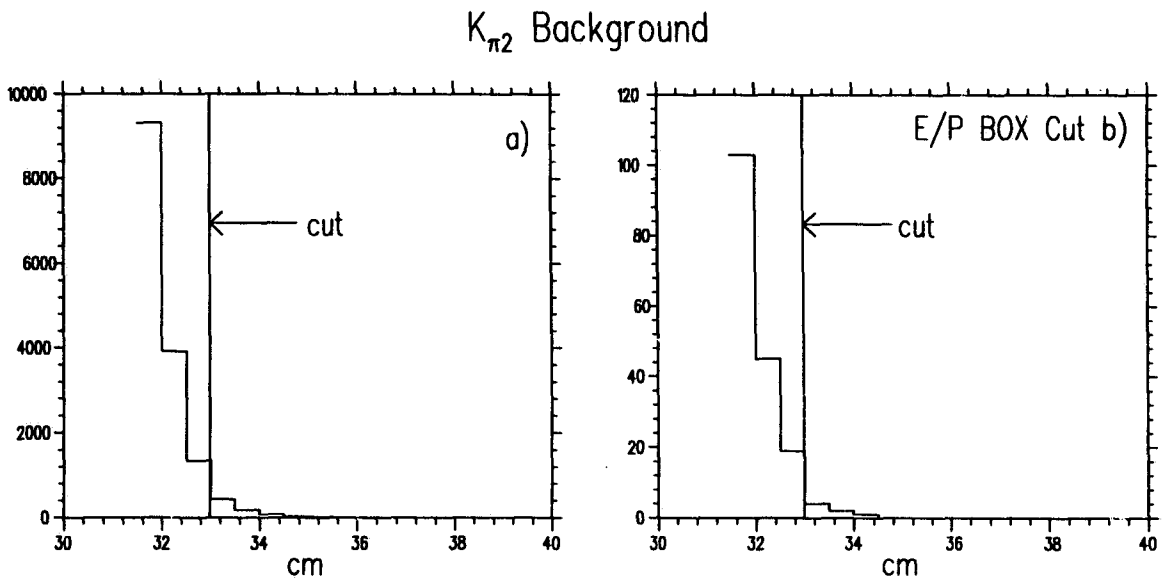

Figure 5.8: $K_{\pi 2}$ total range distribution. Figures a) and b) are before and after application of th energy and momentum kinematic cuts, respectively. The range cut is denoted. Note that the convention used to show the cut is reversed.

5.3 Beam Related Backgrounds

In this section, the evaluation of the beam related backgrounds is described and estimates of the rates for each data run are presented. Beam related backgrounds are due to two types of pion, primary and secondary. Primary beam pions are due to the inherent pion contamination in the LESB-I beam line and are a consequence of the imperfect separation between pions and kaons. A secondary beam pion is due to a kaon entering the detector and producing a pion upstream of the target either by decaying or interacting in the degrader material. Primary beam pions can be identified by the $\check{C}_\pi$ counter, whereas the secondary type are produced downstream of $\check{C}_\pi$ and are not detectable in this manner. There are three types of beam related backgrounds:

1. primary beam pion backgrounds (Type I),
2. secondary beam pion backgrounds from a single beam particle (Type II), and
3. secondary beam pion backgrounds with two beam particles (Type IIa).

The Type IIa class is somewhat artificial and is a consequence of the ability of the detector to discriminate between the different sources of beam related backgrounds.

The beam related backgrounds were estimated using $K^+ \to \pi^+\nu\bar{\nu}$ triggers which had survived the PASS2 analyses described in section 3.3.3. Evaluation of the beam related

backgrounds required inverting one or more cuts to select the background sample. Inverting a cut ensured that the events studied in detail would not be in the final data set. The events passing the inverted cuts were used to estimate the expected number of background events. The estimated background was corrected for the background tagging efficiency of the inverted cut. The rejection, R, of the inverted cut for the background studied was measured using a sample tagged using other cuts. The rejection of the tagging cut is related to the acceptance, A, for tagging the background under study by $A = (1 - 1/R)$; therefore, the background rate can be expressed as

$$N_{bgd} = N_{bgd}^{tag} \times \frac{1}{R-1},$$

where N_{bgd}^{tag} is the number of background events measured in the tagged sample.

5.3.1 Type I Pion Scattering Backgrounds

The Type I $\pi-$scat background occurs when a primary beam pion enters the detector and scatters in the target into fiducial volume. The kaon which generates the kaon Čerenkov hit required for the trigger can either be absorbed or decay upstream of the target with the products undetected. In this case, only the primary beam pion enters the target and the event will be prompt. If the kaon enters the target, the pion scattering can be delayed relative to the kaon. The two cases were studied simultaneously.

The cleanest tag of Type I backgrounds is by identification of the primary beam pion with the pion Čerenkov. The measurement of this background exploits the orthogonality of the pion Čerenkov cut to the other reconstruction cuts. The rejection of the other $\pi-$scat cuts can be reliably evaluated using beam pions tagged in this manner. Similarly, the signature of two BWPC tracks and minimum ionizing dE/dx in the B4 hodoscope can be used to select pion events to measure the rejection of the $\check{C}_\pi$ cut.

The expected number of background events, N_{bgd}, for Type I pion scattering was estimated for each year using

$$N_{bgd} = N_{box} \times \frac{1}{A_{tag}} \times \frac{1}{R_{\rm PS}} \times \frac{1}{R_{\check{C}\pi}}, \qquad (14)$$

where N_{box} was the number of tagged π-scats in the kinematic signal region passing the full set of $\pi \to \mu \to e$ cuts and $K^+ \to \pi^+\nu\overline{\nu}$ signal region cuts, A_{tag} was π-scat tagging efficiency of the $\check{C}_\pi$, $R_{\rm PS}$ was the rejection of the remaining cuts for tagged π-scats and $R_{\check{C}\pi}$ was the rejection of the pion Čerenkov cut. In the estimate of the Type I background, the pion Čerenkov rejection did not enter equation 14 as $1/(1 - R_{\check{C}\pi})$ because the $\check{C}_\pi$ cut was not simply inverted to select the beam pion background.

A sample of primary beam pions was selected by requiring a tight coincidence between $\check{C}_\pi$ and the range stack track time t_{RS}. Table 5.6 summarizes the coincidence windows used for each run and A_{tag}, the tagging efficiency. The method used to measure A_{tag} will be described below. The $\check{C}_\pi$-tagged pions included a residual $K_{\pi 2}$ background ($\sim 1-2\%$) with an uncorrelated hit in the $\check{C}_\pi$ in coincidence with the range stack track time. It was necessary to first remove these $K_{\pi 2}$ events before evaluating the rejection of the remaining cuts. A confidence level for a $K_{\pi 2}$ hypothesis was calculated using a χ^2 test on the total range, energy and momentum. Events with a greater than a 5% probability for a $K_{\pi 2}$ hypothesis were removed.

Type I Pion Scatter Background Tagging		
Run	Coincidence Window (ns)	A_{tag}
1989	$\lvert t_{C\pi} - t_{RS}\rvert < 4.0$	0.831 ± 0.009
1990	$\lvert t_{C\pi} - t_{RS} - 0.7\rvert < 2.5$	0.805 ± 0.009
1991	$\lvert t_{C\pi} - t_{RS} - 2.5\rvert < 2.5$	0.832 ± 0.009

Table 5.6: Summary of the $\check{C}_\pi$ tagging requirements. A_{tag} is the fraction of beam pions tagged.

The rejection of the remaining $\pi-$scat cuts, $R_{\rm PS}$, was defined as the ratio of tagged beam pions to the number of events passing the remaining analysis cuts. Table 5.7 is a summary of the $R_{\rm PS}$ values for each data set. Measurements for individual data sets were limited by the statistical sensitivity of the sample. The row labeled "Combined" in table 5.7 is the rejection obtained by summing over the three data sets.

The measurement of the rejection of the $\check{C}_\pi$ cut, PIBEAM, and the background tagging efficiency, A_{tag}, required an independently selected sample of pions that had entered the detector. The $K^+ \to \pi^+\nu\bar{\nu}$ PASS2 data samples with the $K_{\pi 2}$ events removed were

Rejection of Pion Scattering Cuts, $R_{\rm PS}$				
Run	N_{tag}	N_{pass}	$R_{\rm PS}$	90% C.L.
1989	3479	1	3479 ± 3479	> 881
1990	5427	1	5427 ± 5427	> 1374
1991	3283	0	-	> 1427
Sum	12189	2	6095 ± 4310	> 2291

Table 5.7: Summary of π-scat cut rejections. N_{tag} is the number of beam pion events tagged passing the $K_{\pi 2}$ χ^2 identification cut; N_{pass} is the number of events passing the remaining analysis cuts. The row labeled "Sum" is the rejection obtained by summing over the three data sets.

Pion Čerenkov Rejection			
Run	N_{tag}	N_{pass}	$R_{\check{C}\pi}$
1989	1653	152	10.9 ± 0.8
1990	1953	173	11.3 ± 0.8
1991	1801	117	15.4 ± 1.4

Table 5.8: Summary of the pion Čerenkov cut rejections.

Type I Pion Scatter Background					
Run	N_{box}	$R_{\rm PS}$	$R_{\check{C}\pi}$	A_{tag}	N_{bgd}
1989	825	3479 ± 3479	10.9 ± 0.8	0.831 ± 0.009	0.026 ± 0.026
1990	1128	5479 ± 5479	11.3 ± 0.8	0.805 ± 0.009	0.023 ± 0.023
1991	737	> 1427	15.4 ± 1.4	0.832 ± 0.009	0.000 ± 0.017
Sum					0.05 ± 0.04

Table 5.9: Type I π-scat background calculation factors and estimates.

used. Beam pions were tagged by requiring 2 tracks in the BWPC with one in coincidence with range stack track which was required to be a pion, a pion-like B4 dE/dx and a range stack track time of less than 8 ns. The BWPC tagging was equivalent to inverting the PISCUT cut. The tagging selected events where the kaon was "lost" downstream of the BWPC and upstream of the target with the beam pion entering and scattering in the target. The rejection of the pion Čerenkov cut, $R_{\check{C}\pi}$, was measured on the tagged events for each of the runs. The results are tabulated in table 5.8. The measurement assumed that all two beam particle events with pion-like B4 dE/dx were $\pi - K$ pairs. The contamination from two beam particle events from $K - K$ and K – proton combinations with a π produced downstream of the pion Čerenkov counter was ignored.

Estimate of the Type I Background

The number of expected Type I π-scat background events was evaluated for each year using equation 14. The factors in equation 14 and the expected background levels are tabulated in table 5.9. For the values of $R_{\rm PS}$ calculated from the individual data sets, the expected Type I π-scat background was 0.05 ± 0.04, where the error is purely statistical. For the value of $R_{\rm PS}$ determined from combining the three data sets, the expected background was 0.05 ± 0.03. The values are consistent.

5.3.2 Type II Pion Scattering Backgrounds

Type II $\pi-$scat backgrounds are due to kaon decay-in-flight and pion production from strong interaction kaon scattering downstream of the $\check{C}_K$. The signature for this type of background is distinct: a prompt event with the B4 hodoscope dE/dx consistent with a minimum ionizing particle and only one identifiable beam particle. The events failing the B4 dE/dx (B4DEDX) and target delayed coincidence cuts (PIKTIME, PIKTIME2) defined the Type II π-scat background sample.

The expected number of Type II pion background events, N_{bgd}, was estimated for each year using

$$N_{bgd} = N_{box} \times \frac{1}{(R_{B4}-1)} \times \frac{1}{(R_{DC}-1)}, \tag{15}$$

where N_{box} was the number of events tagged by inverting the target delayed coincidence and B4 dE/dx cuts which passed all remaining analysis cuts, R_{B4} was the rejection of the B4 dE/dx cut, and R_{DC} was the rejection of the off-line delayed coincidence cuts for prompt type events.

The $\check{C}_\pi$-tagged pion beam samples were used to measure the B4 dE/dx cut rejection. Single target track events were selected by vetoing events with extra BWPC tracks or having a hit in the BH counter coincident with the range stack track time. Events consistent with $K_{\pi 2}$ hypothesis were first removed. The target delayed coincidence time was required to be less than 4 ns to reject events consistent with a two particle signature in the target. The B4 dE/dx cut rejection measurements are summarized in table 5.10. For the 1990 data, fingers 1 and 2 of the x hodoscope plane had distorted energy spectra. This would explain the poorer rejection observed.

B4 Hodoscope dE/dx Cut Rejection			
Run	N_{tag}	N_{pass}	R_{B4}
1989	341	114	2.99 ± 0.23
1990	362	164	2.29 ± 0.14
1991	171	47	3.64 ± 0.45

Table 5.10: Summary of the B4DEDX cut rejections.

The $\check{C}_\pi$-tagged beam pion samples were used to determine the rejection of the delayed coincidence cuts for the single beam particle background. The target reconstruction quality cuts were first applied. The delayed coincidence time distributions for target and I-counter based pion times are shown in figure 5.9 for the selected events. The cut position for each type is shown. R_{DC} was evaluated for events with delayed coincidence times of less than 8 ns. The measurements are summarized in table 5.11. For reference, the effect of the target

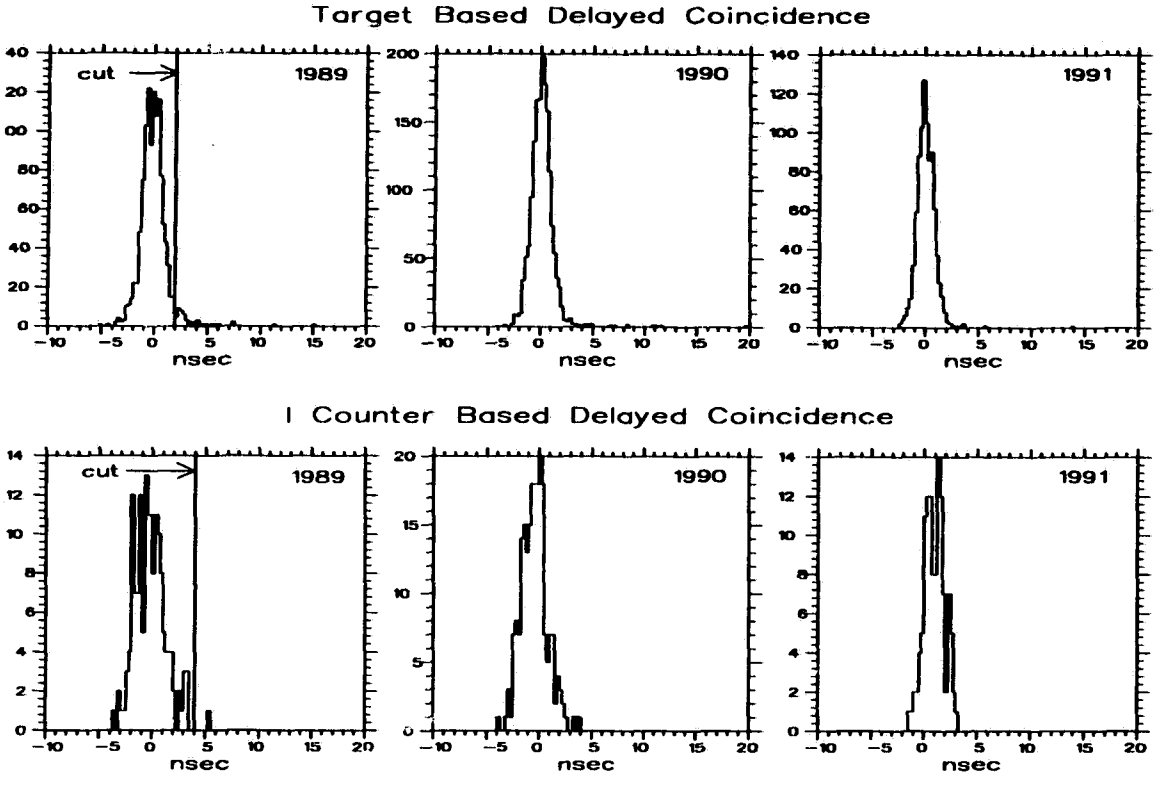

Figure 5.9: Delayed coincidence time distributions, $t_{K-\pi}$, for events used to measure R_{DC}. The same cut was applied to all samples and is shown for the 1989 data. For target fibre based times, the cut required $t_{K-\pi} > 2$ ns and for I-counter based times, the cut was $t_{K-\pi} > 4$ ns.

based cut and the secondary delayed coincidence cuts, TRS and B4DELC is separated. Also shown is the delayed coincidence rejection for events tagged by failing the B4 dE/dx cut. The rejection is significantly higher; however, the value measured without the B4 dE/dx tag was assumed.

Estimate of the Type II Background

The number of expected Type II π-scat backgrounds were evaluated using equation 15 and are summarized in table 5.12. The expected background from this source was 0.10 ± 0.03 events where the error is statistical. If the delayed coincidence rejection calculated with the B4 dE/dx tag is assumed, then the Type II π-scat background is < 0.06 events at the 90% confidence level.

Delayed Coincidence Cut Rejection				
Run	N_{tag}	N_{pass}		R_{DC}
1989	1310	(30)	15	87 ± 22
1990	1841	(45)	19	97 ± 22
1991	998	(10)	5	200 ± 90
With B4 dE/dx tag				
1989	856	(15)	0	> 372
1990	874	(10)	1	> 221
1991	704	(7)	2	> 132

Table 5.11: Summary of delayed coincidence cut rejections, R_{DC}. The figures in parentheses in the N_{pass} column denote the number of events passing the standard target or IC based cuts. The adjacent number is the number passing the full set of cuts including the secondary TRS and B4DELC delayed coincidence cuts. The R_{DC} measurements using pions tagged with the B4DEDX cut are also shown. The upper limits are at the 90% C.L.

Type II Pion Scatter Background				
Run	N_{box}	R_{B4}	R_{DC}	N_{bgd}
1989	4	2.99 ± 0.23	87 ± 22	0.023 ± 0.013
1990	8	2.29 ± 0.14	97 ± 22	0.059 ± 0.025
1991	9	3.64 ± 0.45	200 ± 90	0.017 ± 0.010
Sum				0.10 ± 0.03

Table 5.12: Type II π-scat background calculation factors and estimates.

5.3.3 Type IIa: Kaon Pileup Background

A subset of the Type II $\pi-$scat background is where two kaons enter the detector and one of the kaons produces a pion downstream of the $\check{C}_\pi$ with the other kaon entering the target. The Type I background does not include this contribution because the scattered pion is produced downstream of the Čerenkov. In the Type II background analysis, the B4 dE/dx tagging procedure removed the events where a kaon entered the target. Therefore, the contribution from the two-kaon background must be determined separately. The signature used to tag this type of background was two BWPC tracks with no accompanying signal in the $\check{C}_\pi$. As in the measurement of the $\check{C}_\pi$ rejection, selection of the two BWPC tracks was performed by inverting the PISCUT cut. To increase the statistical sensitivity of the background samples it was necessary to relax certain cuts. The target reconstruction quality cuts were not applied and their rejection was measured separately on a different sample. The expected number of Type IIa $\pi-$scat background events, N_{bgd}, was estimated using

$$N_{bgd} = N_{box} \times \frac{1}{R_{\rm TGT}} \times \frac{1}{(R_{\rm BWPC} - 1)}, \tag{16}$$

where N_{box} was the number of tagged events in the signal region passing all remaining analysis cuts except the target quality cuts, $R_{\rm TGT}$ was the rejection on the target quality cuts not applied above, and $R_{\rm BWPC}$ was the rejection of the BWPC tracking cut.

To estimate the rejection of the remaining target reconstruction cuts, a clean sample of events with a beam pion and kaon in the target was needed. A representative sample was derived from the $\check{C}_\pi$-tagged beam pion samples by requiring a delayed coincidence time in the target of greater than 8 ns. As in the case of the Type I π-scat background, it was necessary to first remove the residual $K_{\pi 2}$ events. A summary of the measured values of $R_{\rm TGT}$ for each year is given in table 5.13.

Target Reconstruction Cut Rejection			
Run	N_{tag}	N_{pass}	$R_{\rm TGT}$
1989	379	7	54 ± 20
1990	646	6	108 ± 44
1991	685	8	86 ± 30

Table 5.13: Rejection of the target reconstruction quality cuts for two beam particle events.

The rejection of the BWPC tracking cut, PISCUT, was measured using the $\check{C}_\pi$-tagged beam pion samples. The target delayed coincidence time was required to be greater than 8 ns and events consistent with a $K_{\pi 2}$ hypothesis were removed. Table 5.14 summarizes the rejections. There is significant variation between the three data sets. For 1990, there was

a known problem with the gas mixture. A calibration problem with the Iso-Butane flow meter resulted in the BWPC operating with only CF_4 for approximately one-half of the run. For the 1989 data, the cause of the low rejection is not known.

BWPC Cut Rejection			
Run	N_{tag}	N_{pass}	R_{BWPC}
1989	352	76	4.6 ± 0.5
1990	746	92	8.1 ± 0.8
1991	663	46	14.4 ± 2.0

Table 5.14: Rejection of the BWPC track based PISCUT cut for tagged two beam particle events.

Estimate of the Type IIa Background

The Type IIa $\pi-$scat or kaon pileup background study results are summarized in table 5.15. Summing over the three data sets gives an expected background level of 0.06 ± 0.02. It should be noted that the Type IIa background estimate includes a component of the Type I $\pi-$scat background. The Type I background that is rejected only by the BWPC tracking cut is double counted in the estimate of the Type IIa background. Given the inability to adequately discriminate between the contribution and the statistical error of the two estimates, no correction was made for the double counting.

Type IIa Pion Scattering Background				
Run	N_{box}	R_{TGT}	R_{BWPC}	N_{bgd}
1989	6	54 ± 20	4.6 ± 0.5	0.031 ± 0.017
1990	16	108 ± 44	8.1 ± 0.8	0.021 ± 0.010
1991	13	86 ± 30	14.4 ± 2.0	0.011 ± 0.005
Sum				0.06 ± 0.02

Table 5.15: Type IIa π-scat background calculation factors and estimates.

5.4 Charge Exchange Background

This section describes the estimate of the kaon charge exchange (CEX) background. CEX occurs when a K^+ enters the target and interacts with a neutron in a nucleus to produce a proton (or nuclear fragments) and a K^0. The proton associated with the K^0 can not be distinguished from the initial K^+ in the target. The K^0 is an equal mixture of K_L^0 and K_S^0. The K_S^0 component decays almost immediately, $\tau = 0.089$ ns, and is therefore highly suppressed by requiring a delayed coincidence between the K^+ and the decay products. Further suppression is gained by the detection of the associated charged pion.[3]

The K_L^0 component has a lifetime of $\tau = 51.7$ ns; therefore, the K_L^0 decay can be delayed relative to the initial beam kaon. The K_L^0 semi-leptonic branching ratio is large; summing over electronic and muonic modes, the fraction of K_L^0 decays with a π^+ in the final state is 0.328. The maximum π^+ momentum for the muonic and electronic modes is 216 MeV/c and 229 MeV/c, respectively; therefore, for each mode, the π^+ momentum spectrum extends into the signal region. Because the K_L^0 decays in-flight, the large phase space suppression from requiring $P_{\pi+} > 211$ MeV/c is only partially realized.

Further suppression of this background mode relies upon detection of the associated lepton and demanding decay vertex consistency. A delayed decay of the neutral K_L^0 implies that there is a gap between the production and decay vertices. Cuts sensitive to target tracking gaps included TGPCA, DPIK, DCTG_XY, RTDIF and KROAD. An irreducible background arises when the decay lepton's transverse and longitudinal momenta are anticollinear with the pion and with the K_L^0, respectively. The energy deposited by the lepton "closes the gap" between the decay and production vertices and partially restores the kaon z versus E correlation. The momentum component anticollinear with the pion can lengthen the observed target track and artificially boost all three kinematic quantities into the $K^+ \to \pi^+\nu\bar{\nu}$ signal region.

Unlike the other backgrounds to $K^+ \to \pi^+\nu\bar{\nu}$, the CEX background was estimated from a Monte Carlo simulation. There is no clear signature with which to tag CEX events in the data without introducing unknown correlations between cuts and unwanted backgrounds of other types.

5.4.1 Monte Carlo Simulation

The Monte Carlo simulation[4] considered the muonic and electronic semi-leptonic modes separately. Charged kaons were generated at the front target face and were propagated

[3]The K_S^0 decays almost exclusively into a two-pion final state, with the $\pi^+\pi^-$ mode accounting for 68% of the total width.

[4]The workings of the E-787 Monte Carlo program, UMC, are described in section 7.2.3.

until they interacted or came to rest. The initial K^+ momentum and momentum bite was chosen to match the observed K^+ target energy distributions. To improve the yield of K_L^0, the Monte Carlo cross sections for charge exchange were scaled up by a factor of 100. Kaon decays and K_S^0 production were turned off. Since the associated proton is indistinguishable from the initial kaon, no cuts on the proton kinetic energy were applied. The yield of K_L^0 per K^+ generated was 0.116.

Three different simulations were run with each simulation progressively restricting the K_L^0 decay timing. The majority of the K_L^0 produced will not decay in the target since the mean decay length, $\lambda = \gamma\beta c\tau$, is significantly larger than the length of the target fiducial volume. The first simulation did not constrain the decay to occur within the target. In subsequent simulations, the following method was used to generate K_L^0 decays. The vector $\vec{l}$ was defined as the vector originating at the production vertex along the K_L^0 directional cosines to the edge of the target volume. The time taken for the K_L^0 to travel the distance l was cut upon. The subsequent simulations required decay times of greater than 0.8 ns and 1.5 ns respectively. The decay probability, w, was used to weight the event where $w = 1 - e^{-\frac{l}{\lambda}}$. The K_L^0 decay position along $\vec{l}$ was selected using $x = -\lambda \ln(1 - yw)$, where y was a random number between 0 and 1. For each K_L^0 produced, 100 semi-leptonic decays were simulated with the fraction of decays with $P_\pi > 180$ MeV/c used to define an additional event weight. The decay kinematics of the last event generated satisfying the momentum cut were then used to simulate the remainder of the event. Events were required to pass the $K^+ \to \pi^+\nu\overline{\nu}$ Level 1 trigger requirements. Pions were allowed to decay and undergo nuclear interactions.

5.4.2 Analysis of CEX Data

The CEX Monte Carlo data analysis included all off-line cuts applicable to Monte Carlo data except as noted. Pions were required to stop in active material in the range-stack and decay as muons. The kinematic particle identification cuts were not applied. The kinematic distributions for the muonic decay mode are shown in figure 5.10 before application of the off-line delayed coincidence and target event quality cuts. The in-flight decays extend the pion spectrum far beyond the 211 MeV/c end point for K_L^0 decays at rest. The delayed coincidence timing distribution for events generated without the target timing cut is shown in figure 5.11; there is a clear tail extending beyond 2 ns from low momenta K_L^0 events. Also shown is the E_K versus z_{vtx} distribution. Compared with the plot for $K_{\pi 2}$ decays, figure 4.6, a large component of decays with small kaon target energies is apparent.

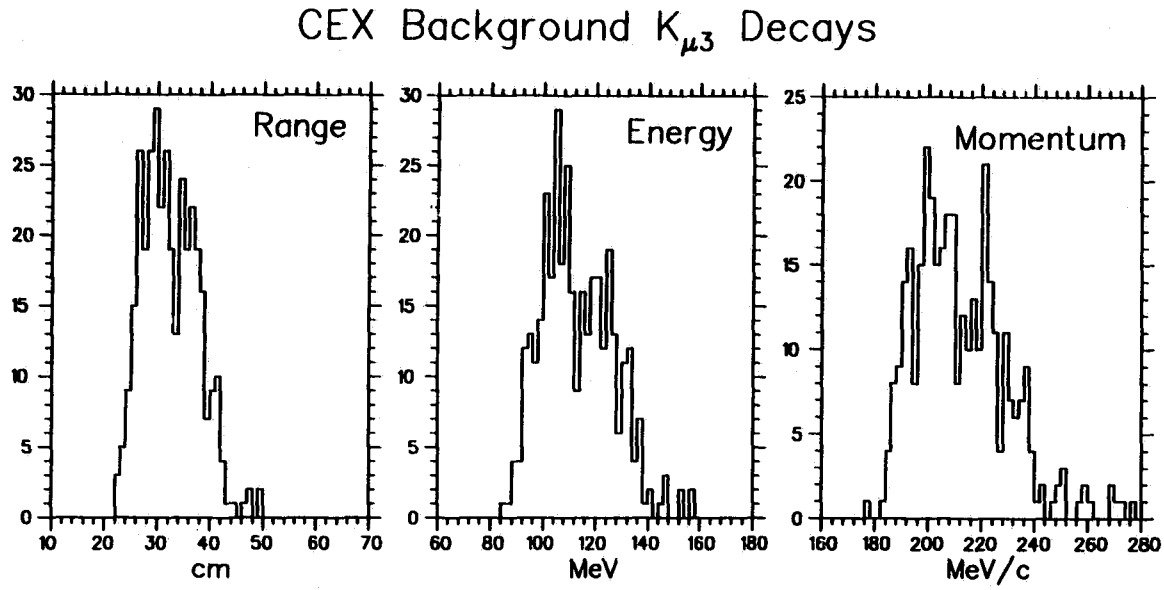

Figure 5.10: Kinematic distributions for muonic semi-leptonic K_L^0 decays before application of the target based delayed coincidence cut. Note the effect of in-flight decays which have boosted the momentum beyond the decay-at-rest 211 MeV/c end-point.

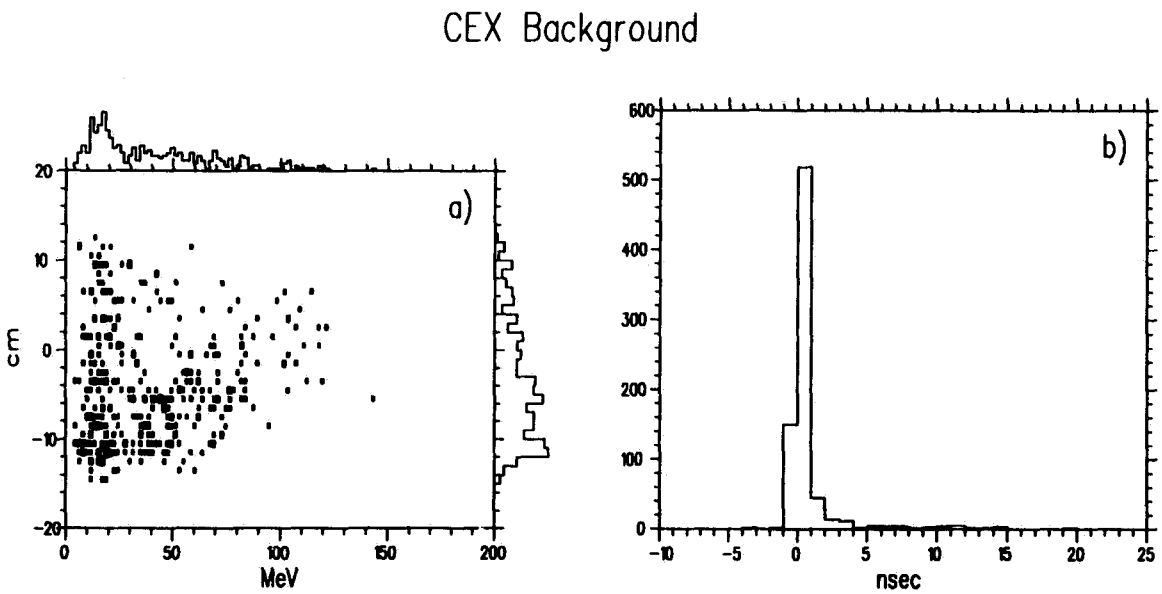

Figure 5.11: CEX background. Figure a) shows the kaon energy versus decay vertex z position. Compare with figure 28 where $K_{\pi 2}$ decays are shown. Figure b) shows the delayed coincidence timing distribution for reconstructed events. The data were generated without the target timing cut.

5.4.3 Estimate of the CEX Background

The CEX background from each semi-leptonic mode was evaluated separately. The background was calculated using,

$$N_{bgd} = \frac{W_{BOX}}{N_{K_L^0}} \times P_{CEX} \times P_{K_L^0} \times \mathrm{BR}(K_{l3}) \times f_A \times N_{KTLive}, \quad (17)$$

where W_{BOX} was the sum of event weights passing the off-line cuts, $N_{K_L^0}$ was the number of K_L^0 decays generated, P_{CEX} was the probability for the kaon to charge exchange in the target, $P_{K_L^0} = 0.5$ was the fraction of K^0 produced decaying as a K_L^0 and $\mathrm{BR}(K_{l3})$ was the K_L^0 semi-leptonic branching ratio with a π^+ in the final state for lepton type l. f_A was an acceptance correction factor for Monte Carlo data and N_{KTlive} was the integrated kaon flux for the 1989-91 data set. For the electronic mode, W_{BOX} was calculated before the application of the final kinematic cut; the rejection of which was inferred from the π^+ kinematic distributions after PASS1 type cuts. This was necessary to increase the statistical sensitivity of the sample as no events passed the full analysis with the signal region cut. The value of P_{CEX} was determined empirically [53] by comparison of the observed rate of $K_S^0 \to \pi^+\pi^-$ decays per incident K^+ with a Monte Carlo simulation. The f_A factor included efficiency losses not accounted for in the off-line analysis. These included the accidental photon veto losses, the off-line $\pi \to \mu \to e$ detection efficiency, kinematic based particle identification efficiency, the Level 1 trigger setup acceptance, and the acceptance of the beam counter cuts. The acceptance correction, f_A, was estimated to be 0.148. A summary of the factors entering into the CEX background measurement is given in table 5.16. The analysis of the muonic mode resulted in 3 events of combined weight and associated statistical error of 0.024 ± 0.016 after the BOX cut. The electronic mode analyses had 1 event of weight 0.0038 survive all cuts excluding the BOX cut.

The estimated background from the muonic decay mode for the combined 1989-91 data set was 0.07 ± 0.05 events; the electronic mode background was estimated to be 0.005 ± 0.005 events where the errors are purely statistical. The difference between the two contributions is due to the higher rejection of the photon veto cuts for the electronic mode. The electronic mode is more easily rejected because of the associated electron showering and producing photons which are detectable. The CEX background estimates have unknown systematic errors. Sources of error included the poor understanding of the near threshold kaon charge exchange process and simulation of the target response in the Monte Carlo.

Kaon Charge Exchange Background		
Factor	Muonic	Electronic
N_{KTLive}	5.18×10^{11}	
f_A	0.148	
P_{CEX}	0.002	
$P_{K_L^0}$	0.5	
BR(K_{l3})	0.135	0.194
$N_{K_L^0}$	3.71×10^6	3.95×10^6
W_{BOX}	0.024 ± 0.016	0.0038 ± 0.0038
Box Cut	-	0.34
N_{bgd}	0.07 ± 0.05	0.005 ± 0.005

Table 5.16: Kaon charge exchange background calculation factors and estimates. All errors are purely statistical.

5.4.4 Hyperon Decay Backgrounds

After the final pass was performed on the $K^+ \to \pi^+\nu\bar{\nu}$ data, possible evidence of a potential new background to $K^+ \to \pi^+\nu\bar{\nu}$ arising from CEX was reported. A class of events which could be interpreted as Σ^+ hyperon decays were observed in the $K^+ \to \pi^+\nu\bar{\nu}$ below the $K_{\pi 2}$ peak analysis. The K_L^0 originating from CEX can produce a Σ^+ hyperon by two possible means:

$$\begin{aligned} K_L^0 + p &\to \Sigma^+ + \pi^0, \\ K_L^0 + n &\to \Sigma^+ + \pi^- \\ &\quad\downarrow \\ &\quad\Sigma^+ \to \pi^+ + n, \end{aligned}$$

before decaying or exiting the target. Only the $\bar{K}^0$ component of the K_L^0 contributes. The Σ^+ decay produces a mono-chromatic π^+ having a momentum of 185 MeV/c. If, however, the Σ^+ decays in flight, the associated pion can be boosted into the kinematic region of interest.

A Monte Carlo simulation[5] of the Σ^+ decay background predicted approximately 4 events of this type with an unknown and large systematic error. The systematic error arises from the unknown cross section for Σ^+ production in carbon with the pion being absorbed by the nucleus and the uncertainty in the low momentum K_L^0 spectrum. In this analysis, no background events consistent with this mechanism were observed. The present evidence for this background is inconclusive.

[5]Data supplied by J. Roy

Chapter 6

Events in the Final Spectrum

We're just two lost souls swimming in a fish bowl, year after year.
Running over the same old ground, what have we found? The same old fears.
Wish you were here.

- Pink Floyd

6.1 The Candidate Events

A summary of the two $K^+ \to \pi^+\nu\overline{\nu}$ candidate events, hereafter referred to as 1990A and 1991A, is given in table 6.1. The events shared the feature that they were both near the lower edge of the signal region.

Signal Region Events		
Quantity	1990A	1991A
Range (cm)	33.6	33.1
Energy (MeV)	116.0	115.3
Momentum (MeV/c)	211.3	211.6
Kaon decay time (ns)	20.4	11.9
Pion decay time (ns)	21.7	42.5

Table 6.1: The $K^+ \to \pi^+\nu\overline{\nu}$ signal region events.

6.1.1 Candidate 1990A

The 1990A event was consistent with being a $K_{\pi 2}$ event having a reconstruction error in the target resulting in a misassigned kaon decay vertex. This error introduced an additional 3 cm of range to the track which artificially boosted the event into the signal region.

The target event display for the event is shown in figures 6.1 and 6.2 for the energy

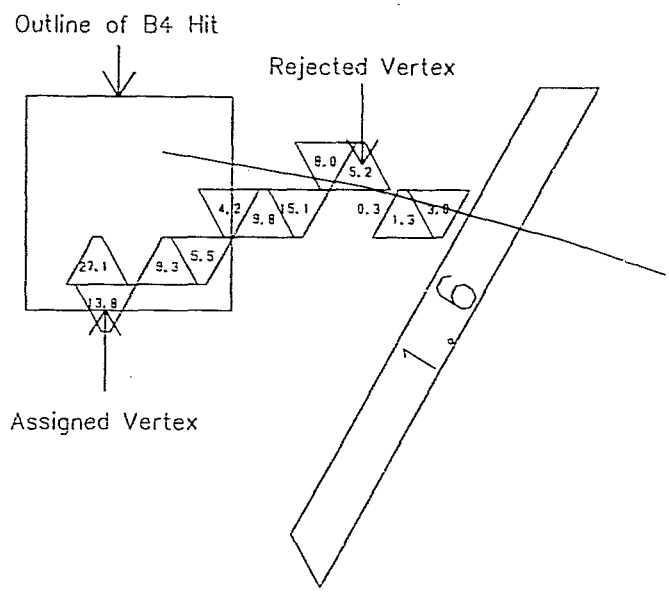

Figure 6.1: Event display of the 1990A candidate event showing the target energy information. The assigned vertex and the area corresponding to the B4 hodoscope hit is shown. Also shown is the position of the vertex rejected by the target fitting. The arc corresponds to the extrapolated DC track.

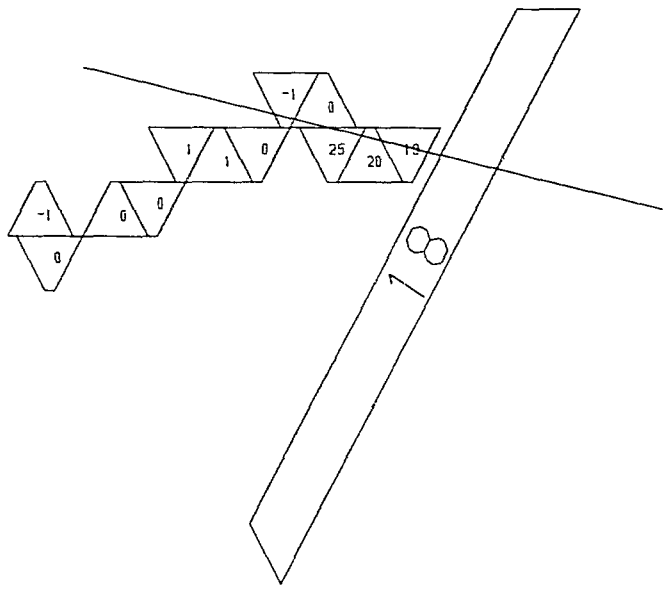

Figure 6.2: Event display of 1990A candidate event showing timing information.

and timing information, respectively. The position of the assigned vertex is shown in figure 6.1 as well as the outline of the B4 hodoscope hit which defines the entry point of the kaon into the target.

Normally, the RTDIF cut, which examines the potential uncertainty in the kaon decay vertex, would remove events with elongated kaon clusters collinear with the pion track; however, the extrapolated DC track overlapped only a short segment of the kaon cluster (1.6 cm vs. a cut at 2 cm). The kaon and pion clusters were, however, sufficiently aligned that the target reconstruction chose the wrong end of the kaon cluster on the basis of a smaller distance of closest approach for the extrapolated pion track. The energy resolution of the target was inadequate to resolve the tracking error using the dE/dx information for the pion track.

6.1.2 Candidate 1991A

The 1991A event was also consistent with a $K_{\pi 2}$ origin. The evidence to support this conclusion was found in the lead glass beam counter where a hit coincident with the pion track time was found. The lead glass hit occurred at -3.0 ns relative to the pion track. A 1 MeV hit occurring at -3.3 ns, relative to the pion track, was also observed in the upstream endcap. The timing of the endcap hit was just outside the coincidence window used by the photon veto cuts. The lead glass and endcap hits were consistent with a photon of $\sim$ 35 MeV converting in the lead glass with 1 MeV deposited in the EC. The lead glass, which was only in place for the 1991 run, was not utilized in the analysis. The lead glass cut that was considered for the analysis would have failed the event with a 3.5% loss of acceptance. The background studies did not suggest that the additional rejection was required.

The 1991A event exhibited the classic $K_{\pi 2}$ background signature; all three kinematic quantities barely satisfying the kinematic cut. Close examination of event 1991A did not suggest the known correlations with the photon veto as the source of the event. The target reconstruction was unambiguous and there was no evidence of anomalously high dE/dx in the range stack or target. The event is consistent with being an event in the Gaussian tail of the $K_{\pi 2}$ background. [1]

6.1.3 Adjusting the Range Cut

The two remaining $K^+ \rightarrow \pi^+ \nu\bar{\nu}$ signal region events can be attributed to a $K_{\pi 2}$ origin. Therefore, following the method outlined in section 3.1.2, the lower edge of the total range cut was moved to 34 cm to remove the two events from the signal region.

[1] Note however that it is possible to interpret this event as a non-$K_{\pi 2}$ background. The lead glass hit could have been due to a beam pion missed by the upstream counters.

6.1.4 Source of the Background Events

If both candidate events are to be interpreted as having a $K_{\pi 2}$ origin, then observation of two events was not consistent with the estimated $K_{\pi 2}$ background 0.13 ± 0.05 events, where the error in the estimate was purely statistical. Neither of the candidate events shows evidence of arising from the correlation mechanisms discussed in section 5.2.2. The 1990A event was due to a non-Gaussian reconstruction error. The 1991A event appears to be completely Gaussian in character. Neither event displays evidence that photon activity was responsible for a mismeasured kinematic quantity. Possible explanations for this include the following:

1. There existed an unknown correlation between the photon veto and kinematic cut rejections.

2. The data samples used to evaluate the background were not representative of the residual $K_{\pi 2}$ sample.

3. The two events represent a statistical fluctuation.

6.2 Study of the Residual $K_{\pi 2}$ Events

6.2.1 Comparison of the Lineshapes

Comparison of the kinematic quantities for the residual $K_{\pi 2}$ events and the $K_{\pi 2}$ background study samples shown in table 6.2 reveals a significant worsening of the resolutions. More illuminating, however, is the comparison of the rejection of the individual components of the kinematic signal region cut for the background samples with the residual $K_{\pi 2}$ spectrum. The results are summarized in table 6.3. For comparison, the expected rejection using Gaussian statistics and the kinematic resolutions for the background samples is also shown.

Despite the poorer range and momentum resolutions, the corresponding rejections were consistent with the expectations from the background data and from Gaussian statistics. It can be seen in figure 6.3 that the peak shift and poorer resolution can be attributed to the presence of a low-side tail in the range and momentum distributions.

The observed energy resolution was also poorer than expected; however, unlike the case of range and momentum, the observed rejection was significantly worse. The ratio of the rejections was 1.7 ± 0.2. A similar factor can be arrived at by comparing the expected rejections using Gaussian statistics and the relative peak and energy box positions with the associated resolutions. For the residual $K_{\pi 2}$ events, the effective BOX is 1.72σ above the peak compared to 1.98σ for the background samples. This corresponds to a factor of 1.7 worse rejection, consistent with the number derived from the BOX cut analysis. If the

$K_{\pi 2}$ Kinematics		
$K_{\pi 2}$ Bgd. Data, 167569 Events		
Quantity	Peak	Sigma
Range (cm)	30.159 ± 0.001	1.079 ± 0.002
Energy (MeV)	108.470 ± 0.005	3.296 ± 0.006
Momentum (MeV/c)	205.00 ± 0.01	5.15 ± 0.01
Final $\pi\nu\bar{\nu}$, 3029 Events		
Range (cm)	29.98 ± 0.02	1.21 ± 0.02
Energy (MeV)	108.67 ± 0.05	3.68 ± 0.05
Momentum (MeV/c)	204.53 ± 0.07	5.54 ± 0.11

Table 6.2: Comparison of the observed and expected $K_{\pi 2}$ lineshapes.

$K_{\pi 2}$ Signal Region Cut Rejection						
Year	Momentum		Energy		Range	
	Obs.	Exp.	Obs.	Exp.	Obs.	Exp.
1989	7.5 ± 0.6	8.4 ± 0.1	38 ± 7	52 ± 2	575 ± 400	220 ± 20
1990	10.8 ± 1.0	9.6 ± 0.2	18 ± 2	36 ± 1	225 ± 100	240 ± 25
1991	8.0 ± 0.8	8.6 ± 0.1	29 ± 5	45 ± 1	200 ± 100	244 ± 11
Sum	8.9 ± 0.5	8.64 ± 0.05	26 ± 2	44.5 ± 0.7	275 ± 80	239 ± 9
Gaussian	8.3 (1.17σ)		42 (1.98σ)		232 (2.63σ)	

Table 6.3: Comparison of observed and expected rejections for the individual components of the signal region cut for $K_{\pi 2}$ backgrounds. The observed rejections, denoted as Obs., were determined from the $K^+ \to \pi^+\nu\bar{\nu}$ data. The expected values, labeled Exp., were obtained from the $K_{\pi 2}$ background study samples. The last row, labeled Gaussian, corresponds to the expected rejection based on a Gaussian detector response using resolutions determined from the background study samples and the relative position of the signal region.

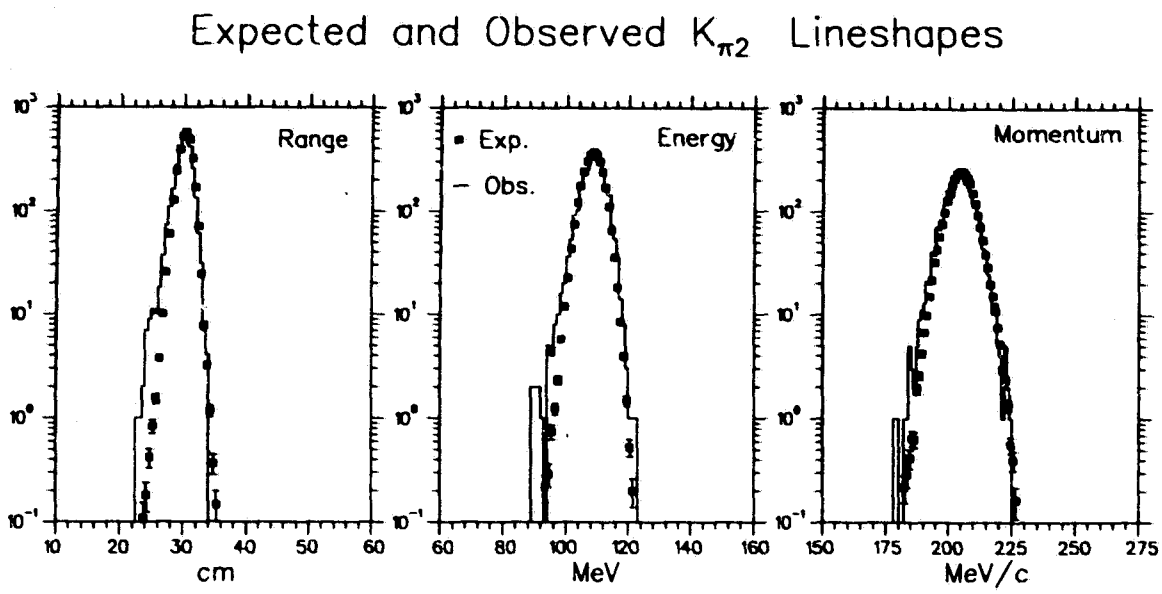

Figure 6.3: Comparison of the observed and expected $K_{\pi 2}$ background lineshapes. The number of counts in the expected distributions have been normalized to the number of observed $K_{\pi 2}$ events.

energy cut were at the same relative position as in the background studies, no events would have remained in the signal region, consistent with the expectations from the background studies. The source of the broadening in the energy distribution is not clear. There is no evidence of a tail which is suggestive of overlapped photons. Although, the source of this effect is not understood, the effect on the energy distribution is consistent with a simple Gaussian broadening.

6.2.2 Comparison of the π^0 Rejection

An estimate of π^0 rejection inefficiency, $\bar{\epsilon}_{\pi^0}$, can be obtained from the observed rate of $K_{\pi 2}$ events with and without the photon veto cuts. The value of $\bar{\epsilon}_{\pi^0}$ was estimated as,

$$\bar{\epsilon}_{\pi^0} \sim \left(\frac{N_{K\pi 2}}{N_{KT}}\right)_{\pi\nu\bar{\nu}} \times \left(\frac{N_{KT}}{N_{K\pi 2} \times A_{L2}}\right)_{\text{monitor}}, \tag{18}$$

where "$\pi\nu\bar{\nu}$" denotes the $K^+ \to \pi^+\nu\bar{\nu}$ data set, "monitor" refers to the $K_{\pi 2}$ monitor trigger samples. Because the Level 1 hextant cut was not applied to the monitor samples, a correction for the acceptance of the on-line $\pi \to \mu$ cut, A_{L2} was necessary (section 7.5.2). The $K_{\pi 2}$ monitor samples for each year were analysed with the identical cuts used in the $K^+ \to \pi^+\nu\bar{\nu}$ analysis with the exception that no explicit photon veto cuts were applied. Table 6.4 summarizes the measurements; the quoted errors are the statistical errors for $N_{K\pi 2}$

which were added in quadrature. The π^0 rejection inefficiency determined in this fashion was $\sim 2 \times 10^{-6}$ per π^0. Comparison of the $\bar{\epsilon}_{\pi^0}$ values for each year show no significant variation.

$K_{\pi 2}$ π^0 Rejection Inefficiency $\bar{\epsilon}_{\pi^0}$		
1989	1990	1991
$(2.22 \pm 0.08) \times 10^{-6}$	$(1.98 \pm 0.08) \times 10^{-6}$	$(2.13 \pm 0.09) \times 10^{-6}$

Table 6.4: Estimated $K_{\pi 2}$ π^0 rejection inefficiency.

6.2.3 Source of Non-Gaussian Events

In an attempt to understand the observed background events, a *post hoc* study examined $K_{\pi 2}$ events with only the total range satisfying the signal region cut. In this study, a clear signature for the vertex misassignment background responsible for event 1990A was observed. Approximately 10% of the $K_{\pi 2}$ background can be associated with this mechanism. Note that the $K_{\pi 2}$ background estimate was based on 7 events; therefore, it is consistent to not have observed an event of this type. It should be stressed that devising cuts using small background samples can lead to large systematic uncertainties due to fluctuations in the sample. These systematic effects are compounded when extrapolating the results to an independent sample. A cut designed to remove only 1 event in the background sample will lead to exactly the same bias that a blind analysis tries to avoid. None of the cuts utilized in this analysis were devised in such a manner.

An additional mechanism arising from target tracking errors was observed. The target range can be artificially shifted upwards for pion tracks nearly collinear with the I-counter face. The error occurs in the estimate of the intersection point with the target-I-counter edge using fitted target pion track. The intersection point is sensitive to the pion direction cosines determined from the fit, which, for pion clusters of 3 or less triangles, can be suspect. In the *a priori* $K_{\pi 2}$ background studies, no events of this type were observed.

6.2.4 Correlation with Photon Veto: Downshifting

The correlation between the photon veto and kinematic cuts arising from π^+ scattering in the target was estimated. As discussed in section 5.2.2, applying the photon veto cuts will preferentially select $K_{\pi 2}$ events where target scatters have removed the $\pi^+ - \pi^0$ collinearity. Defining the number of events with R'_{tot}, E'_{tot} and P'_{tot} simultaneously greater than the nominal $K_{\pi 2}$ peak positions (table 4.5) as N_+, the ratio

$$R_{\mathrm{PV-kin}} = \left(\frac{N_+}{N_{K\pi 2}}\right)_{\mathrm{Bgd}} \times \left(\frac{N_{K\pi 2}}{N_+}\right)_{\pi\nu\bar{\nu}},$$

where "$\pi\nu\bar{\nu}$" denotes the $K^+ \to \pi^+\nu\bar{\nu}$ data set and "Bgd" denotes the background study sample, provides an estimate of the effect of photon vetoing on the $K_{\pi 2}$ lineshape. For the 1989 and 1990 data where only the target and I and V-counter photon veto cuts were applied, $R_{\mathrm{PV-kin}} = 1.2 \pm 0.1$. For the 1991 data, where the full photon veto was applied except for the barrel veto, the measured ratio was 0.97 ± 0.08. The results are summarized in table 6.5. The 1989 and 1990 values of $R_{\mathrm{PV-kin}}$ support the conclusion that the effect of the photon veto is to decrease the relative number of N_+ events by about 20%. The 1991 result suggests that this effect upon the $K_{\pi 2}$ lineshape may be reasonably well simulated by application of a subset of the photon veto cuts. Given that the statistics of the $K_{\pi 2}$ background estimate were dominated by the 1991 data, where no difference in the relative rate of N_+ was observed, no correction to $K_{\pi 2}$ background estimate was made.

Photon Veto Correlation			
Factor	1989	1990	1991
$N_{K\pi 2}$ (Bgd)	27766	22012	117791
N_+ (Bgd)	4449	4561	20298
$N_{K\pi 2}$ ($\pi\nu\bar{\nu}$)	1142	1118	769
N_+ ($\pi\nu\bar{\nu}$)	152	189	136
$R_{\mathrm{PV-kin}}$	1.20 ± 0.10	1.22 ± 0.09	0.97 ± 0.08

Table 6.5: Effect of photon veto on the $K_{\pi 2}$ lineshape. See text for description of the quantities.

6.2.5 Conclusions

The combined $K_{\pi 2}$, Type I and Type IIa $\pi-$scat backgrounds were estimated to be 0.24 events with a 25% statistical error.[2] Ignoring possible systematic effects, observation of 2 events corresponded to a 2% probability. It is therefore unlikely that the events represented a statistical fluctuation.

If it is assumed that both events were due to $K_{\pi 2}$ decays, then their observation was not consistent with the expected $K_{\pi 2}$ background level measured in the *a priori* studies. Subsequent investigation uncovered a factor of 1.7 difference between the expected background estimated from the residual $K_{\pi 2}$ spectrum and the background study samples. Accounting for this factor resulted in a revised expectation of 0.22 ± 0.09 $K_{\pi 2}$ background events.

The 1990A event can be explained by a rare pathological target reconstruction error. The *a priori* background studies did not uncover this type of background. Comparison

[2] From the kaon decay time for the two events, it is difficult to reconcile the events with a Type II $\pi-$scat or CEX background hypothesis. Likewise their kinematics are not suggestive of a muon origin.

of the expected and the observed rejections, based on Gaussian statistics, supports the conclusion that the Gaussian component of the background was reasonably well estimated. The observation of a candidate like the 1991A event was not inconsistent with the 18% probability (accounting for the factor of 1.7) of observing a $K_{\pi 2}$ background from Gaussian effects. The systematic error in the expected $K_{\pi 2}$ background was significant; the order of an event. The estimate of the non-Gaussian background was statistics limited and was possibly underestimated by a large factor.

6.3 Residual $K_{\mu 2}$ Events

The 9 events remaining above the kinematic signal region were reasonably consistent with the expected number of events. In section 5.1, the expected number of residual events was estimated to be 4.6 ± 0.7 where the error was purely statistical. Recall that for the Poisson distribution, the width is related to the mean by $\sigma^2 = \mu$, therefore, the excess of events represents approximately a 2 sigma discrepancy. A breakdown by individual data sets, table 6.6, reveals that the bulk of the discrepancy was due to the 1989 and 1991 data sets. For the 1990 data, no events above the signal region were observed versus 1.07 ± 0.33 expected.

Residual Muon Events				
	1989	1990	1991	Sum
Expected	2.25 ± 0.50	1.07 ± 0.33	1.28 ± 0.39	4.6 ± 0.7
Observed	5	0	4	9

Table 6.6: Expected and observed number of residual muon events.

To investigate the possibility of a systematic underestimate of the $K_{\mu 2}$ type background, the PASS3 $K^+ \to \pi^+ \nu\bar{\nu}$ analyses were rerun without applying the final $\pi \to \mu \to e$ cuts. The expected and observed number of muon events remaining are given in table 6.7 for above and in the $K^+ \to \pi^+ \nu\bar{\nu}$ signal region. For each run there is evidence of a systematic excess of residual muon events in or above the signal region.

Residual Muon Events for Relaxed TD Cuts						
	1989		1990		1991	
	N_{above}	N_{BOX}	N_{above}	N_{BOX}	N_{above}	N_{BOX}
Expected	96 ± 10	1.9 ± 0.3	49 ± 12	0.6 ± 0.6	56 ± 12	0.8 ± 0.2
Observed	119	7	95	3	70	3

Table 6.7: Expected and observed number of residual muon events before application of the final TD $\pi \to \mu \to e$ cuts.

6.3.1 1989 Data Set

The discrepancy in the final number of events observed above the signal region in the 1989 data can be explained by a systematic difference between the range stack stopping distributions. Figure 6.4a shows the stopping layer versus the stopping sector distributions for the muon data set used to measure the rejection of the final TD cuts (section 5.1.1); figure 6.4b is for residual muon events before application of the final TD cuts for the $K^+ \rightarrow \pi^+\nu\overline{\nu}$ data. The stopping counter distributions are different. The distorted stopping distribution in figure 6.4b was due to hextants and/or counters with poorer on-line $\pi \rightarrow \mu$ rejection.[3]

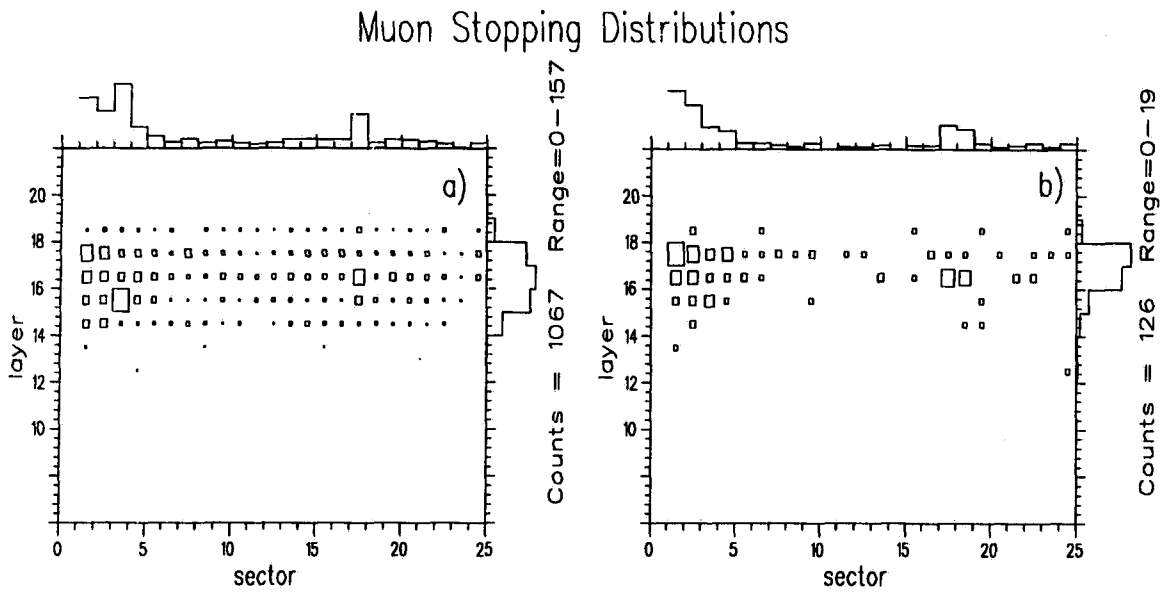

Figure 6.4: Muon background stopping distributions before final TD cuts for the 1989 data. Figure a) shows the stopping distribution of events used to measure the rejection of the final TD cuts. Figure b) is for muon events in the $K^+ \rightarrow \pi^+\nu\overline{\nu}$ sample before application of the final TD cuts. Note that the stopping layer distribution is different and the large excess of events in sector 3, layer 15 in figure a).

The major difference in the stopping layer distributions was a large excess of events in sector 3, layer 15 for the TD study data. This excess is more apparent in figure 6.5, where the number of counts shown has been suppressed with the actual count being 157 events. The excess events are of the tail fluctuation type. The observed excess most likely led to a systematic overestimate of the TD rejection, hence, an underestimate of the expected number of residual events. If the excess number of events in sector 3, layer 15 is ignored,

[3]The 1989 on-line TD cut employed a single pulse height to area calibration. A number of counters exhibited significantly worse than average rejection.

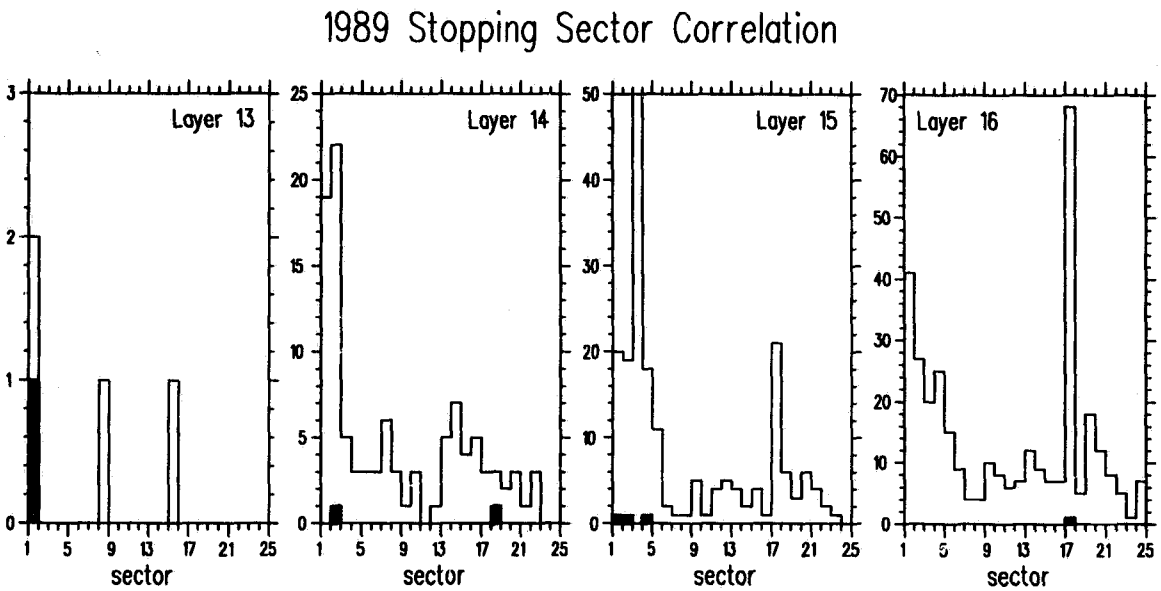

Figure 6.5: Stopping sector distributions for events passing the standard $\pi \rightarrow \mu \rightarrow e$ cuts for the 1989 data. The solid histogram entries are for the events in the signal region before application of the final $\pi \rightarrow \mu \rightarrow e$ cuts for the $K^+ \rightarrow \pi^+\nu\bar{\nu}$ muons. Note the apparent correlation with sectors known to have problems with tail fluctuation backgrounds. The number of counts in layer 15, sector 3 has been suppressed; the actual count is 157 events.

the corresponding TD rejection is a factor of 1.15 worse. For the 1989 data set, the revised number of expected $K_{\mu 2}$ type events and their associated statistical errors after all cuts is 0.05 ± 0.01 and 2.6 ± 0.6 for in and above the signal region, respectively.

There is strong evidence that the excess events observed in the signal region, before application of the final TD cuts, were due to problems with individual TD channels or counters. It can be seen in figure 6.5, that of the 7 events in the signal region, 6 of them are associated with individual counters or hextants that were known to exhibit problems with fluctuation type backgrounds. It should be stressed that the muons in the signal region and the muons used to measure the TD rejection are from orthogonal data samples. Note that the most powerful cut against the tail fluctuation background, the multivariate analysis based TD_ANAL cut, has not been applied.

6.3.2 1990 Data Set

The calculation of the $K_{\mu 2}$ type background for the 1990 data set utilized samples derived from the monitor triggers. The background estimate required a value for the on-line TD rejection, $R_{TD}^{\text{on-line}}$, which was evaluated using the same monitor data. It was observed that $R_{TD}^{\text{on-line}} = 21.4 \pm 0.9$ from inspection of the trigger information for reconstructed events

before application of the Level 1 refined range and Level 1.5 energy cuts. The measured value was consistent with the rejection observed on-line for $K^+ \to \pi^+\nu\overline{\nu}$ triggers at the time the data was acquired. The value of $R_{TD}^{\text{on-line}}$ based on the remaining 84 events in the kinematic background study sample (table 5.4) was observed to be 9 ± 3. This suggests a correlation between the on-line $\pi \to \mu$ cut and the kinematic rejection. The source of this correlation is not clear. Note that this effect is not present for the 1989 and 1991 data as their respective background estimates were performed using data with the on-line cut already applied. If the background level for the 1990 data is recalculated using the lower value for $R_{TD}^{\text{on-line}}$, then the expected and observed number of $K_{\mu 2}$ type events above and in the $K^+ \to \pi^+\nu\overline{\nu}$ signal region is consistent before and after application of the final TD cuts.

For the 1990 data set, the revised estimates for the expected number of residual $K_{\mu 2}$ type events, after all cuts, were 0.03 ± 0.03 and 2.5 ± 1.2 for in and above the $K^+ \to \pi^+\nu\overline{\nu}$ signal region, respectively. Similarly, for the number of residual events, before application of the final TD cuts, the revised estimates were 117 ± 47 and 1.4 ± 1.4 events for above and in the signal region, respectively. The errors on the estimates are purely statistical.

6.3.3 1991 Data Set

The 4 residual muons in the 1991 data set shared the feature that all are associated with pion decay times of less than 9 ns. This is inconsistent with the background study expectation of a flat timing distribution. Events with small t_μ^{av} are usually associated with TD pulse tail fluctuations or hardware problems.

The fraction of events with $t_\mu^{av} < 22$ ns, from the 1991 TD background studies, compared to that observed in the $K^+ \to \pi^+\nu\overline{\nu}$ data before application of the final TD cuts, did not exhibit any discrepancy. This suggests that the rejection of the tail fluctuation background was systematically underestimated. A similar mechanism to that observed in the 1989 data may be responsible; however, the limited statistics preclude a definite conclusion.

6.3.4 Conclusions

Based on the further studies of the $K_{\mu 2}$ type background and the observation of two sources of possible systematic effects, the expected number of $K_{\mu 2}$ type background events was reevaluated. The revised number of expected events in the signal region for the combined data set was 0.10 ± 0.03, where the error is purely statistical. The revised number of expected residual events above the $K^+ \to \pi^+\nu\overline{\nu}$ signal region was 6.4 ± 1.4, where again the error is statistical. The revised estimates are given in table 6.8.

Revised $K_{\mu 2}$ Type Background Estimates				
	1989	1990	1991	Sum
N_{bgd}	0.05 ± 0.01	0.03 ± 0.03	0.018 ± 0.007	0.10 ± 0.03
N_{above}	2.6 ± 0.6	2.5 ± 1.2	1.28 ± 0.39	6.4 ± 1.4

Table 6.8: Revised $K_{\mu 2}$ type background estimates. The "sum" column is the combined estimate over the three data sets. All errors quoted are purely statistical.

6.4 Revised Background Estimates

Based on the study of the residual events in the final spectrum, the expected total number of background events expected in the $K^+ \rightarrow \pi^+ \nu \overline{\nu}$ signal region has been revised. The new estimates are summarized in table 6.9 and are denoted by an $*$. All errors quoted are purely statistical. The revised total number of expected background events from all sources studied was 0.62 ± 0.12. The error was obtained by summing the individual errors in quadrature and is purely statistical in nature. The estimated total background is for the signal region range cut at 33 cm.

Estimated Background Levels		
Background	Combined 1989-1991	
$K_{\mu 2}$ Type	0.10 ± 0.03	$*$
$K_{\pi 2}$	0.22 ± 0.09	$*$
Type I $\pi-$scat	0.05 ± 0.04	
Type II $\pi-$scat	0.10 ± 0.03	
Type IIa $\pi-$scat	0.06 ± 0.02	
CEX $K_{\mu 3}$	0.07 ± 0.05	
CEX K_{e3}	0.005 ± 0.005	
Total	0.62 ± 0.12	$*$

Table 6.9: Revised summary of background estimates. Quantities denoted by an $*$ have been revised. All errors quoted are purely statistical.

Chapter 7

Determination of the Sensitivity

Render unto Caesar those things that are Caesar's...

- Matthew 22:21

7.1 Overview

In this section, the measurement of the $K^+ \to \pi^+\nu\overline{\nu}$ sensitivity is described. The measurement requires that two factors be evaluated: one, the detection efficiency for $K^+ \to \pi^+\nu\overline{\nu}$ per stopped kaon and, two, the total number of stopped kaons examined by the spectrometer or the kaon flux normalization. The product of the kaon flux with the $K^+ \to \pi^+\nu\overline{\nu}$ acceptance gives the overall $K^+ \to \pi^+\nu\overline{\nu}$ sensitivity. The measurement of the acceptance for $K^+ \to \pi^+X^0$ where X^0 is any weakly interacting massless particle is also described. The term "rare decay modes" refers to both $K^+ \to \pi^+\nu\overline{\nu}$ and $K^+ \to \pi^+X^0$.

It is a standard practice to "normalize" a branching ratio measurement or an upper limit to that of a well known decay mode of similar topology. Good examples of this are the measurement of $K_L^0 \to \mu^+\mu^-$ branching ratio, and the upper limit for $K_L^0 \to \mu e$ where, the acceptance relative to the decay $K_L^0 \to \pi^+\pi^-$ is computed [54]. In the case of $K^+ \to \pi^+\nu\overline{\nu}$, taking into account the design of the detector, there is no suitable candidate to normalize the sensitivity. Although the $K_{\mu 2}$ decay has a similar single-charged-track topology with no other observable energy in the detector, the effects of nuclear interactions and the pion detection efficiency must be corrected for separately. The $K_{\pi 2}$ decay is not suitable because of associated photons from π^0 decay. The $K^+ \to \pi^+\nu\overline{\nu}$ acceptance was measured by computing the acceptance of individual cuts. The product of the individual acceptances defined the overall acceptance.

The $K^+ \to \pi^+\nu\overline{\nu}$ acceptance was calculated for kaons decaying at rest; therefore, the fraction of kaons entering and stopping within the target fiducial volume was required. The kaon stopping fraction, defined as f_s, was determined by normalizing the observed

rate of tagged $K_{\mu 2}$ events to the known $K_{\mu 2}$ branching ratio. To verify the kaon flux normalization, the $K_{\pi 2}$ branching ratio was measured for each data set. The $K_{\pi 2}$ branching ratio measurement also served as a cross check for the measured acceptance of the $\pi \rightarrow \mu \rightarrow e$ pion identification cuts, and the reliability of the Monte Carlo to simulate the effects of pion interactions and decay-in-flight.

As in the case of background estimates, an attempt has been made to reduce the reliance on Monte Carlo simulation to a minimum. Where possible, acceptance factors were determined using real data. The acceptance measurements can be broken down into 4 categories which are classified according to the data type used:

1. Monte Carlo: Losses for trigger, fiducial volume and kinematic signal region cuts, nuclear interactions and decay-in-flight.

2. $K_{\mu 2}$: Losses for track reconstruction, accidentals, beam counter and event quality cuts.

3. $K_{\pi 2}$: Losses for pion dependent event quality cuts, Level 1.5 energy trigger.

4. π-scat: TD $\pi \rightarrow \mu \rightarrow e$ and kinematic particle identification cuts.

Uniformly sampled $K_{\mu 2}$, $K_{\pi 2}(1)$, π-scat monitor triggers spanning the same range of $K^+ \rightarrow \pi^+ \nu \overline{\nu}$ data runs were employed. The sample selection ensured that variations in detector performance and in beam characteristics were accounted for. The $K_{\pi 2}$ and $K_{\mu 2}$ monitor data samples utilized are summarized in table 7.1.

The acceptances for individual cuts were measured using the "counting method". In the counting method, the acceptances of the cuts are computed sequentially with the cuts already applied acting as selection criteria for the latter cuts. For example, $K_{\mu 2}$ events were selected using tight kinematic constraints to measure the acceptance of the photon veto cuts. The $K_{\mu 2}$ triggers passing the photon veto cut were then used to measure various event quality cuts. A beam related accidental can cause an event to fail an event quality or photon veto cut. Measuring the event quality cut acceptance after applying the photon veto cuts ensures that the losses are not double counted. There were two acceptance factors computed using an alternative method. They were the drift chamber/range stack (DC/RS) reconstruction efficiency and the TD $\pi \rightarrow \mu$ fitting acceptance. The acceptance of each individual cut was determined for each of the 1989, 1990 and 1991 data sets.

7.2 Acceptance: Monte Carlo Based Measurements

A Monte Carlo calculation was used to determine the following factors:

$K_{\pi 2}$ and $K_{\mu 2}$ Monitor Data Samples				
Trigger	Quantity	1989	1990	1991
$K_{\pi 2}(1)$	Trigger prescale	20480	65536	131072
	Off-line prescale	15	5	1
	Net K_{Tlive}	570313	603942	1103973
	Events Analysed	86212	95043	166713
$K_{\mu 2}$	Trigger prescale	131072	131072	131072
	Off-line prescale	3	3	3
	Net K_{Tlive} (N_{KT}^{ps})	445556	503285	367991
	Events Analysed	93108	113655	73766
$K_{\pi 2}$-$K_{\mu 2}$ prescale ratio f_{ps}		25/32	5/6	1/3

Table 7.1: The monitor trigger data used to measure the kaon stopping fraction and $K_{\pi 2}$ branching ratio.

- Losses from solid angle and range cuts in the trigger.
- Losses from pions stopping in dead material and wrong stopping counter assignment.
- Acceptance of the DIPANG, LAYER14 and RS_Z2_D fiducial volume cuts.
- Losses from nuclear interactions and in-flight decays.
- Acceptance of the $K^+ \rightarrow \pi^+ \nu\overline{\nu}$ signal region BOX cut.

The Monte Carlo based acceptances were determined using "perfect" pions. Two sets of data were generated for each rare decay mode and year; one set was generated with pion nuclear interactions and decay turned off, the other data set was generated with these effects turned on. Nuclear interactions and pion decay-in-flight can cause an event to fail a number of different selection criteria. Their overall effect was estimated separately. This was done by comparing the rate of rare decay events surviving the full analysis with the effects "turned on", to the rate with the effects "turned off". The Monte Carlo data was analysed using the same cuts applicable to real data. For the data generated with pion decays turned off, the nominal 4 MeV decay muon energy was not subtracted from the stopping counter energy.

7.2.1 UMC: The E-787 Monte Carlo

The E-787 Monte Carlo simulation program, UMC, was a stand-alone program used to generate kaon decays. The data was formatted so as to be transparent to the standard KOFIA analysis with some minor differences. The primary kaon beam and beam counters were not simulated, because, it is more efficient and realistic to use the observed kaon

stopping distribution determined from real data. To simulate the kaon energy deposition in the target, the kaon was "backed up" and given enough kinetic energy, $\sim$ 50 MeV, to reach the chosen stopping position. The kaon was forced to decay at rest according to the pre-selected decay mode. Particles from the kaon decay were placed on the "stack" and individually propagated until they came to rest by dE/dx energy loss, decayed in-flight or were absorbed in a nuclear interaction. The simulation of electromagnetic showers of photons and electrons was performed using EGS [55]. Nuclear interactions were simulated using measured nuclear cross sections for pion and kaon elastic, inelastic and pseudo-elastic interactions [56]. Particles with finite lifetimes were allowed to decay. The by-products of nuclear interactions and particle decays were added to the "stack". During the event generation, the energy and timing information of hits in individual counters was recorded. The TD based pulse shape information was not simulated since real data could be used instead.

The Level 0 trigger was simulated by applying the same on-line "discriminator" threshold to individual counters and by requiring the same logic. The Level 1 refined range trigger simulation was performed using RSPC and target responses determined using real data. The higher level triggers, Level 1.5 and Level 2, were not simulated in the Monte Carlo as their efficiencies were estimated using real data.

The Monte Carlo data generated is summarized in table 7.2. For each data set, 25K events passing the trigger requirements were generated. The $K^+ \to \pi^+ X^0$ data was generated assuming a massless X^0. For data generated with pion decay enabled, the muon was also allowed to decay. The $K_{\mu 2}$ data was also generated with muon decay enabled. The UMC based rare decay acceptances were evaluated using the samples with pion decay and nuclear interactions turned off.

7.2.2 Trigger Acceptance

The trigger acceptance factors were extracted from the UMC job summary statistics. The Level 0 trigger cuts evaluated were the solid angle acceptance of the $(T \cdot A)$ requirement for stopped kaons, and the acceptance of the stopping layer cut which required that the charged track make it to layer B and stop before layer 19. The Level 1 trigger acceptances include the efficiency of the layer 11 requirement and the fraction of tracks satisfying the Level 1 refined range cut. The factors are summarized in tables 7.4 and 7.5 for $K^+ \to \pi^+ \nu\overline{\nu}$ and $K^+ \to \pi^+ X^0$, respectively. The definitions of the trigger are summarized in table 7.3. Differences in the trigger acceptance between $K^+ \to \pi^+ \nu\overline{\nu}$ and $K^+ \to \pi^+ X^0$are due to losses from requiring the track reach layer 11 for $K^+ \to \pi^+ \nu\overline{\nu}$. Factoring out the solid angle, the trigger accepts 40% of the $K^+ \to \pi^+ \nu\overline{\nu}$ pion spectrum.

Data Generated for UMC Based Efficiencies					
Decay	Trigger	N_{Kstop}			Comments
		1989	1990	1991	
$K^+ \to \pi^+\nu\overline{\nu}$	$\pi\nu\overline{\nu}$ L1	238378	238279	238577	NI, DIF, muon decay
$K^+ \to \pi^+\nu\overline{\nu}$	$\pi\nu\overline{\nu}$ L1	152818	151684	150473	no NI or DIF
$K^+ \to \pi^+X^0$	$\pi\nu\overline{\nu}$ L1	112262	111959	113456	NI, DIF, muon decay
$K^+ \to \pi^+X^0$	$\pi\nu\overline{\nu}$ L1	66115	66216	66975	no NI or DIF
$K_{\pi 2}$	Level 0	65954	65783	66235	NI, DIF, muon decay
$K_{\mu 2}$	Level 0	55560	55641	55724	muon decay

Table 7.2: UMC data generated for efficiency measurements. N_{Kstop} denotes the number of stopped kaons in the target. NI denotes nuclear interactions and DIF, decay-in-flight. The π^+X^0 data was generated for massless X^0. The "Level 0" trigger required an event to satisfy either the $K_{\pi 2}$ or $K_{\mu 2}$ Level 0 requirements.

Trigger Efficiency Definitions	
Quantity	Definition
Level 0 $T \cdot A$	$K_{stop} \cdot (T \cdot A)/K_{stop}$
Level 0 μ-veto, B	$(B \leq S_L \leq 18)/(T \cdot A)$
Level 1 Layer 11	$R11+/(B \leq S_L \leq 18)$
Level 1 Mask	$L1_{\text{mask}}/Q_{\text{single-hit}}$

Table 7.3:

$K^+ \to \pi^+\nu\overline{\nu}$ Trigger Efficiency			
Quantity	1989	1990	1991
Level 0 $T \cdot A$	0.4081 ± 0.0013	0.4068 ± 0.0013	0.4102 ± 0.0013
Level 0 μ-veto, B	0.8268 ± 0.0015	0.8273 ± 0.0015	0.8292 ± 0.0015
Level 1 Layer 11	0.5377 ± 0.0022	0.5405 ± 0.0022	0.5426 ± 0.0015
Level 1 Mask	0.9793 ± 0.0009	0.9784 ± 0.0009	0.9762 ± 0.0010
$A_{Trig}^{\pi\nu\nu}$	0.1777 ± 0.0019	0.1780 ± 0.0019	0.1802 ± 0.0019

Table 7.4:

$K^+ \to \pi^+X^0$ Trigger Efficiency			
Quantity	1989	1990	1991
Level 0 $T \cdot A$	0.4513 ± 0.0019	0.4521 ± 0.0019	0.4535 ± 0.0019
Level 0 μ-veto, B	0.9979 ± 0.0003	0.9986 ± 0.0003	0.9979 ± 0.0003
Level 1 Layer 11	0.9971 ± 0.0003	0.9974 ± 0.0003	0.9971 ± 0.0002
Level 1 Mask	0.9182 ± 0.0017	0.9159 ± 0.0017	0.9082 ± 0.0018
$A_{Trig}^{\pi X}$	0.4123 ± 0.0043	0.4124 ± 0.0043	0.4078 ± 0.0042

Table 7.5:

7.2.3 Acceptance of Off-line Cuts

The analysis applied to determine the acceptance of the off-line cuts consisted of the complete set of cuts applicable to Monte Carlo data. Pions were required to stop in active scintillator material. Pions stopping in the RSPC material will not satisfy the $\pi \to \mu$ decay requirements. The $K^+ \to \pi^+ X^0$ decay mode has slightly lower acceptance because the stopping distribution peaks at the outer layer RSPC location. The condition that the off-line stopping hextant agree with the true stopping hextant was imposed. The true stopping region of the pion was recorded at the time of event generation. The measurement of the $\pi \to \mu \to e$ detection acceptance assumed that the stopping hextant was correct; therefore, the loss was estimated separately.

The acceptance of the fiducial volume cut, RS_Z2_D, was estimated from the fraction of rare decays passing the kinematic signal region cut, and which stopped beyond layer 14 with $|\cos\theta_D| > 0.30$. The correction for outer layer RSPC efficiency and z cut was determined from the $\check{C}_\pi$-tagged beam pion samples. The outer layer RSPC efficiency varied from 0.940 to 0.963. The acceptances of the remaining off-line fiducial volume cuts were determined by the usual counting method.

The acceptance of the signal region BOX cut was evaluated for a total range cut of

$$34 < R'_{tot} < 40 \text{ cm}.$$

Movement of the cut from 33 to 34 cm resulted in an 13% loss of acceptance. The Monte Carlo based acceptance measurements are summarized in tables 7.6 and 7.7 for $K^+ \to \pi^+ \nu\overline{\nu}$ and $K^+ \to \pi^+ X^0$, respectively.

7.2.4 Pion Nuclear Interactions and Decay

The loss arising from nuclear interactions and decay-in-flight was defined as,

$$A_{\text{Nuc/DIF}} = \left(\frac{N_{pass}}{N_{\text{KStop}}}\right)_{\text{ON}} \times \left(\frac{N_{\text{KStop}}}{N_{pass}}\right)_{\text{OFF}},$$

where N_{pass} was the number of rare decay triggers passing the off-line analysis that were generated with nuclear interactions and pion decay turned "ON" and "OFF". For the "ON" samples, the pion was required to come to rest by normal dE/dx loss. The condition was imposed using information recorded at the time of event generation. Cuts whose efficiencies were measured using real data with tagged pions were not applied. The results are summarized in tables 7.8 and 7.9 for $K^+ \to \pi^+ \nu\overline{\nu}$ and $K^+ \to \pi^+ X^0$, respectively. The loss from nuclear interactions is larger for the $K^+ \to \pi^+ X^0$ decay because of higher pion momentum and the sharply rising total pion cross section.

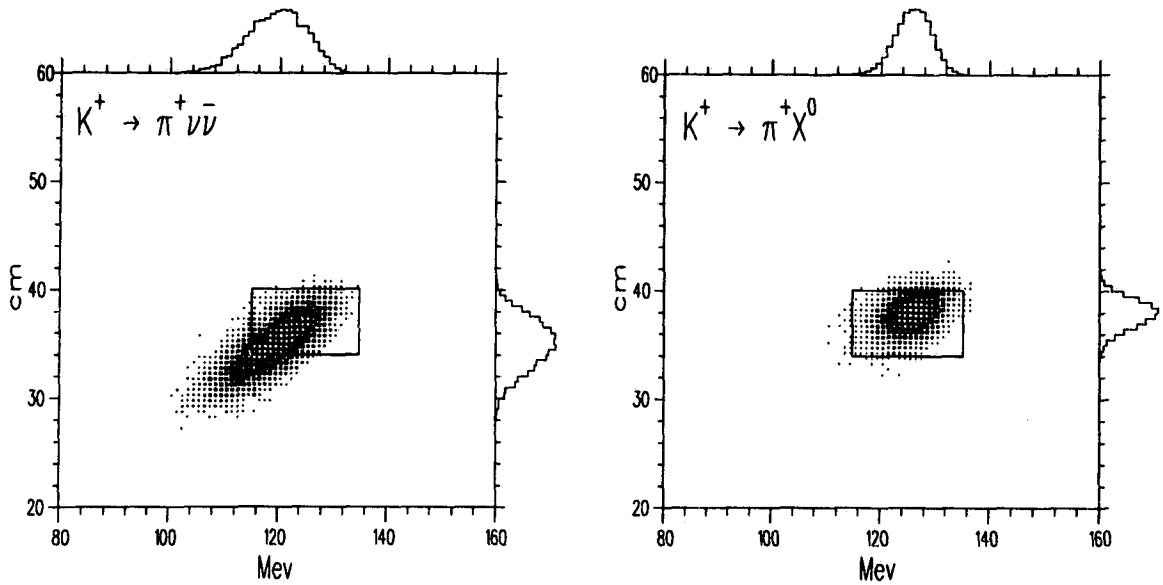

Figure 7.1: Range vs. energy for rare decay modes after application of the $211 < P'_{tot} < 243$ MeV/c momentum cut. The energy and range signal regions are enclosed by the rectangle.

Monte Carlo Based $K^+ \to \pi^+\nu\bar{\nu}$ Acceptances			
Cut	1989	1990	1991
STMED	0.9748 ± 0.0010	0.9755 ± 0.0010	0.9754 ± 0.0010
USTPHEX	0.9930 ± 0.0005	0.9928 ± 0.0005	0.9941 ± 0.0005
STLAY_RS	1.0000 ± 0.0000	1.0000 ± 0.0000	1.0000 ± 0.0000
DIPANG	0.9899 ± 0.0006	0.9929 ± 0.0005	0.9900 ± 0.0006
LAYER14	0.9836 ± 0.0008	0.9845 ± 0.0008	0.9837 ± 0.0008
RS_Z2_D	0.997 ± 0.009	0.996 ± 0.009	0.998 ± 0.009
4SEC	1.0000 ± 0.0000	1.0000 ± 0.0000	1.0000 ± 0.0000
BOX	0.3244 ± 0.0035	0.3366 ± 0.0036	0.3319 ± 0.0036
$A^{\pi\nu\bar{\nu}}_{UMC}$	0.3047 ± 0.0046	0.3173 ± 0.0048	0.3129 ± 0.0047

Table 7.6: Monte Carlo based $K^+ \to \pi^+\nu\bar{\nu}$ efficiency measurements. The STMED cut required the pion to stop in scintillator. The USTPHEX required the true stopping hextant to agree with that found in the off-line tracking.

Monte Carlo Based $K^+ \to \pi^+ X^0$ Acceptances			
Cut	1989	1990	1991
STMED	0.9540 ± 0.0013	0.9548 ± 0.0013	0.9553 ± 0.0013
USTPHEX	0.9935 ± 0.0005	0.9942 ± 0.0005	0.9934 ± 0.0005
STLAY_RS	1.0000 ± 0.0000	1.0000 ± 0.0000	1.0000 ± 0.0000
DIPANG	0.9841 ± 0.0008	0.9868 ± 0.0007	0.9872 ± 0.0007
LAYER14	0.9591 ± 0.0013	0.9629 ± 0.0013	0.9649 ± 0.0012
RS_Z2_D	0.995 ± 0.009	0.994 ± 0.009	0.996 ± 0.009
4SEC	1.0000 ± 0.0000	1.0000 ± 0.0000	1.0000 ± 0.0000
BOX	0.9344 ± 0.0019	0.9485 ± 0.0018	0.9377 ± 0.0020
$A_{UMC}^{\pi X}$	0.8317 ± 0.0088	0.8503 ± 0.0090	0.8443 ± 0.0089

Table 7.7: Monte Carlo based $K^+ \to \pi^+ X^0$ efficiency measurements. The STMED cut required the pion to stop in scintillator. The USTPHEX required the true stopping hextant to agree with that found in the off-line tracking.

Nuclear Interaction and Decay-in-Flight Effects for $K^+ \to \pi^+ \nu\bar{\nu}$						
	1989		1990		1991	
Factor	Off	On	Off	On	Off	On
N_{Kstop}	152818	238378	151684	238279	150473	238577
N_{pass}	6458	5039	6792	5124	6687	4947
$A_{\text{Nuc/DIF}}$	0.500 ± 0.009		0.480 ± 0.009		0.467 ± 0.009	

Table 7.8: Acceptance losses from nuclear interactions and decay-in-flight for $K^+ \to \pi^+ \nu\bar{\nu}$. The columns labeled "On" and "Off" denote whether nuclear interactions and pion decay were turned on.

Nuclear Interaction and Decay-in-Flight Effects for $K^+ \to \pi^+ X^0$						
	1989		1990		1991	
Factor	Off	On	Off	On	Off	On
N_{Kstop}	66115	112262	66216	111959	66975	113456
N_{pass}	16348	12909	16778	13211	16584	13111
$A_{\text{Nuc/DIF}}$	0.462 ± 0.005		0.466 ± 0.005		0.467 ± 0.005	

Table 7.9: Acceptance losses from nuclear interactions and decay-in-flight for $K^+ \to \pi^+ X^0$. The columns labeled "On" and "Off" denote whether nuclear interactions and pion decay were turned on.

7.3 Acceptance: $K_{\mu 2}$ Based Measurements

The efficiencies of two major classes of analysis and trigger cuts were measured using $K_{\mu 2}$ monitor triggers. The single charged track topology of the $K_{\mu 2}$ decay makes it an excellent candidate for measuring reconstruction efficiencies and accidental losses. It possible to obtain a relatively clean $K_{\mu 2}$ sample with simple trigger requirements because of the large separation in range between $K_{\mu 2}$ and $K_{\pi 2}$. Essentially all tracks reaching the outermost layers of the range stack will be a $K_{\mu 2}$. [1]

7.3.1 Track Reconstruction

Before performing measurements, further trigger requirements were imposed off-line:

- the Level 0 delayed coincidence, and
- Level 0 layer 21 charged track veto, $(\overline{21_{CT}})$.

The I-counter requirement in the Level 0 delayed coincidence selected decays originating from within the target fiducial volume. The Level 0 Layer 21 cut restricted the charged track to remain within the range stack, thereby ensuring the integrity of the range and energy measurements. The surviving events were then prescaled in software by a factor of 3 to reduce the data to a manageable size.

The target tracking efficiency (TARGET cut) was evaluated first. Target tracking losses were due primarily to accidentals confusing the pattern recognition. The drift chamber reconstruction efficiency was measured by comparing the number of events in the $K_{\mu 2}$ energy peak before and after the DC track fit and full RS reconstruction. The track energy was computed from the sum of the range-stack and target track segments. The ADC based RS track finding algorithm was used. The target/RS energy sum was fit to a Gaussian distribution in the range $115 < E < 165$ MeV with a flat background term before and after the full DC/RS reconstruction. The tracking efficiency was defined as the ratio of counts in the $K_{\mu 2}$ peaks. The track energy distributions before and after the DC/RS reconstruction are shown in figure 7.2. The DC/RS tracking efficiency was corrected for the inefficiency of the ADC based RS tracking using $K_{\mu 2}$ triggers with momentum $220 < P_{tot} < 248$ MeV/c. The RS ADC tracking acceptance was typically 0.9975 for each of the three data sets. The events passing the DC/RS reconstruction were then used to evaluate the track time reconstruction efficiency of the range stack and target, the TRKTIM and TICTG cuts, respectively. The combined reconstruction efficiency was defined as A_{recon}. A summary of the reconstruction measurements is given in table 7.10.

[1] Recall that only other common kaon decay modes with range greater than the $K_{\pi 2}$ are $K_{\mu 3}$ and $K_{\mu 2\gamma}$. Both are suppressed by a factor of 100 by the low branching ratio and/or phase space suppression.

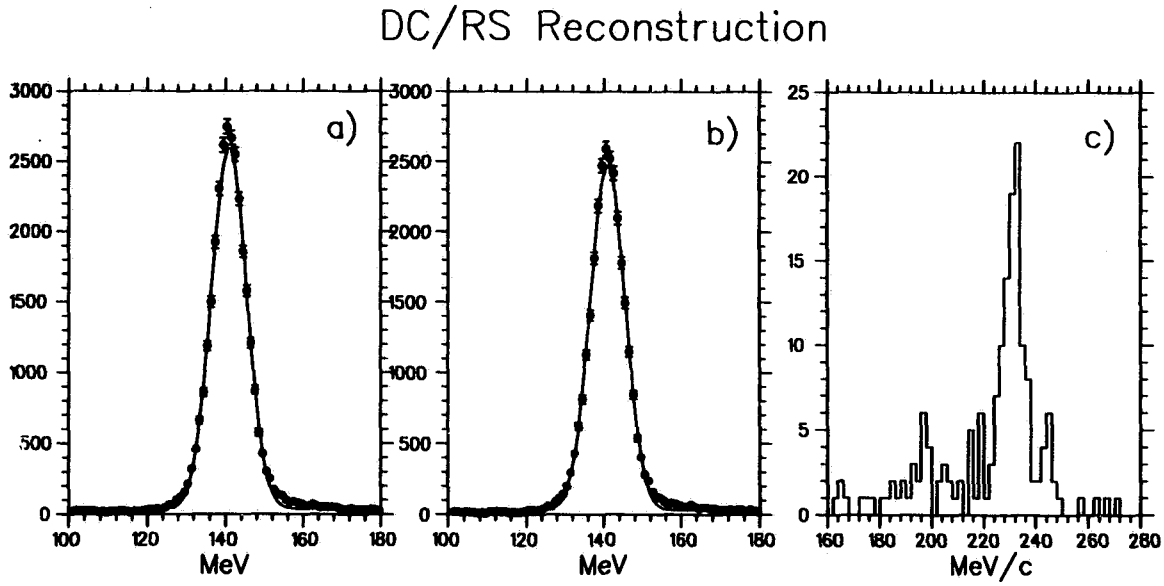

Figure 7.2: Range Stack and target energy sums for $K_{\mu 2}$ triggers for a) before the DC/RS reconstruction and b) passing the DC/RS reconstruction showing the fits used to normalize the number of $K_{\mu 2}$ events in the peak. Figure c) shows the total momentum for DC tracks without an associated RS track.

Reconstruction Efficiency						
Cut	1989		1990		1991	
	N_{ex}	Acceptance	N_{ex}	Acceptance	N_{ex}	Acceptance
TARGET	28599	0.9831 ± 0.0008	34450	0.9819 ± 0.0007	19970	0.9877 ± 0.0008
DC/RS	-	0.851 ± 0.008	-	0.946 ± 0.012	-	0.950 ± 0.016
TRKTIM	23595	0.9999 ± 0.0001	31447	0.9988 ± 0.0002	18220	0.9993 ± 0.0002
TICTG	23593	0.9981 ± 0.0003	31409	0.9988 ± 0.0002	18208	0.9982 ± 0.0003
A_{recon}	0.835 ± 0.008		0.927 ± 0.012		0.936 ± 0.016	

Table 7.10: Summary of the charged track reconstruction efficiencies determined from $K_{\mu 2}$ data. A_{recon} is the overall reconstruction efficiency.

7.3.2 Photon Veto, Trigger Setup and Event Quality

The basic reconstruction cuts were not sufficient to ensure a pure sample of $K_{\mu 2}$ decays. From figure 7.2, it is apparent that a residual background remained after the basic reconstruction criteria. To remove this undesired background which would result in a systematic underestimate of the acceptance, further event selection criteria were applied to tag clean $K_{\mu 2}$ decays from stopped kaons.

$K_{\mu 2}$ events were kinematically tagged using a χ^2 confidence level test for a $K_{\mu 2}$ hypothesis based on the the total range, energy and momentum. Events were required to have greater than a 5% probability for a $K_{\mu 2}$ hypothesis. The PIKTIME and PIKTIME2 delayed coincidence cuts were applied to select decays from stopped kaons. A range-momentum cut requiring a 5% probability for a muon hypothesis was also applied.[2] The off-line stopping counter was required to satisfy $11 < S_L \leq 20$ and the dip-angle cut, $|\cos\theta_D| < 0.55$, was imposed.

The $K_{\mu 2}$ based acceptance measurements are summarized in table 7.11. The combined acceptance of all cuts for reconstructed single charge track topologies, determined using $K_{\mu 2}$ triggers, was defined as A^{μ}_{SCT}. The INTIME categories PASS1 and PASS3 refer to the two stages of the off-line photon veto cuts. The trigger categories: Level 0 and Level 1 photon veto, Level 1 setup and Level 1.5 setup were evaluated by testing the corresponding trigger bit derived from the trigger words written simultaneously with the event. The Level 0 photon veto entry corresponds to the barrel veto and the endcaps. The Level 0 μ-veto corresponding to the $\overline{(19_{\rm CT} + 20_{\rm CT} + 21_{\rm CT})}$ trigger requirement was evaluated by examining RS sectors not associated with the range stack track. The loss from accidentals was not simulated within the Monte Carlo. The trigger was simulated by calculating the leading edge and pulse overlap times of the end-to-end coincidences and then strobing the resulting "logic pulse" with an appropriately offset t_{RS}. The Level 1 photon veto was the range stack hextant cut, which required no more than 2 adjacent hextants with more than 10 MeV. The Level 1 trigger setup was fraction of time that a single inner-layer RSPC hit in the correct sector was found. The Level 1 setup losses were due to inter-sector gaps, chamber inefficiencies and spurious hits. The Level 1.5 trigger setup cut required that only one $(T \cdot A)$ coincidence was found.

The remaining cuts are described in chapter 4. Event quality cuts where the pion and muon dE/dx difference could affect the acceptance were not evaluated using $K_{\mu 2}$ triggers. The B4DELC and TRS delayed coincidence cut acceptances were evaluated independently of the standard target based cuts. For future use, the overall acceptances of the beam counter cut, A_{BM}, and photon veto cuts, $A_{\bar{\gamma}}$, are given in table 7.13. The net efficiency

[2] The value of σ_{PR} used was 3.7 cm to account for the poorer range-momentum resolution for long range tracks.

$K_{\mu 2}$ Based Efficiency Measurements						
Cut	1989		1990		1991	
	N_{ex}	Acceptance	N_{ex}	Acceptance	N_{ex}	Acceptance
Selection	22109	0.7452 ± 0.0029	29605	0.7234 ± 0.0026	17078	0.7474 ± 0.0033
Photon Veto Cuts: INTIME and Trigger						
PASS1	16476	0.9442 ± 0.0018	21416	0.9571 ± 0.0014	12764	0.9327 ± 0.0022
PASS2	15556	0.9174 ± 0.0022	20497	0.8777 ± 0.0023	11905	0.8627 ± 0.0032
Level 0	14271	0.9664 ± 0.0015	17991	0.9502 ± 0.0016	10270	0.9448 ± 0.0023
L0 μ-veto	13792	0.9977 ± 0.0004	17095	0.9985 ± 0.0003	9703	0.9981 ± 0.0004
Level 1	13760	0.9903 ± 0.0008	17069	0.9885 ± 0.0008	9685	0.9829 ± 0.0013
Level 1 and 1.5 Trigger Setup						
Level 1	13626	0.8797 ± 0.0028	16872	0.8628 ± 0.0026	9519	0.8356 ± 0.0038
Level 1.5	11987	0.9979 ± 0.0004	14558	0.9975 ± 0.0004	7954	0.9987 ± 0.0004
Event Quality Cuts						
ENERK	11962	0.9882 ± 0.0010	14521	0.9869 ± 0.0009	7944	0.9848 ± 0.0014
NTRIK	11821	0.9910 ± 0.0009	14331	0.9913 ± 0.0008	7823	0.9845 ± 0.0014
TIMEKS	11715	0.9926 ± 0.0008	14206	0.9922 ± 0.0007	7702	0.9966 ± 0.0007
DPIK	11628	0.9931 ± 0.0008	14095	0.9920 ± 0.0008	7676	0.9878 ± 0.0013
KROAD	11548	0.9985 ± 0.0004	13982	0.9984 ± 0.0003	7582	0.9974 ± 0.0006
RTDIF	11531	0.9852 ± 0.0011	13960	0.9875 ± 0.0009	7562	0.9646 ± 0.0021
DCTG_XY	11360	0.9903 ± 0.0009	13785	0.9893 ± 0.0009	7294	0.9886 ± 0.0012
TGT_Z	11250	0.9933 ± 0.0008	13638	0.9944 ± 0.0006	7211	0.9958 ± 0.0008
DC_Z	11175	0.9996 ± 0.0002	13561	0.9996 ± 0.0002	7181	1.0000 ± 0.0000
Secondary Delayed Coincidence Cuts						
B4DELC	11171	0.9799 ± 0.0013	13556	0.9900 ± 0.0009	7181	0.9971 ± 0.0006
TRS	10947	0.9884 ± 0.0010	13421	0.9985 ± 0.0003	7160	0.9999 ± 0.0001
Beam Counter Cuts						
KBEAM	10820	0.9809 ± 0.0013	13401	0.9925 ± 0.0007	7159	0.9953 ± 0.0008
PIBEAM	10613	0.9872 ± 0.0011	13301	0.9793 ± 0.0012	7125	0.9951 ± 0.0008
BHTRS	10477	0.9838 ± 0.0012	13026	0.9947 ± 0.0006	7090	0.9958 ± 0.0008
B4DEDX	10307	0.9978 ± 0.0005	12957	0.9976 ± 0.0004	7060	0.9984 ± 0.0005
PISCUT	10284	0.9668 ± 0.0018	12926	0.9418 ± 0.0021	7049	0.9662 ± 0.0022
Photon Veto Cuts: Target						
TGVET	9943	0.9461 ± 0.0023	12174	0.9483 ± 0.0020	6811	0.9247 ± 0.0032
IC_E	9407	0.9898 ± 0.0010	11545	0.9973 ± 0.0005	6298	0.9903 ± 0.0012
Events Out	9311		11514		6237	
A^{μ}_{SCT}	0.5651 ± 0.0039		0.5376 ± 0.0034		0.4886 ± 0.0044	

Table 7.11: Summary of the $K_{\mu 2}$ based acceptance measurements. The combined acceptance of all the cuts was defined as A^{μ}_{SCT}. N_{ex} is the number of events examined by the corresponding cut.

of the photon veto cuts was determined by combining the individual INTIME, trigger and target cut acceptances.

7.3.3 Delayed Coincidence

The target based and Level 0 delayed coincidence cut acceptances, defined as A_{DC}, were determined as follows:

1. Remove the stopping kaon requirements from the $K_{\mu 2}$ event selection.

2. Apply the complete acceptance analysis excluding the secondary delayed coincidence cuts, B4DELC and TRS.

3. Measure the fraction passing the Level 0 and target based PIKTIME and PIKTIME2 delayed coincidence cuts.

The Level 0 cut was evaluated using the pre-recorded trigger bit. The measurement is summarized in table 7.12.

Delayed Coincidence Efficiency Measurements						
Cut	1989		1990		1991	
	N_{ex}	Acceptance	N_{ex}	Acceptance	N_{ex}	Acceptance
Level 0	12753	0.8082 ± 0.0035	15447	0.8038 ± 0.0032	8457	0.7868 ± 0.0045
PIKTIME(2)	10307	0.9346 ± 0.0024	12416	0.9403 ± 0.0021	6654	0.9352 ± 0.0030
Events Out	9633		11675		6223	
A_{DC}	0.7554 ± 0.0038		0.7558 ± 0.0035		0.7358 ± 0.0048	

Table 7.12: Delayed coincidence acceptance, A_{DC}, measurements. The PIKTIME entry includes both the PIKTIME and PIKTIME2 cuts.

Photon Veto and Beam Counter Cut Acceptances			
Factor	1989	1990	1991
$A_{\bar{\gamma}}$	0.781 ± 0.003	0.746 ± 0.003	0.689 ± 0.003
A_{BM}	0.919 ± 0.003	0.908 ± 0.003	0.951 ± 0.003

Table 7.13: Overall acceptance of the photon veto cuts, $A_{\bar{\gamma}}$ and beam counter cuts A_{BM} for individual data sets.

7.4 Acceptance: $K_{\pi 2}$ Based Measurements

7.4.1 Pion Dependent Event Quality Cuts

The target reconstruction event quality cuts, which examined the dE/dx and timing consistency, were evaluated using $K_{\pi 2}$ monitor triggers. These cuts included the TGPCA, EPIMAX, EPIBAR, EKMAX and EKBAR cuts. The combined acceptance of these cuts, including the RS_Z1 cut, was defined as A^{π}_{SCT}.

$K_{\pi 2}$ events were selected using the following cuts:

- The standard PASS1 reconstruction cuts.
- The DIPANG and STLAY_RS cuts.
- The Level 0, PIKTIME and PIKTIME2 delayed coincidence cuts.
- The TD based particle ID cuts, FITPI, TMUAV, CHITD and ELVETO.
- All non-photon veto type cuts evaluated using $K_{\mu 2}$ triggers.
- The I-counter energy and target photon veto cuts, IC_E and TGVET.

The target photon veto cut was applied to remove events with photons converting in the target, which would otherwise contribute to the cut inefficiencies.

The acceptance of the TMUBM cut, which looked for Černkov activity at the pion decay time, was evaluated using $K_{\pi 2}$ events. The π-scat monitors were not a representative sample to evaluate this cut with because of the pion Čerenkov requirement in the π-scat trigger and the prompt nature of the pion track. The $K_{\pi 2}$ events surviving the above analysis were then subjected to the ELVETO, ELVETO2 and ELCTRN cuts. The surviving events were then used to evaluate the efficiency of the TMUBM cut. The results are summarized in table 7.14. The acceptance of the TMUBM cut was included in the calculation of the overall $\pi \rightarrow \mu \rightarrow e$ detection efficiency The values of A^{π}_{SCT}, given in table 7.15, were computed using the results for the acceptance of the RS_Z1 cut (section 7.5.1).

7.4.2 Level 1.5 Trigger

The acceptance of the Level 1.5 trigger energy cut was measured using $K_{\pi 2}$ triggers. The measurement exploits mono-chromatic nature of the $K_{\pi 2}$ energy; albeit, at a lower value than the $K^+ \rightarrow \pi^+ \nu \bar{\nu}$ spectrum endpoint. The $K_{\pi 2}$ event selection criteria were:

- The standard PASS1 reconstruction cuts.
- The complete set of fiducial volume, delayed coincidence and beam counter cuts.

$K_{\pi 2}$ Based Efficiency Measurements						
Cut	1989		1990		1991	
	N_{ex}	Acceptance	N_{ex}	Acceptance	N_{ex}	Acceptance
TGPCA	3796	0.9299 ± 0.0041	4565	0.9203 ± 0.0040	6569	0.9278 ± 0.0032
EPIMAX	3530	1.0000 ± 0.0000	4201	0.9979 ± 0.0007	6095	0.9979 ± 0.0006
EPIBAR	3530	0.9938 ± 0.0013	4192	0.9843 ± 0.0019	6082	0.9806 ± 0.0018
EKMAX	3508	1.0000 ± 0.0000	4126	0.9998 ± 0.0002	5964	0.9998 ± 0.0002
EKBAR	3508	0.9949 ± 0.0012	4125	0.9966 ± 0.0009	5963	0.9948 ± 0.0009
Net	3490	0.9194 ± 0.0044	4111	0.9005 ± 0.0044	5932	0.9077 ± 0.0036
TMUBM	2620	0.9740 ± 0.0031	3084	0.9491 ± 0.0040	4447	0.9638 ± 0.0028

Table 7.14: Summary of the $K_{\pi 2}$ based acceptance measurements. N_{ex} is the number of events examined by the cut.

Acceptance for Pion Based Tracking Cuts			
Factor	1989	1990	1991
A^{π}_{SCT}	0.8543 ± 0.0053	0.8617 ± 0.0047	0.8207 ± 0.0053

Table 7.15: Combined acceptance for the tracking cuts measured using pion samples, A^{π}_{SCT}. The cuts included in this factor are TGPCA, EPIMAX, EPIBAR, EKMAX, EKBAR, and RS_Z1.

- The Level 1 hextant, target and range stack portion of the photon veto cuts.
- The TD based $\pi \rightarrow \mu \rightarrow e$ identification cuts, FITPI, TMUAV, CHITD, ELVETO, ELVETO2, and ELCTRN.
- The TGPCA cut and the range-momentum cut, RNGMOM0.

The photon veto cuts for the range stack and target were applied to avoid double counting losses already determined using $K_{\mu 2}$ events. The complete set of $K_{\pi 2}$ monitors were employed. [3] The $K_{\pi 2}$ selection resulted in 15122, 16062 and 1231 events for 1989, 1990 and 1991, respectively.

The Level 1.5 acceptance was evaluated after the signal region cut using 2 different methods. Each method was evaluated for 2 different Level 1.5 energy calibrations. The spread between the 4 measurements provided an estimate of the error. The Level 1.5 energy extracted from a data bank recorded on-line. The off-line energy, E'_{tot}, was computed as outlined in section 4.2.2. The methods were:

- Method 1: Shift the energy BOX and Level 1.5 cut to equivalent positions above the $K_{\pi 2}$ peak.

[3] For 1989 and 1990, the outputs of the first pass for the $K_{\pi 2}$ background study were utilized.

- Method 2: Position the energy BOX above the $K_{\pi 2}$ peak by an equivalent number of standard deviations using the estimated energy resolution.

The $K_{\pi 2}$ and $K^+ \to \pi^+ X^0$ peaks are separated by 18.5 MeV; therefore in method 1, the Level 1.5 acceptance was evaluated by shifting the on-line and energy BOX cuts accordingly. The corresponding energy BOX for $K_{\pi 2}$ event was,

$$135 - 18.5 = 116.5 \text{ MeV}.$$

The on-line cut applied to the Level 1.5 energy sum was 17024 counts. For the nominal calibration of 128 counts/MeV, the equivalent position of the Level 1.5 cut for $K_{\pi 2}$ events was,

$$17024 - 18.5 \times 128 = 14656 \text{ ADC counts}.$$

For a 110 count/MeV calibration, the equivalent on-line cut was 14989 ADC counts.[4]

In method 2, the relative position of the energy BOX cut was estimated using a model for the energy resolution. The energy resolutions listed in table 4.5 can be described by a function of the form $\sigma/E = A/\sqrt{E}$, where A varied from 0.33 to 0.36 for the different years. Relative to the $K_{\pi 2}$ peak, the 135 MeV BOX cut corresponds to approximately 115.3 MeV.

The acceptance of the Level 1.5 trigger was defined as:

$$A_{L15} = \frac{(\#\text{ in spectrum}) - (\#\text{ failing BOX}) - (\#\text{failing L1.5})}{(\#\text{ in spectrum}) - (\#\text{ failing BOX})}.$$

The results for the various methods and calibrations are given in tables 7.16 and 7.17 for $K^+ \to \pi^+ X^0$ and $K^+ \to \pi^+ \nu\bar{\nu}$, respectively. The $K^+ \to \pi^+ \nu\bar{\nu}$ result was obtained by moving the BOX cut in 1 MeV steps and performing a weighted bin-by-bin sum over the $K^+ \to \pi^+ \nu\bar{\nu}$ spectrum. The bin weights were determined from the true pion energy distribution after the full analysis and BOX cut.

7.5 Acceptance: π-scat Measurements

The kinematic and TD based particle identification cuts were evaluated using the pion scattering monitor triggers and the PNPS samples described in section 5.3.1.

7.5.1 Kinematic Particle Identification

The acceptance of the kinematic particle identification was measured using the $\check{C}_\pi$-tagged scattered beam pion samples. The beam pion background in the $K^+ \to \pi^+ \nu\bar{\nu}$ data was an

[4]From the peak positions of the $K_{\pi 2}$ and $K_{\mu 2}$ Level 1.5 energy distributions, calibrations of 110 and 117 counts/MeV were obtained, respectively. The variation in scales was likely due to the on-line treatment of the target ADC information and the differences in the target stopping distribution.

Level 1.5 Trigger $K^+ \to \pi^+ X^0$ Acceptance			
Method	1989	1990	1991
1 (128 cnts/MeV)	0.988 ± 0.001	0.989 ± 0.001	0.986 ± 0.003
2 (128 cnts/MeV)	0.988 ± 0.001	0.989 ± 0.001	0.986 ± 0.003
1 (110 cnts/MeV)	0.992 ± 0.001	0.993 ± 0.001	0.991 ± 0.002
2 (110 cnts/MeV)	0.992 ± 0.001	0.993 ± 0.001	0.991 ± 0.002
$A_{L1.5}^{\pi X}$	0.990 ± 0.002	0.991 ± 0.002	0.988 ± 0.004

Table 7.16: Level 1.5 energy trigger acceptance for $K^+ \to \pi^+ X^0$

Level 1.5 Trigger $K^+ \to \pi^+ \nu\bar{\nu}$ Acceptance			
Method	1989	1990	1991
1 (128 cnts/MeV)	0.992 ± 0.001	0.993 ± 0.001	0.991 ± 0.003
2 (128 cnts/MeV)	0.993 ± 0.001	0.993 ± 0.001	0.991 ± 0.003
1 (110 cnts/MeV)	0.995 ± 0.001	0.995 ± 0.001	0.994 ± 0.002
2 (110 cnts/MeV)	0.995 ± 0.001	0.995 ± 0.001	0.994 ± 0.002
$A_{L1.5}^{\pi\nu\nu}$	0.994 ± 0.002	0.994 ± 0.001	0.993 ± 0.002

Table 7.17: Level 1.5 energy trigger acceptance for $K^+ \to \pi^+ \nu\bar{\nu}$

essentially pure sample of pions that had already been subjected to extensive photon vetoing, TD based particle identification and reconstruction cuts. The Level 1 trigger requirement of an inner layer RSPC z hit insured that the quality of the range measurement would be similar to that for real $K^+ \to \pi^+ \nu\bar{\nu}$ pions. Furthermore, the resulting yield of useable pions was much greater than that obtained using π-scat monitor triggers.

The analyses are summarized in table 7.18; the combined acceptance of the kinematic particle ID cuts was defined as A_{Kin}. The inner layer RSPC z tracking cut was first applied and the acceptance evaluated. Although it is strictly not a particle identification cut; the acceptance was calculated using the $\check{C}_\pi$-tagged pion samples to properly account for the muon-pion differences. The A_{Kin} factor did not include the RS_Z1 acceptance. The range-momentum cut for 1990 was evaluated independently using the pion-scattering monitor data. The 1990 $\check{C}_\pi$-tagged sample had already had the cut applied at PASS1.

The kinematic dependence of the acceptance for the particle identification cuts was investigated. The acceptance, as a function of stopping layer, was observed to be uniform. This was intuitively expected, as the principal component analysis used in the KINPCA cut was performed for individual layers, thereby including the kinematic dependence of the resolutions.

Kinematic Particle ID Cuts						
Cut	1989		1990		1991	
	N_{ex}	Acceptance	N_{ex}	Acceptance	N_{ex}	Acceptance
RS_Z1	4533	0.9340 ± 0.0037	6823	0.9635 ± 0.0023	4181	0.9041 ± 0.0046
PHOTOV	4212	0.9554 ± 0.0032	6529	0.9701 ± 0.0021	3774	0.9671 ± 0.0029
KINPCA	4024	0.8979 ± 0.0048	6334	0.8759 ± 0.0041	3650	0.8729 ± 0.0055
RS_DEDX	3613	0.9502 ± 0.0036	5548	0.9387 ± 0.0032	3186	0.9476 ± 0.0039
RNGMOM0	3433	0.9983 ± 0.0007	-	0.9990 ± 0.0005	3019	1.0000 ± 0.0000
A_{Kin}	0.8136 ± 0.0060		0.7969 ± 0.0050		0.7999 ± 0.0065	

Table 7.18: Acceptances of the kinematic particle identification cuts. The 1990 RNGMOM0 cut was measured separately. Note that A_{Kin} does not include the RS_Z1 cut.

7.5.2 TD cuts: $\pi \rightarrow \mu \rightarrow e$ Identification

The acceptance of the TD based particle identification was measured using a clean sample of pions that have stopped in scintillator by normal dE/dx energy loss. The TD cut acceptances were evaluated using the π-scat monitor triggers selected with the following cuts:

- the Level 1 hextant cut,
- track segment reconstruction,
- a stopping layer requirement of $11 \leq S_L \leq 18$,
- the range stack INTIME photon veto cuts,
- a range stack energy cut, $E_{RS} < 127$ MeV, and,
- a 5% pion likelihood range-momentum cut.

The $\pi \rightarrow \mu$ fitting algorithm, FITPI, was applied to the events selected. The events failing were prescaled by a factor of 50 and skimmed off to a separate data stream. The events passing FITPI had the 8 ns pion lifetime cut TMUAV applied, and the survivors were used to measure the remaining TD particle identification cuts using the standard counting method.

Nuclear interactions and decay-in-flight effects preclude selection of a sufficiently clean sample using only kinematic particle identification cuts; therefore, to evaluate the acceptance of the TD fitting algorithm, an alternative to the counting method was employed. The acceptance of the FITPI and TMUAV cuts was evaluated using the "area" method [49]. The area method assumes that all of the acceptance loss is due to early $\pi \rightarrow \mu$ decays

where the secondary muon pulse is indistinguishable from the primary pion pulse. This method is schematically represented in figure 7.3. In practice, a pion can fail the fitting procedure even when the muon pulse is clearly detached. A handscanning procedure was necessary to determine the correction for the following effects:

- Accidental hits in the stopping hextant obscuring the two-pulse signature.
- Tertiary pulses from complete $\pi \rightarrow \mu \rightarrow e$ decay sequences with the electron pulse occurring within the fitting time window.
- The primary pion depositing too little energy in the stopping counter resulting in a poorly defined pulse shape.
- The primary pion depositing too much energy in the stopping counter leading to an overflow in the TD system.

The observed pion decay time distribution for events passing FITPI and TMUAV was fit to the exponential function,

$$N(t; N_A) = (N_A \times \lambda_\pi) \times e^{-\lambda_\pi t},$$

where N_A corresponds to the number of pions integrated over all lifetimes and λ_π is the pion decay rate (inverse of the mean pion lifetime). In this 1-parameter (1-P) fit, the value of N_A was allowed to vary and λ_π was constrained to the accepted value of $1/26.03$ ns^{-1}. The purity of the pion sample was verified by performing a 2-parameter (2-P) fit to the observed distribution by allowing the decay rate to vary as well. The fit results are summarized in table 7.19. The pion lifetime distribution and corresponding (2-P) fit are shown in figure 4.23 for the 1991 data.

The acceptance of the fitter, $A_{\rm TDFIT}$ was defined as,

$$A_{\rm TDFIT} = \frac{N_P}{N_A + \Delta N_A} \times \epsilon_{\mu-\rm escape},$$

where N_P was the number of events passing the FITPI and TMUAV cuts, N_A was the 1-parameter fit normalization, ΔN_A was the handscan correction to N_A, and $\epsilon_{\mu-\rm escape}$ was a correction for the stopping counter thickness.

The ΔN_A correction for missed $\pi \rightarrow \mu$ decays was determined by handscanning the prescaled events failing the FITPI cut. To enable unambiguous identification of missed pions, the search for candidate $\pi \rightarrow \mu$ decays was limited to decay times greater than 26 ns. The number passing the handscanning was then multiplied by Euler's number e, to correct for the fraction of pion lifetimes examined. The handscan correction, ΔN_A, was given by,

$$\Delta N_A = N_{HS}^{pass} \times e \times 50$$

where N_{HS}^{pass} was the number of events passing the handscan criteria, e is Euler's number and 50 was the prescale factor used to select events failing the TD fitting procedure. The handscanning corrections to N_A are summarized in table 7.19.

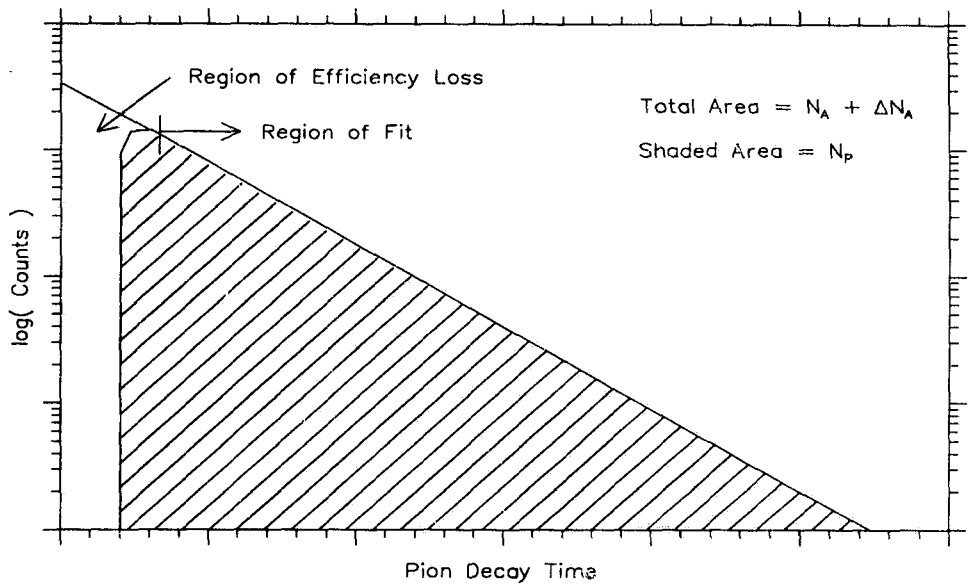

Figure 7.3: The area method of determining the $\pi \rightarrow \mu$ TD fitter acceptance. The algorithm assumes all losses are due to early $\pi \rightarrow \mu$ decays, where the muon pulse has merged with the pion pulse. The observed pion lifetime distribution, denoted by the shaded area and corresponding to N_P pions, is fit to an exponential curve to determine the total area. The accepted pion lifetime is used to constrain the fit. The fitted area, N_A, is corrected by ΔN_A, to account for delayed $\pi \rightarrow \mu$ decays missed by the TD fitter.

The muon escape correction was due to the finite volume of the stopping counter. The TD cuts require the muon to deposit approximately 2 MeV in the stopping hextant corresponding to a minimum range, $R_{min} = 1.37$ mm. Assuming a uniform pion stopping distribution within the counter (thickness t), the fraction of muons with the requisite range is,

$$\epsilon_{\mu-\text{escape}} = 1 - \frac{1}{2} \times \frac{R_{min}}{2t} = 1 - \frac{1}{2} \times \frac{1.37}{2 \times 19.5} = 0.982,$$

the factor of $1/2$ accounts for the case where a muon exits the counter and stops in $S_L + 1$. This results in the erroneous assignment of the stopping layer and the loss was accounted for separately.

The acceptances of the individual $\pi \rightarrow \mu \rightarrow e$ TD cuts and combined overall acceptances are summarized in table 7.20. The STHEX entry corresponds to the fraction of events in which the on-line and off-line determined stopping hextants agree. The L2_TD cut

TD Fitter Acceptance Factors			
Quantity	1989	1990	1991
# π selected	7486	8124	9993
N_P	4032	4233	5129
τ_π (2-P fit)	25.09 ± 0.51	25.84 ± 0.51	25.98 ± 0.44
χ^2 (2-P fit)	1.37	1.24	1.63
N_A (1-P fit)	5475 ± 88	5757 ± 90	7050 ± 100
N_{HS}	59	68	89
N_{HS}^{pass}	5	8	8
ΔN_A	678 ± 302	1084 ± 383	1084 ± 383
A_{TDFIT}	0.644 ± 0.034	0.608 ± 0.036	0.620 ± 0.032

Table 7.19: Summary of the quantities used to evaluate the $\pi \rightarrow \mu$ fitter acceptance defined in the text. τ_π is the fitted average pion lifetime. The quantities denoted by (1-P) and (2-P) refer to the number of free parameters in the fit. In the (1-P) fits, only the integrated number of counts is varied; the (2-P) fits varied the normalization and pion decay rate.

refers to the on-line $\pi \rightarrow \mu$ cut, the acceptance of which was determined by inspection of Level 2 information recorded with the event. The combined acceptance of all the TD cuts, defined as A_{TD}, was the product of the individual TD cut acceptance with A_{TDFIT}. The TD acceptance includes the acceptance of the TMUBM cut measured using $K_{\pi 2}$ events.

TD Based Particle ID Cuts						
Cut	1989		1990		1991	
	N_{ex}	Acceptance	N_{ex}	Acceptance	N_{ex}	Acceptance
RSHEX	4032	0.9821 ± 0.0021	4233	0.9778 ± 0.0023	5129	0.9772 ± 0.0021
ELVETO	3960	0.9889 ± 0.0017	4139	0.9831 ± 0.0020	5012	0.9789 ± 0.0020
ELVETO2	3916	0.9242 ± 0.0042	4069	0.9309 ± 0.0040	4906	0.9203 ± 0.0039
ELCTRN	3619	0.8226 ± 0.0064	3788	0.8603 ± 0.0056	4515	0.8396 ± 0.0055
TDFOOL	2977	0.9876 ± 0.0020	3259	0.9932 ± 0.0014	3791	0.9918 ± 0.0015
TMUBV	2940	0.9806 ± 0.0025	3237	0.9759 ± 0.0027	3760	0.9769 ± 0.0025
TD_PCA	2883	0.9501 ± 0.0041	3159	0.9307 ± 0.0045	3673	0.9515 ± 0.0035
TD_ANAL	2739	0.8346 ± 0.0071	2940	0.7949 ± 0.0074	3495	0.8189 ± 0.0065
TMUADC	2286	0.9549 ± 0.0043	2337	0.9465 ± 0.0047	2862	0.9396 ± 0.0045
PREFIT	2183	0.9995 ± 0.0005	2212	1.0000 ± 0.0000	Not applied	
CHITD	2182	0.9931 ± 0.0018	2212	0.9991 ± 0.0006	2689	0.9877 ± 0.0021
STHEX	2167	0.9700 ± 0.0037	2210	0.9751 ± 0.0033	2656	0.9597 ± 0.0038
L2_TD	2102	0.9458 ± 0.0049	2155	0.9039 ± 0.0063	2549	0.9572 ± 0.0040
Net	1988	0.4931 ± 0.0079	1948	0.4603 ± 0.0077	2440	0.4757 ± 0.0070
TMUBM	0.9740 ± 0.0031		0.9491 ± 0.0040		0.9638 ± 0.0028	
A_{TDFIT}	0.644 ± 0.034		0.608 ± 0.036		0.620 ± 0.032	
A_{TD}	0.309 ± 0.019		0.266 ± 0.016		0.284 ± 0.015	

Table 7.20: Measurement and summary of the TD $\pi \rightarrow \mu \rightarrow e$ cut acceptance factors. STHEX corresponds to the correct on-line stopping counter assignment. L2_TD is the acceptance of the on-line $\pi \rightarrow \mu$ cut.

7.6 Determination of the Flux

The unit of kaon flux for E-787 is K_{Tlive} , where "live" implies that the detector and the data acquisition were ready to accept and process a new event. Not every K_T corresponds to a kaon stopping in the target; therefore, a correction to the kaon flux is needed. This factor, f_s, is defined as the fraction of K_T that result in a kaon stopping within the fiducial volume of the target. The number of K_{Tlive} was determined from scaler data, which was recorded for each beam spill and written to the tape.

The f_s factor depended on the details of the beam distribution, degrader position and upstream detector elements. It is because of these potential uncertainties, that the kaon stopping fraction was determined by normalizing to the accepted $K_{\mu 2}$ branching ratio. Defining the stopping fraction in this way also has the advantage that potential systematic errors in the photon veto, delayed coincidence and tracking acceptances, are absorbed into f_s.

The value of f_s was calculated using,

$$f_s = \frac{\#K_{\mu 2}}{\mathrm{BR}(K_{\mu 2}) \times N_{KT}^{ps}} \times \frac{1}{A_{K\mu 2}^{MC}} \times \frac{A_{recon}^{MC}}{A_{recon}} \times \frac{1}{A_{DC}} \times \frac{1}{A_{\bar{\gamma}}} \times \frac{1}{A_{BM}}, \tag{19}$$

where $\#K_{\mu 2}$ was the number of $K_{\mu 2}$ events passing the analysis, $\mathrm{BR}(K_{\mu 2}) = 0.635$ is the accepted $K_{\mu 2}$ branching ratio, N_{KT}^{ps} was the number of kaons entering the target prescaled by the overall $K_{\mu 2}$ trigger prescale (table 7.1), $A_{K\mu 2}^{MC}$ was the Monte Carlo calculated acceptance for $K_{\mu 2}$, A_{recon} and A_{recon}^{MC} were the reconstruction efficiencies for data and Monte Carlo, respectively.

The number of $K_{\mu 2}$ events was determined using an analysis similar to the A_{SCT}^{μ} measurement. To ensure that the kaon was stopped, both on and off-line delayed coincidence requirements are imposed. Full track reconstruction and photon vetoing was performed. The stopping layer was required to satisfy $18 < S_L < 21$. A final range cut of $45 < R'_{tot} < 65$ cm was used to tag $K_{\mu 2}$ events. The analyses are summarized in table 7.21. The analyses of the Monte Carlo $K_{\mu 2}$ data and the measurement of $A_{K\mu 2}^{MC}$ and A_{recon}^{MC} are summarized in table 7.22. The same stopping layer and range cuts were applied. The total range distributions for the 1990 $K_{\mu 2}$ data and for Monte Carlo $K_{\mu 2}$ data are shown in figure 7.4.

A summary of the factors entering into the f_s measurement and the calculated f_s values are given in table 7.23. The year-to-year differences can be explained by the differing beam line kaon momenta, BeO degrader thicknesses and the addition of the lead glass active degrader in 1991. The calculation of the stopping kaon flux for the three data sets is also summarized in table 7.23. The integrated stopping flux was $(3.47 \pm 0.03) \times 10^{11}$ kaons for the combined 1989 to 1991 data set.

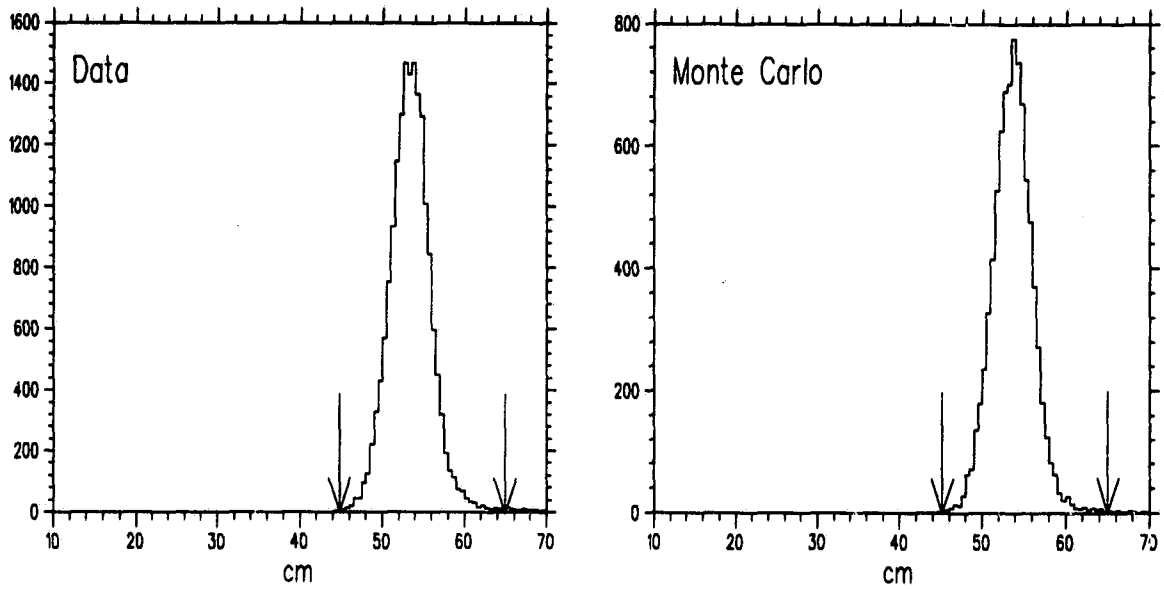

Figure 7.4: Total range for $K_{\mu 2}$ events used to estimate the kaon stopping fraction, f_s. The position of the range cut, $45 < R'_{tot} < 65$ cm, used to select $K_{\mu 2}$ events is shown. The 1990 $K_{\mu 2}$ data is shown.

Kaon Stopping Fraction Analyses			
Cut	1989	1990	1991
L0_DC	93108	46211	28818
L0_LAY15	65566	-	-
Track Reconstruction	28599	34450	19970
STLAY_RS	23548	31370	18175
DIPANG	22058	29177	16840
Photon Veto Cuts	21644	28864	16654
DCTG_XY	17532	22291	12219
DC_Z	17010	21677	11798
Delayed Coincidence	16993	21657	11789
Beam Counter Cuts	15934	20518	11110
TGVET	14615	18553	10571
IC_E	13651	17290	9688
RCUT	13486	17207	9594
$\#K_{\mu 2}$	13423	17079	9538

Table 7.21: Analysis summary for the measurement of the number of $K_{\mu 2}$ events, $\#K_{\mu 2}$, used in the estimate of f_s. The number of events examined by each cut is tabulated. The L0_LAY15 cut was the off-line application of the Layer 21 charged track trigger veto. It had already been applied to the 1990 and 1991 data. The STLAY_RS cut required the stopping layer to satisfy $18 < S_L < 21$. The RCUT required $45 < R'_{tot} < 65$ cm.

Monte Carlo $K_{\mu 2}$ Analyses						
Cut	1989		1990		1991	
	$N_{\rm ex}$	Acceptance	$N_{\rm ex}$	Acceptance	$N_{\rm ex}$	Acceptance
TARGET	25000	0.9950 ± 0.0004	25000	0.9952 ± 0.0004	25246	0.9955 ± 0.0004
DC_FIT	24875	0.9849 ± 0.0008	24879	0.9858 ± 0.0007	25133	0.9860 ± 0.0007
NTRK_RS	24499	0.9993 ± 0.0002	24526	0.9994 ± 0.0002	24781	0.9992 ± 0.0002
TRKTIM	24483	1.0000 ± 0.0000	24512	1.0000 ± 0.0000	24761	1.0000 ± 0.0000
TICTG	24483	0.9999 ± 0.0001	24512	0.9999 ± 0.0001	24761	0.9999 ± 0.0001
STLAY_RS	24481	0.3493 ± 0.0030	24509	0.3526 ± 0.0031	24759	0.3499 ± 0.0030
DIPANG	8552	0.9944 ± 0.0008	8642	0.9942 ± 0.0008	8663	0.9910 ± 0.0010
DCTG_XY	8504	0.9948 ± 0.0008	8592	0.9953 ± 0.0007	8585	0.9934 ± 0.0009
IC_E	8460	0.9940 ± 0.0008	8552	0.9942 ± 0.0008	8528	0.9933 ± 0.0009
RCUT	8409	0.9969 ± 0.0006	8502	0.9973 ± 0.0006	8471	0.9992 ± 0.0003
Events Out	8383		8479		8464	
$N_{\rm Kstop}$	55560		55641		55724	
$A^{MC}_{K\mu 2}$	0.1509 ± 0.0015		0.1524 ± 0.0015		0.1519 ± 0.0015	
A^{MC}_{recon}	0.9793 ± 0.0009		0.9805 ± 0.0009		0.9807 ± 0.0009	

Table 7.22: Summary of the $K_{\mu 2}$ Monte Carlo data acceptance measurements. The value of $A^{MC}_{K\mu 2}$ is given by the ratio of surviving events to the number of K_{stop}. The value A^{MC}_{recon} was determined from the number of events passing the reconstruction cuts. The STLAY_RS cut required the stopping layer to satisfy $18 < S_L < 21$. The RCUT required $45 < R'_{tot} < 65$ cm.

Evaluation of the Kaon Stopping Flux			
Factor	1989	1990	1991
$\#K_{\mu 2}$	13423	17079	9538
N^{ps}_{KT}	445046	503285	367991
$A^{MC}_{K\mu 2}$	0.1509 ± 0.0015	0.1524 ± 0.0015	0.1519 ± 0.0015
A_{recon}	0.835 ± 0.008	0.927 ± 0.012	0.936 ± 0.016
A^{MC}_{recon}	0.9793 ± 0.0009	0.9805 ± 0.0009	0.9807 ± 0.0009
A_{DC}	0.7554 ± 0.0038	0.7558 ± 0.0038	0.7358 ± 0.0048
$A_{\bar{\gamma}}$	0.781 ± 0.003	0.746 ± 0.003	0.689 ± 0.003
A_{BM}	0.919 ± 0.003	0.908 ± 0.003	0.951 ± 0.003
f_s	0.681 ± 0.011	0.726 ± 0.012	0.584 ± 0.011
N_{KT} Live	1.75×10^{11}	1.98×10^{11}	1.45×10^{11}
Stopping Flux	$(1.19 \pm 0.02) \times 10^{11}$	$(1.44 \pm 0.02) \times 10^{11}$	$(0.84 \pm 0.02) \times 10^{11}$
Total Stopping Flux	$(3.47 \pm 0.03) \times 10^{11}$		

Table 7.23: Summary of the factors used to evaluate the kaon stopping fraction, f_s, and the the stopping kaon flux for each data run.

7.7 Measurement of BR($K_{\pi 2}$)

The measurement of the $K_{\pi 2}$ branching ratio served as a consistency check for the following factors:

- The simulation of nuclear interaction and decay-in-flight effects in the Monte Carlo.
- The calculated acceptance of the TD based particle identification cuts, in particular, A_{TDFIT}.
- The estimated kaon stopping fraction, f_s.

The $K_{\pi 2}$ branching ratio was calculated using,

$$\mathrm{BR}(K_{\pi 2}) = \frac{\#K_{\pi 2}}{f_s \times N_{KT}} \times \frac{1}{A^{MC}_{K\pi 2}} \times \frac{A^{MC}_{recon}}{A_{recon}} \times \frac{1}{A_{DC}} \times \frac{1}{A'_{TD}} \times \frac{1}{A_{BM}}. \tag{20}$$

To avoid correlated errors, the expression for f_s given by equation 19 can be substituted for, yielding

$$\mathrm{BR}(K_{\pi 2}) = \mathrm{BR}(K_{\mu 2}) \times f_{ps} \times \frac{\#K_{\pi 2}}{\#K_{\mu 2}} \times \frac{A^{MC}_{K\mu 2}}{A^{MC}_{K\pi 2}} \times \frac{1}{A'_{TD}} \times A_{\bar{\gamma}}, \tag{21}$$

where $\#K_{\pi 2}$ was the number of tagged $K_{\pi 2}$ events measured using monitor triggers, f_{ps} was the ratio of the $K_{\pi 2}$ to $K_{\mu 2}$ prescale factors, $A^{MC}_{K\pi 2}$ was the Monte Carlo based $K_{\pi 2}$ acceptance and A'_{TD} was the acceptance for the subset of the $\pi \to \mu \to e$ cuts applied to the $K_{\pi 2}$ data.

The measurement of $\#K_{\pi 2}$ is summarized in table 7.24. $K_{\pi 2}$ events were tagged with a range cut of $26 < R'_{tot} < 34$ cm. The measurement of A'_{TD} used the $\pi-$scat monitor trigger samples described in section 7.5.2 [57]. The analysis of the Monte Carlo data is summarized in table 7.25. The factors entering into the $K_{\pi 2}$ branching ratio calculations are given in table 7.27. Table 7.27 summarizes the calculated $K_{\pi 2}$ branching ratios showing separately the statistical error of the $K_{\pi 2}$ and $K_{\mu 2}$ samples and the statistical error in the $K_{\pi 2}$ acceptance. The errors in the individual $K_{\pi 2}$ acceptances were approximately 6% and were dominated by the A_{TDFIT} factor. The average $K_{\pi 2}$ branching ratio for the three data sets was measured to be:

$$\mathrm{BR}(K_{\pi 2}) = 0.214 \pm 0.002\ _{(\mathrm{stat})} \pm 0.008\ _{(\mathrm{acc})}, \quad (\text{Accepted Value } = 0.2117 \pm 0.0016),$$

where the statistical error of the $K_{\pi 2}$ and $K_{\mu 2}$ samples and the estimated error in the $K_{\pi 2}$ acceptance are separately shown. The errors were obtained by adding the individual errors in quadrature. The measured $K_{\pi 2}$ branching ratios for the individual data sets were also consistent with the accepted value.

$K_{\pi 2}$ Branching Ratio Analyses			
Cut	1989	1990	1991
L0_DC	86212	95043	166713
Track Reconstruction	51015	57558	87983
STLAY_RS	39170	49696	73959
DIPANG	27903	35306	51910
FITPI	27184	34698	50924
TMUAV	8144	9448	13383
CHITD	7220	8519	12382
TARGET	6813	8106	11682
TICTG	6813	7917	11682
DCTG_XY	6813	7910	11682
Delayed Coincidence	6278	7289	10629
Beam Counter	5786	6849	9950
ELVETO	5111	5916	8962
ELCTRN	4951	5725	8615
RCUT	4168	4809	7265
$\#K_{\pi 2}$	4118	4770	7171

Table 7.24: Measurement of $\#K_{\pi 2}$ for the $K_{\pi 2}$ branching ratio stimate. The number of events examined by each cut is tabulated. The STLAY_RS cut required the $11 \leq S_L \leq 18$. The RCUT required $26 < R'_{tot} < 34$ cm.

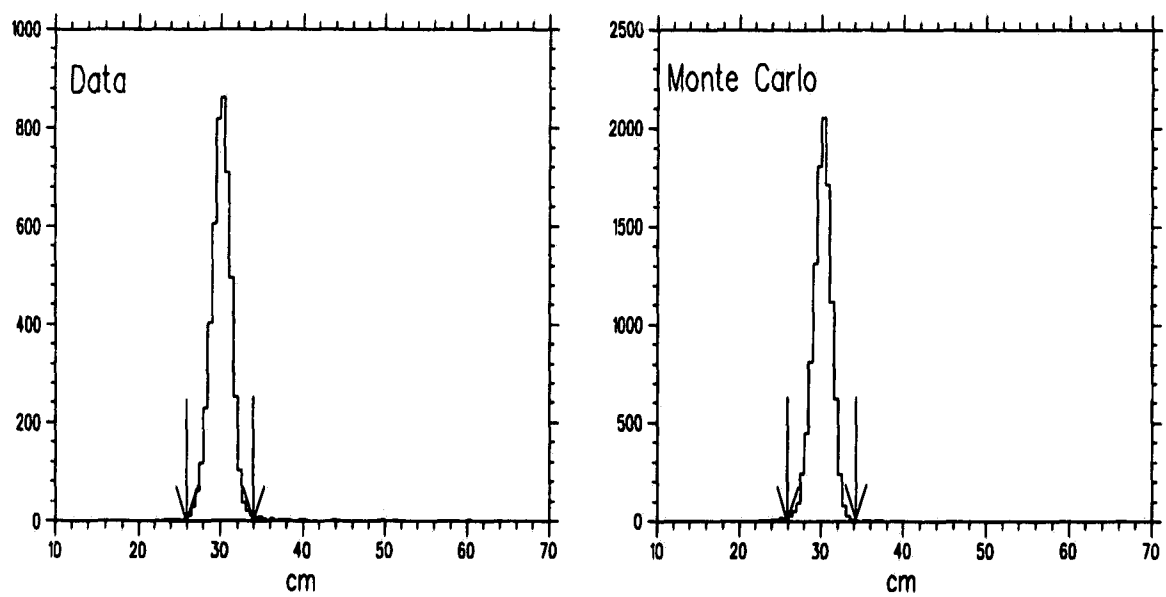

Figure 7.5: Total range for $K_{\pi 2}$ events used to estimate BR($K_{\pi 2}$). The position of the range cut, $26 < R'_{tot} < 34$ cm, used to select $K_{\pi 2}$ events is shown. The data distribution is for the 1990 $K_{\pi 2}$ monitor data.

Monte Carlo $K_{\pi 2}$ Analyses						
Cut	1989		1990		1991	
	N_{ex}	Acceptance	N_{ex}	Acceptance	N_{ex}	Acceptance
PIFATE	25000	0.8390 ± 0.0023	25000	0.8416 ± 0.0023	25000	0.8389 ± 0.0023
STMED	20975	0.9457 ± 0.0016	21039	0.9441 ± 0.0016	20973	0.9452 ± 0.0016
TARGET	19837	0.9901 ± 0.0007	19863	0.9902 ± 0.0007	19823	0.9907 ± 0.0007
DC_FIT	19640	0.9785 ± 0.0010	19669	0.9825 ± 0.0009	19639	0.9803 ± 0.0010
NTRK_RS	19217	0.9419 ± 0.0017	19325	0.9397 ± 0.0017	19252	0.9421 ± 0.0017
USTPHEX	18100	0.7738 ± 0.0031	18160	0.7793 ± 0.0031	18138	0.7745 ± 0.0031
TRKTIM	14006	1.0000 ± 0.0000	14152	1.0000 ± 0.0000	14047	1.0000 ± 0.0000
TICTG	14006	0.9997 ± 0.0001	14152	0.9998 ± 0.0001	14047	0.9997 ± 0.0001
STLAY_RS	14002	0.8143 ± 0.0033	14149	0.8108 ± 0.0033	14043	0.8053 ± 0.0033
DIPANG	11402	0.9921 ± 0.0008	11472	0.9920 ± 0.0008	11309	0.9933 ± 0.0008
DCTG_XY	11312	0.9585 ± 0.0019	11380	0.9589 ± 0.0019	11233	0.9546 ± 0.0020
RCUT	10842	0.9904 ± 0.0009	10912	0.9926 ± 0.0008	10723	0.9911 ± 0.0009
Events Out	10738		10831		10628	
N_{Kstop}	65954		65783		66325	
$A^{MC}_{K\pi 2}$	0.1628 ± 0.0014		0.1646 ± 0.0014		0.1602 ± 0.0014	

Table 7.25: Summary of the $K_{\pi 2}$ Monte Carlo data acceptance measurements. The value of $A^{MC}_{K\pi 2}$ is given by the ratio of surviving events to the number of K_{stop}. The PIFATE cut required that the pion to stop and decay normally. The STLAY_RS cut required the stopping layer satisfy $11 \leq S_L \leq 18$. The range cut, RCUT, required $26 < R'_{tot} < 34$ cm.

$K_{\pi 2}$ Branching Ratio Factors			
Factor	1989	1990	1991
$\#K_{\pi 2}$	4118	4770	7171
$\#K_{\mu 2}$	13423	17079	9538
f_{ps}	25/32	5/6	1/3
$A^{MC}_{K\pi 2}$	0.1628 ± 0.0014	0.1646 ± 0.0014	0.1602 ± 0.0014
$A^{MC}_{K\mu 2}$	0.1509 ± 0.0015	0.1524 ± 0.0015	0.1519 ± 0.0015
A'_{TD}	0.498 ± 0.028	0.493 ± 0.030	0.485 ± 0.026
$A_{\bar{\gamma}}$	0.781 ± 0.003	0.746 ± 0.003	0.689 ± 0.003

Table 7.26: Factors used in the evaluation of BR($K_{\pi 2}$).

BR($K_{\pi 2}$) Measurements		
Year	BR($K_{\pi 2}$)	Discrepancy
1989	$0.221 \pm 0.004 \pm 0.013$	0.7σ high
1990	$0.207 \pm 0.003 \pm 0.013$	0.4σ low
1991	$0.214 \pm 0.003 \pm 0.012$	0.2σ high
Average	$0.214 \pm 0.002 \pm 0.008$	0.3σ high
Accepted	0.2117 ± 0.0016	-

Table 7.27: Summary of BR($K_{\pi 2}$) measurements. The first error corresponds to the statistical error of the $K_{\pi 2}$ and $K_{\mu 2}$ samples; the second error corresponds to the estimated error in the $K_{\pi 2}$ acceptance.

7.8 Rare Decay Mode Acceptances and Sensitivities

The total acceptances for $K^+ \to \pi^+ \nu\overline{\nu}$ and $K^+ \to \pi^+ X^0$ were computed using,

$$A_{tot} = A_{data} \times A_{Trig} \times A_{UMC} \times A_{Nuc/DIF} \times A_{L1.5},$$

where,

$$A_{data} = A_{recon} \times A^{\mu}_{SCT} \times A^{\pi}_{SCT} \times A_{TD} \times A_{DC} \times A_{Kin},$$

was the acceptance of the cuts common to both decay modes measured using real data. The factors entering A_{data} are summarized in table 7.28. The total sensitivity, S, for each decay mode was the sum over the 1989, 1990 and 1991 sensitivities,

$$S = \sum_{89-91} S_i = \sum_{89-91} (A_{tot} \times N_{\mathrm{Kstop}})_i.$$

The acceptance factors for each year and corresponding sensitivities for $K^+ \to \pi^+ \nu\overline{\nu}$ and $K^+ \to \pi^+ X^0$ are summarized in tables 7.29 and 7.30, respectively. The year-by-year stopping flux weighted acceptance for $K^+ \to \pi^+ \nu\overline{\nu}$ was 1.8×10^{-3} per stopped kaon, corresponding to a net sensitivity of $(6.48 \pm 0.29) \times 10^8$ kaons. Similarly, for $K^+ \to \pi^+ X^0$, the weighted acceptance was 1.1×10^{-2} per stopped kaon corresponding to a net sensitivity of $(3.85 \pm 0.15) \times 10^9$ kaons.

Data Based Rare Decay Acceptances				
Description	Symbol	1989	1990	1991
Track Recon.	A_{recon}	0.835 ± 0.008	0.927 ± 0.012	0.936 ± 0.016
$K_{\mu 2}$ Based	A^{μ}_{SCT}	0.5651 ± 0.0039	0.5376 ± 0.0034	0.4886 ± 0.0044
Pion Based	A^{π}_{SCT}	0.8543 ± 0.0053	0.8617 ± 0.0047	0.8207 ± 0.0053
$\pi \to \mu \to e$ ID	A_{TD}	0.309 ± 0.019	0.266 ± 0.016	0.284 ± 0.015
Dlyd. Coin.	A_{DC}	0.7554 ± 0.0038	0.7558 ± 0.0035	0.7358 ± 0.0048
Kinematic ID	A_{Kin}	0.8136 ± 0.0060	0.7969 ± 0.0050	0.7999 ± 0.0065
Combined	A_{data}	0.077 ± 0.005	0.069 ± 0.004	0.063 ± 0.004

Table 7.28: Summary of common acceptance factors for the rare decay modes determined from real data.

$K^+ \to \pi^+ \nu\overline{\nu}$ Acceptance Factors and Sensitivities				
Description	Symbol	1989	1990	1991
Common	A_{data}	0.077 ± 0.005	0.069 ± 0.004	0.063 ± 0.004
Trigger	$A^{\pi\nu\nu}_{Trig}$	0.1777 ± 0.0019	0.1780 ± 0.0019	0.1802 ± 0.0019
Off-line	$A^{\pi\nu\nu}_{UMC}$	0.3047 ± 0.0046	0.3173 ± 0.0048	0.3129 ± 0.0047
Nuc./DIF	$A_{\mathrm{Nuc/DIF}}$	0.500 ± 0.009	0.480 ± 0.009	0.467 ± 0.009
Level 1.5	$A^{\pi\nu\nu}_{L1.5}$	0.994 ± 0.002	0.994 ± 0.001	0.993 ± 0.002
Combined	$A_{\pi\nu\nu}$	$(2.06 \pm 0.14) \times 10^{-3}$	$(1.88 \pm 0.13) \times 10^{-3}$	$(1.33 \pm 0.10) \times 10^{-3}$
Kaon flux	N_{Kstop}	$(1.19 \pm 0.02) \times 10^{11}$	$(1.44 \pm 0.02) \times 10^{11}$	$(0.84 \pm 0.02) \times 10^{11}$
Sensitivity	S_i	$(2.44 \pm 0.17) \times 10^{8}$	$(2.66 \pm 0.20) \times 10^{8}$	$(1.38 \pm 0.09) \times 10^{8}$
Total	$\sum S_i$	$(6.48 \pm 0.27) \times 10^{8}$		

Table 7.29: Summary of $K^+ \to \pi^+ \nu\overline{\nu}$ acceptance factors and sensitivities.

$K^+ \to \pi^+ X^0$ Acceptance Factors and Sensitivities				
Description	Symbol	1989	1990	1991
Common	A_{data}	0.077 ± 0.005	0.069 ± 0.004	0.063 ± 0.004
Trigger	$A^{\pi X}_{Trig}$	0.4123 ± 0.0043	0.4124 ± 0.0043	0.4078 ± 0.0042
Off-line	$A^{\pi X}_{UMC}$	0.8317 ± 0.0088	0.8503 ± 0.0090	0.8443 ± 0.0089
Nuc./DIF	$A_{\mathrm{Nuc/DIF}}$	0.462 ± 0.005	0.466 ± 0.005	0.467 ± 0.005
Level 1.5	$A^{\pi X}_{L1.5}$	0.990 ± 0.002	0.991 ± 0.002	0.988 ± 0.004
Combined	$A_{\pi X}$	$(1.20 \pm 0.08) \times 10^{-2}$	$(1.11 \pm 0.07) \times 10^{-2}$	$(0.99 \pm 0.06) \times 10^{-2}$
Kaon flux	N_{Kstop}	$(1.19 \pm 0.02) \times 10^{11}$	$(1.44 \pm 0.02) \times 10^{11}$	$(0.84 \pm 0.02) \times 10^{11}$
Sensitivity	S_i	$(1.43 \pm 0.10) \times 10^{9}$	$(1.59 \pm 0.10) \times 10^{9}$	$(0.83 \pm 0.05) \times 10^{9}$
Total	$\sum S_i$	$(3.85 \pm 0.15) \times 10^{9}$		

Table 7.30: Summary of $K^+ \to \pi^+ X^0$ acceptance factors and sensitivities for massless X^0.

Chapter 8

Results and Conclusions

Hanging on in quiet desperation is the English way.
The time is gone, the song is over, thought I'd something more to say.

- Pink Floyd

8.1 Rare Decay Upper Limits

The upper limits for the rare decay modes were evaluated using the method suggested by Cousins and Highland [58] for incorporating systematic uncertainties in sensitivity. The upper limits for the rare decay mode branching ratios were calculated using,

$$\mathrm{BR} \leq \frac{2.3 \times (1 + 2.3\frac{\sigma_S^2}{2})}{\text{Sensitivity}}, \tag{22}$$

where 2.3 is the standard factor for Poisson statistics for an upper limit at the 90% confidence level for the mean number of expected events with no observed events. The second term in the numerator containing σ_S represents the contribution of the systematic error in the sensitivity where σ_S is the relative error in the sensitivity.

Contributions to the error in the total sensitivity include the statistical error in the acceptance factors, systematic errors in target stopping distribution, the effect of nuclear interactions in the target on the acceptance of the tighter target tracking cuts and the systematic error in the acceptance of the final kinematic cut due to uncertain knowledge of the kinematic response between the $K_{\pi 2}$ and $K_{\mu 2}$ peaks. The acceptance of the tighter target tracking cuts was evaluated using $K_{\pi 2}$ events, which have lower momentum pions than the rare decays, hence, different interaction cross sections.

The measurements of the $K_{\pi 2}$ branching ratios, which served as a cross check of the estimated kaon stopping fractions, the acceptance of the $\pi \rightarrow \mu \rightarrow e$ identification cuts and the ability of the Monte Carlo to simulate the effects of nuclear interactions,

were all found to be consistent with the accepted value of 0.2117 ± 0.0016. Based on the $5-7\%$ uncertainties in the measured $K_{\pi 2}$ branching ratios, the systematic error in the total sensitivity is conservatively estimated to be 10%. Substituting 0.1 for σ_S in equation 22 results in a numerator of 2.33.

8.1.1 $K^+ \to \pi^+\nu\bar{\nu}$ Upper Limit

In the analysis, 2 candidate events were observed in the initially defined signal region. Both events were found to have signatures consistent with $K_{\pi 2}$ backgrounds. These events were removed by moving the lower edge of the range cut used to define the signal region. Substituting for the measured $K^+ \to \pi^+\nu\bar{\nu}$ sensitivity, an upper limit for the $K^+ \to \pi^+\nu\bar{\nu}$ branching ratio of,

$$\begin{aligned} \mathrm{BR}(K^+ \to \pi^+\nu\bar{\nu}) &\leq \frac{2.33}{\sum_{89-91} (A_{\pi\nu\nu} \times N_{\mathrm{Kstop}})_i}, \\ &\leq \frac{2.33}{6.48 \times 10^8}, \\ &\leq 3.6 \times 10^{-9}, \ 90\% \ \mathrm{C.L.}, \end{aligned}$$

is obtained. The results, based on no observed events and a Standard Model π^+ spectrum, are for the kinematic region,

$$34 < R'_{tot} < 40 \ \mathrm{cm},$$

$$115 < E'_{tot} < 135 \ \mathrm{MeV},$$

$$211 < P'_{tot} < 242 \ \mathrm{MeV}/c.$$

This result corresponds to a factor of 2.1 improvement over our published result of $\leq 7.5 \times 10^{-9}$ based on the 1989 data set alone [11]. For the sensitivity achieved with the combined 1989 to 1991 data set, the limit is consistent with the Standard Model calculation of the $K^+ \to \pi^+\nu\bar{\nu}$ decay rate. The $K^+ \to \pi^+\nu\bar{\nu}$ result is approximately an order of magnitude away from constraining Standard Model parameters.

8.1.2 $K^+ \to \pi^+ X^0$ Upper Limit

Similarly, for $K^+ \to \pi^+ X^0$ where X^0 is any weakly interacting massless particle, an upper limit of

$$\begin{aligned} \mathrm{BR}(K^+ \to \pi^+ X^0) &\leq \frac{2.33}{\sum_{89-91} (A_{\pi X} \times N_{\mathrm{Kstop}})_i} \\ &\leq \frac{2.33}{3.85 \times 10^9} \\ &\leq 6.1 \times 10^{-10},\ 90\%\ \mathrm{C.L.}, \end{aligned}$$

is obtained. This result represents a factor of 2.8 improvement over the published result of 1.7×10^{-9} for massless X^0 [11]. For the case of the Wilczek "familon" [10], the upper limit corresponds to a lower limit for the mass scale of 2×10^{11} GeV/c^2 for family symmetry breaking.

8.2 Outlook for the Future

At the time of this writing, the E-787 experiment is entering a new phase. With this analysis of the the 1989-1991 data set, the first phase of the search for $K^+ \to \pi^+ \nu\overline{\nu}$ is completed. Since the last data was taken in 1991, there have been many substantial upgrades to experiment. These upgrades will enable E-787 to meet its desired goal of measuring the $K^+ \to \pi^+ \nu\overline{\nu}$ branching ratio at the 1×10^{-10} level.

Foremost among these upgrades is the new LESB-III beam line. The new beam line, commissioned during the 1992 AGS run, has two stages of electrostatic separation and larger solid angle acceptance. The LESB-III beam line reduces the beam pion contamination by a factor of 4, while simultaneously increasing the kaon flux per incident proton by a factor of 2. This corresponds to twice the kaon flux for the same instantaneous rate in the detector. The AGS has commissioned a new "Booster" ring, which enables operating the accelerator at 4 times the nominal beam current; hence, producing 4 times the kaon flux.

The E-787 detector has also been upgraded in anticipation of the increased kaon flux. The existing drift chamber has been replaced with a foil-type chamber having 1/5 the mass. The momentum resolution of the previous chamber was limited by multiple scattering effects. Tests performed on prototypes of the new chamber indicate that the design goal of 1% momentum resolution is achievable. The improvement in resolution will translate into higher rejection for the mono-chromatic $K_{\pi 2}$ and $K_{\mu 2}$ backgrounds. The present lead scintillator endcap photo veto has been upgraded to a completely active pure Cesium Iodide system. The new endcaps will improve the timing resolution and will allow the utilization

of lower energy thresholds. The photon veto system is being augmented by a set of "collar vetos", which will help to close a weak spot along the beam axis.

To further reduce the dead material in the fiducial volume, the range stack multi-wire proportional counters are being replaced with "straw" chambers, which will reduce the mass by a factor of 5. The inner 9 layers of the range stack, which had been ganged into the A, B and C layers have been "demultiplexed". The target has also been upgraded. The new target, constructed out of 5 mm $\times$ 5 mm scintillating fibers, is almost completely active and has 3 times the light yield of the old target. The new target will offer significantly improved timing and energy resolution. The target and endcaps will be instrumented with 500 MHz transient recorders based on a Gallium Arsenide CCD design. For the target, the direct observation of the $K \rightarrow \pi$ decay in the CCD system will provide additional suppression of the kaon charge exchange and beam related backgrounds. The CCDs should also address backgrounds arising from ambiguity in the location of the kaon decay vertex. To handle the order of magnitude increase in the kaon flux, the trigger and data acquisition systems have been completely upgraded.

It is anticipated that the improvements in the detector and beam line, combined with some steady data taking, will enable observation of the $K^+ \rightarrow \pi^+\nu\overline{\nu}$ decay in the not so distant future. Once a signal is in hand, the Standard Model will be confronted with a unique test of its internal consistency. The search for $K^+ \rightarrow \pi^+\nu\overline{\nu}$ continues.

References

[1] S.L Glashow, J. Illiopoulos, L. Maiani, *Phys. Rev.* **D2**, 1285 (1970).

[2] M.K. Gaillard and B.W. Lee, *Phys. Rev.* **D10**, 897 (1974).

[3] T. Inami, C.S Lim, *Prog. Theor. Phys.* **65**, 297 (1981).

[4] G. Belanger and C. Q. Geng, *Phys. Rev.* **D43**, 140 (1991);
J. Ellis, J. S. Hagelin, S. Rudaz, and D.-D. Wu, *Nucl. Phys.* **B304**, 205 (1988).

[5] C. O. Dib, I. Dunietz, and F. J. Gilman, *Mod. Phys. Lett.* **A6**, 3573 (1991).

[6] A.J. Buras and M.K. Harlander, *A Top Quark Story* in Heavy Flavours,
eds. A.J. Buras and M. Linder, World Scientific, 1992, pg. 58.

[7] U. Türke, *Phys. Lett.* **168B**, 533 (1986).

[8] J. Ellis and J. S. Hagelin, *Nucl. Phys.* **B217**, 189 (1983);
M. K. Gaillard, Y. C. Kao, I-H. Lee, and M. Suzuki, *Phys. Lett.* **123B**, 241 (1983);
S. Bertolini and A. Masiero, Phys. Lett. **174B**, 343 (1986).

[9] G. B. Gelmini and M. Roncadelli, *Phys. Lett.* **99B**, 411 (1981);
S. Bertolini and A. Santamaria, Nucl. Phys. **B315**, 558 (1989).

[10] F. Wilczek, *Phys. Rev. Lett.* **49**, 1549 (1982)

[11] M.S. Atiya *et al.*, (The E-787 Collaboration) *Phys. Rev. Lett.* **70**, 2521 (1993);
ibid. **71**, 305 (1993)

[12] M. Gell-Mann, *Phys. Rev.* **92**, 833 (1953);
K. Nishijima, *Prog. Theor. Phys.* **13**, 285 (1955).

[13] T.D. Lee and C.N. Yang, *Phys. Rev.* **104**, 254 (1956).

[14] C.S. Wu, E. Ambler, R. Hayward, D. Hoppes, and R. Hudson,
Phys. Rev. **105**, 1413 (1957).

[15] R.P. Feynman and M. Gell-Mann, *Phys. Rev.* **109**, 193 (1958).

[16] A.S. Goldhaber, M.L. Grodzins and A. Sunyar, *Phys. Rev.* **109**, 1015 (1958).

[17] N. Cabbibo, *Phys. Rev. Lett.* **10**, 255 (1963).

[18] J.H. Christenson, J. Cronin, V. Fitch, and R. Turlay, *Phys. Rev. Lett.* **13**, 138 (1964).

[19] S.L. Glashow, *Nucl. Phys* **22**, 579 (1961);
S. Weinberg, *Phys. Rev. Lett.* **19**, 1264 (1967);
A. Salam, *Elementary Particle Theory* (ed. N. Svartholm), Almquist and Wiksells, Stockhlom, 1968.

[20] C. Quigg, *Gauge Theories of the Strong, Weak and Electromagetic Interactions*, Frontiers in Physics v. 56, Benjamin/Cummings, 1983.

[21] J.J. Aubert *et al., Phys. Rev. Lett.* **33**, 1404 (1974);
J.E. Augustin, *et al., Phys. Rev. Lett.* **33**, 1406 (1974).

[22] M. Kobayashi and T. Maskawa, *Prog. Theor. Phys.* **49**, 652 (1973).

[23] M. Perl *et al., Phys. Rev. Lett.* **35**, 1489 (1975); *Phys. Lett.* **63B**, 366 (1976).

[24] L. Wolfenstien, *Phys. Rev Lett.* **51**, 1945 (1983).

[25] G. Buchalla and A.J. Buras, *Nucl. Phys* **B400**, 225 (1993).

[26] D. Rein and L.M. Sehgal, *Phys. Rev.* **D39**, 3325 (1989);
J.S Hagelin and L.S. Littenberg, *Prog. Part. Nucl. Phys.* **23**, 1 (1989);
M. Lu and M.B. Wise, Caltech Preprint Calt-68-1911.

[27] The LEP Collaborations ALEPH, DELPHI, L3, OPAL and the LEP Electroweak Working Group, *Updated Parameters of the Z^0 Resonance ...*, CERN/PPE/93-157

[28] F. Abe *at al.*, FERMILAB-PUB-94/097-E, Submitted to Physical Review D.

[29] S. Abachi *at al., Phys. Rev. Lett.* **72**, 2138 (1994).

[30] J. S. Haggerty, "Determination of Standard Model Parameters from $K^+ \to \pi^+ \nu\overline{\nu}$," in *Research Directions for the Decade*, ed. E. L. Berger, Snowmass Co., 1990, pg. 275.

[31] Particle Data Group, *Phys. Rev.* **D45**, 1 (1992).

[32] G. Buchalla, A.J. Buras, and M.K. Harlander, *Nucl. Phys.* **B349**, 1 (1991).

[33] N. G. Deshpande and G. Eilam, *Phys. Rev. Lett.* **53**, 2289 (1984).

[34] M.S. Atiya *et al.*, (The E-787 Collaboration) *Phys. Rev. Lett.* **71**, 305 (1993).

[35] M.S. Atiya *et al.*, *Nucl. Instr. and Meth.* **A321**, 129 (1992).

[36] J.S. Frank and R.C. Strand, Proc. Workshop on Scintillating Fibre Detector Developement for the SSC, vol. 1 (Fermilab, Batavia, 1988) pg. 359.

[37] J.V. Cresswell *et al.*, *IEEE Trans. Nucl. Science* NS-35, 440 (1988).

[38] M. Atiya, M. Ito, J. Haggerty, C Ng, F.W. Sippach, *Nucl. Instr. Methods* **A279**, 180 (1989).

[39] IEEE Standard FASTBUS Modular High-Speed Data Acquisition and Control System, IEEE, New York (1985).

[40] CAMAC: A Modular Instrumentation System for Data Handling-Revised Description and Specification, AEC Reference Reports TID-25875, TID-25876, and TID-25877 (1972).

[41] T. Barklow, T. Glanzman, A.J. Lankford and K. Riles, *IEEE Trans. on Nucl. Science*, **33** 775 (1986).

[42] I. Gaines *et. al.*, *The ACP Multiprocessor System at Fermilab* in Proceedings of Computing in High Energy Physics, Asilomar State Beach, California, 1987, or Fermilab Report Fermilab-Conf-87/21.

[43] M.S. Atiya *et al.*, (The E-787 Collaboration) *Phys. Rev. Lett.* **66**, 2189 (1991).

[44] M.S. Atiya *et al.*, (The E-787 Collaboration) *Phys. Rev. Lett.* **65**, 1188 (1990).

[45] H.Y. Cheng, *Phys. Rev.* **D42** 72 (1990);
G. Ecker, A. Pich, and E. de Rafael, *Phys. Lett.* **237B**, 481 (1990).

[46] KOFIA *version* 1.5, TRIUMF Data Aquisition Group, (1991)

[47] FIOWA, *version* 3.0 A.K. Haynes and A.W. Bennett, TRIUMF, 1981

[48] W.H. Barkas and M.J. Berger, *Tables of Energy Losses and Ranges of Heavy Charged Particles*, Scientific and Technical Information Division, NASA, 1964

[49] D.S. Akerib, D.R. Marlow and P.D. Meyers, E-787 Technical Note 168 (July 11, 1989).

[50] J.B. Birks *The Theory and Practice of Scintillation Counting,* Pergammon Press, Oxford, 1964

[51] T. Nakano and Y. Kuno, E-787 Technical Note 256 (July 24, 1993).

[52] M.S. Atiya *et al.*, (The E-787 Collaboration) *Phys. Rev. Lett.* **69**, 733 (1992).

[53] D. Wright and D.R. Marlow, E-787 Technical Note 269 (June 28, 1989)

[54] K. Arisaka *et al.*, *Phys. Rev. Lett.* **70**, 1049 (1993).

[55] R.L. Ford and W.L. Nelson, SLAC Report 210, June, 1978.

[56] A.J. Stevens, E-787 Technical Note 112 (May 1, 1986)

[57] A.S. Turcot, E-787 Technical Note 281, (March 2, 1993)

[58] R.D. Cousins and V.L. Highland, *Nucl. Inst. and Meth.* **A320**, 331 (1992).

[59] Formulae and Methods In Experimental Data Evaluation, Vol. 3, Articles on Statistical and Numerical Methods, Eds. Bock *et al.,* European Physical Society, CERN, 1984

[60] S. Wilks, *Mathematical Statistics,* J. Wiley and Sons, 1962

[61] E. Edberg, CERN Computer Center Program Library, 1974

[62] C. Letertre, CERN Computer Center Program Library, 1971

[63] G.A. Erskine, CERN Computer Center Program Library, 1979

Appendix A

The E-787 Collaboration (1989-1991)

S. Adler, M.S. Atiya, I-H. Chiang, J.S. Frank, J.S. Haggerty, T.F. Kycia, K.K. Li, L.S. Littenberg, A. Sambamurti, A. Stevens, R.C. Strand, and C. Witzig

Brookhaven National Laboratory

W.C. Louis

Los Alamos National Laboratory

D.S. Akerib, M. Ardebili, M. Convery, M.M. Ito, R.A. McPherson, D.R. Marlow, P.D. Meyers, M.A. Selen, F.C. Shoemaker, and A.J.S. Smith

Joseph Henry Laboratories, Princeton University

E.W. Blackmore, D.A. Bryman, L. Felawka, P. Kitching, A. Konaka, V. Kujala, Y. Kuno, J.A. Macdonald, T. Nakano, T. Numao, P. Padley, J-M. Poutissou, R. Poutissou, J. Roy, R. Soluk, and A.S. Turcot

TRIUMF

Appendix B

Multivariate Analysis

Multivariate analysis (MVA) is a statistical discipline developed for the general problem of population classification. An excellent reference on the application of PCA to track-finding which also gives a clear mathematical formulation is given by Wind [59]. A detailed mathematical treatment of PCA and DFA can be found in Wilks [60]. The use of MVA was motivated by the desire to optimize the $K^+ \rightarrow \pi^+\nu\overline{\nu}$ signal acceptance for a given prerequisite background rejection without having to tune cuts on individual variables in an arbitrary manner. Furthermore, since MVA based cuts are not solely on the individual variable values but also on the correlations between variables, it makes it possible to reject certain types of backgrounds that otherwise would not be possible without incurring large acceptance losses. There were two different multivariate techniques employed in the $K^+ \rightarrow \pi^+\nu\overline{\nu}$ analysis: discriminant function analysis (DFA) and principal component analysis (PCA).

The first step in performing a MVA is the calculation of the dispersion matrix A, whose elements are defined as:

$$a_{ij} = \frac{1}{N}\sum_{\alpha}^{N}(x_{i\alpha} - \bar{x}_i)(x_{j\alpha} - \bar{x}_j), \tag{23}$$

where N is number of events in the sample, $\alpha = 1, \ldots, N$, $x_{i\alpha}$ is the ith component of the vector x_α, whose elements are the variables used to define the sample. The individual variables should exhibit "gaussian" behaviour. Variables with flat or exponential distributions are not suitable for MVA. The data set used to define the dispersion matrix is the called the "training" sample. A simple example would be a sample of $K_{\pi 2}$ events each defined by a 3 dimensional vector containing the total range, energy and momentum, the vector $\bar{x}_\alpha$ would be mean values of the kinematic quantities.

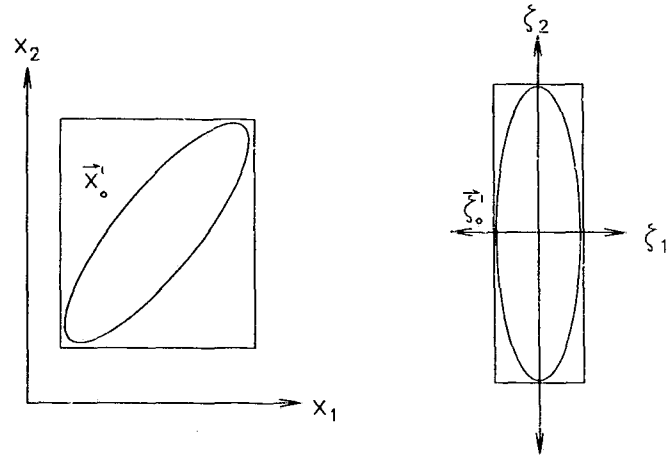

Figure B.1: Illustration of the PCA transformation. Note that the new coordinates, ζ_1 and ζ_2 have been decoupled and the effect on a arbitrary vector $\vec{x'}$ which has been transformed into $\vec{\zeta'}$.

B.1 Principal Component Analysis

Performing a principal component analysis (PCA) is tantamount to diagonalizing the dispersion matrix for the population under study. The power of a PCA lies in fact that the "volume" required to contain the m dimensional "hyper-swarm" is minimized by the PCA transformation. The volume itself does not change, only the projections upon the basis vectors defining the space. The classification of an arbitrary trial vector using projections upon the original basis vectors may be ambiguous, whereas a PCA may reveal that the transformed coordinates are clearly not consistent with assigning the trial vector to the population in question. This effect of the PCA transformation is illustrated in figure B.1 for a vector $\vec{x'}$. A PCA decouples the variables and diagonalizes the dispersion matrix.

Consider N vectors $\vec{x}_\alpha$ of m dimensions, $\alpha = 1, \ldots, N$ with the x_i "Gaussian" representing some given population $\mathcal{A}$. Performing a PCA is equivalent to finding the orthonormal transformation, W, and translation, $\vec{c}$,

$$\vec{\zeta} = W(\vec{x} - \vec{c}) \tag{24}$$

such that

$$\bar{\zeta}_j^2 = \frac{1}{N} \sum_{\alpha}^{N} \zeta_{j\alpha}^2 \tag{25}$$

is minimized. Skipping the details of the solution, it is found that $c_i = \bar{x}_i$ and W is the transformation which diagonalizes the dispersion matrix A. The eigenvalues of A are λ_i which correspond to the variances of the new coordinates ζ_i. The transformed coordinates can be used to form a χ^2 sum,

$$\chi^2 = \sum_{i=1,m} \frac{\zeta_i^2}{\lambda_i}, \tag{26}$$

and a confidence level can be evaluated for m D.O.F. The PCA transformation can be applied to a test vector of unknown nature and the confidence level for it belonging to same population as that used to define the dispersion matrix can be computed.

In practice, the diagonalization of the the dispersion matrix is done using the CERNLIB routine EISRS1 [61]. The confidence level can be computed using the CERNLIB routine PROB [62].

It should be stressed that a PCA assumes a linear correlation between variables. A PCA with variables that are non-linear functions of each other can be performed if an approximate linear correlation exists. An example of this is the stopping z position of the kaon versus the energy deposited by the kaon. The true correlation is not linear; however, resolution effects and the limited range over which z and E are examined allow us to assume a linear correlation.

B.2 Discriminant Function Analysis

Consider two sets, $\mathcal{A}$ and $\mathcal{B}$ with each member described by an m dimensional vector $\vec{x}_\alpha^{A,B}$ with $\alpha = 1, \ldots, N_{A,B}$ and the x_i "Gaussian" and having dispersion matrices A and B, respectively. Discriminant Function Analysis (DFA) is systematic way to classify whether an arbitrary $\vec{x}$ is more likely to belong to $\mathcal{A}$ or $\mathcal{B}$ such that the error is minimized. The discriminant function defines an axis onto which the projections of the vectors $\bar{x}_i^A$ and $\bar{x}_i^B$ have maximum relative separation in variance space. In other words, the discriminant function weights an individual variable based on its separation between the samples relative to its variance. The value of this projection in variance space is the Fischer or F variable.

The discriminant function $\vec{w}$ or linear combination of x_i that achieves the minimum error is given by, [1]

$$\vec{w} = V^{-1}\vec{d}, \tag{27}$$

where,

$$d_i = \bar{x}_i^A - \bar{x}_i^B \tag{28}$$

[1] A proof of this is found in Wilks [60].

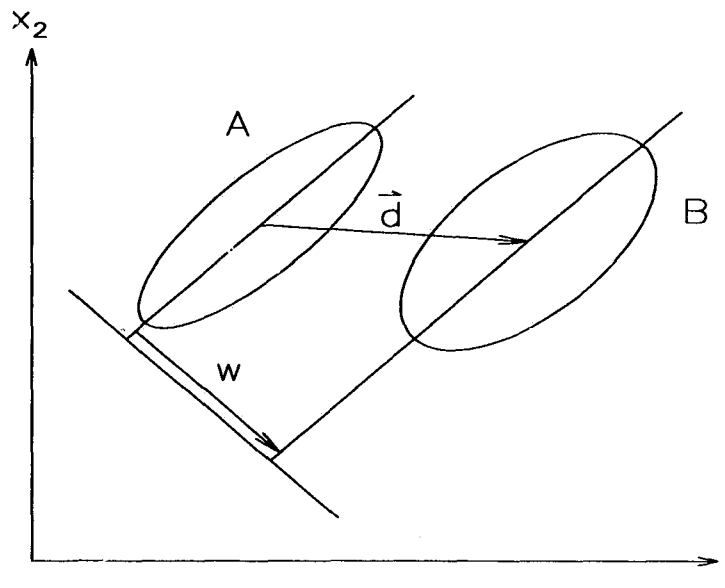

Figure B.2: Illustration of DFA for populations A and B, $\vec{d}$ is vector connecting the centroids of A and B, w is the axis along which the separation between the two populations is maximized.

and V is the weighted sum of the respective dispersion matrices defined in equation 23,

$$v_{ij} = \frac{1}{(N_A + N_B - 2)}(N_A \times a_{ij} + N_B \times b_{ij}). \tag{29}$$

The "distance" in variance space, D, between the two samples is used to normalize $\vec{w}$, where D is defined as

$$D^2 = \vec{d}^{\mathrm{T}} V^{-1} \vec{d} \tag{30}$$

The projection of $\vec{x}$ onto $\vec{w}$ is called the Fischer variable where $F(\vec{x}) = \sum w_i x_i$. The Fisher variable for an arbitrary vector $\vec{x}$ can be compared to F values for the means of the training samples, $F(\bar{x}_i^A)$ and $F(\bar{x}_i^B)$, to classify $\vec{x}$ as more likely to belong to $\mathcal{A}$ or $\mathcal{B}$. It is possible to assign a confidence level for a test vector to belong to given set based on the value of F; however, in practice, it is convenient to simply use F to reject events clearly belonging to the unwanted population. To use F to form a confidence level assumes certain characteristics of the dispersion matrices that may not be met in physics applications.

In practice, determining the discriminant function is straightforward. The matrix V is calculated for the two populations and inverted using the CERNLIB routine RINV [63].

It should be clear that there are limitations in using a DFA. Proper interpretation of Fischer variable relies on the assumption that the two data sets each consist of a unique population. If a given training population is actually composed of two subsets, then the ob-

tained weights will be optimized for the relative fraction of the two subsets. The subsequent event classification procedure is compromised. [2] An example of this is in $\pi - \mu$ separation using TD information. The muon background consists of tail fluctuation events and accidental pulses. Each background requires a separate DFA to ensure that the rejection is optimized.

[2]There are generalizations of DFA to m populations. It is essentially identical to performing $m - 1$ separate DFA's and simultaneously comparing the Fischer variables.

Appendix C

Index of Terms

B4 Hodoscope: The 4×4 (6×6 in 1991) scintillator hodoscope which was part of the beam counter instrumentation. Used to identify kaons entering the target by their dE/dx within the counter.

BH Counter: The Beam Hole counter was a scintillation counter with a hole corresponding to the active region of the Čerenkov counter. Used to veto events due to scattered pions in the beam halo.

BV: The Barrel Veto, part of the photon veto system.

BWPC: The beam multi-wire proportional counter; used to monitor the beam profile and to reject multiple beam particle events.

$\check{C}_\pi$**:** The pion Čerenkov counter, used to identify beam pions.

$\check{C}_K$**:** The kaon Čerenkov counter, used to identify beam kaons.

CEX: Charge-exchange, the process by which a K^+ interacts with a nucleus producing a K^0.

DC: Drift Chamber, used to measure the momentum of charged particles and to define their trajectory.

Delayed Coincidence: Requirement that the charged tracks from the kaon decay appear delayed compared to the initial kaon.

DFA: Discriminant Function Analysis, a discipline of multivariate analysis.

EC: Endcap, part of the photon veto system.

Hextant: Group of 4 range stack sectors.

Monitor Trigger: Events selected with very loose trigger requirements. Used in calibration of the detector subsystems and to evaluate certain acceptance factors for $K^+ \to \pi^+\nu\overline{\nu}$. The three primary monitor triggers were $K_{\pi 2}$, $K_{\mu 2}$ and beam pion scattering.

MUBG: The sample of $K^+ \to \pi^+\nu\overline{\nu}$ triggers selected at the PASS1 stage of the analysis used in studies of the $K_{\mu 2}$ type backgrounds.

MVA: Multivariate Analysis, a method of population classification using statistical techniques.

PASS0: First stage of the analysis where physics and monitor triggers were sorted to facilitate the analysis.

PASS1: Analysis stage where the basic charged track reconstruction criteria, requirement of a $\pi \to \mu$ decay signature and photon veto cuts were imposed.

PASS2: An intermediate stage of the analysis designed to reduce the data set to a smaller size while retaining the beam related background events for detailed study.

PASS3: Final stage of the analysis which included the kinematic signal region cut.

PCA: Principal Component Analysis, a discipline of multivariate analysis.

π–scat: An event due to a beam pion scattering in the target into the fiducial volume of the range stack. A potential background if the pion is misidentified as a kaon by the beam counters.

RS: Range Stack, used to measure the charged track energy and range. Also part of the photon veto system and the detection medium for the $\pi \to \mu \to e$ decay sequence.

RSPC: Range Stack Proportional Counter, one of 48 multi-wire proportional counters used to provided positional information for tracking the charged particle through the range stack.

Stopping Counter: The range stack counter in which the pion came to rest.

TD: Transient Digitizer, used to sample the phototube output to enable detection of the $\pi \to \mu \to e$ decay sequence.

TG or TGT: Target, kaon stopping medium, also used to identify the kaon decay vertex.

$(T \cdot A)$: Trigger level requirement that the charged track produce a coincidence between the T and A counters within the same range stack sector.

Appendix D

Event Selection Criteria and Variables

To aid the reader, the lists of commonly referred to variables have been duplicated in this appendix. A complete list of the event selection criteria is also given; the tables give a brief description of the cut and the sections where a detailed description may be found and the acceptance measurement is described.

Target Variables	
Variable	Description
R_{tgt}^{x-y}	Transverse pion target range
x_{vtx}, y_{vtx}	Kaon decay vertex
t_{π}^{tgt}	Target pion time
t_{K}^{tgt}	Target kaon time
σ_{t}^{π}	R.M.S. deviation of target pion triangles times
σ_{t}^{K}	R.M.S. deviation of target kaon triangles times
N_{Δ}^{π}	Number of pion fibers (triangles)
N_{Δ}^{K}	Number of kaon fibers (triangles)
$\delta_{tgt}^{K-\pi}$	Distance between kaon cluster and pion cluster
$x_{tgt}^{ex}, y_{tgt}^{ex}$	coordinates of pion track at target periphery
E_{tgt}	Charged track energy in target
E_{K}	Kaon energy in target
$t_{K-\pi}$	Kaon decay time, $t_{\pi}^{tgt} - t_{K}^{tgt}$
E_{IC}	Charged track energy in I-counter
R_{IC}	Charged track range in I-counter

Table D.1: List of target variables utilized in the analysis.

Drift Chamber Variables	
Variable	Description
P_{DC}	Drift chamber momentum
$\cos\theta_D$	Cosine of DC track dip-angle
dr	Sine of DC track dip-angle
R_C	DC track radius-of-curvature
x_c, y_c	DC track center-of-curvature
z_{ow}	DC based track z position at DC outer wall
z_{vtx}	DC based z position of kaon decay vertex
z^i_{DC}	DC based track z position at RSPC radii ($i = 1, 2$)

Table D.2: List of drift chamber variables utilized in the analysis.

Range Stack Variables	
Variable	Description
R_{RS}	Range of track in range stack
E^{raw}_{RS}	Energy of track in range stack
S'_L	Stopping layer in $T, A, B, C, 11 \ldots 21$ convention
S_L	Stopping layer in $T, 2 \ldots 21$ convention
S_S	Stopping sector
z^i_{RS}	z coordinate of inner ($i = 1$) and outer ($i = 2$) RSPC hit
E_{SL}	Energy deposited in stopping layer
t_{RS}	Time of track in range stack

Table D.3: List of range stack variables utilized in the analysis.

Summary of the Off-Line Selection Criteria (Part A)			
Cut	Def.	Acc.	Description
4SEC	4.6	7.2.3	Veto range stack tracks crossing 3 sector boundaries
B4DEDX	4.7	7.3.2	B4 hodoscope dE/dx consistent with a single kaon
B4DELC	4.3	7.3.2	$t_{RS} > t_K^{B4}$: t_K^{B4} was the average B4 time
BHTRS	4.7	7.3.2	Veto on beam hole-counter hits coincident with t_{RS}
BOX	4.10	7.2.3	Require total range $33 < R'_{tot} < 40$ cm Require total energy $115 < E'_{tot} < 135$ MeV Require total momentum $211 < P'_{tot} < 242$ MeV/c
CHITD	4.9.4	7.5.2	Require a 1% C.L. for $\pi \rightarrow \mu$ fit quantities
DC_FIT	4.1.2	7.3.1	Drift chamber track reconstruction
DCTG_XY	4.6	7.3.2	Require match in $x-y$ plane of drift chamber-target tracks at target periphery to within 1.5 cm (3 cm at PASS1)
DC_Z	4.4	7.3.2	DC based z position at DC outer wall: $\lvert z_{ow}\rvert < 25$ cm
DIPANG	4.4	7.2.3	DC track dip-angle cut: $\lvert\cos\theta_D\rvert < 0.55$
DPIK	4.6	7.3.2	Cut on minimum $K-\pi$ separation in the target in the $x-y$ plane
EKBAR	4.6	7.4.1	Average kaon fiber excluding maximum kaon fiber > 3 MeV for $N_\Delta^K > 2$
EKMAX	4.6	7.4.1	Maximum kaon fiber energy: $\max(E_\Delta^K) \geq 8$ MeV
ELVETO	4.9.5	7.5.2	Veto on "local region" RS activity at pion decay time
ELVETO2	4.9.5	7.5.2	Expansion of local region of ELVETO cut
ENERK	4.6	7.3.2	Target kaon energy: $20 \leq E_K \leq 140$ MeV
EPIBAR	4.6	7.4.1	Dip-angle corrected average pion triangle energy: $\langle E_\Delta^\pi\rangle < 2.0$ MeV
EPIMAX	4.6	7.4.1	Dip-angle corrected maximum pion triangle energy: $\max(E_\Delta^\pi) < 5.0$ MeV
ELCTRN	4.9.3	7.5.2	Require electron to complete $\pi \rightarrow \mu \rightarrow e$ decay sequence
FITPI	4.9.1	7.5.2	Stopping counter $\pi \rightarrow \mu$ double pulse fit
IC_E	4.6	7.3.2	I-counter energy $E_{IC} < 5$ MeV
INTIME	4.5	7.3.2	Veto on photon activity in the RS, BV, EC, IC and VC
KBEAM	4.7	7.3.2	Require a coincidence between $\check{C}_K$ and target kaon
KINPCA	4.8.2	7.5.1	Overall energy-momentum-range correlation: $\mathrm{CL_{kin}} > 0.20$
KROAD	4.6	7.3.2	Extrapolated DC track intersects at least one kaon fiber
LAYER14	4.4	7.2.3	For events with $S_L = 14$, DC track dip-angle cut: $-0.35 < \cos\theta_D < 0.50$ Veto on outer layer RSPC in the S_S or $S_S + 1$ sector

Table D.4: The column denoted "Def." gives the section where the cut is described in detail. The column labeled "Acc." gives the section where the acceptance measurement of the cut is described.

Summary of the Off-Line Selection Criteria (Part B)			
Cut	Def.	Acc.	Description
NTRIK	4.6	7.3.2	Number of kaon triangles: $N_{\Delta}^{K} < 11$
NTRK_RS	4.1.3	7.3.1	One and only one DC/RS track match
PHOTOV	4.8.3	7.5.1	Require that maximum excess of energy in a given RS layer be less than 4σ.
PIBEAM	4.7	7.3.2	Veto on $\check{C}_{\pi}$ hits coincident with t_{RS}
PIKTIME	4.3	7.3.3	$t_{\pi}^{tgt} - t_{K}^{tgt} > 2$ ns for fiber based t_{π}^{tgt}
PIKTIME2	4.3	7.3.3	$t_{\pi}^{tgt} - t_{K}^{tgt} > 4$ ns for I-counter based t_{π}^{tgt}
PISCUT	4.7	7.3.2	Veto on secondary BWPC tracks coincident with t_{RS}
PREFIT	4.9.1	7.5.2	Single pulse fit quality, $C_{\mu} > 1.8(1.6)$ for 1989 (1990)
P_DC	4.1.2	7.2.3	Require $P_{DC} < 270$ MeV/c
RNGMOM0	4.8.1	7.5.1	Range-momentum mass hypothesis: $\mathrm{CL}_{\pi} > 0.01$ for RS tracks with longer than expected range
RSHEX	4.9.6	7.5.2	Require $4 < E_{SL} < 35$ MeV, < 3 counters hit in S_H and no unused ADC hits
RS_DEDX	4.8.3	7.5.1	RS energy deposition topology consistent with a pion
RS_Z1	4.6	7.5.1	Require an inner RSPC z hit with $\lvert z_{RS}^{1} - z_{DC}^{1}\rvert < 12$ cm
RS_Z2_D	4.4	7.2.3	For $S_L > 14$ and $\lvert\cos\theta_D\rvert > 0.30$, require outer RSPC z hit with $\lvert z_{RS2}^{2} - z_{DC}^{2}\rvert < 12$ cm
RTDIF	4.6	7.3.2	Maximum K-π target cluster overlap of 2 cm
STLAY_RS	4.4	7.2.3	Off-line stopping layer cut: $11 \leq S_L \leq 18$
TARGET	4.1.1	7.3.1	Target reconstruction
TDFOOL	4.9.5	7.5.2	Veto on double pulse signature in $S_L - 1$ or $S_L - 2$ counters
TD_ANAL	4.9.4	7.5.2	Combined PCA $\mathrm{CL}_{\mathrm{TD}}$ and Fisher variable cut
TD_PCA	4.9.4	7.5.2	6 variable PCA based confidence level cut $\mathrm{CL}_{\mathrm{TD}} > 0.01$
TGPCA	4.6	7.4.1 7.4.1	8 variable PCA based confidence level of target timing and energy distributions: $\log(\mathrm{CL}_{\mathrm{tgt}}) > -1.8$
TGT_Z	4.4	7.3.2	DC based z position of the decay vertex: $-12 < z_{vtx} < 16$ cm
TGVET	4.5.1	7.3.2	Veto on photon activity in the target
TICTG	4.1.1	7.3.1	Require valid target or I-counter time
TIMEKS	4.6	7.3.2	RMS deviation of t_{K}^{tgt}, $\sigma_{t}^{K} < 2$ ns
TMUADC	4.9.2	7.5.2	Require $t_{\mu}^{av} < 75$ ns
TMUAV	4.9.2	7.5.2	Require pion decay time $t_{\mu}^{av} > 8$ ns
TMUBM	4.9.6	7.5.2	Veto on $\check{C}_{\pi}$ and $\check{C}_{K}$ activity at pion decay time
TMUBV	4.9.6	7.5.2	Veto on BV activity in proximity to S_S at pion decay time
TRKTIM	4.1.3	7.3.1	Require valid range stack track time
TRS	4.3	7.3.2	$t_{RS} > t_{K}^{BM}$: where t_{BM} was the beam strobe time
TRSTG	4.6	7.4.1	$\lvert t_{RS} - t_{tgt}^{\pi}\rvert < 8$ ns: Target-range stack track time match

Table D.5: The column denoted "Def." gives the section where the cut is described in detail. The column labeled "Acc." gives the section where the acceptance measurement of the cut is described.

VITA

Surname:	Turçot	Given Names:	André Spence
Place of Birth:	Halifax, Nova Scotia, Canada	Date of Birth:	23 September 1962

Educational Institutions Attended:

Concordia University	Fall 1982 to Spring 1985
University of Victoria	Fall 1985 to Spring 1994

Degrees Awarded:

B.Sc.	Concordia University	Spring 1985
M.Sc.	University of Victoria	Fall 1987

Honours and Awards:

University of Victoria Graduate Teaching Fellowship 1988-93

Publications:

M.S. Atiya *et al.*, Search for the decays $K^+ \to \pi^+ \nu\overline{\nu}$ and $K^+ \to \pi^+ X^0$ for $150 < M_{X^0} < 250$ MeV/c^2, Physical Review D, Volume 48, p. 1 (1993).

M.S. Atiya *et al.*, Search for the decay $K^+ \to \pi^+ \nu\overline{\nu}$, Physical Review Letters, Volume 70, p. 2521-2524 (1993).

D. Axen *et al.*, The lead liquid argon sampling calorimeter of the SLD detector. Nuclear Instruments and Methods in Physics Research A, Volume 328, p. 472-494, (1993).

M.S. Atiya *et al.*, A detector to search for $K^+ \to \pi^+ \nu\overline{\nu}$, Nuclear Instruments and Methods in Physics Research A, Volume 321, p. 129-151 (1992).

M.S. Atiya *et al.*, Search for the decay $\pi^0 \to \gamma X$, Physical Review Letters, Volume 69, p. 733-736 (1992).

PARTIAL COPYRIGHT LICENSE

Title of Thesis: The Search for the Decay $K^+ \rightarrow \pi^+ \nu\bar{\nu}$

Author: _____
Signature

André Spence Turcot
(Name in Block Letters)

May 25 1994
(Date)